

# UNIVERSITÉ DE GRENOBLE

## THÈSE

POUR OBTENIR LE GRADE DE

DOCTEUR DE L'UNIVERSITÉ DE GRENOBLE

Spécialité: Matériaux, Mécanique, Génie Civil,  
Électrochimie

Arrêté ministériel : 7 août 2006

PRÉSENTÉE PAR

**Valentina PESCHETOLA**

THÈSE DIRIGÉE PAR **Claude VERDIER** ET **Valérie LAURENT**  
**Luigi PREZIOSI** ET **Davide AMBROSI**

PRÉPARÉE AU SEIN DU **Laboratoire Interdisciplinaire de Physique,**  
**Université de Grenoble** ET DU **Dipartimento di Matematica,**  
**Politecnico di Torino**

DANS L'École Doctorale: **IMEP2** ET L'École Doctorale: **DIMAT**

## Détermination des forces de traction au cours de la migration de cellules cancéreuses sur des gels

THÈSE SOUTENUE PUBLIQUEMENT LE **14 Novembre 2011**,  
DEVANT LE JURY COMPOSÉ DE:

**M. François GALLET**

PU, Paris VII, Rapporteur

**M. Francesco MOLLICA**

PU, Università di Ferrara, Rapporteur

**M. Claude VERDIER**

DR, Université de Grenoble, Membre

**Mme. Valérie LAURENT**

MC, Université de Grenoble, Membre

**M. Luigi PREZIOSI**

PU, Politecnico di Torino, Membre

**M. Davide AMBROSI**

PU, Politecnico di Milano, Membre



## Acknowledgments

It is a pleasure to thank the many people who made this thesis possible. I would like to thank all my advisors, Dr. Claude Verdier and Dr. Valérie Laurent in Grenoble and Prof. Luigi Preziosi in Torino and Prof. Davide Ambrosi in Milano for giving me the opportunity to pursue my PhD thesis research under their guidance.

I would like to express my gratitude to Prof. François Gallet and Prof. Francesco Mollica to have accepted the duty to be referees.

This thesis would not have been possible without Dr Alain Duperray (IAB) whose expertise, and patience help me considerably in the graduate experience. Thanks to Alexeï Grichine (IAB) for his kind assistance on the microscope facilities.

Many thanks to Richard Michel for helping me writing the FFTC programs and for showing me the Matlab tricks.

I would also like to thank all DyFCom group, all the PhD students at Liphy and in the Dimat of Torino for having create a special atmosphere.

Finally thanks to my family for their constant encouragements and appreciation.



---

## Abstract

The migration process is a physically integrated molecular phenomena that contributes to many physiological motility *in vivo* processes such as development, immune surveillance and cancer metastasis. To understand cell migration it is necessary to consider the cell's environment, cell type and morphology as well as the internal organization of the cells, i.e. its cytoskeleton and focal adhesions. This work focuses on the study of migrating bladder cancer cells on two-dimensional deformable substrates. The analysis of a panel of three cell lines with different invasive capacity is presented. The ability of cancer cells to respond to their environment is analysed and the migration process is described in terms of traction stresses. The internal reorganization of cells structure is studied by microscopic observation of the actin filaments, the myosin motors and the sites of force transmission, i.e. the focal adhesions. The complementary relationship among different invasive capacities of cancer cells, traction stresses as well as the forces exerted on the lamellipodium and internal structures of cells are discussed. It is found that several parameters can be used for discriminating invasiveness, such as migration type, traction forces, focal adhesion areas, as well as the migration diffusivity index. This study therefore constitutes a first attempt to differentiate various invasive cells using migration on soft substrates.

## Résumé

Le processus de migration est un processus moléculaire intégré qui contribue à de nombreux processus physiologiques de motilité *in vivo*, comme le développement, la surveillance immunitaire et les métastases du cancer. Pour comprendre la migration cellulaire, il est nécessaire de considérer l'environnement de la cellule, le type cellulaire et la morphologie ainsi que l'organisation interne, i.e. son cytosquelette et ses adhérences focales. Ce travail se concentre sur l'étude de la migration des cellules cancéreuses de la vessie sur un support déformable. L'analyse de trois lignées cellulaires présentant des capacités métastatiques différentes est présentée. La capacité des cellules cancéreuses à réagir à leur environnement est analysée et le processus de migration est

décrit en termes de contraintes de traction. La réorganisation interne de la structure cellulaire est étudiée par l'observation microscopique des filaments d'actine, les moteurs de myosine et les sites de transmission de force, i.e. les adhérences focales. La relation de complémentarité entre les différentes capacités invasives des cellules cancéreuses, les forces de traction ainsi que les forces exercées sur le lamellipode et les structures internes des cellules sont discutées. Il est constaté que plusieurs paramètres peuvent être utilisés pour discriminer la capacité métastatique, comme le type de migration, les forces de traction, les zones d'adhérence focale, ainsi que l'indice de diffusivité de migration. Cette étude constitue donc une première tentative de différencier diverses cellules invasives utilisant la migration sur des substrats mous.

# Contents

<b>1</b>	<b>Introduction</b>	<b>9</b>
1.1	Introduction en français . . . . .	16
<b>2</b>	<b>Basic properties of eukaryotic cells</b>	<b>23</b>
2.1	The cell and its environment . . . . .	23
2.1.1	The cell membrane . . . . .	26
2.1.2	The cell cytoskeleton . . . . .	27
2.1.3	The focal adhesion sites . . . . .	30
2.1.4	Myosin motors . . . . .	32
2.1.5	The extra-cellular matrix . . . . .	34
2.2	Particular features of cancer cells . . . . .	35
<b>3</b>	<b>Determination of traction forces</b>	<b>41</b>
3.1	Overview of available models . . . . .	41
3.1.1	Boundary element method (BEM) . . . . .	44
3.1.2	Fourier transform traction cytometry (FTTC) . . . . .	47
3.1.3	Traction reconstruction with point force (TRPF) . . . . .	48
3.2	The adjoint method (AM) . . . . .	49
3.3	A critical comparison . . . . .	55
<b>4</b>	<b>Experimental methods</b>	<b>59</b>
4.1	Cell types . . . . .	59
4.1.1	Cell culture and invasivity . . . . .	60
4.1.2	Cell migration assays and mean square displacement . . . . .	60
4.1.3	Cell mechanical properties . . . . .	63

4.2	Gels . . . . .	67
4.2.1	Gel preparation . . . . .	67
4.2.2	Rheometry . . . . .	68
4.2.3	AFM measurements . . . . .	69
4.3	Microscopy . . . . .	71
4.3.1	Immunofluorescence staining of cells . . . . .	73
4.4	Determination of the displacement field . . . . .	76
4.5	Computation of the traction stresses . . . . .	78
4.6	Forces exerted on lamellipodium . . . . .	79
4.7	Statistical analysis . . . . .	81
<b>5</b>	<b>T24 traction forces on gels with different rigidities</b>	<b>83</b>
5.1	Cell morphology on different substrates . . . . .	84
5.2	Traction forces . . . . .	87
5.3	Discussion . . . . .	90
<b>6</b>	<b>Comparison between three different cancer cell lines</b>	<b>95</b>
6.1	Time-dependent traction stresses for each cell line . . . . .	96
6.2	Global forces exerted on the lamellipodium . . . . .	102
6.3	Characterization of the cell motion . . . . .	109
6.4	Actin and myosin networks . . . . .	112
6.5	Focal adhesion zones . . . . .	116
6.6	Discussion . . . . .	122
<b>7</b>	<b>Conclusions</b>	<b>129</b>
7.1	Conclusions en français . . . . .	132
	<b>Bibliography</b>	<b>137</b>
	<b>Appendix 1</b>	<b>149</b>
	<b>Appendix 2</b>	<b>157</b>
	<b>Appendix 3</b>	<b>171</b>

CONTENTS	7
----------	---

---

Appendix 4	181
------------	-----



# Chapter 1

## Introduction

This thesis concerns the study of the individual 2D migration of cancer cells on deformable substrates.

Cell migration plays a crucial role in many aspects of healthy physiology, and its misregulation can lead to a variety of pathologies. *In vivo* single-cell and collective migration are mutually exclusive purposes during morphogenesis, tissue regeneration, and in pathological conditions. Shaping, building, and remodelling complex tissues and tissue compartments, such as epithelia, and vessels, are driven by collective cell migration that also contributes to cancer progression by local invasion [44]. In contrast, single-cell migration allows cells either to cover local distances and penetrate tissues, such as neural crest cell migration, or to move from one location in the body to another and fulfil effector functions, such as immune cell trafficking [45, 68]. The latter process is recapitulated during cancer metastasis to distant sites.

When cells move as single entities, the cell motility is affected by adhesion strength, the type of substratum (including extracellular matrix ligands and other cells), environmental cues, differences in the rigidity and pliability of the matrix, dimensionality, and the organization of the cytoskeleton.

Migration is usually analysed as a set of processes (figure 1.1) which are often regulated by the same effectors regardless of the cell type and the migration mode. These processes include polarization, protrusion and adhesion, translocation of the cell body and retraction of the rear [70, 98]. Signalling

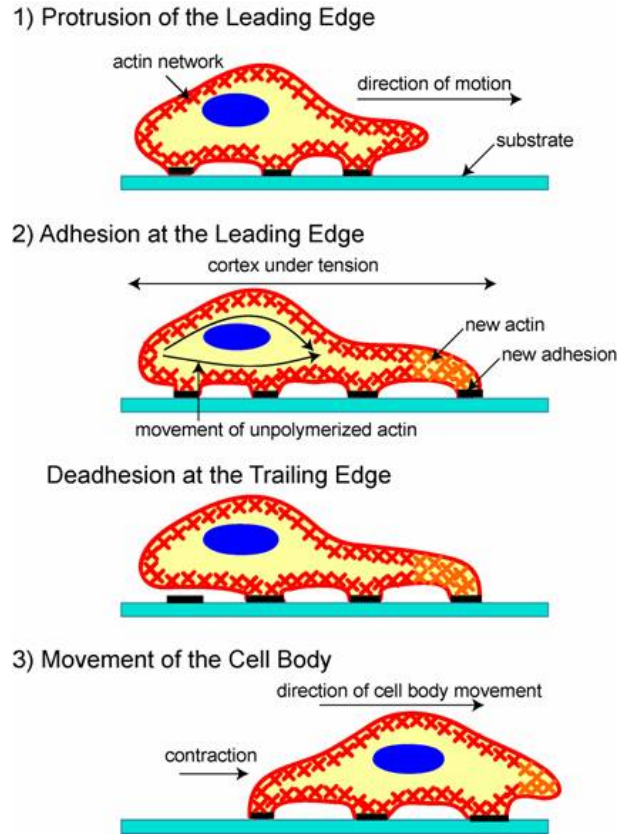


Figure 1.1: Schematic illustration of cell locomotion: the cell extends its protrusions in the direction of the movement, then it adheres on the substrate. The actin–myosin contraction drives the body translocation. Finally the cell disassembles its adhesions in rear part. Picture taken from Molecular Biology of the Cell [9].

networks coordinate and integrate these processes. Polarization is the ability of migrating cells to form a stable and distinct front and rear. Intense actin polymerization that generates a protrusive structure, and adhesion to the substratum characterize the leading edge. The trailing edge is characterized by stable bundles and the release and disassembly of adhesions. Nucleus and microtubules (which exhibit different degrees of polarization depending on the cell type) usually occupy the central part of the cell. Protrusion is the *de novo* formation of membrane extensions at the leading edge in the direction of migration [27]. It is mainly driven by actin polymerization that results



from the nucleation of new filaments and the availability and addition of new monomers [88]. Protrusion establishes contacts with the substratum, which provides traction for the movement of the rest of the cell body and signals that regulate actin polymerization. Integrin receptors allow the cell to adhere on the substrate and at the same time make the link between the substratum and the cytoskeleton. Over 150 different molecules populate sites of adhesion. Some are organized into signalling complexes that contain kinases and adapter proteins that serve to bring different signalling components together. Paxillin and focal adhesion kinases (FAK) are two among many important signalling components in adhesions. Signalling molecules and their downstream effectors drive the spatio-temporal regulation of these structures; the most prominent of these are the Rho family GTPases [64, 90]. A coordinated contraction of the acto-myosin cytoskeleton drives body translocation. Myosin II and microtubules are responsible of the nucleus translocation. Rear retraction requires the coordinated contraction of the actin cytoskeleton and disassembly of the adhesions at the trailing edge [56]. Adhesion disassembly is controlled by several mechanisms like acto-myosin contraction that exerts force against the adhesion promoting its ripping [80] (many cell types even leave footprint of integrin receptors behind [70]), microtubule-induced adhesion disassembly.

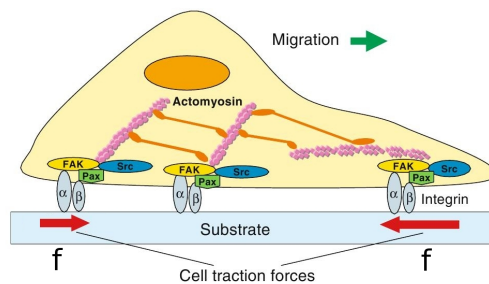


Figure 1.2: The traction forces are generated from the actin-myosin contractility and are transmitted to the substrate through the focal adhesion sites.

Migration depends on the spatial and temporal organization of multiple forces. The forces generated by the actin-cytoskeleton are transmitted to the extracellular matrix through the focal adhesions; these forces are usually

referred to as *traction stresses*, figure 1.2. The study of the cell–substrate interaction was strongly developed during the last twenty years. The idea to measure the traction stresses exerted by moving cells on 2D deformable substrates has been developed in 1980 by Harris and co-workers [60]: they can qualitatively analyse these forces observing the magnitude and shape of wrinkles on a soft elastic film below a cell. Further developments by Burton *et al.* [19], based on the study of keratocytes locomotion, revealed to be quite quantitative. The two techniques that led to interesting results for the migration process are due to Dembo and Wang [31, 32] and to Balaban and co-workers [15]. The first approach use the displacement of fluorescent beads embedded in an elastic gel deformed by a cell in order to obtain the forces; the latter one measures directly the force of the cells looking at the deformation of micro-patterned substrates. Experimental improvements were made thanks especially to the method developed by Balaban. In particular, the micro-fabricated force sensor substrate has been replaced by an array of microneedles of silicone elastomer by Tan *et al.* [100] allowing at the same time to manipulate the mechanical compliance and the surface chemistry. Du Roure and co-workers [37] improved the spatial force resolution of this last technique by increasing the pillar density. Ghibaudo *et al.* [53] show a force–rigidity relationship for migrating 3T3 fibroblasts on substrates with different rigidities.

The technique of Dembo and Wang [32] has been the hint for the development of several models for the computation of the traction forces. The basic idea is to measure the displacements of fluorescent beads embedded in rigid substrates of polyacrylamide in order to obtain the value of traction forces. All these method require the resolution of an inverse problem. Dembo and Wang used the boundary element method (BEM) to achieve this aim, using a Tikhonov regularization scheme. Butler *et al.* [20] solved the same elastic problem but in the Fourier space, simplifying the computational cost of the boundary element method, the so called Fourier Transform Traction Cytometry (FTTC). Adding the information of the position of the focal adhesion sites, Schwarz and co-workers [97] managed to solve a system of linear equations rather than an integral one. Ambrosi [10] proposed a different ap-

proach based on the formulation arising from the minimization of an energy, combined with the use of a penalty parameter. Merkel *et al.* [76] improved the spatial resolution of Dembo technique with the use of a thin elastic film. They explicit the equations for the mechanical response of an elastic layer of finite thickness to point forces.

As pointed out by Schwarz and co-workers [97] the regularization schemes were necessary for cellular force reconstruction from the sampled displacement data. Sabass *et al.* [93] analysed the approaches based on the integral boundary element method (BEM) [32], the one using the Fourier Transform Traction Cytometry (FTTC) [20], and the one using Traction Recovery with Point Forces (TRPF) [97]. The TRPF procedure seems to be the most promising one, as long as focal adhesions are well developed, but requires of course more sophisticated experiments. Huang and co-workers [63] stabilized the force reconstruction by modifying the Green's function such that the regularizations can be avoided under proper conditions.

The use of flat elastic substrates as well as the microneedles system helped understanding the cell-substrate interactions. Micro-contact printing of adhesive patterns was used to show that cell fate depends not on the amount of ligand for adhesion receptors, but on its spatial distribution [85]. The fabrication of elastic substrates with a rigidity gradient by Lo *et al.* [74] shows that cultured cells can guide their movements by probing the substrate rigidity (durotaxis) and that cells usually exert larger traction forces on more rigid substrates. This behaviour has been correlated with an increased contact surface and a reduced migration velocity. The traction force increases for larger stiffness until a critical rigidity is reached (around  $80kPa$ ), where the force exhibits a plateau [53].

The adhesion structures and cytoskeleton of adherent cells strongly adapt to substrate stiffness [85, 74, 36]. It has been shown that differentiation of mesenchymal stem cells is strongly influenced by substrate stiffness [41]. Geiger *et al.* [51] underline the importance of physical factors, such as pliability, ligand spacing and dimensionality of the substrate, as well the biochemical one for the cellular response to its substrate. Buxboim *et al.* [21] use the technology of soft elastic substrates to measure how far mesenchymal

stem cells can mechanically sense into their substrate.

A same cell can assume different migratory modes in different environments and there are different modes of cell migration depending on the cell type and the context in which it is migrating. It is particularly striking that tumour cells have the ability to switch between different modes of locomotion in response to environmental changes [46]. This allows them to overcome obstacles for a given type of motility, a behaviour that renders the task of fighting metastasis particularly difficult.

The ability to metastasise is a hallmark of malignant tumours [58, 59]. Metastasis is the process whereby cancer cells spread throughout the body, establishing new colonies in organs at a distance from the one where the primary tumour originated. Cancer cells possess a broad spectrum of migration and invasion mechanisms. In a three-dimensional environment, the protrusive force of actin polymerization drives cells into an elongated, or mesenchymal morphology that is sufficient to push through the extracellular matrix. However, a second mode of motility may be observed in a three-dimensional context in which cells adopt a rounded morphology and migrate through the extracellular matrix by an amoeboid form of movement using actin-myosin contractile force to generate bleb-like protrusions that push and squeeze cells through the matrix [105]. Sanz-Moreno *et al.* [95] revealed the ability of the tumour cells to switch between different modes of movement, demonstrating the tight interplay between Rho and Rac in determining different modes of tumour cell movement.

Paszek *et al.* [84] investigated the role that the extracellular matrix plays in tumour cell growth. Tumours are generally stiffer than surrounding healthy tissue, a characteristic that has been exploited in certain diagnostic procedures such as breast self-examination. Paszek and co-workers revealed that even a small increase in matrix rigidity enhanced epithelial cell growth. These results suggest that factors causing a sustained increase in matrix stiffness, for example, a chronic inflammatory response, may promote malignant transformation. Another factor that we have to consider is the mechanical stiffness of individual tumour cells: several authors [29, 47] showed that cancer cells were significantly softer than normal cells.

Few studies have been done on the forces exerted by tumour cells. Li *et al.* [72] used silicone nanowire arrays and showed that cancer cells exhibit larger traction stresses than normal cells. Results go in the same direction as the finding of Ghosh *et al.* [55] and the recent work of Mierke and co-workers [77]: tumour cells are more contractile than normal cells and exhibit a higher migration speed. Conflicting results have been found by Munevar *et al.* [79] and Indra *et al.* [65] who found that the traction stresses are inversely related to the metastatic capacity of the cells.

These discrepancies may be could be related to local mechanism of force transmission. Recent works of the Gardel's group [12, 13, 99] underline the complexity of the force transmission mechanism to the substrate. In fact, Aratyn-Schaus and Gardel [12] claim that this process cannot be correlated directly with the focal adhesions size across an entire cell. The local traction stresses are correlated with focal adhesions morphologies only during a process called “frictional slip” [24], the rapid retrograde displacement of the focal adhesion relative to the extracellular matrix. The correlation fails once the focal adhesions reach the maturation stage. Mature focal adhesions can sustain larger stresses without changes in elongation [99].

Even though the migration is a multi-step process, often the time evolution analysis of the forces is missing. In this work, we will focus on the study of migrating bladder cancer cells on two-dimensional deformable substrates. We will analyse a panel of three cell lines with different invasive capacity. We will investigate the ability of cancer cells to respond to their environment and we will try to understand the locomotion of the cell in terms of traction stresses. In order to understand how these cancer cells reorganize their internal structure, we will analyse the actin filaments, myosin II and the sites of force transmission, the focal adhesions.

The aim of this thesis is to investigate the complementary relationship among the different invasive capacities of the cancer cells, the traction stresses as well as the forces exerted on the lamellipodia and the focal adhesion sites. Moreover, we would like to correlate the velocity of the cells, the type of migration and the internal structure of the cancer cells.

This thesis is organized in five chapters. Chapter 2 will be a general

introduction of the cell and its characteristics with a particular attention to the structure of the cell cytoskeleton. In chapter 3 we will discuss the mathematical model presented in the literature, and it will be focused on the adjoint model that was used in this work for the computation of the traction force and we will outline the differences among the models. Chapter 4 will introduce all the experimental methods adopted in this work, the necessary steps for preparing the experiments, from beads detection to the computation of the traction stresses. Chapter 5 will present the features of the T24 cancer cells on substrates of different rigidities by analysing the morphology of the cell, the traction stresses exerted on the underlying gel and the cytoskeleton organization. In chapter 6 we will study three different cancer cell lines: we will analyse the migration process of the cells in time, characterizing the traction forces, the force exerted on the lamellipodium and migration parameters. We will observe the internal organization of these cells in terms of actin cytoskeleton, myosin motors and focal adhesion sites.

## 1.1 Introduction en français

Cette thèse concerne l'étude de la migration individuelle des cellules cancéreuses sur un substrat déformable 2D.

La migration cellulaire joue un rôle crucial dans de nombreux aspects de la physiologie, et sa dérégulation peut conduire à une variété de pathologies. *In vivo* la migration d'une cellule isolée et la migration collective sont deux processus mutuellement exclusif lors de la morphogenèse, la régénération des tissus, et dans des conditions pathologiques.

La construction et le remodelage des tissus complexes ou des compartiments tissulaires, comme l'épithélium et les vaisseaux sanguins, sont liés à la migration collective des cellules qui contribuent également à la progression du cancer par l'invasion locale [44]. En revanche, la migration d'une cellule isolée permet de couvrir des distances importantes et pénétrer dans les tissus ou se déplacer dans le corps humain d'un endroit à l'autre. Ce dernier processus est présent lors de la métastase.

Lorsque les cellules se déplacent individuellement, la motilité des cellules

est affectée par les forces d'adhérence, le type de substrat (y compris les ligands de la matrice extracellulaire et d'autres cellules), les signaux environnementaux, les différences de rigidité et souplesse de la matrice, la dimension, et l'organisation du cytosquelette.

La migration est généralement analysée comme un ensemble de processus (fig. 1.1) qui sont souvent réglementés par les effecteurs quel que soit le type de cellule et le mode de migration. Ces processus comprennent la polarisation, la protrusion et l'adhérence, la translocation du corps cellulaire et la rétraction de l'uropode [70, 98]. Les réseaux de signalisation permettent de coordonner et d'intégrer ces processus. La polarisation est la capacité des cellules qui migrent à former un front et un uropode stable et distinct. Le front de la cellule est caractérisé par une intense polymérisation d'actine qui génère une structure de propulsion, et l'adhérence au substrat. L'arrière de la cellule est caractérisé par le désassemblage des sites d'adhérences. Le noyau et les microtubules (qui présentent différents degrés de polarisation en fonction du type cellulaire) occupent généralement la partie centrale de la cellule. La protrusion est la formation de protubérances membranaires au front de la cellule dans la direction de migration [27]. Elle est principalement induite par la polymérisation de l'actine qui résulte de la nucléation de nouveaux filaments et de la disponibilité de nouveaux monomères [88]. Avec la protrusion, la cellule établit des contacts avec le substrat; les adhérences assurent la traction pour le déplacement du reste du corps cellulaire. Les intégrines permettent à la cellule d'adhérer sur le substrat et en même temps, faire le lien entre le substrat et le cytosquelette. Plus de 150 molécules différentes peuplent les sites d'adhérence. Certaines sont organisées en complexes de signalisation qui contiennent des kinases et des protéines adaptatrices qui servent à assembler les différents composants de signalisation. La paxilline et les kinases d'adhésion focale (FAK) sont deux parmi les nombreuses composantes importantes de signalisation dans les adhérences. La signalisation des molécules et de leurs effecteurs conduit à la régulation spatio-temporelle de ces structures, les plus éminentes d'entre elles sont les Rho GTPases [64, 90]. Une contraction coordonnée du cytosquelette d'actomyosine permet à la cellule de se déplacer vers l'avant. La myosine II et les microtubules sont responsables

de la translocation du noyau. La rétraction de l'arrière nécessite la contraction coordonnée du cytosquelette d'actine et le désassemblage des adhérences à l'arrière [56]. Le désassemblage des sites d'adhésions à l'arrière de la cellule est contrôlé par plusieurs mécanismes comme la contraction d'actomyosine qui génère des forces contre l'adhésion et permet à la cellule de se déplacer vers l'avant [80]; de nombreux types cellulaires laissent des "empreintes" de récepteurs d'intégrine [70].

La migration dépend de l'organisation spatiale et temporelle de plusieurs forces. Les forces générées par le cytosquelette d'actine sont transmises à la matrice extracellulaire par les adhérences focales, et sont généralement dénommées *forces de traction* (figure 1.2). L'étude de l'interaction cellule-substrat a été fortement développée au cours des vingt dernières années. L'idée de mesurer les tractions exercées par les cellules sur des supports déformables a été développée en 1980 par Harris et co-auteurs [60]: ils peuvent qualitativement analyser ces forces en observant l'amplitude et la forme des plis sur un film souple et élastique sous la cellule. Cette méthode a été exploitée de façon quantitative par Burton *et al.* [19] pour étudier la locomotion des kératocytes. Les deux techniques qui ont conduit à des résultats intéressants pour le processus de migration sont dûs à Dembo et Wang [31, 32] et à Balaban et co-auteurs [15]. La première approche utilise le déplacement de billes fluorescentes incorporées dans un gel élastique déformé par une cellule pour obtenir des forces; la deuxième mesure directement la force des cellules en regardant la déformation des micro-pilier.

La technique de Dembo et Wang [32] a permis le développement de plusieurs modèles pour le calcul des forces de traction. L'idée de base est de mesurer les déplacements de billes fluorescentes intégrées dans les substrats rigides de polyacrylamide en vue d'obtenir la valeur des forces de traction. Toutes ces méthodes nécessitent la résolution d'un problème inverse. Pour atteindre cet objectif, Dembo et Wang utilisent la méthode des éléments de frontière (BEM), en utilisant un schéma de régularisation de Tikhonov. Butler *et al.* [20] ont résolu le même problème élastique, mais dans l'espace de Fourier, en simplifiant le coût de calcul de la méthode des éléments de frontière (FTTC). En ajoutant l'information de la position des



sites d'adhésion focale, Schwarz *et al.* [97] ont réussi à résoudre un système d'équations linéaires. Ambrosi [10] a proposé une approche différente basée sur la formulation résultant de la minimisation d'une énergie, combinée à l'utilisation d'un paramètre de pénalité. Merkel *et al.* [76] ont amélioré la résolution spatiale de la technique de Dembo avec l'utilisation d'une couche élastique moins épaisse.

Schwarz *et al.* [97] ont mis en relief la nécessité des schémas de régularisation pour la reconstruction de la force cellulaire à partir des données de déplacement échantillonnées. Sabass *et al.* [93] ont analysé les trois approches, BEM , FFTC et TRPF. La procédure TRPF semble être la plus prometteuse, tant que les adhérences focales sont bien développées, mais nécessite bien sûr des expériences plus sophistiquées.

L'utilisation de substrats élastiques ainsi que le système de micro-piliers ont aidé dans la compréhension des interactions cellule-substrat. Les micro-piliers ont été utilisés pour montrer que la distribution spatiale de ligands pour les récepteurs d'adhérence plutôt que la quantité peut influencer la locomotion des cellules [85]. La fabrication de substrats élastiques avec un gradient de rigidité par Lo *et al.* [74] a montré que les cellules cultivées peuvent guider leurs mouvements en sondant la rigidité du substrat (durotaxie) et que les cellules exercent habituellement des forces de traction plus importantes sur les substrats plus rigides. Ce comportement a été corrélé avec une augmentation de la surface de contact et une vitesse de migration réduite. La force de traction augmente pour les grandes rigidités jusqu'à une rigidité critique où la force présente un plateau [53]. Les structures d'adhérence et le cytosquelette s'adaptent fortement à la rigidité du substrat [85, 74, 36]. Il a été montré que la différenciation des cellules souches mésenchymateuses est fortement influencée par la rigidité du substrat [41]. Geiger *et al.* [51] ont souligné l'importance des facteurs physiques, tels que flexibilité, espacement des ligands et dimensionnalité du substrat, ainsi que biochimiques pour la réponse cellulaire sur son substrat.

Une même cellule peut assumer différents modes migratoires dans différents environnements et il y a différents modes de migration cellulaire en fonction du type cellulaire et le contexte dans lequel elle migre. La capacité des cel-

lules tumorales de changer entre différents modes de locomotion en réponse aux changements environnementaux il est particulièrement remarquable [46]. Cela leur permet de surmonter les obstacles pour un type donné de motilité, un comportement qui rend la mission de combattre les métastases particulièrement difficile.

La capacité de développer des métastases est une caractéristique des tumeurs malignes [58, 59]. La formation de métastase est le processus par lequel les cellules cancéreuses se propagent dans tout le corps, établissent de nouvelles colonies dans les organes distants de celui de la tumeur primaire. Les cellules cancéreuses possèdent un large éventail de mécanismes de migration et d'invasion. Dans une matrice 3D, la polymérisation de l'actine des cellules de morphologie allongée, ou mésenchymateuses, est suffisant pour favoriser la migration à travers la matrice extracellulaire. Cependant, un second mode de motilité peut être observé dans un contexte tridimensionnel: les cellules adoptent une morphologie arrondie et migrent à travers la matrice extracellulaire avec une forme amiboïde de mouvement à l'aide de la force contractile de l'actine-myosine qui permet de générer des structures de "bleb" qui poussent et entraînent les cellules à travers la matrice [105]. Sanz-Moreno *et al.* [95] ont révélé la capacité des cellules tumorales à basculer entre différents modes de migration, démontrant l'interaction étroite entre Rho et Rac dans la détermination de différents modes de migration des cellules tumorales.

Paszek *et al.* [84] ont étudié le rôle que joue la matrice extracellulaire dans la croissance des cellules tumorales. Les tumeurs sont généralement plus rigides que les tissus sains, une caractéristique qui a été exploitée dans certaines procédures de diagnostic tels que l'auto-examen. Ils ont révélé que même une faible augmentation de la rigidité de la matrice cellulaire peut augmenter la croissance épithéliale. Ces résultats suggèrent que des facteurs provoquant une augmentation soutenue de la rigidité de la matrice, par exemple, une réponse inflammatoire chronique, peuvent favoriser la transformation maligne. Un autre facteur que nous avons à considérer est la rigidité mécanique des cellules tumorales isolées: plusieurs auteurs [29, 47] ont montré que les cellules cancéreuses étaient significativement plus molle

que les cellules normales.

Peu d'études ont été réalisées sur les forces exercées par les cellules tumorales. Li *et al.* [72] ont utilisé des micro-pilules en silicone et ont montré que les cellules cancéreuses présentent des contraintes de traction plus grandes que les cellules normales. Ces résultats vont dans la même direction que le résultats de Ghosh *et al.* [55] et les récents travaux de Mierke *et al.* [77]: les cellules tumorales sont plus contractiles que les cellules normales et présentent une plus grande vitesse de migration. Des résultats contradictoires ont été trouvés par Munevar *et al.* [79] et Indra *et al.* [65] qui ont constaté que les tractions sont inversement proportionnelles à la capacité métastatique des cellules.

Ces divergences pourraient être liés à un mécanisme local de transmission de force. Des travaux récents du groupe de Gardel [12, 13, 99] soulignent la complexité du mécanisme de transmission de force sur le substrat. En fait, Aratyn-Schaus et Gardel [12] soutiennent que ce processus ne peut pas être directement corrélé avec la taille des adhérences focale dans une cellule. Les contraintes locales sont corrélées avec la taille des adhérences focales seulement pendant un processus de “glissement” [24], i.e. le déplacement rapide rétrograde de l'adhérence focale par rapport à la matrice extracellulaire. La corrélation disparaît une fois que les adhérences focales atteignent le stade de maturation. Les adhérences focales matures peut résister à de grandes contraintes, sans modifier leur élongation [99].

Même si la migration est un processus à plusieurs étapes, il manque souvent l'analyse de l'évolution des forces dans le temps. Dans ce travail, nous allons nous concentrer sur l'étude de la migration de cellules cancéreuses de la vessie sur un support déformable en deux dimensions. Nous allons analyser trois lignées de cellules de capacité invasive différente. Nous allons étudier la capacité des cellules cancéreuses à répondre à leur environnement et nous allons essayer de comprendre la migration des cellules en termes de forces de traction. Afin de comprendre comment ces cellules cancéreuses réorganisent leur structure interne, nous allons analyser les filaments d'actine, la myosine II et les sites de transmission de force, i.e. les adhérences focales.

L'objectif de cette thèse est d'étudier la relation de complémentarité entre

la capacité invasive des différentes cellules cancéreuses, les tractions ainsi que les forces exercées sur les lamellipodes et les sites d'adhésion focale. Par ailleurs, nous voudrions corrélérer la vitesse des cellules, le type de migration et la structure interne des cellules cancéreuses.

Cette thèse est organisée en cinq chapitres. Le chapitre 2 sera une introduction générale de la cellule et de ses caractéristiques avec une attention particulière à la structure du cytosquelette de la cellule. Dans le chapitre 3, nous discuterons les modèles mathématiques présentés dans la littérature, et il sera centré sur le modèle adjoint qui a été utilisé dans ce travail pour le calcul des forces de traction; nous expliquerons les différences entre les modèles. Le chapitre 4 présentera toutes les méthodes expérimentales adoptées dans ce travail, les mesures nécessaires pour préparer les expériences. Le chapitre 5 présentera les caractéristiques des cellules cancéreuses T24 sur des substrats de rigidités différentes, en analysant la morphologie de la cellule, les forces de traction exercées sur le gel et l'organisation du cytosquelette. Dans le chapitre 6, nous allons étudier trois lignées cellulaires de cancer différentes. Nous allons analyser le processus de migration de ces cellules dans le temps, la caractérisation des forces de traction, la force exercée sur les lamellipodes et les paramètres de migration. Nous allons ensuite observer l'organisation interne de ces cellules en termes de cytosquelette d'actine, de myosine et de sites d'adhésion focale.

## Chapter 2

# Basic properties of eukaryotic cells

In this chapter, a short description of eukaryotic cells will be presented and the structures involved during the cell migration process will be detailed. The characteristics of the tumour cells will be described.

*Dans ce chapitre, nous présenterons une courte description des cellules eucaryotes, et les structures impliquées pendant le processus de migration cellulaire seront détaillées. Les caractéristiques des cellules tumorales seront décrites.*

### 2.1 The cell and its environment

The word cell comes from the Latin *cellula* and it means “small room”. This was the name that the English scientist Robert Hooke coined in 1665 when he compared the cork cells he saw through his microscope to the small rooms monks lived in. Only two centuries later, in 1839, two German scientists, Schleiden and Schwann, formally articulated the basis of the cell theory. Subsequent discoveries and the works of many scientists, leads to the modern tents of the cell theory that includes:

- the cell is the unit of structure, physiology and organization in living

things;

- everyone knows that living things are made up of one (unicellular organisms) or more cells (multi-cellular organisms);
- all cells come from pre-existing cells by division (*omnis cellula e cellula*, the dictum of Rudolph Virchow);
- the hereditary information cells contain is passed from cell to cell during cell division;
- metabolism and biochemistry, the energy flow of life, occur within cells;
- all cells have basically the same composition;
- the activity of organisms is determined by the activity of independent cells.

For these reasons the cell is often referred to as the fundamental units of life. Millions of types of cells exist: cells that are organisms themselves, like bacteria or microscopic amoeba, or cells that function as part of a larger organism, like the cells of our body.

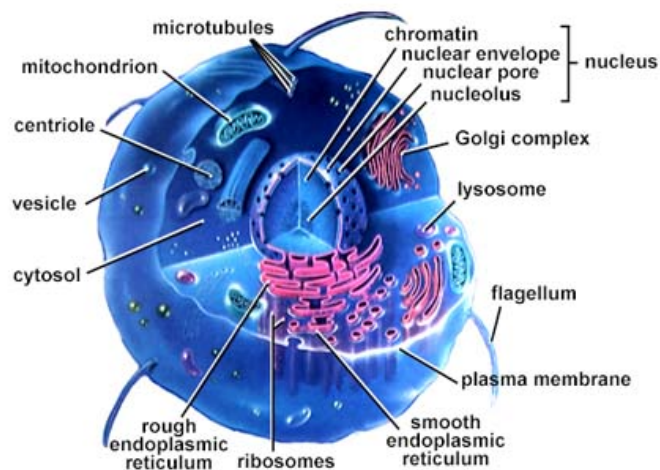


Figure 2.1: The major features of eukaryotic cells. It consists of many organelles ranging from the nucleus, mitochondria, Golgi apparatus, membrane and cytoskeleton. Picture taken from On-Line Biology Book [6].

All the cells have unique functions and features as well as some recognizable similarities. Figure 2.1 shows the major components of eukaryotic cells. The cell is an intricate network of organelles (membrane-enclosed compartments) that have a unique function and allow the cell to function properly. The nucleus contains the DNA, the genetic code that coordinates protein synthesis. Ribosomes participate to proteins synthesis. Mitochondria are the energy factories of the cells. They convert energy into forms that are usable by the cell. The Golgi apparatus is a stack of flattened compartments and modifies proteins and lipids that have been built in the endoplasmatic reticulum and prepares them to be exported outside of the cell or to be transported to other locations in the cell. Lysosomes are organelles that contain enzymes responsible for the digestion of nutrient molecules and others materials.

In our body, cells are assembled into a variety of types of tissue such as epithelia, connective tissue, muscle and nerve tissue. The features of these types of tissues are related to the cell number and the cell spacing, that define a precise tissue geometry. The task of adhesive molecules is to help maintain contact between nearby cells and structures in order to preserve proper tissue architecture. Tiny gap junctions allow the passage of ions and small molecules between adjacent cells. In the meantime, signalling molecules relay positional information among the cells in a tissue, as well as between these cells and the extracellular environment.

The important class of adhesive molecules is the *integrins*. The integrins are the mechanical links that allow cells to maintain contact with structures in the extracellular matrix. These molecules also supply signal both to and from cells and play an important role in sensing the environment and controlling cell shape and motility. The integrins are a family of transmembrane receptors and each individual integrin consist of  $\alpha$  and  $\beta$  subunits. Some integrins are connected to actin filaments. After the binding of a typical integrin to its ligand in the matrix, the cytoplasmic tail of the  $\beta$  subunit binds to several intracellular anchor proteins, including paxillin, vinculin, talin,  $\alpha$ -actinin, and filamin [89]. These anchor proteins can bind directly to actin or to other anchor proteins such as vinculin, thereby linking the integrin to

actin filaments in the cell cortex, an actin-rich layer responsible for movements of the cell surface. Given the right conditions, the clustering of the integrins lead to the formation of focal adhesions between the cell and the extracellular matrix. In this way, the cell can generate traction and starts to move. The migration of a cell involves a complex interaction of all the cell internal structures with the external environment. Although complex, this process is usually decomposed into four–five discrete steps: protrusion of the leading edge, adhesion to the extracellular matrix, generation of traction against the adhesions and finally, disassembly of the focal adhesions at the rear with cell body contraction, [70, 98]. For efficient cell movement, these processes must be highly coordinated.

In the next sections, the cell membrane, the cytoskeleton, the focal adhesion sites, the myosin motors and the extra–cellular matrix will be analysed in more details in particular how they are involved in the cell migration process. These description are mainly taken from “Molecular Biology of the Cell” [9] and ”The Cell: A Molecular Approach” [28].

### **2.1.1 The cell membrane**

The cell membrane or plasma membrane is the most important organelle that surrounds all the living cell. It serves to protect and separate the cell from the external environment. It is composed of phospholipids, proteins and carbohydrates arranged in a fluid mosaic structure as schematized in figure 2.2.

The phospholipids form a thin flexible sheet and they are arranged into a bilayer: the polar, hydrophilic phosphate heads face outwards and the non-polar, hydrophobic fatty acid tails face each other in the middle of the bilayer.

The carbohydrates are localised on the outer surface of the cell membrane and can be attached to the proteins or to the phospholipids. The carbohydrates are short polysaccharides composed of a variety of different monosaccharides, and form a cell coat, or glycocalyx, outside the cell membrane. The glycocalyx is involved in protection and cell recognition as well



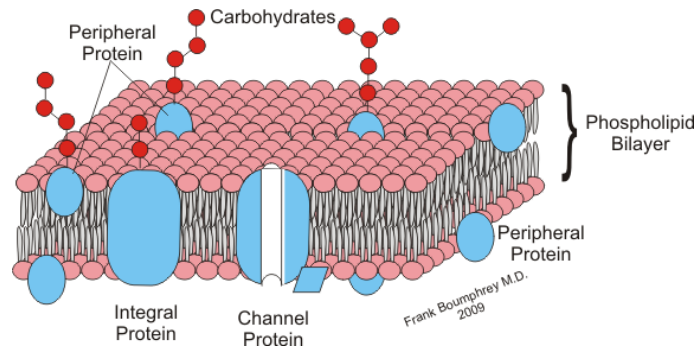


Figure 2.2: The cell membrane is a bilayer of phospholipids embedded with several kinds of proteins: proteins attached to one side (peripheral proteins) or proteins that penetrate the membrane (integral protein). On the outer surface, the carbohydrates can be attached to the proteins or to the phospholipids. Picture taken from wikibooks [3].

in cell–adhesion molecules that enable cells to adhere to each other and guide the movement of cells during embryonic development.

The proteins comprise about 50% of the plasma membrane and are responsible for most of the membrane properties. There are several kinds of proteins: the integral proteins and the peripheral one. The first set of proteins spans from one side of the phospholipid layer to the other and are usually involved in transporting substances across the membrane. The peripheral proteins sit on one of the surfaces; in particular the ones inside the cell surface are attached to the cytoskeleton and are involved in cell’s motility and in maintaining the cell shape. The proteins outside the surface of the cell can act as receptors by having a specific binding site where hormones or other chemicals can bind.

### 2.1.2 The cell cytoskeleton

The cytoskeleton is a cohesive network of fibers throughout the cell cytoplasm and is the structure that define cell shape. Despite the connotation of the word *skeleton*, the cytoskeleton is not a fixed structure but it is a dynamic and adaptive frame whose component polymers and proteins are in constant movement [43].

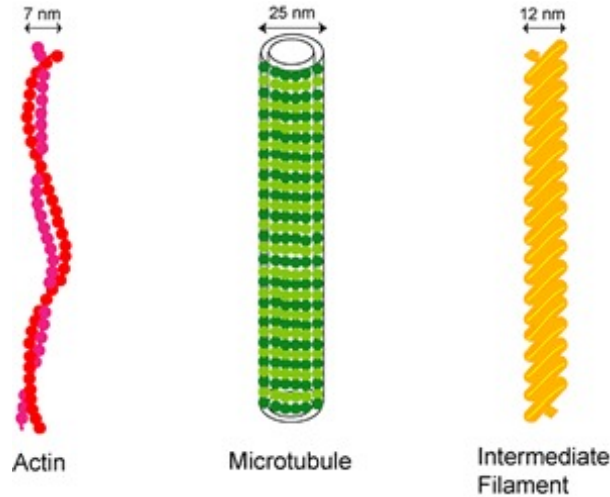


Figure 2.3: Schematic representation of three principal cytoskeleton filaments: actin (left), microtubules (middle), intermediate filaments (right). The interaction of the cytoskeleton polymer assemblies results in a composite network that spans the interior of the cell. Picture taken from <http://www.accessexcellence.org/LC/BEOn/data/phasethree/0030-beon/submission.php> [4]

Three principal types of filaments can be found: microtubules, actin filaments, and intermediate filaments as depicted in figure 2.3. Each of these filaments has a distinctive protein composition and structure.

Microtubules are the stiffest of the three polymers and are characterized by a complex assembly and disassembly dynamics. Microtubules are large, hollow cylinders with a diameter of about 25 nm and lengths that range from tens of nanometers to tens of microns. They originate and irradiate from a pair of centrioles in the center of the cell, the microtubule organization center (MTOC). Protein subunits, tubulin, rapidly assemble and elongate the microtubules that extend from the microtubule organization center to the cell surface. A microtubule holds an intrinsic dynamic instability: it can switch a stably growing state and another rapidly shrinking one. By this way, the microtubule cytoskeleton can reorganize rapidly and search for cellular space quickly [88, 78].

The actin filaments are much less rigid structures than microtubules and are formed by the polymerization of globular monomeric actin into a twisted

strand of filamentous actin (7-9 nm in diameter) with structural polarity having a barbed end and a pointed end. The actin is organized in different structures and the most important one in the cell cortex are lamellipodia and filopodia.

Actin filaments in lamellipodia form a planar meshwork of unipolar actin filaments whose barbed end are oriented towards the membrane. Lamellipodia extend or retract through a combination of actin polymerization at the plasma membrane, depolymerization within the cytoplasm and myosin-mediated rearward movement of the actin fiber. A lamellipodium is a thin highly dynamic actin-rich band, typically less than  $0.5\mu m$  which is situated at the periphery of many motile cell types. Filopodia are long and thin cylindrical extensions of the lamellipodium. Actin filaments form bundles in these structures and are all oriented in the same direction. Actin filaments exhibit a highly assembly-disassembly dynamic as well as a translocation dynamics that are dictated by the differential distribution and activities of actin regulatory proteins. The protrusion and the ability to contract of the cells are regulated by these patterns and drive whole-cell movement [50].

The intermediate filaments are the least stiff of the three types of cytoskeleton polymers. They form a super family of proteins containing more than fifty different members. These filaments have in common a structure consisting of  $\alpha$ -helical region of over 300 residues that form a coiled coil. The intermediate filaments are dynamic structures but turn over much more slowly than do actin filaments and microtubules.

The main process that allows the cell to act as a coherent and integrated structure is the polymerization. In fact, during the polymerization of actin, tubulin or intermediate filament protein molecules can interact with the ends of their cognate protein filaments at rates that are limited only by diffusion. Polymerization proceeds until the concentration of soluble proteins has dropped to a point where the rate of subunit addition to the fiber ends exactly balance the rate of subunit loss, resulting in a polymerization equilibrium.

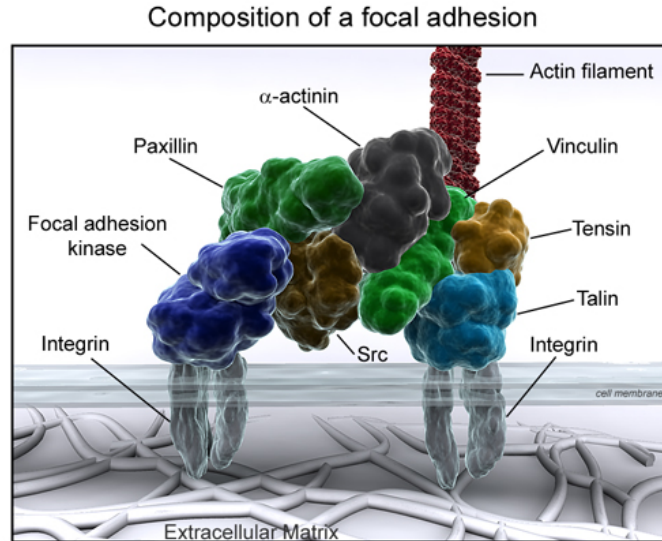


Figure 2.4: Composition of focal adhesion site. It is made of large number of proteins and is largely composed of integrins, paxillin, vinculin, talin,  $\alpha$ -actinin and functions to increase adhesion. Picture taken from Cell Migration Lab, <http://www.reading.ac.uk/cellmigration/adhesion.htm> [1].

### 2.1.3 The focal adhesion sites

The focal adhesion sites are the anchoring points of cells to the surface. These mechanical link between the cytoskeleton and the extracellular matrix facilitate directly the cell migration and spreading during through continuous regulation and dynamic reinforcement. They are also important sites of signal transduction; the signals come from the activation of integrins following their engagement with the extracellular matrix proteins such as collagen, fibronectin, vitronectin and laminin, and are propagated through the components of the focal adhesion sites. Focal adhesion consists of a complex network of trans-plasma-membrane integrins and cytoplasmic proteins as depicted in the figure 2.4.

Even if they can be classified based on size, stability and location in the cells, adhesion formation, maturation and disassembly is a continuous process guided by the equilibrium of actin polymerization and actomyosin contraction [82].

The major transmembrane components in FAs are integrins. These pro-

teins are so named because they integrate the function of the cell with the outside world. An extracellular component is bound to the external domain of the integrins, while the cytoplasmic domain is linked to actin filaments in stress fibers. Multiple attachment proteins mediated this indirect linkage. The cytoplasmic domain of the integrin binds to the protein talin, which in turn binds to vinculin. Vinculin associates with  $\alpha$ -actinin and is thereby linked to an actin filament.

During spreading, different forms of adhesion sites are built by cells in a highly spatially and temporally ordered manner. It is possible to subdivide them in at least three types with different molecular composition, dynamics and adhesive properties and describe them as morphological cycle where the maturation and turnover of adhesions involve protein recruitment and elongation followed by protein dissociation and shrinkage.

*Nascent focal complexes* are highly dynamic dot-like structures, initially small ( $0.25 \mu m^2$ ), and assemble under the lamellipodium during initial cell spreading and migration [56]. They consist of integrins and some of the adapter proteins, such as talin and paxillin. Many of these complexes fail to mature and are disassembled as the lamellipodium withdraws; others mature into *focal adhesions*. Mature focal adhesions ( $1-5 \mu m^2$ ) have both scaffolding (as paxillin) and signalling (focal adhesion kinase and Src) functions. The process is triggered by Rho-dependent acto-myosin contractility and is strongly dependent on substrate stiffness [94] and local force. Nascent focal complex and focal adhesions are predominantly required for probing the environment.

Focal adhesions at the cell periphery either become disassembled during cell migration or slide under the body of the migrating cell and evolve into *fibrillar adhesions*. Fibrillar adhesion are mainly composed of thin actin cables that are crosslinked by the actin binding protein, tensin, and attached to fibronectin fibrils via  $\alpha 5 \beta 1$ -integrin. They have low levels or lack most of the common adhesion components, such as vinculin, paxillin, and they also lack attachment to stress fibers.

Studies on integrin-mediated cell-matrix adhesion in two dimensional cell cultures, [49, 66], have provided evidence that the molecular composition and

spatial organization of the adhesions are controlled by mechanical stimuli and that different adhesion sites have distinct mechano-sensory properties.

The reorganization of the cell cytoskeleton as well as the morphology and the motility of cells has been correlated with changes in cells surroundings. The crosstalk between the assembly of focal adhesions, and the forces generated in the cytoskeletal network, is responsible for the capability of the cells to recognize and respond to the diversity of the extracellular environment both from a biochemical point of view and from a physical and topographical one [51].

#### 2.1.4 Myosin motors

Myosin as other motor proteins are the heart of cell movements. They summarize the connection between the structure of biomolecules and the movement of living organisms.

Myosin is a superfamily of molecular motor proteins responsible of muscle contraction as well as movement and functions load-dependent actin anchoring protein in all eukaryotic cells. Myosin motors are involved in a wide range of cellular processes, including movement of cells, cytokinesis, vesicle transport, Golgi organization and sensory transduction.

Most of the myosin molecules are formed of a head, neck and tail domain. The head domain bind directly the actin filament and uses the energy of ATP hydrolysis to generate force and to walk usually along the filament towards the barbed (+) end. The neck domain acts either as a linker and as a lever arm for transducing force generated by the catalytic motor domain either as binding site for myosin light chains (distinct proteins that form part of a macromolecular complex and generally have regulatory functions). The interaction with cargo molecules and/or other myosin subunits are usually mediated by the tail domain. In some cases, it may play a role in regulating motor activity.

More than 35 classes of myosin have been discovered, 13 of which are represented in humans.

The most common type of myosin is nonmuscle myosin II (figure 2.5)

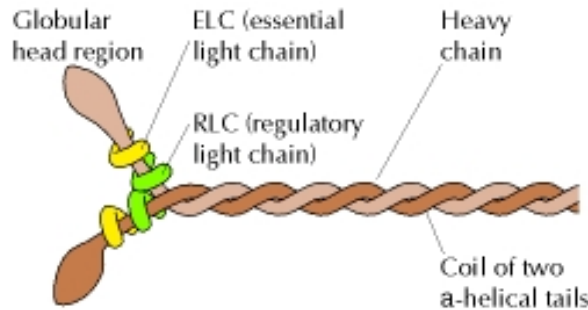


Figure 2.5: Myosin II consist of two heavy chains and two pairs of light chains. The heavy chains have globular head region and long  $\alpha$ -helical tails, which coil around each other to form dimers. Picture taken from *The Cell: a molecular approach* [28].

and is a component of the myofibers in skeletal, smooth, and cardiac tissue. Myosin II molecules are built up from six polypeptide chains: two identical heavy chains and two pairs of light chains. The C-terminal halves of the two heavy chains assemble into a coiled-coil rod, while their N-terminal sequences fold to form two globular heads.

Myosin motors do work on actin filaments through a general three-step process of binding, power stroke, unbinding and recovery stroke [62]. This process is continuously repeated, and leads to the generation of the acto-myosin contractile force, thought to be essential in pulling the nucleus of the cell forward during movement.

The intracellular contractile forces and tension are generated by myosin II that has been involved in driving cell spreading, locomotion, cytokinesis, and other cellular processes [26]. Most non-muscle cells have three isoforms of myosin II, termed IIA, IIB, and IIC [42]. Each myosin II motor protein exists as a complex consisting of two copies each of myosin II heavy chain, essentially light chains, and regulatory light chain. Differences in their motor activities, molecular interactions, cellular, and tissue distributions can be found for these myosin II molecules.

Myosin IIA is associated with functions that depend on Rho-kinase such as formation of stress fibers and focal adhesion. Myosin IIB is involved in stabilizing cell polarity. Myosin IIC is believed to have roles in regulating

cell membrane extensions and focal contact formation.

### 2.1.5 The extra-cellular matrix

Cells are not the only members of tissues: extracellular space occupies a considerable part of their volume and is fulfilled by the extra-cellular matrix (ECM), figure 2.6. This matrix is a network of a variety of macromolecules, such as proteins and polysaccharides, that are secreted locally and are in close relation with the cell surface that produced them.

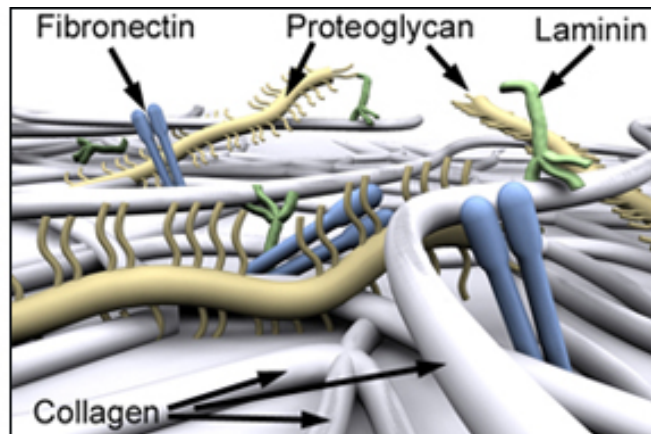


Figure 2.6: The extracellular matrix. It is composed of structural proteins, collagen and elastin, specialized protein, like fibrillin, fibronectin, laminin, and proteoglycans. Picture taken from Cell Migration Lab, [www.reading.ac.uk/cellmigration/matrix.htm](http://www.reading.ac.uk/cellmigration/matrix.htm) [1].

Polysaccharide chains and fibrous proteins are the two main classes of macromolecules that make up the matrix. The first class are usually found covalently linked to the protein to form proteoglycans. Proteoglycans bind secreted signal molecules controlling their diffusion, their range of action, enhancing or inhibiting their activity. The fibrous proteins can be divided in proteins with a structural function, such as collagens and elastin, and proteins with an adhesive ones, such as fibronectin and laminin.

Collagens are the most abundant proteins in mammals, constituting 25% of the total protein mass. Collagen molecule has a long, stiff, triple-stranded helical structure made of aminoacids, in which three  $\alpha$ -chains, i.e. collagen



polypeptide chains, are wound around one another in a ropelike superhelix. Up to now, about 25 distinct  $\alpha$ -chains have been identified, each encoded by a separate gene. Several families of collagen exist and are classified in relation to the structure that collagen form: the fibrillar collagen, (type I, II, III, V and XI) with a rope-like structure; collagen types IX and XII are called fibril-associated collagens and link the fibrils to one another and to other components in the extracellular matrix. Types IV and VII are network-forming collagens.

Fibronectin is an adhesive protein with multiple domains, each with specific binding sites. It is a glycoprotein, a dimer composed of two large subunits crosslinked by disulfide bonds at one end. Each subunit is collapsed into a series of domains with distinct functions. There are multiple isoforms of fibronectin that assembly into fibrils only on the surface of certain cells. Fibronectin is involved in adhesion of cell to the extracellular matrix and guidance of cell during embryogenesis. Integrins on cell surface are receptors for fibronectin as well as for collagens.

The multiple binding domains of these proteins, collagen and fibronectin, help organize the matrix and help cells adhere to it. Matrix components such as collagens, laminins, and fibronectin are collected into fibrils or networks on the cells surface and the production processes depends on the underlying actin cortex of the cells. Mutually, the structure of the matrix can direct the organization of the cell's cytoskeleton and affect cell spreading [83].

## 2.2 Particular features of cancer cells

In order to preserve the body healthy, normal cells grow and divide in a controlled way to produce more cells. When cells become old or damaged, they die and are replaced with new cells. However, sometimes the DNA of a cell can be damaged or changed. These mutations affect normal cell growth and division. The cells do not follow the controlled process, do not die when they should and new cells form when the body does not need them. The extra cells may form a mass of tissue called a *tumour*.

The hallmarks of cancer cells have been described by Hanahan and Wein-

berg [58, 59]. The most distinguishing mark of tumour cells involves their ability to sustain *chronic proliferation*. Normal cells divide only when they receive outside signals that cause the cells to enter into the cell cycle. These signals, caught on the cell surface and sent into the cell, come from different sources, such as growth factors, cell-cell adhesion molecules and extracellular matrix components. Cancer cells deregulate the growth-promoting signals and produce their own growth factors, overexpress or change growth receptors and bias cells to produce growth signals. At this point, tumour cells begin to behave more like independent entities living without regard for the organism as a whole. The contact with neighbouring cells prevents the division of the normal cell while such contact inhibition is abolished in various types of cancer cells, that continue to double regardless of the extra cells which gives to the part of the body where the cancer is growing. Differentiation is an alternative mechanism to stop cell division. This is the process by which a precursor cell acquires its final specialized capabilities. The cancer cells are de-differentiated: they lose their specialization. Cancer cells have the capacity to divide endlessly or they may self destruct more slowly than they reproduce, so that their numbers continue to increase. Avoidance of cell death and continued cell division leads to the growth of the tumour.

Like normal tissues, tumours require nutrients and oxygen and at the same time they have to evacuate metabolic wastes and carbon dioxide. Tumour neovasculature takes care of these requisites and is generated by the process of *angiogenesis*. The angiogenesis is the formation of new blood vessels and during tumour progression, an angiogenic switch is almost always activated and remains on: new vessels are continually developed sustaining neoplastic growths.

Definitely, the critical event in tumour is linked to the capacity of cells to leave the original location and to spread into other parts of the body: the ***metastasis*** (figure 2.7). This process is considered highly inefficient from a cellular point of view but virtually constitutes the many cause of death for the patient. The multi-steps process of invasion and metastasis has been depicted as a sequence of discrete steps, often termed the invasion-metastasis cascade. This process begins with the local invasion of the nearby

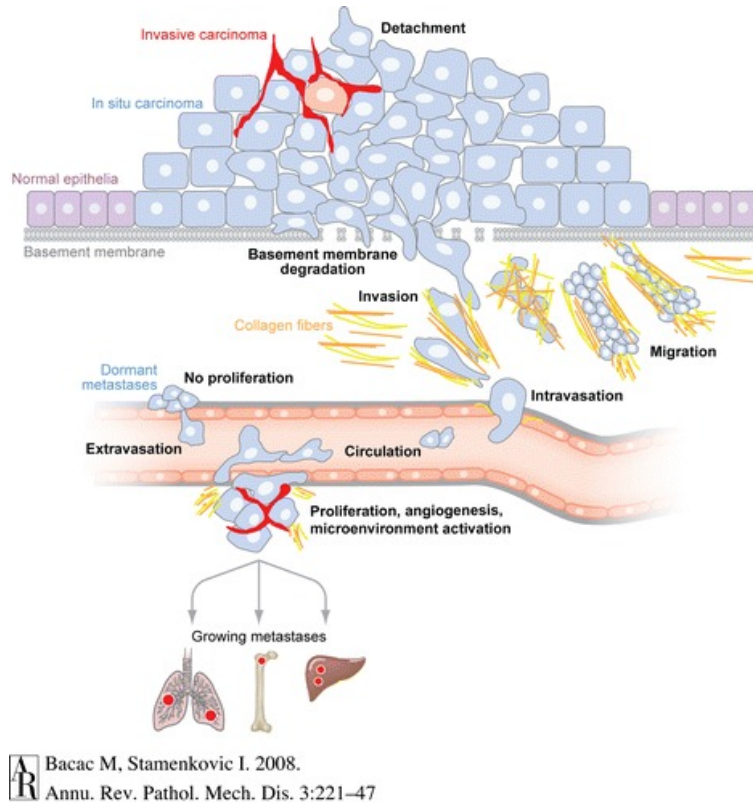


Figure 2.7: The invasion-metastasis cascade. Transformation of normal epithelial cells leads to carcinoma in situ. Tumour cells lose adherent junctions, detach from the primary tissue and invade it locally. Afterwards, the cells migrate and penetrate into blood or lymphatic vessels until they arrest in the capillaries of a distant organ. Finally, tumour cells divide to form new tumours. Picture taken from Bacac and Stamenkovic [14].

body tissues. As the tumour grows and takes up more volume, it pushes on the normal tissue, it squeezes and blocks small blood vessels in the area. The lack of oxygen gives rise to the death of normal cell and facilitates the progress of the tumour.

A cancer cell has to interact with the local micro-environment, migrates, invades, resists to apoptosis and finally induces angiogenesis. All these functions are controlled by adhesion and proteolysis that determine also the interaction of the tumour cell with other cells and with the extra-cellular matrix and help create a path for migration. The cancer cells are affected by many

phenotype changes, [14, 67]. Often malignant cells display an elevated level and activity of focal adhesion kinase (FAK), which is associated with change of shape, podosome formation and induction of invadopodia.

In epithelial cells, adherent junctions are constituted primarily by E-cadherin. Loss of these junctions is one of the fundamental effector of metastasis. Inhibition of E-cadherin functions can alter the phenotype of the epithelial cells from non-invasive to invasive as has been shown by *in vivo* and *in vitro* experiments [104]. Loss of E-cadherin in malignant cells may be replaced by other cadherins, most commonly, N-cadherin. This process is associated, *in vitro*, with a phenotypic change known as epithelial-to-mesenchymal transition (EMT). The EMT was first recognized as a feature of embryogenesis, which is vital for morphogenesis during embryonic development. During the process of epithelial-to-mesenchymal transition, non-motile epithelial cells with normal cell-cell junctions and adhesion, lose their cell-cell junctions and convert into individual, motile and invasive mesenchymal phenotypic cells. Actin cytoskeleton reorganization and increased cell motility and invasion are implied in this process. The acquisition of an EMT phenotype of tumour cells can allow cells to acquire the capacity to penetrate surrounding tissues, and thus enable these cells to metastasise in distant sites. The reverse transition, Mesenchymal-to-Epithelial Transition (MET), is the process that can happen at the site of metastasis: tumour cells with a mesenchymal phenotype acquire the pathology of their corresponding primary tumours. This process is a critical step by which metastatic tumour cells grow at the secondary sites [22, 67].

Several modes of migration are observed for cancer cells [45, 44]. The remodelling of the extracellular matrix and the activation of fibroblast stroma create favourable conditions for the migration of cancer cells. Different patterns of migration have been observed for cancer cells. Mesenchymal cells migrate along a classical scheme with the protrusion of lamellipodia, formation of focal contacts with the extracellular matrix, and detachment of the trailing edge. However, amoeboid migration has been observed as well, a movement based on the cell deformability and relatively weak interactions with the extracellular matrix. Finally, tumour cells can also migrate in group

or aggregates. One consists of chain migration, where cells follow each other in single file and form a chain-like image. In the second one, cells migrate like a sheet.

In this thesis we will focus on the migration of bladder cancer cells and we will try to understand how the processes presented above can be described in terms of traction stresses and how they affect the cell cytoskeleton and the focal adhesion sites.



## Chapter 3

# Determination of traction forces

In this chapter we will discuss how to compute the traction forces that the cells exert on a flat substrate during migration. We will present models available in the literature with some details, and we will describe the model used in this work.

*Dans ce chapitre, nous allons discuter de la façon de calculer les forces de traction que les cellules exercent sur leur substrat lors de la migration. Nous allons présenter les modèles disponibles dans la littérature et nous allons décrire le modèle utilisé dans ce travail.*

### 3.1 Overview of available models

Cell migration is an important feature occurring during many biological processes such as tissue invasion, the immunologic response, etc. and involves sophisticated mechanisms such as the development of focal adhesions, possible extra-cellular matrix degradation, and activation of the actin–myosin complex, in order to develop forces necessary for traction. Depending on their type and the environment, cells can move according to different types of locomotion, either in 2D or 3D.

The migration process can depend on cell type and ligand matrix densities, as shown in previous works on substrates covered by different densities of extra-cellular matrix [81]. The migration velocity vs. ligand density curve usually exhibits a bell-shaped curve with a maximum velocity at an intermediate ligand density, which is the signature of an optimum affinity between receptor and ligand molecules. This is the basis for understanding the complex machinery provided by cells developing focal adhesions at the front while removing them at the back in the conventional five-step motion [98]. To better understand these features, fluorescence microscopy is a very useful tool to show the precise location of adhesion complexes involved during cell migration. The formation of such focal contacts [15] allows the development of important forces that the cell uses to move forward.

The word *traction forces* is usually used to define the forces that are generated by the acto-myosin machinery and are transmitted to the substrate through the focal adhesion site. Such forces are difficult to determine by straightforward analysis. Therefore, many attempts have been made in the past ten years to measure such forces in an indirect way and different techniques have been developed in this respect:

- The original technique of Harris and co-workers [60] consisting of observing the magnitude and shape of wrinkles on a soft elastic film below a cell
- The most classical one by Dembo and co-authors [31, 32] measures the motion of fluorescent beads embedded in a gel deformed by a cell
- Micro-patterned substrates [15, 37, 100] with thin poles whose deflection directly gives the forces exerted by the cell

All these techniques have been tested *in vitro* and were quite effective for the study of the motion of cells on 2D-rigid substrates. The first technique [60] was initially rather qualitative, but further developments by Burton *et al.* [19], in particular devoted to the study of keratocytes locomotion, revealed to be quite quantitative. The last one, introduced by Balaban *et al.* [15], has received recently a lot of interest [53] and important results concerning cell



migration of 3T3 fibroblasts on rigid substrates have been obtained regarding the influence of substrate rigidity. Indeed, as earlier understood by Lo *et al.* [74], cells usually exert larger traction forces on more rigid substrates, this behaviour being correlated with an increased contact surface and a reduced migration velocity. Traction force increases for larger stiffness until a critical rigidity is reached (around  $80kPa$ ), where the force exhibits a plateau [53]. Although very elegant, the technique due to Balaban *et al.* still poses questions like whether cells behave similarly on micro-patterned substrates as compared to classical polyacrylamide gels or when migrating *in vivo*.

We choose to study the cells on flat elastic substrates in order to study the spontaneous migration of the cell and to let the cell free to adhere everywhere on the substrate. We will focus our attention on the methods of Dembo and Wang, the boundary element method (BEM) [32], the method of Butler, the Fourier transform traction cytometry (FTTC) [20], the method used by Schwarz, the traction reconstruction with point force (TRPF) [97], and the method implemented by Ambrosi, the adjoint method (AM) [10]. Common characteristic of all these methods is that they have to solve an *inverse problem* [39]. The concept of inverse problem begins with the assumption that there is a direct problem: given a complete description of a physical system, we can predict the outcome of some measurements. The inverse problem consists of using the actual results of some measurements to infer the values that characterize the system. Most direct problems can be reduced to finding values  $y = F(x)$ , of an operator  $F$  from a topological space  $X$  into a topological space  $Y$ . The inverse problem is then connected with the inverse operator  $F^{-1}$  or with solving the equation

$$F(x) = y. \quad (3.1.1)$$

The problem is said to be well-posed (with the respect to  $X$  and  $Y$ ) if the operator  $F$  satisfies the following conditions:

- a solution  $x$  of equation (3.1.1) is unique, i.e., if  $F(x_1) = F(x_2)$ , with  $x_j \in X$ , then  $x_1 = x_2$  (uniqueness of solution);

- a solution  $x$  of equation (3.1.1) exists for any  $y \in Y$ , i.e., for any  $y \in Y$  there is  $x \in X$  satisfying equation (3.1.1) (existence of solution);
- a solution of the equation (3.1.1) is stable, i.e., if  $\bar{y} \rightarrow y$  then the related solution  $\bar{x} \rightarrow x$ , (stability of solution).

The problem is said to be well-posed in the sense of Hadamard, if both  $X$  and  $Y$  are spaces  $C^k$  or  $H^{k,p}$ . If a problem violates one of these conditions, it is said to be *ill-posed*. Only a well-posed problem can correctly describe a physical phenomena. Usually, an inverse problem does not satisfy one or more of the previous conditions. In fact, once the physical model has been fixed, the available experimental data are usually noisy and there are no guarantees that the measurements came from such a model. If a solution exists, it is possible that different parameters lead to the same observations. If various solutions exist, we have to choose among them and supplementary informations are necessary. The critical point is the absence of continuity among the data: it will not be possible to reach the solution of the inverse problem in a satisfactory way since the available data are near but different of the real data due to the presence of the noise in the data. Arbitrarily small perturbations of data and parameters can produce arbitrarily large perturbations of the solution.

The methods previously cited, BEM, FTTC, TRPF and AM, deal with this problem in different ways.

### 3.1.1 Boundary element method (BEM)

Dembo and Wang [32] were the first ones to use a quantitative approach to reconstruct the traction forces exerted on elastic substrates.

The basic idea is to measure the displacements of fluorescent beads embedded in rigid substrates of polyacrylamide gel. As cells are laid onto the functionalized substrate, they adhere and start to exert tractions which deform the substrate so that fluorescent beads located in the underlying gel are displaced.

The gel is considered as isotropic and elastic, the displacements are small enough so that linear elasticity applies, the gel depth being large enough

so that it can be approximated by a half space. Since the response of the substrate is linear, the displacement  $\mathbf{u}$  is related to the traction field  $\mathbf{T}$  via the integral transform

$$\mathbf{u}(\mathbf{r}) = \int \mathbf{G}(\mathbf{r} - \mathbf{r}') \mathbf{T}(\mathbf{r}') d\mathbf{r}' \quad (3.1.2)$$

where  $\mathbf{G}$  is the Green's tensor of the elasticity operator. For each position in the material, the term  $g_{\alpha\beta}(\mathbf{r})$  of the Green's tensor represents the component of the  $\alpha$ -displacement due to the  $\beta$ -component of a concentrated unit force exerted at the origin of coordinates. The Green's tensor in case of infinite elastic half-space can be derived from the theory of Boussinesq [69]:

$$\mathbf{G}(\mathbf{r}) = \frac{1 + \nu}{\pi E} \left( (1 - \nu) \frac{\mathbf{1}}{r} + \nu \frac{\mathbf{r} \otimes \mathbf{r}}{r^3} \right) \quad (3.1.3)$$

while  $r$  denotes the modulus of  $\mathbf{r}$ ,  $E$  is the Young modulus and  $\nu$  the Poisson coefficient.

In the approach of Dembo and Wang [32], the relaxed and the loaded position of the beads are recorded; the misalignment of the two images is corrected on the basis of the similarity in area contrast between the images. The in-plane projection of the displacement vector of each marker bead is computed by subtracting the reference position of the beads from the loaded one. Then an irregular quadrilateral mesh is introduced to tessellate and define the domain of the traction field. The number of quadrilaterals is increased until the results become independent on the details of the mesh.

The in-plane traction components are approximated by standard bilinear shape functions on each node of the mesh, where the functions are of the type  $\mathbf{T}_\beta(\mathbf{r}) \simeq T_{k\beta} H_k(\mathbf{r})$ , with  $H_k(\mathbf{r})$  standard bilinear shape function and  $T_{k\beta}$  the components of the nodal traction vectors. The solution is constrained to maximize its probability to estimate the experimental data in a least-square sense and to incorporate a prior information about the expected traction field.

This method has been improved by Sabass *et al.* [93]: they use a Tikhonov regularization scheme and split the calculation of the Green tensor into three

different subroutines for near, intermediate and far fields. The idea was to compute the displacement field emanating from each triangular element, in analogy to a multipole field, depending on the distance. When computing the near field, the major problem is to avoid the divergent integral: this difficulty is avoided by usage of polar coordinates and setting a node on top of each displacement. The analytical integrals are calculated with the integration boundaries being determined by the nearest triangles that gives the accuracy of the approximation. In the intermediate field, the displacement is in the surrounding of the node and the use of a Gaussian quadrature is required. Re-writing the integral with the barycentric coordinates facilitates the implementation. When the displacement is far from the node the integrand is expanded up to the third order around the center of mass of the triangle and the multipolar expansion is used to evaluate this field.

The Tikhonov regularization scheme has been added in order to rich a robust force estimation. In particular, the traction field  $T_{j\mathbf{r}'}$  minimizes the following target function:

$$J(f) = ||u_i(\mathbf{r}') - \sum_{j,\mathbf{r}'} G_{ij}(\mathbf{r} - \mathbf{r}') \mathbf{T}_j(\mathbf{r}')||^2 + \lambda^2 || \sum_{j,\mathbf{r}'} \mathbf{L}_{ij}(\mathbf{r} - \mathbf{r}') \mathbf{T}_j(\mathbf{r}') ||^2, \quad (3.1.4)$$

where  $L$  gives the order of regularization and  $\lambda$  is the regularization parameter. If  $L$  is the identity matrix,  $0^{th}$  order regulation, the prior information is that the force are localized in small area and zero elsewhere. When a first order regulation is chosen,  $L$  is a discrete difference between the nodes and the prior assumptions is that the forces field is widespread rather than localized. For their experiments, usually, the  $0^{th}$  order regulation works better than the first one.

The analysis of the particular structure of the equation (3.1.2) has been the starting point for the development of other methods, like the Fourier transform traction cytometry, developed by Butler [20] and the method worked out by Schwartz [97].

### 3.1.2 Fourier transform traction cytometry (FTTC)

By defining the forces acting at the nodes of a periodic grid and transforming the relation between the displacements and the tractions into Fourier domain, Butler *et al.* [20] proposed a method of Fourier transform traction cytometry (FTTC). The main point is that the equation (3.1.2) is a convolution equation and in the Fourier space can be easily solved.

In details, one can compute the Fourier transform  $\tilde{\mathbf{F}}(\mathbf{k}) = \int_{-\infty}^{\infty} e^{-i\mathbf{k}\cdot\mathbf{r}} \mathbf{F}(\mathbf{r}) d\mathbf{r}$  on both sides of Eq.(3.1.2),  $\mathbf{k}$  being the wave vector:

$$\tilde{\mathbf{u}}(\mathbf{k}) = \tilde{\mathbf{G}}(\mathbf{k})\tilde{\mathbf{T}}(\mathbf{k}) \quad (3.1.5)$$

In this form,  $\tilde{\mathbf{G}}$  is a two-by-two diagonal matrix and  $\tilde{\mathbf{G}}^{-1}$  is trivial to compute. The solution of the inverse problem in the Fourier space is given by

$$\tilde{\mathbf{T}}(\mathbf{r}) = FT_2(\tilde{\mathbf{G}}^{-1}(\mathbf{k}) \tilde{\mathbf{u}}(\mathbf{k})) \quad (3.1.6)$$

where  $FT_2$  denotes the two-dimensional Fourier Transform.  $\tilde{\mathbf{G}}(\mathbf{k})$  can be computed explicitly thanks to simple manipulations in the Fourier space [20]:

$$\tilde{\mathbf{G}}(\mathbf{k}) = \frac{2(1+\nu)}{Ek^3} \begin{pmatrix} (1-\nu)k^2 + \nu k_y & \nu k_x k_y \\ \nu k_x k_y & (1-\nu)k^2 + \nu k_y \end{pmatrix} \quad (3.1.7)$$

Note that there is a sign error in the matrix written by Butler for the off-diagonal elements [20]. Two different ways to evaluate the traction field have been proposed. The first way, unconstrained FTTC, does not use any constraints to recover the traction and consists to take directly the inverse Fourier transform of the Eq.(3.1.6). The second one, the constrained FTTC, is the solution to the mixed boundary value problem: it ignores the displacement field outside the boundary of the cell and constrains the traction outside the cell boundary to be zero. This method required the additional information of the location of the cell boundary, extracted from data. Even though the effect on the force field of the noise in the displacement data were investigated, no regularization procedures were applied by the authors: they

did not find large oscillations in the recovered traction field.

Sabass *et al.* [93] modified the FTTC method testing different smoothing procedure for the displacement field, including an adaptive Wiener filter and a Gaussian filter. While Gaussian filter are designed for a desired frequency response, the Wiener filter is based on a stochastic approach: the signal and the noise are linear stochastic processes with known spectral characteristics or known autocorrelation and cross-correlation. The filter is optimal in the sense of the minimum mean-square error. As an alternative approach, they use, in analogy to the boundary element method, a regularization scheme, where the equation to inverse in the Fourier space reads:

$$\tilde{T}_{ik} = \left\{ \sum_{l,j} \left[ \sum_m \tilde{G}_{ml} \tilde{G}_{mi} + \lambda^2 \tilde{H}_{il} \right]^{-1} \tilde{G}_{jl} \tilde{u}_j \right\}_k \quad (3.1.8)$$

For the regularization kernel  $H_{ij}$  the identity matrix,  $0^{th}$  order approximation, or the square of an approximation for the Laplace operator (second order approximation) were chosen.

The main drawback of this method is that despite its simplicity, it requires to have a periodic displacement field in order to compute the Fast Fourier Transforms.

### 3.1.3 Traction reconstruction with point force (TRPF)

One further work [97] investigates the forces exerted by the cell including information single focal adhesions. Always in the framework of the linear elasticity, Schwarz and co-workers [97] assume that all the tractions are localized at discrete and known positions, the focal adhesions. The positions  $r_i$  of the focal contacts are reconstructed from the fluorescent images. The traction field is described by a sum of delta functions and the integral equation is turned into a set of linear equations, in which each measured displacement is connected to the set of force locations:

$$\mathbf{u} = \mathbf{GT} \quad (3.1.9)$$

where the displacement  $\mathbf{u} = (u_1(r_1), u_2(r_1), u_1(r_2), u_2(r_2), \dots)$  is a  $2N$ -vector,  $\mathbf{T} = (T_1(r_1), T_2(r_1), T_1(r_2), T_2(r_2), \dots)$  is  $2M$ -vector and  $G$  is the following  $2N \times 2M$  matrix:

$$\begin{pmatrix} G_{11}(r_1 - r'_1) & G_{12}(r_1 - r'_1) & G_{11}(r_1 - r'_2) & G_{12}(r_1 - r'_2) & \dots \\ G_{21}(r_1 - r'_1) & G_{22}(r_1 - r'_1) & G_{21}(r_1 - r'_2) & G_{22}(r_1 - r'_2) & \dots \\ G_{11}(r_2 - r'_1) & G_{12}(r_2 - r'_1) & G_{11}(r_2 - r'_2) & G_{12}(r_2 - r'_2) & \dots \\ G_{21}(r_2 - r'_1) & G_{22}(r_2 - r'_1) & G_{21}(r_2 - r'_2) & G_{22}(r_2 - r'_2) & \dots \\ \vdots & \vdots & \vdots & \vdots & \vdots \\ \vdots & \vdots & \vdots & \vdots & \vdots \\ \vdots & \vdots & \vdots & \vdots & \vdots \end{pmatrix} \quad (3.1.10)$$

Following the procedure for the ill-posed inverse problems, they add a zero-order Tikhonov regularization where one minimize the square of the difference  $|G\mathbf{T} - \mathbf{u}|$  under the constrain that the forces should not become exceedingly large:

$$\min_f \{ |G\mathbf{f} - \mathbf{u}|^2 - \lambda^2 \mathbf{T}^2 \} \quad (3.1.11)$$

where  $\lambda$  is the regularization parameter, chosen with the L-curve criterion.

In their work, they pointed out the need of regularization for the inverse problems. The study the effect of the noise of the obtained traction field and showed that the force reconstruction without regularization yields an erratic force pattern.

According to the analysis worked out by Sabass and co-workers [93], this method seems to be the most promising one, able to describe the force magnitude independent of adhesion size, as long as focal adhesions are well developed, but requires of course more sophisticated experiments.

## 3.2 The adjoint method (AM)

An alternative approach to obtain the pattern of the traction stresses exerted by a cell on a flat substrate is the adjoint method proposed by Ambrosi [10, 11]. The mathematical model is based on the classical functional analysis framework due to Lions [73]; the general theory is applied to the specific

problem of small deformation of a homogeneous elastic material subjected to body forces only in the plane.

Let  $\Omega$  be the whole domain and  $\mathbf{u}(\mathbf{x})$  the displacement vector field,  $\mathbf{x} \in \Omega \subset \mathbb{R}^3$ . The displacement is known only in a subset  $\Omega_0 \subset \Omega$  where beads are located; the related function  $\mathbf{u}_0(\mathbf{x})$  has support in  $\Omega_0$ . Let  $\Omega_c \subset \Omega$  be the region covered by the cell and where the shear stress is applied. As explained before, the traction forces are generated through the actin–myosin interactions and act on the underlying substrate through focal adhesion sites. These areas are not localized precisely in our experiments and we do not restrict the force support to these sites as is done in the algorithm of Schwarz *et al.* [97] although it can be easily done if the information is provided.

Consider the following elastic problem in the whole domain  $\Omega$

$$-\mu\Delta\mathbf{u} - (\mu + \lambda)\nabla(\nabla \cdot \mathbf{u}) = \mathbf{f}, \quad \mathbf{u}|_{\partial\Omega} = 0 \quad (3.2.12)$$

where  $\mu$  and  $\lambda$  are the Lamé constants that characterize the material. The problem can be rewritten in the form  $A\mathbf{u} = \mathbf{f}$ , where  $A$  is a linear operator in the above equation. The aim is to obtain the force field  $\mathbf{f}$ , that is inferred by a known displacement (inverse problem). If we try to invert directly the equation, we find that the problem is ill-posed since the displacement is known only in a subset  $\Omega_0$  of  $\Omega$ . It is necessary to introduce the projector  $P$ ,  $P : \Omega \rightarrow \Omega_0$ , and a functional  $J(\mathbf{f})$ ,  $J : L^2(\Omega) \rightarrow \mathbb{R}$ , defined as

$$J(\mathbf{f}) = \int_{\Omega_0} |\mathbf{u} - \mathbf{u}_0|^2 dV + \varepsilon \int_{\Omega} |\mathbf{f}|^2 dV, \quad (3.2.13)$$

where  $\varepsilon$  is a real positive number. This functional measures the difference between the displacement field produced by  $\mathbf{f}$  and the experimental one defined by  $\mathbf{u}_0$  under penalization of the square norm of the force field itself. We look for  $\mathbf{g}$  minimizing  $J$ :

$$J(\mathbf{g}) \leq J(\mathbf{f}), \quad \forall \mathbf{f} \in V_c, \quad (3.2.14)$$

where  $V_c \subset L^2(\Omega)$  is the space of the finite energy functions with support



in  $\Omega_c$ . The minimization of  $J$  accomplishes the minimization of the distance of the solution from the measured value  $\mathbf{u}_0$  under penalization of the magnitude of the associated force  $\mathbf{f}$  per unit surface. The penalty parameter  $\varepsilon$  balances the two requirements. An equivalent condition of Eq. (3.2.14) is given by  $J'(\mathbf{g})[\mathbf{f} - \mathbf{g}] \geq 0$ ; making the Gateaux derivative explicit suggests the introduction of the adjoint equations,  $A^* : L^2(\Omega) \rightarrow \Omega_0$

$$A^* \mathbf{q} = P\mathbf{u}(\mathbf{g}) - \mathbf{u}_0, \quad \mathbf{q}|_{\partial\Omega} = 0 \quad (3.2.15)$$

Substituting back in the functional derivative permits to obtain the solution of equation (3.2.14) that represents the optimal body force:

$$\mathbf{g} = -\frac{\chi_c}{\varepsilon} \mathbf{q},$$

$\chi_c$  is the characteristic function of the domain  $\Omega_c$  and  $\mathbf{q}$  is a volume force.

In short, the set of equations that we need to solve is given by two elliptic partial differential equations, one for the displacement  $\mathbf{u}$  and the adjoint one for the volume force  $\mathbf{q}$ .

The reduction of the three dimensional half space elasticity problem to a two dimensional one can be done on the basis of dimensional arguments. In fact, vertical averaging along an effective thickness  $h$  allows to introduce two parameters  $\hat{\mu}$  and  $\hat{\lambda}$ :

$$\hat{\mu} = h \frac{E}{2(1 + \nu)}, \quad \hat{\lambda} = h \frac{E\nu}{1 - \nu^2}.$$

$E$  and  $\nu$  are the Young modulus and the Poisson ratio respectively.  $h$  is the averaging height fixed by the depth of field of the microscope that is 1.5 microns in our case. Below this depth, the beads are not in focus and their positions are not measured; the displacement  $\mathbf{u}$  should be understood as the average displacement along  $h$ , which is nearly the displacement of the center of the beads.

Finally, the two-dimensional system to solve in the domain  $\Omega$ , figure 3.1,

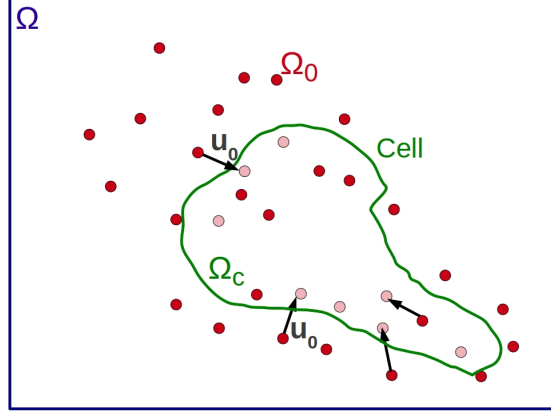


Figure 3.1: The domain  $\Omega$  of the elasticity equation contains the subdomain  $\Omega_c$ , the area covered by the cell, where the force applies: in the figure it is enclosed by the continuous bold line. The dashed circles are centered at the beads location and their collection represents the  $\Omega_0$  subdomain where the displacement is known.

becomes

$$\begin{aligned} -\hat{\mu}\Delta\mathbf{u} - (\hat{\mu} + \hat{\lambda})\nabla(\nabla \cdot \mathbf{u}) &= -\frac{\chi_c}{\varepsilon}\mathbf{p} - \bar{\mathbf{p}}, & \mathbf{u}|_{\partial\Omega} &= 0, \\ -\hat{\mu}\Delta\mathbf{p} - (\hat{\mu} + \hat{\lambda})\nabla(\nabla \cdot \mathbf{p}) &= \chi_o\mathbf{u} - \mathbf{u}_0, & \mathbf{p}|_{\partial\Omega} &= 0, \end{aligned} \quad (3.2.16)$$

where  $\chi_c$  and  $\chi_o$  are the characteristic functions related to  $\Omega_c$  and  $\Omega_0$  respectively. Note that the structure of the two equations is the same because the A operator is self-adjoint. Here  $-\mathbf{p}/\varepsilon$  represents the traction stresses previously introduced as  $\mathbf{f}$  and is determined once the two equations are solved.

In the ill-posed problem the penalty parameter,  $\varepsilon$  in our case, plays an important role. In order to fix  $\varepsilon$  it is possible to re-interpret the system (3.2.16) on the basis of arguments suggested by modal analysis. Suppose that  $\Omega_0 = \Omega_c = \Omega$  under periodic boundary conditions, the previous system of equations rewrites like a Tikhonov filter. The amplitude of the Fourier

components of the solution  $u_k, p_k$  satisfy the algebraic relations

$$\begin{aligned} hEk^2 u_k &\simeq -\frac{1}{\varepsilon} p_k, \\ hEk^2 p_k &\simeq u_k - u_{0,k}, \end{aligned} \quad (3.2.17)$$

that is

$$u_k \simeq \frac{u_{0,k}}{1 + \varepsilon h^2 E^2 k^4}. \quad (3.2.18)$$

where  $u_{0,k}$  represents the amplitude of the  $k$ -th Fourier component of  $u_0$ . According to equation (3.2.18), if the data is known all over the domain the system of equations (3.2.16) is a filter damping the modes corresponding to wave numbers  $k > \varepsilon^{-1/4} h^{-1/2} E^{-1/2}$ . The choice of  $\varepsilon$  can be interpreted in terms of filtering modes falling below the experimental accuracy. Equation (3.2.18) shows that the key parameter of the inversion procedure is actually  $\varepsilon h^2$  and the solution does not change for combinations of the averaging layer  $h$  and penalty parameter  $\varepsilon$  that preserve this quantity.

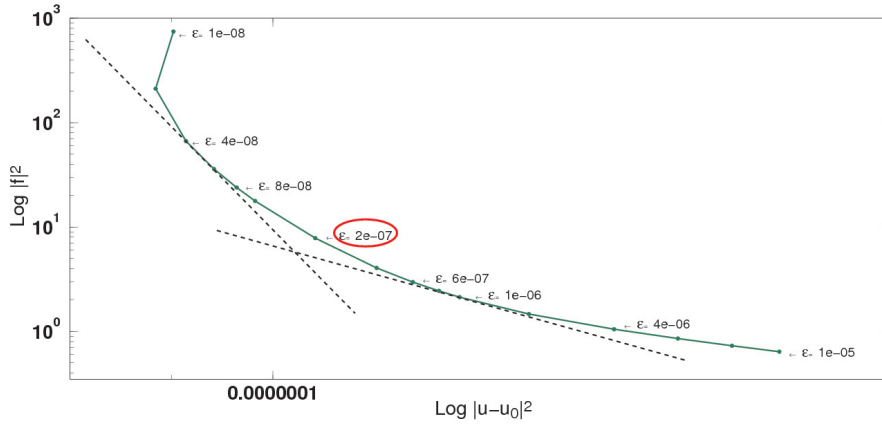


Figure 3.2: Discrete L-curve with 17 values of  $\varepsilon$  obtained for our model in the case of the stiff gel ( $E = 10kPa$ ). The corner corresponds to the optimal balance between data agreement and regularization.

A convenient tool for the analysis of discrete ill-posed problems is the L-curve criterion which is a log-log plot, for all valid regularization parameters, of the norm of the regularized solution  $\|f\|_2$  versus the corresponding residual norm  $\|u - u_0\|_2$ . In this way, the L-curve displays the minimization of these

two quantities and its corner, which is intrinsic to the data, corresponds to the optimal balance between data agreement and regularization. Figure 3.2 shows an example of the discrete L-curve obtained for 17 values of the  $\varepsilon$  parameter for our model in the case of the stiff gel ( $E = 10kPa$ ). In our work we take the minimum value of  $\varepsilon$  that does not yield erratic results in the displacement, that is the corner of the L-curve. We also plot the functional  $J$  as a function of  $\varepsilon$  and show that this L-curve solution gives an optimal  $\varepsilon$  corresponding to the minimum of  $J$ , as we can see in figure 3.3.

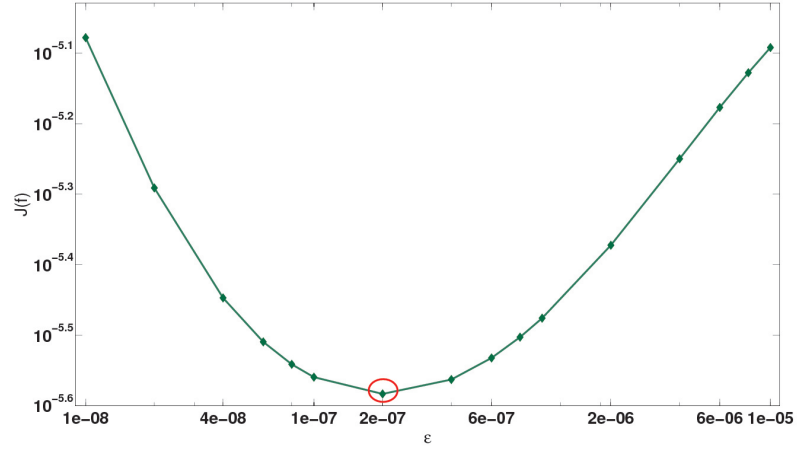


Figure 3.3: Functional  $J$  as a function of  $\varepsilon$ . The value of  $\varepsilon$  that minimize the functional is  $2 \cdot 10^{-7}$ .

The system of equations (3.2.16) has been discretized by a finite element method using linear basis functions on an unstructured mesh. In order to avoid iterative coupling between the two equations in (3.2.16), a global conjugate method has been used to solve the resulting system of linear equations numerically. The triangular mesh satisfies two constraints: it has a node in every point where displacements are known (beads location) and a sequence of element sides coincides with the cell contour. In particular, the boundary  $\Omega_c$  of the cell, is described as a piecewise linear curve following the shape of the cell and represents the boundary between the intracellular domain over the substrate and the rest of the domain where the forces are not applied.

### 3.3 A critical comparison

The methods presented in this chapter deal with an inverse problem and its numerical regularization to stabilize the reconstruction results.

The classical method of Dembo and Wang (BEM) [32] and the Fourier transform traction cytometry (FTTC) [20] are based on the knowledge of the exact solution of the elasticity equation in a half plane under linearity assumptions, and for an isotropic and homogeneous medium. In the boundary element method, by numerical quadrature such an exact solution is part of a discrete minimization algorithm that provides the shear stress under regularization based on the Tikhonov method. Conversely, the adjoint method does not exploit the knowledge of an exact solution and does not decouple the direct and inverse problems: variational arguments yield two coupled sets of partial differential equations to be solved by a finite element method method. Schwarz and co-workers solve the equations 3.1.6 on a rectangular mesh without applying any regularization scheme.

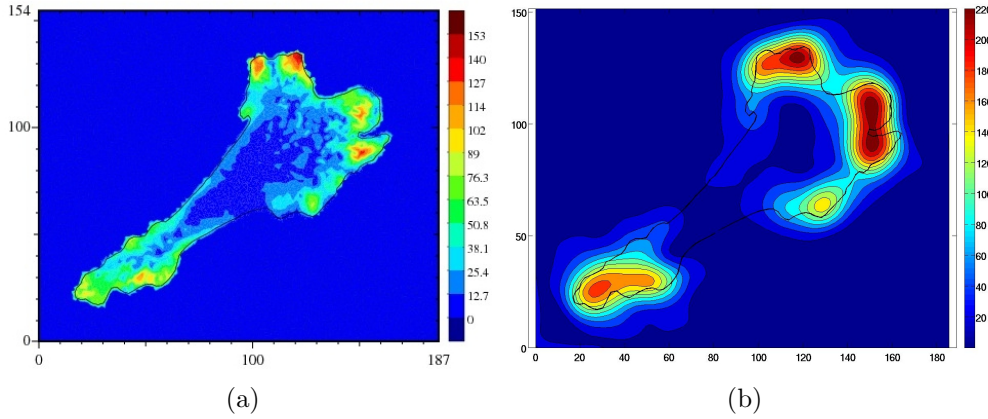


Figure 3.4: Semi-quantitative comparison of the adjoint method and the fast Fourier traction cytometry. The color bar are in Pa.

A fast comparison has been made between the force field obtained with adjoint method and the fast Fourier traction cytometry as described by Butler [20], respectively figure 3.4(a) and 3.4(b).

The unconstrained FTTC has been implemented with a Gaussian filter applied in the Fourier space,  $H(k_x, k_y) = \exp(-D^2(k_x, k_y)/2/D_0^2)$ , where  $D_0$

is the cut off frequency ( $D_0 = 0.16$  in our case), see appendix 1. The two methods give a similar approximation of the force field, detecting the peak of the traction stresses in the same areas, i.e. at the leading edge and at the rear of the cell. Nevertheless, with the Fourier method these areas are wider than the ones detected with the adjoint method. For the latter one, the peaks detected in the small zones probably correspond to the focal adhesion sites. It is appropriate to underline the importance of the filtering in both methods (as well as in any others methods). In particular the use of a Tikhonov filter either a Weiner filter could improve the results of FTTC method.

The computational cost of these methods can be estimated for a shear force  $\mathbf{T}$  to be calculated at  $N$  points. The method by Dembo and Wang requires  $N$  sums to compute the integral (3.1.2) for all the  $N$  nodes, while the solution of the linear system arising from the finite element discretization is usually solved by an iterative linear solver that typically involves order  $N$  operations. Therefore the computational cost of the adjoint method scales like  $N$ , while the usual one scales like  $N^2$ . This difference is essentially due to the local nature of the finite element basis, leading to a sparse stiffness matrix. Conversely, the quadrature (3.1.2) is an explicit sum spanning the whole computational domain. This issue has been addressed by Sabass *et al.* [93] who proposed a splitting of the elastic field into spatial ranges that require a different numerical accuracy.

The adjoint method is approximate because it does not use an exact solution of the elasticity equation, but a vertically averaged system of equations between 0 and  $-h$ , see figure 3.5. However, the non-dimensional number characterizing the differential equations involves this somehow arbitrary vertical height through a combination of  $h$  and  $\varepsilon$ , which is an actual parameter to be fixed by the regularization method.

The locations of the beads are used as nodes in the construction of the triangular mesh of the boundary element method and adjoint one. On the contrary, in the Fourier approach, a rectangular mesh is used for the computation. In this way one additional approximation is introduced: the reconstruction of the beads displacements on that mesh. Due to the inverse character of the problem, the norm of the traction field can diverge.

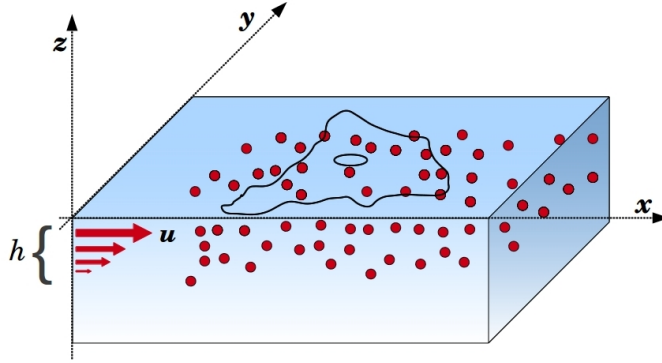


Figure 3.5: With the adjoint method the solution is approximate by a vertical integration between 0 and  $-h$ . The beads displacements  $\mathbf{u}$  rapidly decay to zero far from the gel surface.

For the adjoint method, introducing three Lagrange multipliers, the condition of the null-average force, that must hold for an isolated system, can be inferred:

$$\int_{\Omega} \mathbf{f} = \mathbf{0}.$$

In this work, the adjoint method has been used for the computation of the traction stresses due its flexibility.





# Chapter 4

## Experimental methods

This chapter will describe the experimental set-ups used in this work. The cell type will be characterized from a biological and mechanical point of view. We will explain how the polyacrylamide gels have been prepared and we will present their local and global properties. The microscope facilities for the observation of the cells will be detailed. Finally, we will explain how the experimental displacements can be measured and how to compute the force field.

*Ce chapitre décrit les montages expérimentaux utilisés pour ce travail. Le type de cellule sera caractérisé d'un point de vue biologique et mécanique. Nous allons expliquer comment les gels de polyacrylamide ont été préparés et nous présenterons leurs propriétés locale et globale. Les installations de microscopie pour l'observation des cellules seront détaillées. Enfin, nous allons expliquer comment obtenir les déplacements expérimentaux et comment calculer le champ des forces.*

### 4.1 Cell types

In this thesis we use human cancer cells and more precisely cells that come from bladder cancer. The cells coming from this cancer are referred to as transitional cell carcinoma: it is a cancer that begins within cells in the

innermost tissue layer of the bladder. These cells are able to stretch when the bladder is full and shrink when it is emptied. In particular, we used a panel of three cell lines: RT112, J82 and T24. These cell types represent progression from well to poorly differentiated phenotypes and arise from superficial to invasive bladder cancer. The RT112 are moderately differentiated and are characterized by a cytological grade (or differentiation) 2 [23]. The T24 and J82 cancer cells are poorly differentiated and have a cytological grade 3 [23]. The doubling time of the three lines is 24 hours.

#### 4.1.1 Cell culture and invasivity

The three cancer cell lines were obtained from ATTC (Rockville, USA) and were cultured in RPMI 1640 (Sigma Chemical Co.) supplemented with 10% fetal bovine serum and antibiotics. Cultures were kept at 37°C in 5% CO<sub>2</sub> humidified atmosphere. For the experiments, 10<sup>6</sup> cells/ $\mu$ l were seeded on the polyacrylamide gels and incubated for 12 hours to allow cells to adhere and spread on the substrate.

The invasive capacity of these cancer cells has been taken from the literature. Briefly, cell invasion assays consist in seeding the cell on the top of 3D collagen matrices and culture them for several days (depending on the protocol used) at 37°C, 5%CO<sub>2</sub> and 95% humidity. Invasive cells are able to degrade the matrix and migrate to the underside of the matrix into the lower compartment. The depth at which the cells are found define their invasive capacity. *In vitro*, T24 and J82 cell lines display a high invasive capacity, whereas RT112 have a moderate invasive capacity [17]. The invasiveness has been correlated with the expression of E-cadherin: *in vitro* RT112 cancer cells have homogeneous expression of E-cadherin while T24 and J82 cells do not present expression of E-cadherin at the cell membrane [17].

#### 4.1.2 Cell migration assays and mean square displacement

The ability of cells to migrate on the surface of the gels has been measured.

$10^6$  cells/ $\mu\text{l}$  were seeded on the polyacrylamide gels ( $E = 10$  kPa), incubated for 12 hours and observed for at least 6 hours. The images were recorded every 5 minutes with the help of a dynamic microscope, Zeiss AxioVert 200M. Only those cells that were isolated, did not touch other cells and did not undergo cell division were used for the study of the migration parameters. Using the ImageJ software (National Institute of Health) [91] with a manual tracking plug-in, pixel coordinates for each cell's centroid in each image frame, and migration paths for each cell were determined.

A parameter that allows to characterize the migration of the cells is the mean square displacement. The mean square displacement (MSD) describes the mean of the squared distances between a common starting point at time  $t_0$  and the actual positions of a cell at time  $t$ ,

$$MSD(t) = \langle [x(t + t_0) - x(t_0)]^2 + [y(t + t_0) - y(t_0)]^2 \rangle, \quad (4.1.1)$$

where  $\langle \dots \rangle$  denotes an average over all starting times  $t_0$ .

The means square displacement is often discussed in terms of the slope as this relates directly to a classification of the behaviour of the motion. The increase of the mean square displacement can be quantified by the logarithmic derivative

$$\alpha = \frac{d \ln(MSD(t))}{d \ln(t)}$$

leading to a time dependent power law

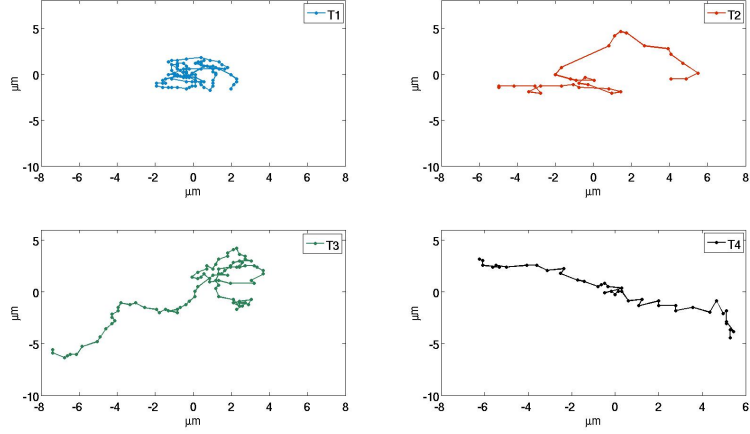
$$MSD(t) \propto t^\alpha \quad (4.1.2)$$

where  $0 < \alpha < 2$

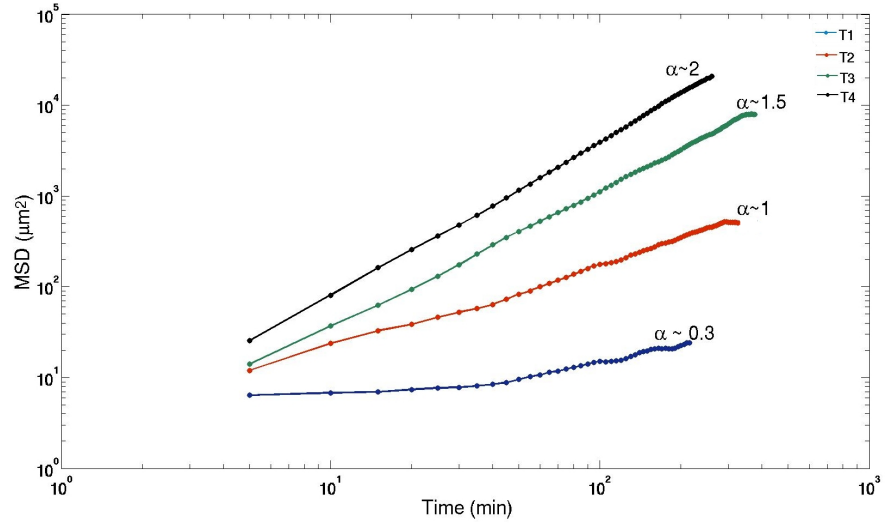
The value of  $\alpha$  characterizes the motion, the persistence of the motion. It can be characterized as

- sub-diffusive for  $0 < \alpha < 1$ ;
- diffusive (or Brownian ) for  $\alpha = 1$ ;
- super-diffusive for  $1 < \alpha < 2$ ;

- ballistic (directional motion with no diffusion) for  $\alpha = 2$ .



(a)



(b)

Figure 4.1: Four different trajectories (a) and the corresponding log-log plot of MSD (b) that represent particles with a sub-diffusive behaviour (T1), diffusive (T2), super-diffusive (T3) and ballistic (T4).

If the cell encounters no other cell and travels in a ballistic way, then the distance  $d$  it travels should be proportional to the time interval and the mean square displacement would increase quadratically with time,  $MSD(t) \propto t^2$ .

Beyond this time the motion is better described as a random walk, for which the mean square displacement increases only linearly with time  $MSD(t) \propto t$ . The rate of growth of the mean square displacement depends on how often the cell suffers collisions or changes direction. When  $\alpha \neq 1$ , often the migration is described as anomalous: slower diffusion for small times, the sub-diffusive motion, while long-time motion is faster (super-diffusive).

### 4.1.3 Cell mechanical properties

The mechanical properties of the cytoskeleton of the cells have been measured with the help of the atomic force microscope (AFM).

#### Atomic Force Microscopy (AFM)

AFM allows to measure forces between a sharp probe, supported on a flexible cantilever as a type of spring, and the surface of a sample at very short distance. The tip touches the surface and records the local force between the probe and the sample. The basic idea of this microscopy is that the local attractive or repulsive forces between the tip and the sample are converted into a bending, or deflection, of the cantilever according to the Hooke law. These deflections are detected using a laser beam that is reflected from the back of the cantilever onto a detector. Matching the signals from different sections of the detector makes it possible to measure the position of the laser spot.

In force spectroscopy the cantilever-tip assembly acts as a force sensor. In this mode the cantilever and the tip are moved directly toward the sample until are in contact with it, and then retracted again, while the interaction between the tip and the specimen is measured.

In order to derive the Young modulus ( $E$ ) from the force curves we have to focus on the extend curve (light red) since it contains no interactions, like adhesion, that make determination of the contact point impossible.

The first step of the batch process is to remove any offset or tilt from the curve and find the contact point. Finding the indentation ( $\delta$ ) is a critical step: one takes the difference between the piezo movement ( $z$ ) and the can-

tilever vertical deflection ( $d$ ). Once these operations have been performed, the Young modulus can be obtained fitting the curve with the Hertz model [61] (figure 4.2).

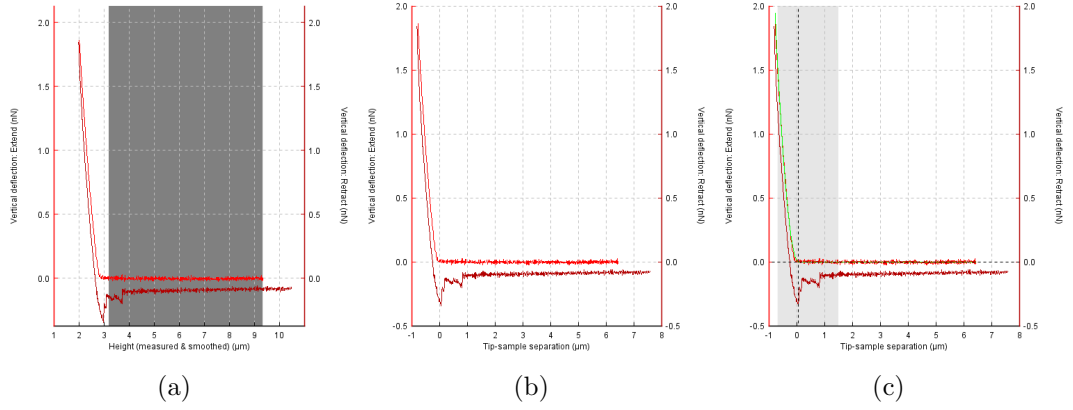


Figure 4.2: Operation of the batch process: (a) removal of the offset and the tilt from the curve; (b) calculation the tip-sample separation: the cantilever deflection in units of length is subtracted from the piezo height; (c) selection of the range for the elasticity fit. All the operations are performed on the extend curve (light red), the only that has no adhesion in the case.

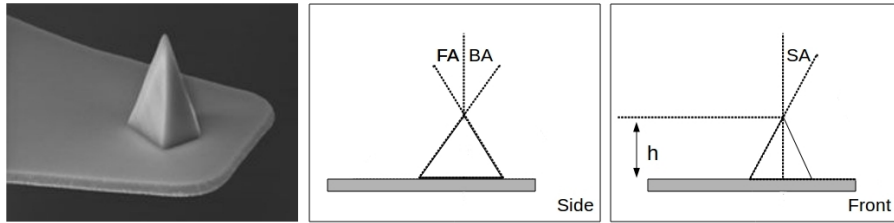


Figure 4.3: Characteristics of the pyramidal tip used for the measurements. Front angle (FA):  $15^\circ$ , back angle (BA):  $25^\circ$ , side angle (SD):  $17.5^\circ$ . Tip height ( $h$ ):  $7.5 \mu m$

The Hertz model is based on the hypothesis that the sample is an isotropic and linear elastic solid occupying an infinite half space, the indenter is undeformable with no interaction between the tip and the sample. We have to specify the properties of the sample and the parameter of the indentation. Poisson's ratio  $\nu$  describes the sample and is set to 0.5 (incompressible materials). For a tip with a pyramidal geometry, the equation that is used in

the model is:

$$F = 0.75 \frac{E}{1 - \nu^2} \tan(\alpha) \delta^2 \quad (4.1.3)$$

where  $\alpha$  is the face angle, and  $\delta$  is the indentation of the tip in the sample. For a pyramidal tip with a radius of 20 nm, the value of the angle  $\alpha$  is obtained taking the mean of the four angle: the front angle ( $15^\circ$ ), the back ( $25^\circ$ ) and the two side angles ( $17.5^\circ$ ), this gives a mean value of  $18.75^\circ$  (figure 4.3).

### Mechanical stiffness of the cells, preliminary results

In order to investigate the mechanical properties of cancer cells, we measured the nucleus and the cellular extensions with the atomic force microscope using the force spectroscopy mode, as explained before. We choose a cantilever with a pyramidal tip. For a living cell seeded on the cover-glass several points within the cells were inspected, as shown in figure 4.4.

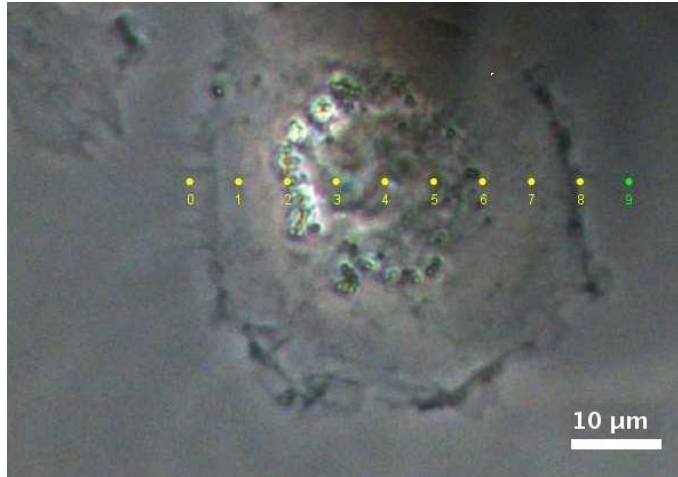


Figure 4.4: T24 cancer cell analysed under the atomic force microscope. The points n.1 and n.7 were used in the calculation of the stiffness of the cellular extensions, while the point number 4 for that of the nucleus.

For example, for that cell, the measurements obtained for the points n.1 and n.7 were used in the calculation of the stiffness of the cellular extensions, while the point number 4 for that of the nucleus. We collected around 5 cells for each cell line and from 9 to 11 points were used to obtain the mean

value of the Young modulus of the cell extensions and the nucleus, as we can see in figure 4.5. We choose a compressive force of 200 pN, a weak value to avoid to indent too much and a constant approaching speed of  $2 \mu\text{m/s}$  since it has been shown that the measurements of the Young modulus of the cytoskeleton of the cells can depend on frequency. These preliminary results that we are going to show are encouraging and can give us an indication about the mechanical stiffness of the cells.

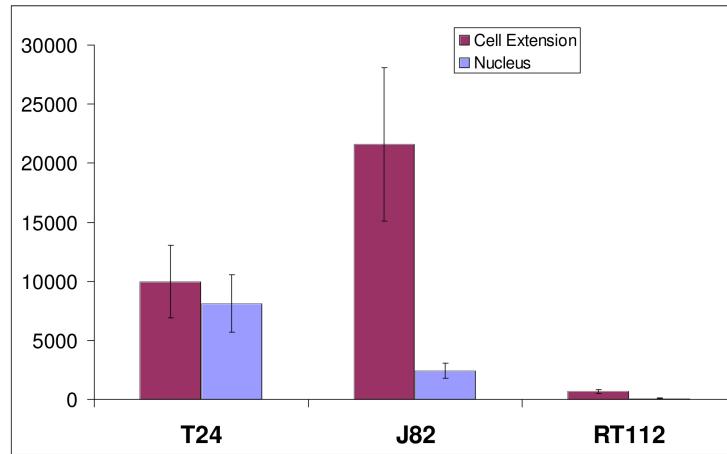


Figure 4.5: Young modulus of cell extensions and of the nucleus obtained for the three cancer cell lines seeded on cover-glass.

We found that the nucleus of the RT112 cancer cells, the less invasive line, are less rigid in comparison with the two other cell lines:  $142 \pm 39$  Pa for the RT112, while a mean value of  $8110 \pm 2436$  Pa for the T24 and  $2450 \pm 633$  Pa for the J82. The values obtained for the cellular extensions shows the same trend: a value of  $683 \pm 173$  Pa for the RT112,  $9989 \pm 3072$  Pa for the T24 and even higher values for the J82,  $21591 \pm 6506$  Pa. It is appropriate to underline that the values found for the cellular extensions could be overestimate: due to the thin thickness of the extensions of the cells, the measurements can be sensible to the substrate stiffness. So we choose a small indentation. Models that correct the values of the Young modulus exist where the thickness of the sample is taken in account [35].



## 4.2 Gels

Polyacrylamide gel is known to offer several advantages for applications as a biomaterial for cell culture. One of the well-known properties of this material is that the modulus of elasticity of the gel can be easily tuned changing relative concentrations of acrylamide and bis-acrylamide [11, 85, 101]. Polyacrylamide is generally non fouling, meaning that the adsorption of serum proteins or the non specific binding of cell surface receptors is typically negligible. As a result, only adhesive molecules chosen to be covalently attached to the surface of the gel can serve as ligands for cell attachment [52]. The pore sizes of the gel are on the order of 100 *nm*, preventing cells and their extensions from entering the substrates. Immunofluorescence is also possible at high magnifications because of the thin, translucent quality of the gels. Therefore thin gels need to be used (50-100  $\mu m$ )

### 4.2.1 Gel preparation

This protocol is based on original work of Pelham and Wang [85]. For gel preparation, we need to dispose of one square cover-glass 22*mm* x 22*mm* and a circular one, 35*mm* in diameter. We leave the square glass into pure silane (Sigmacote SL-2, Sigma-Aldrich, USA) for about 30 minutes. During this time, we wash the round cover-glass with 0.1M NaOH. The side of the cover-glass which needs to be activated was treated with APTMS for 10 minutes, washed with distilled water and then treated with 200  $\mu l$  of glutaraldehyde 0.5% for 30 minutes. Once the surface is silaned, we prepare 500 $\mu l$  of gel solution by mixing the 167  $\mu l$  of 30% acrylamide and 15  $\mu l$  of 1% bis-acrylamide in distilled water (315 $\mu l$ ). 2.5  $\mu l$  of fluorescent beads (Molecular Probes, 0.2 micrometer in diameter) were seeded before addition of the cross-linker. In order to catalyze the polymerization of the gels, 2.5  $\mu l$  of ammonium persulfate (APS) and 0.5  $\mu l$  of TEMED (tetramethylethylenediamine) were added to the gel solution. 34 $\mu l$  of solution were quickly pipeted on the square cover-glass and the circular cover-glass was brought carefully to capture the gel by capillarity, this avoiding to flip the preparation. Indeed beads need to sediment fast so that there are located closer to the gel

upper surface where measurements are made. The gel volume was chosen so that gels have a thickness of about  $70\ \mu m$ , as described in other works [11, 85]. The gel was left to polymerize for nearly 90 minutes in a humidified atmosphere.

After polymerization, the square cover-glass was gently removed. In this protocol, Sulfo-Sanpah, a heterobifunctional protein cross-linker is used to covalently bind the protein to the polyacrylamide surface. Exposure of the gel in a solution of Sulfo-Sanpah with a UV light source covalently links this product to the polyacrylamide hydrogel and then the N-hydroxy-succinimide ester in Sulfo-Sanpah can react with the primary amines of proteins to complete the attachment of proteins to the gel surface. In order to activate the polyacrylamide surface, we mixed 1 mg/ml Sulfo-Sanpah 1mM, with DMSO to dissolve it and HEPES. Then we placed 200  $\mu l$  of this solution onto the surface and incubated under UV for 15 minutes. This procedure was repeated twice, then the surface was rinsed with HEPES. Finally a 100 $\mu g/ml$  collagen solution was used overnight to bind the above surface at 4°C (no light).

#### 4.2.2 Rheometry

The mechanical properties of the gels have been measured by conventional dynamic rheometry tests (Malvern rheometer, Gemini 150). Sinusoidal oscillations with a known deformation  $\gamma = \gamma_0 \sin(\omega t)$  are applied within the linear regime (small enough deformation  $\gamma_0 \sim 0.01$ ) at different angular frequencies  $\omega$ . The stress response  $\sigma = \sigma_0 \sin(\omega t + \phi)$  (where  $\sigma_0$  is a constant stress and  $\phi$  is the phase angle) is measured and the elastic ( $G'$ ) and viscous moduli ( $G''$ ) are deduced.

Experiments show a constant  $G'$  (elastic modulus) when the frequency  $f$  ranges from 0.1 to 10Hz. The loss modulus  $G''$  is usually lower by two orders of magnitude (data not shown). We deduce the value of the elastic modulus  $E = 3G'$  and find 1.95 kPa, 6.3 kPa and 9.9 kPa for the soft, medium and hard gels respectively. Note that the hypothesis that  $E = 3G'$  is relevant here in view of a recent work [18] showing that  $\nu \sim 0.48$  in such polyacrylamide

gels. This means that our hypothesis of incompressible material (i.e.  $\nu = 0.5$ ) is quite good, and is not responsible for the differences found as compared to other methods. Such comparisons are shown in Figure 4.6 where our results are found to be close to the ones obtained by Pelham and Wang [85] or Boudou *et al.* [18]. Since our method relies on no further hypotheses and is based on the use of large samples, we have good confidence in our data. Other techniques which can be used are traction tests [85, 40], micropipette experiments [18], AFM [40, 48], or rheometry [106].

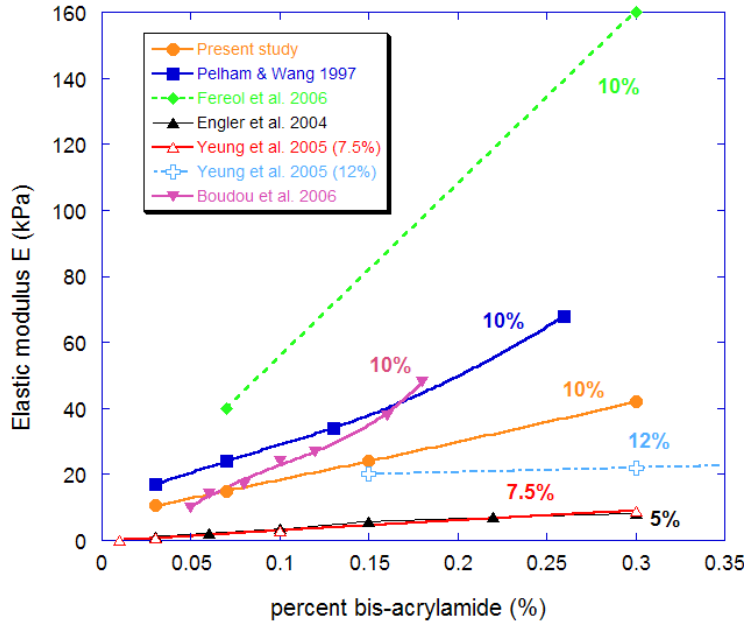


Figure 4.6: Elastic moduli  $E$  (kPa) as a function of the bis-acrylamide percent. Values from other authors are also reported [48, 18, 85, 106, 40] for the case of 10% polyacrylamide concentration and a few other concentrations.

### 4.2.3 AFM measurements

The local properties of the gels have been measured with the atomic force microscope, as explained in the section 4.1.3. We choose a cantilever with a pyramidal tip.

The fitting was been done for four different polyacrylamide gels with or

without collagen and exposed to UV light for two times 5 or 10 minutes. For each gel, we have carried out the measurements in four different regions and for each region on a square grid with 16 points. The values of Young modulus  $E$  obtained fluctuate between 7 and 16 kPa almost for all the gels, as shown in figure 4.7. These value are in the same range of the values obtained with reometry measurements.

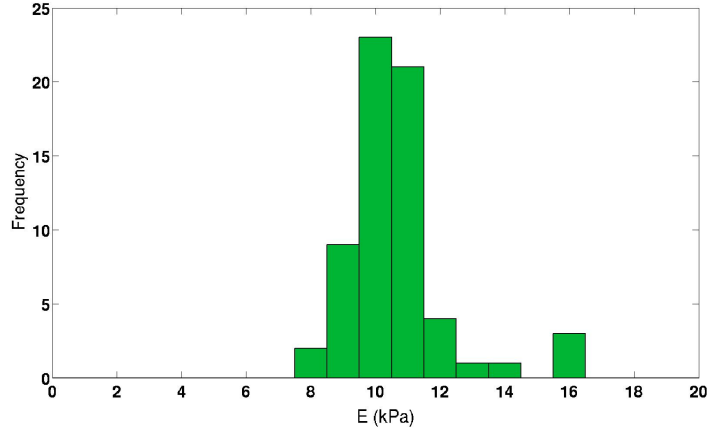


Figure 4.7: Young modulus of the polyacrylamide gel measured locally with the help of the atomic force microscope.

Figure 4.8 shows an example of the surface topography obtained in contact mode for a polyacrylamide gel without collagen.

While scanning the sample's surface, static deflection of the cantilever is recorded. The AFM is used in constant force mode: the tip is moving in  $z$ -direction to obtain a constant deflection and therefore a constant distance from the surface. The  $z$ -movement of the tip corresponds to the topographic images. Figure 4.8(a) shows the fluorescent beads present on the gel surface. Figure 4.8 (b) represents the topography of a small area of that gel. The scan was done on a square region of  $40\ \mu\text{m} \times 40\ \mu\text{m}$ . On the topographic map are located some beads, the ones that are on top of the gel. The gel's surface is quite uniform, with a mean surface roughness of  $0.76\ \mu\text{m}$ .

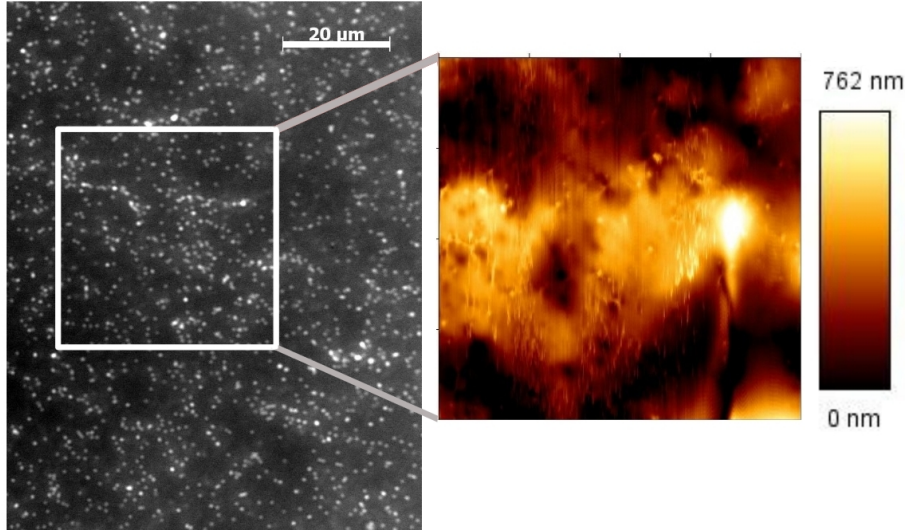


Figure 4.8: On the right: gel surface scanned with AFM. The scale bar at the upper right corner is  $20\ \mu\text{m}$  long. On the left, topography of the gel surface reconstructed with the AFM. A roughness of around  $0.76\ \mu\text{m}$  was found for the gel surface. The scan was done on a region  $40\ \mu\text{m} \times 40\ \mu\text{m}$ .

### 4.3 Microscopy

In order to perform the computation of traction forces, we need to observe at the same time the cell position and the displacement of the beads. We have to record simultaneously a phase-contrast image focused on the cell and a fluorescent one, related to the beads position (figure 4.9). To achieve this aim, we used the dynamic microscope, Zeiss Axiovert 200M inverted, at Institut Albert Bonniot (IAB). One of its potentiality is to combine the phase-contrast technique with the fluorescent one.

The phase contrast microscopy technique is widely used for examining specimens such as biological tissues. It is a type of light microscope that enhances contrast of transparent and colourless objects by influencing the optical path of light. The phase contrast microscope is able to show components in a cell or bacteria, which would be very difficult to see in an ordinary light microscope. This microscope uses the fact that the light passing through a transparent part of the specimen travels slower and, due to this, is shifted

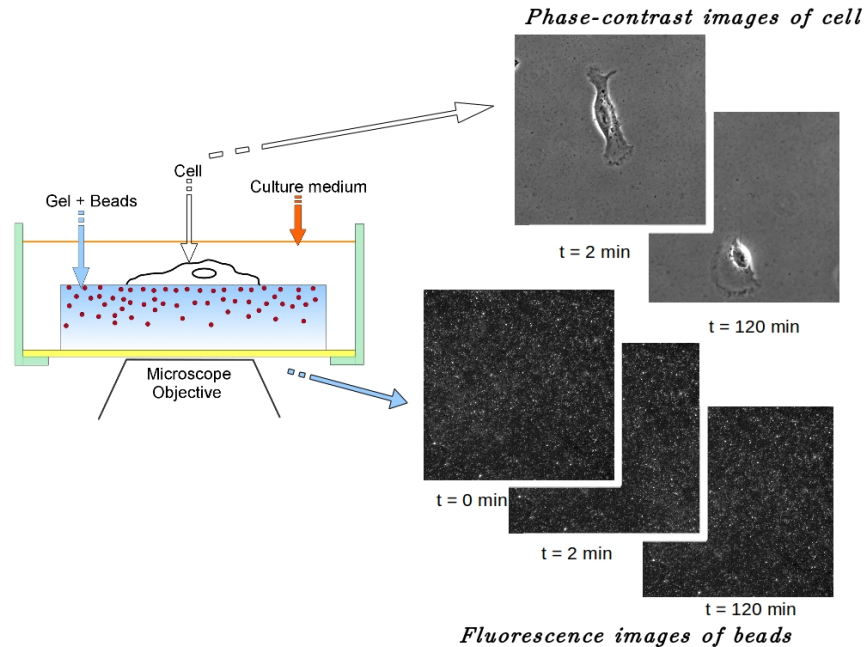


Figure 4.9: Simplified scheme of the images recording process. Phase-contrast images of the cell and fluorescent beads recorded with the microscope. The time  $t = 0 \text{ min}$  is related to the undisturbed position of the beads.

compared to the uninfluenced light. This difference in phase is not visible to the human eye. However, the change in phase can be increased to half a wavelength by a transparent phase-plate in the microscope and thereby causing a difference in brightness. This makes the transparent object shine out in contrast to its surroundings.

Fluorescence microscopy technique is based upon the concept that there are certain materials that emit energy which can be detected as a visible light. Each of these materials must be irradiated with a different specific light wavelength in order to cause an energy reaction in the form of light. The sample being used can either be treated with some fluorescing substances or it can be fluorescing in its original form. The visible light in the microscope eyepieces is not the original light emitted by the light source but the one fluoresced from the specimen itself. In order to receive such a response a high intensity light source must be used. The specimen fluoresces and it

is this fluorescing light that passes back through the fluorescence emission filter and goes to the microscope eyepieces or camera to provide a bright and colourful fluorescence image of the specimen.

Living cells were maintained at 37°C in 5% CO<sub>2</sub> atmosphere under the Zeiss Axiovert 200M inverted microscope equipped with a CoolSNAP HQ2 camera and were observed with a 40x plan-Neofluar objective. In the application submenu of the MetaMorph software [5] time lapse, multi stage position, multiple wavelength, Z series were selected. Two wavelengths have been selected: transmission always on, for the phase-contrast image of the cells and Rhodamine one for the beads position. The time-lapse option allows us to choose the time interval among the recording images and the total acquisition time. In our experiments, we decide to use a time interval of two minutes for two hours, that give us a stack of 60 frames roughly. Thanks to the multi stage position options, we were able to select different cells, at least 5, on the gel. Once the focus plane of the cell is detected, a Z-series of images for the rhodamine wavelength are acquired: in this way, at the end of the experiment, it is possible to choose the images of the beads corresponding to the best focus. Usually, a step size of 0.5  $\mu m$  was used.

### 4.3.1 Immunofluorescence staining of cells

Immunofluorescence is a technique allowing the visualization of a specific protein or antigen in cells or tissue sections by binding a specific antibody chemically conjugated with a fluorescent dye. These labelled antibodies bind (directly or indirectly) to the antigen of interest.

Antibody molecules are roughly Y-shaped molecules consisting of three equal-sized portions and bind specifically to a particular substance, the antigen. The two antigen-binding sites are at the tips of the arms of the Y, the variable region, while the trunk defines the constant region which determines the particular effector function of the antibody and it is usually labelled with a fluorochrome.

The two main methods of immunofluorescent staining are direct and indirect, as shown in figure 4.10. In direct immunofluorescence, the antibody

against the molecule of interest is chemically conjugated with a fluorescent dye. In indirect immunofluorescence, the antibody specific for the molecule of interest (called the primary antibody) is unlabelled, and a second anti-immunoglobulin antibody directed toward the constant portion of the first antibody (called the secondary antibody) is tagged with the fluorescent dye, as shown in figure 4.10.

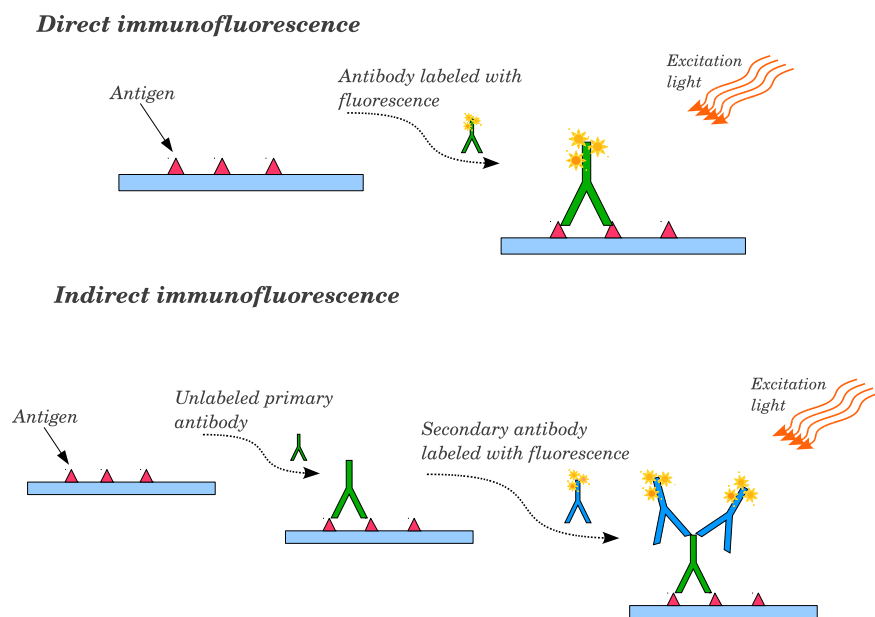


Figure 4.10: Scheme of the direct and indirect immunofluorescence. In the first method, the fluorochrome is directly linked to the primary antibody. In indirect immunofluorescence, the secondary antibody is labelled with a fluorochrome and binds the unlabelled primary antibody specific for the molecule of interest.

We decide to observe the organization of the cell cytoskeleton when the cells were seeded on polyacrylamide gels or on cover-glass. We want to stain the nucleus, the actin, the myosin and the focal adhesion sites at the same time. For the latter, we decide to stain the paxillin, a protein present in mature focal adhesions. For the nucleus we used Hoechst dyes, part of a family of blue fluorescent dyes that has specificity for DNA. The cytoskeleton was labelled with Phalloidin, a toxin that binds specifically the filamentous actin.



For staining paxillin and myosin we used the indirect immunofluorescence. The protocol used for staining the cells seeded on the cover-glass or on the polyacrylamide gels is the same. More precisely, the cells were plated on the selected substrate at least 12 hours before the fixation and incubated at 37°C in 5% CO<sub>2</sub> humidified atmosphere. The cells were fixed and rendered permeable at the same time at room temperature: after washing two times the cells with PBS 1x, 500  $\mu$ ml of a solution containing 2% paraformaldehyde (PFA), Triton X100 0.5% and 2% sucrose were added to the sample for 30 minutes. The sucrose avoids cell retraction. The sample was washed three times with PBS/Tween20 0.05% in order to remove the paraformaldehyde. The samples are now ready for the immunofluorescent staining. We first prepare the solution with the primary antibodies: in 100  $\mu$ l of a solution of PBS/BSA 0.2% and Tween20 0.05%, we added 1  $\mu$ l of mouse antibody against the paxillin and rabbit antibodies against myosin. This solution was added to the sample, covered with a parafilm in order to avoid evaporation and incubated for 30-45 minutes at room temperature. To remove the surplus of antibodies not fixed inside the cells, the samples were washed first quickly and then three times for 5 minutes with PBS/Tween20 0.05%. Successively, the antibodies labelled with a fluorescent dye were diluted. Phalloidin Alexa 488 was used to label the actin, Hoechst for the nucleus, goat anti-mouse Alexa 568 to stain the paxillin and donkey anti-rabbit Dylight 649 for the myosin and, as the primary antibodies, they were included in a solution of PBS/BSA 0.2% and Tween20 0.05%. For incubation, the sample was placed in the dark for 30 minutes at room temperature. Again, the sample was washed several times with a solution of PBS/Tween20 0.05% to remove the not fixed antibodies. Following a final washing step with distilled water, excess liquid was removed and the cover slips were mounted onto slides with Dakomount mounting media (DAKO) to prevent fading. The slides were dried overnight in the dark and analysed the next day with a dynascope (confocal) microscope, Zeiss AxioObserver Z1, at Institut Albert Bonniot. The observations were made with an objective EC Plan-Neofluar 40x Oil.

## 4.4 Determination of the displacement field

The basic step for the calculation of the traction field is the determination of the beads displacements. The displacement field was extracted from a stack of images: the first one showed the beads in the undeformed position and the other images showed the gel deformed under cell traction. Usually a stack of 30 images was used and the times between frames were chosen to be two or three minutes. This enabled to capture sufficient changes in the beads positions but not too much so that beads could be followed along their trajectories. The undeformed position of the beads is obtained at the end of the experiment: distilled water is added into the sample in order to detach the cells from the gels. The substrate release the elastic energy and the beads return to their undisturbed position.

The processing of these images began with the correction of the images for relative translational shifts. Here we used the ImageJ software, in particular the “Align Slice” plug-in in order to perform a recursive alignment of a stack of images. The alignment proceeded by propagation: each image was used as a template with respect to which the next slice was aligned.

From the corrected images sequences, we localized cells and divided images into small areas typically  $150\mu m \times 150\mu m$ , each containing one isolated cell. Beads detection was made using “Particle Tracker”, another ImageJ plug-in. The plug-in implemented point detection and a tracking algorithm as described in Sbalzarini and Koumoutsakos work [96]; it performed two different steps: first the detection of the beads positions in each image and then the beads link into trajectories. The estimation of the bead center location was done by finding the maximum local intensity in the image. The point locations were refined under the assumption that the beads local intensity maxima were near the true geometric centers of the beads and finally spurious detections such as dust or particle aggregates were rejected. The linking algorithm identified centers corresponding to the same physical particle in subsequent frames, using a graph technique theory, and linked these positions into trajectories.

An example of the image processing technique is provided in Fig.4.11; in

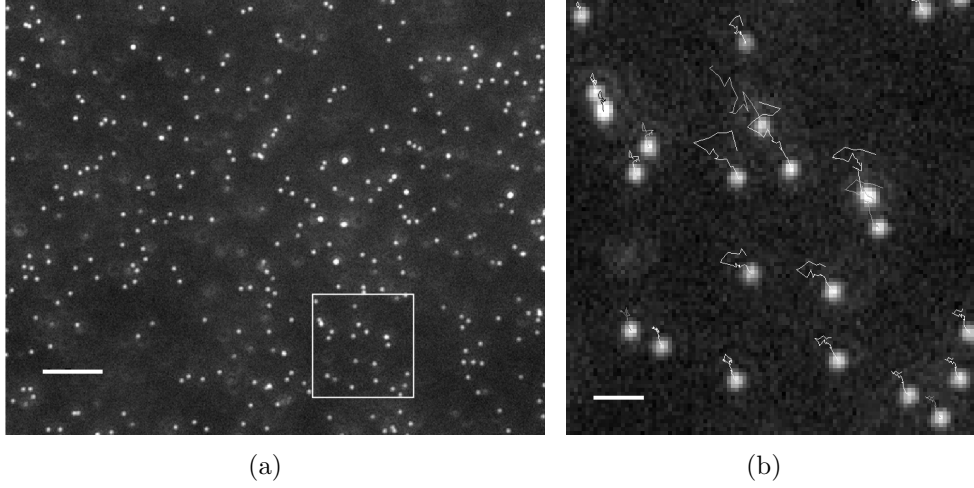


Figure 4.11: (a) Image of undisturbed positions of the fluorescent beads as recorded with the microscope. The scale bar is  $10\mu m$ . (b) Beads trajectories detected with ImageJ after processing a stack containing 30 images. The scale bar is  $2\mu m$ .

particular, Figure 4.11(a) represents the fluorescent beads as recorded with the microscope, this configuration being related to the undisturbed position of the markers. Figure 4.11(b) shows the trajectories of these fluorescent markers under cell traction after 70 minutes. They are obtained after treatment of a stack containing 30 images.

The precision with which we detected the beads position is linked to the resolution of microscope objective. The resolution ( $R$ ), i.e. the smallest resolvable distance between two objects, can be computed as the ratio of the wavelength spectrum  $\lambda$  of light used to image the sample, and the resolving power of an objective, i.e. the numerical aperture ( $NA$ ),  $R = \lambda/(2NA)$ , ( $\lambda = 0.5\mu m$ ,  $NA = 0.6$  for the 40x objective and  $R=0.4\mu m$ ). The precision can be estimated on the basis of convolution computations. In our case, we obtain that the precision is around  $0.08\mu m$ .

## 4.5 Computation of the traction stresses

Once the first step of the beads detection and the displacements computation settled, the next step is to build a triangular mesh in order to solve numerically the system 3.2.16. An example of computational domain is given in the figure 4.12.

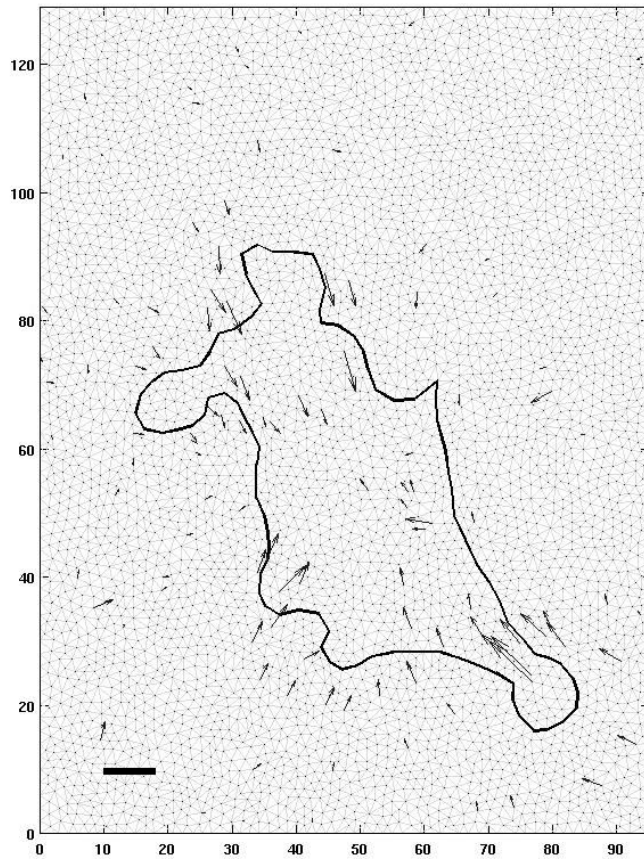


Figure 4.12: Example of the numerical set-up. The computational mesh, made of triangles, is represented in light grey. The mesh satisfies two constraints: it has one node at every point where the displacement is known and a sequence of element sides coincides with the boundary of the cell. The arrows indicate the experimental beads displacement. The reference bar at the bottom left corner is 0.5 micron long.

The mesh is built using the software Triangle [8] and it has at least a node in every point where displacements are known (beads location) and a

sequence of element sides coincides with the cell contour. In particular, the cell boundary is described as a piecewise linear curve following the shape of the cell and represents the boundary between the intracellular domain over the substrate and the rest of the domain where the forces are not applied. This can only be done by hand because of the weak contrast difference between cells and gels.

The system (3.2.16) can be now solved. The results will be presented either in terms of vector field, either in terms of colormap.

For the time evolution, the traction stress field will be represented in the form of a boxplot, see figure 4.13. The boxplot is an efficient tool for a qualitative description of the data sets and summarizes the basic information of the sample: median, quartiles, maximum, and minimum. The box itself contains the middle 50% of the data. The upper edge (hinge) of the box indicates the 75th percentile of the data set, and the lower hinge indicates the 25th percentile. The range of the middle two quartiles is known as the inter-quartile range. The ends of the vertical lines or "whiskers" indicate the minimum and maximum data values, unless outliers are present in which case the whiskers extend to a maximum of 1.5 times the inter-quartile range. The points outside the ends of the whiskers are outliers.

In our case, the outliers represent the higher values of the stresses, as we can see in figure 4.13(b) and figure 4.13(c) and these are the values we are interested in. For each cell, we look at the variation of the mean value of the outliers in time.

## 4.6 Forces exerted on lamellipodium

The protrusion of the lamellipodium is the first step of the migration process and its extension drive the cell locomotion. We wondered about the global forces exerted by the lamellipodium on the substrate. Defining the lamellipodium extension for each cell is quite difficult. The difficulty is enhanced by the fact that the cell polarity is not all the time well established and by the fact that the area varies with time. So far, we decided to approximate these extensions with the a sector of the cell, as explained later on. For

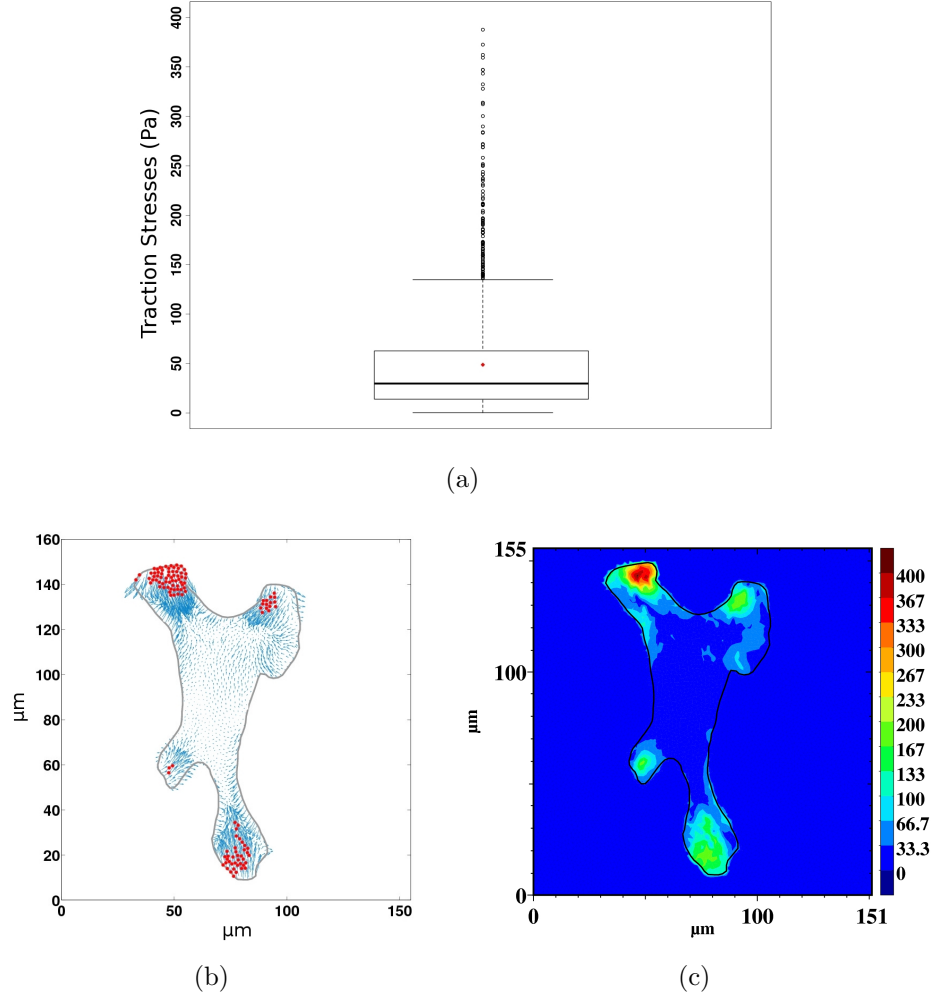


Figure 4.13: (a) Boxplot representations of the traction forces. The red dot represents the mean value of the stresses. The circles are the outliers. (b) Localization of the outliers (red points) found in the box-plot. In blue the traction vector. (c) Colour map of the stress field. The position of the outliers corresponds to the areas with the higher value of traction stresses. The scale bar is in Pascal.

each cell and for each time step, we determine the mass center the cell and we detected the direction of migration connecting at least three subsequent center points. Once the direction was detected, we considered the perpendicular to this line through the mass center and we divided the cell in to two regions. Then we proceeded with the computation of the total forces in one

of the two regions. Since the global integral on the domain of the cell has to be zero, the choice of one of the two sections is completely equivalent.

The computation of the forces exerted on the lamellipodium has been done starting from components of the traction vectors obtained solving the system (3.2.16). An example of the obtained force is given in figure 4.14. Usually typical forces vary between 10 and 50 nN.

## 4.7 Statistical analysis

Data were expressed as mean values  $\pm$  s.e.m. Statistical analysis was performed using GEE-test with R software [7]. Generalized Estimating Equations (GEE) are a general method for analysing data collected in clusters where observation may be correlated (time dependency for the stresses within a cell, focal adhesion sites presents in one cell) and observation in separate clusters are independent (three cell lines).

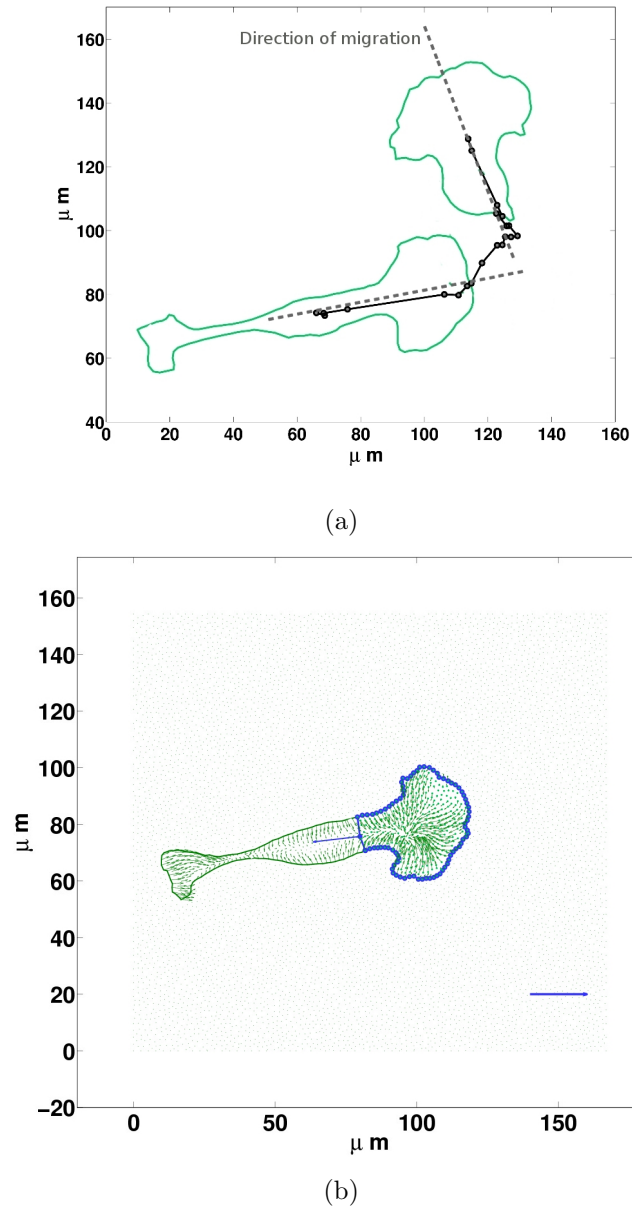


Figure 4.14: (a) Approximation of the direction of migration for a T24 cells. (b) Computation of the force exerted on lamellipodium for the first position. In green the traction stresses, in blue the domain for the computation of the force. The scale bar at the bottom right corner is 10 nN.



## Chapter 5

# T24 traction forces on gels with different rigidities

In this chapter we will apply the adjoint method for studying the traction forces of T24 cancer cells. In particular we will analyse the effect of environment on these cells looking at the ability of cancer cells to discriminate between soft and rigid substrates. We will discuss the link between traction forces, the morphology of cells and the influence of the substrates. Fibronectin-coated polyacrylamide substrata was prepared as described in the “Experimental Methods” chapter. T24 cells were observed for two hours and images were recorded every two minutes. T24 are found to migrate in a four-step motion as previously described by Sheetz [98]. This chapter is part of a paper published in Journal of Mathematical Biology [11], that can be found in appendix, and a book chapter [86].

*Dans ce chapitre, nous allons appliquer la méthode adjointe pour étudier les forces de traction des cellules cancéreuses T24. En particulier nous allons analyser l'effet de l'environnement sur ces cellules en regardant la capacité des cellules cancéreuses à discriminer entre des substrats souples et rigides. Nous allons discuter du lien entre les forces de traction, la morphologie des cellules et l'influence du substrat. Les substrats (polyacrylamide) fonctionnalisés avec de la fibronectine ont été préparés comme décrit dans la section*

*“Experimental methods”. Les Cellules T24 ont été observés pendant deux heures et les images ont été enregistrées toutes les deux minutes. Ce chapitre fait partie d’un article publié dans le Journal of Mathematical Biology [11], qui peut être trouvé en annexe, et un chapitre de livre [86].*

## 5.1 Cell morphology on different substrates

The ability of cells to feel and respond to their environment is well known and the morphology of the cell can be indicative of the cell phenotype or the cell function. Pelham and Wang, [85], showed that the normal rat kidney epithelial cell and 3T3 fibroblasts respond to differences in flexibility of the substrate by altering both their adhesion structures and motile behaviour. Lo *et al.*, [74] show that cultured cells like fibroblasts guide their movement by sensing the substrate rigidity and in turn the substrate deformations regulate the formation and the retraction of the lamellipodium. Yeung *et al.*, [106] showed that endothelial cells and smooth muscle cells respond to the stiffness of the environment changing their morphology whereas neutrophils do not seem to be affected by the mechanical stiffness of the substrate. Variations in matrix stiffness for differentiated cells is known to influence the focal-adhesion structure and the cytoskeleton [16, 40, 36].

For these series of experiments, T24 cancer cells were seeded on polyacrylamide gels of different rigidities. Gels with a Young modulus of 2, 6.5 and 10 kPa were used. The gels were prepared as described in the experimental methods section and different concentrations of bis-acrylamide were used in order to obtain three different rigidities. The gels were coated with fibronectin. On all these substrates the cells were observed to adhere, migrate and divide.

Figure 5.1 shows the phase-contrast images of T24 cancer cells adhering on the polyacrylamide gels with different rigidities. Observing the images, we can remark at once a different morphology of the cells. On the gel with a Young modulus of 10 kPa, the cell is well elongated on the substrate and it has an irregular contour. It exhibits a fibroblast-like morphology with a well spread lamellipodium unlike it does on softer gels. In fact, on the other gels,

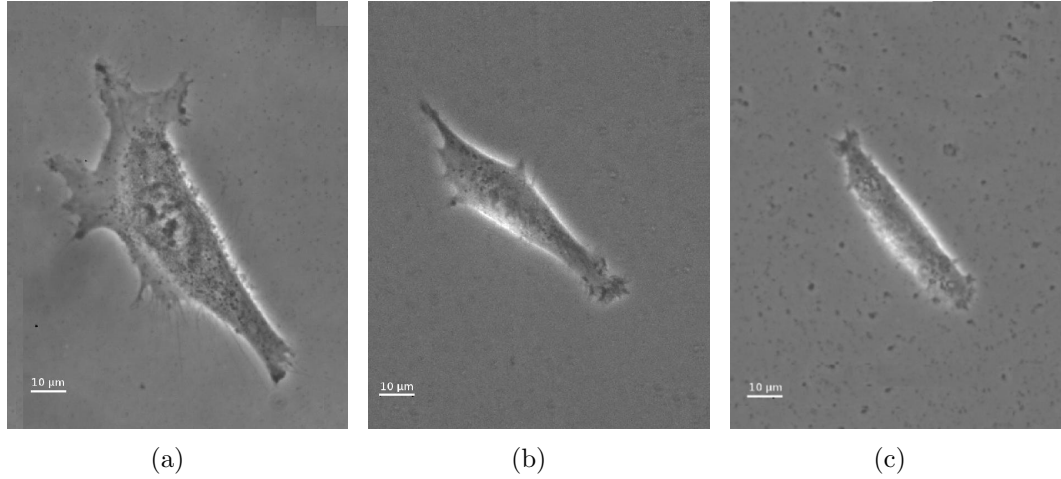


Figure 5.1: T24 cells adhering on substrates with various stiffness  $E = 10 - 6.5 - 2 \text{ kPa}$  (decreasing from left to right). Note the formation of widespread lamellipodium and a large cell area on the more rigid substrate. In the case of the very soft gel, on the contrary, the cell does not exhibit any extended lamellipodia and the cell shows a small contact area.

this structure is less and less defined, it is very thin on the gel with a rigidity of 6.5 kPa and it is definitely absent on the gels with a Young modulus of 2 kPa.

These different morphologies of the cells on the different substrates, reflect the different internal organization of the cytoskeleton. T24 cancer cells were transfected with GFP in order to visualize the actin cytoskeleton and observed under a confocal microscope.

Figure 5.2 shows the cytoskeleton of the T24 cancer cells seeded on the three sets of polyacrylamide gels with different rigidities. The observation of these pictures allows to verify that the development of the actin stress fibers is well defined on the rigid gels. On the soft gel ( $E = 2 \text{ kPa}$ ), the actin cytoskeleton structure is less defined and does not really form stress fibers. The stress fibers come close to the cell edge where it is known that the focal adhesion sites are localized. For T24 cancer cells adhering on the intermediated rigid gel ( $E = 6.5 \text{ kPa}$ ), stress fibers are still present but they are less numerous as compared to the case of the rigid gel.

The velocity of these cells varies also with the substrate rigidity (figure

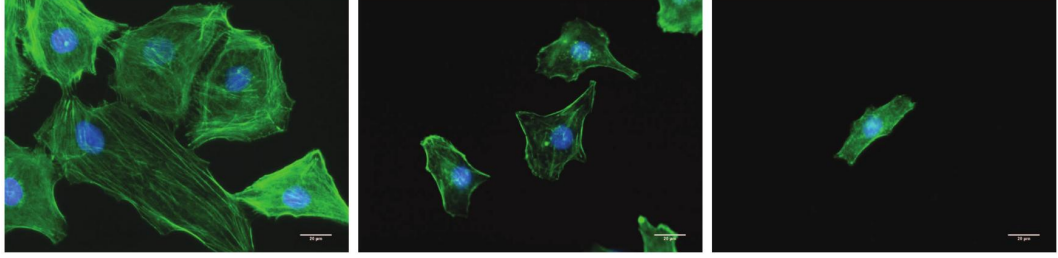


Figure 5.2: T24 cells adhering on substrates with various stiffness  $E = 10 - 6.3 - 2 \text{ kPa}$  (decreasing from left to right). The actin cytoskeleton has been marked with GFP. Note the formation of stress fibers and a large cell area on the more rigid substrate. In the case of the very soft gel, on the contrary, the actin structure is less developed and the cell barely adheres to the substrate, showing a very small contact area. The scale bar represents  $5 \mu\text{m}$ .

5.3). From the displacement of the mass center of the cells, we found that cells on the rigid gel move quite slowly, around  $0.2 \mu\text{m}/\text{min}$ : the actin cytoskeleton is well formed as well (probably) the focal adhesion sites and the cell needs more time to de-assemble them. On the other hand, on a soft substrate, the rate of migration is higher than the previous one, around  $1 \mu\text{m}/\text{min}$ : a possible explanation is that the cell is less anchored to the substrate with a less defined actin structure and can move easily.

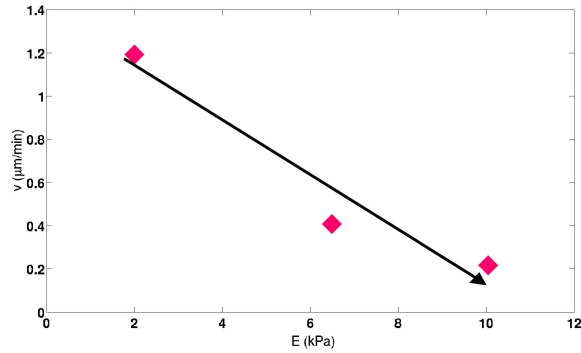


Figure 5.3: Trend of the velocity of migration  $v$  for T24 cells as a function of Young modulus  $E$ .

## 5.2 Traction forces

As cells exhibit different behaviours on the gels with various Young modulus, we wondered how cells respond in terms of traction forces that they exert on such substrates. We computed the traction stresses using the method developed by Ambrosi, [10]. As explained in the section 4.4 and 4.5, we first detected and computed the beads displacements and then we used these informations as inputs for solving the equations 3.2.16.

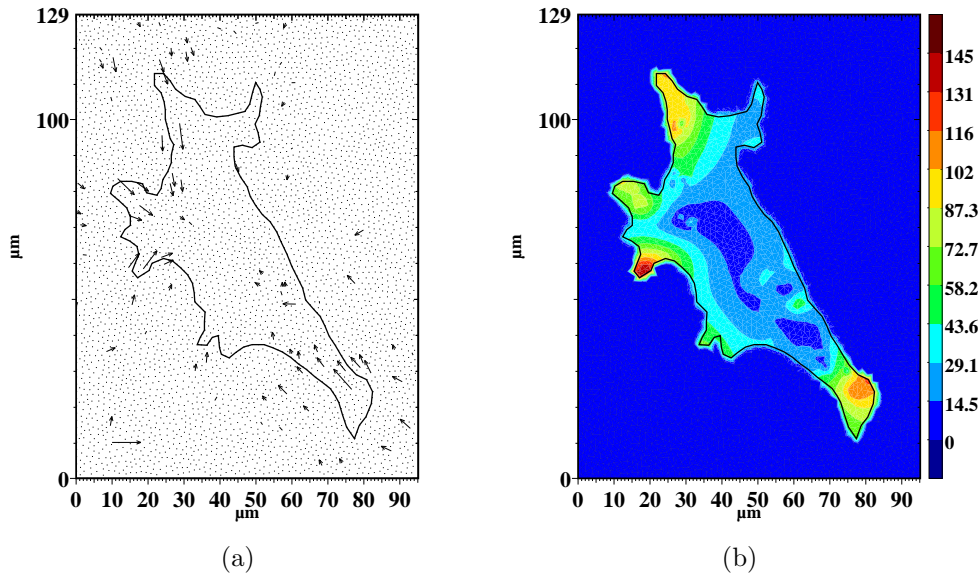


Figure 5.4: T24 cell adhering on a stiff polyacrylamide substrate ( $E = 10 \text{ kPa}$ ). (a) The displacement field under and around the cell as detected with the ImageJ software. The reference vector for displacements is  $0.5 \mu\text{m}$  long. (b) The traction field has a maximum magnitude around 145 Pa. The colour map is in Pa.

Figure 5.4 shows the experimental beads displacements (a) and the colour map of the traction stresses (b) of the T24 cancer cell shown in fig. 5.1(a) on a rigid gel ( $E = 10 \text{ kPa}$ ). The cell is moving toward the upper left corner of the picture. Around 70 beads were detected and used for the computation. The main displacements occur at the front and at the tail of the cell and the beads maximum displacements are around  $0.5 \mu\text{m}$ , as shown in figure 5.4(b). In the same areas higher values of stresses were found. The cell is anchored

by the tail at the bottom right side where the stress reaches its maximum value, around  $145Pa$ .

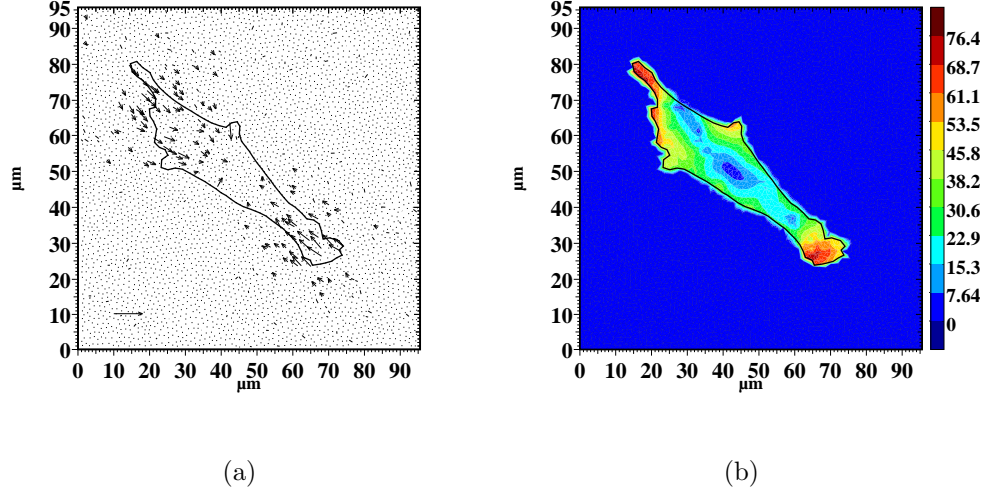


Figure 5.5: T24 cell adhering on an intermediate stiff polyacrylamide substrate ( $E = 6.5kPa$ ). (a) The displacement field under and around the cell has roughly the same magnitude as figure 5.4. The reference vector for displacements is  $0.5 \mu m$  long. (b) The traction field has a maximum magnitude around  $80Pa$ . The colour map is in Pa.

Figure 5.5 shows the beads displacement (a) and the stresses (b) of the T24 cancer cell of figure 5.1(b) on a 6.5 kPa gel. The cell is moving toward the bottom right corner of the picture. Even though the beads displacements are in the same range as in the previous case, the traction stresses are small along the cell edges with peaks at the front and tail where the maximum force is around  $80Pa$ .

By decreasing gel rigidity, we prevent the cell from adhering properly and from forming stable focal adhesions. This is translated in lower values of the traction forces, as we can see in figure 5.6 (b) showing the T24 cell on a soft gel ( $E = 2 kPa$ ) moving toward the bottom right corner of the figure. The higher traction stresses are reached at the tail and at the leading edge in the range of 50 Pa. There are many beads whose displacements are significant, usually around  $0.5\mu m$ ; they occur essentially at the cell edges, as seen in figure 5.6(a).

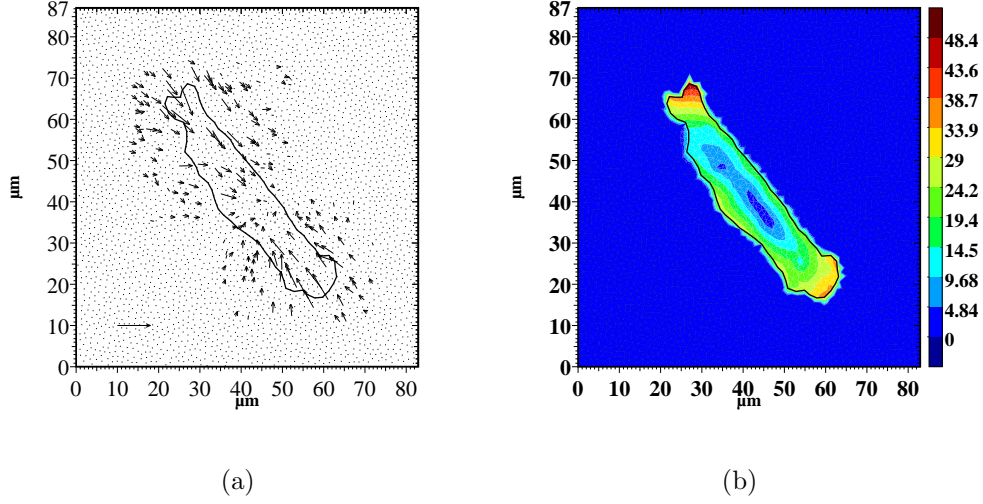


Figure 5.6: T24 cell adhering on a soft polyacrylamide gel ( $E = 2 \text{ kPa}$ ). (a) The displacement detected under and around the cell has roughly the same magnitude as figure 5.4. The reference vector for displacements is  $0.5 \mu\text{m}$  long. (b) The traction field has a maximum magnitude around  $50 \text{ Pa}$ . The colour map is in Pa.

From the above, the maximum displacements in these three experiments seem to be in the same range (around  $0.5 \mu\text{m}$ ), independently of the rigidity of the substrate. Therefore, we found that traction stresses increase with the Young modulus.

## Time dependence

T24 cells were well adherent with a extended lamellipodium on the substrate with a Young modulus of  $10 \text{ kPa}$ . For the T24 cancer cell adhering on this gel, maximum values of the traction stresses were recorded and vary between  $90 \text{ Pa}$  and  $190 \text{ Pa}$  as presented in figure 5.7. Cells move in a non continuous way [98]: their motion requires the development of protrusions until corresponding stable focal adhesions can be developed. After this is achieved, cells can retract their uropod by pulling on focal adhesions. This is precisely the significance of figure 5.7 where an unsteady regime of traction stress is observed changing abruptly from one value to another due

to rapid pulling on focal adhesion sites. Spatial and temporal regulation are required during the locomotion process; we can study this process more accurately in terms of traction stress maps, as proposed in figure 5.8 on the rigid gel. The cell first adheres and binds to the lower right part (a), then it extends protrusions (b-e), probably with the formation of stable adhesion sites (d-f). This corresponds to the red regions (large stresses). The T24 cells starts to pull on these new adhesion sites until it moves (f-g). The disassembly of adhesions at the rear of the cell and the retraction of the tail completes the migration picture and enable cell translocation. This mechanism of locomotion for the T24 cancer cell is comparable with the four or five-step picture [9, 98] which describes motion of many cell types and is summarized as follows:

- formation of a lamellipodium at the front by actin polymerization
- development of new focal adhesions coupled with the actin cytoskeleton
- force traction due to cell contraction
- release of bonds at the rear - Actin and proteins recycling

### 5.3 Discussion

The study presented here demonstrates one application of the adjoint method [10]. The major interest is that, instead of solving the CPU-consuming integral equation [32], it directly forces the 2D-averaged problem of partial differential equations to be solved by finite element method. In this respect, the resolution becomes easier, and can be done in a few seconds. The longest part is the data processing of images for the determination of the displacements whatever the method [20, 32, 97]. The approximation of the displacement field is quite good, we obtain an error  $\|\mathbf{u} - \mathbf{u}_0\|_2 \sim 3.0 \cdot 10^{-3} \mu m$ , which is small compared to displacements in the range  $[0.05 - 0.5 \mu m]$ . This clearly indicates a good resolution as compared to experimental data.

Recent works by two groups [76, 93] suggest how the resolution can still be enhanced. Merkel *et al.* [76] use thinner substrates allowing an analytical



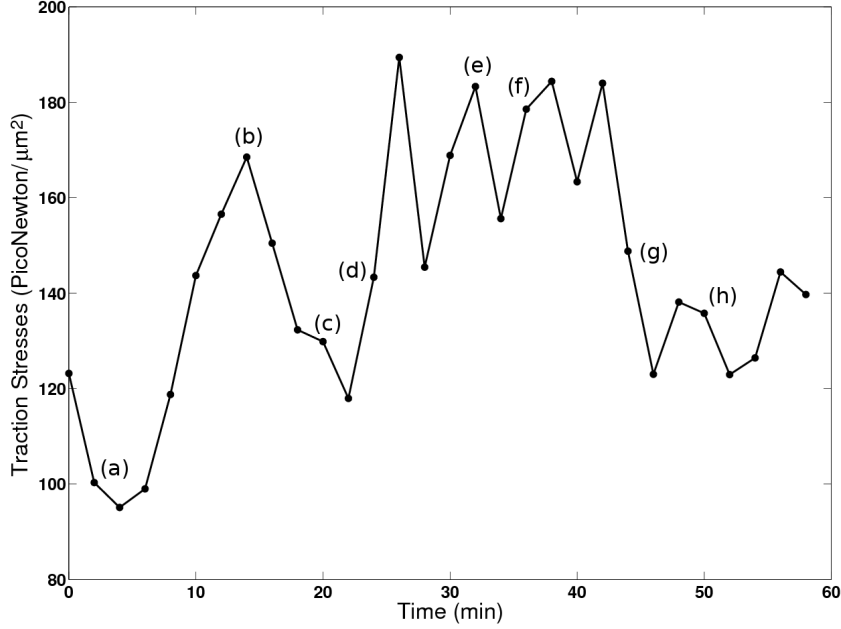


Figure 5.7: Evolution of the maximum value of the traction stresses during T24 cell migration on rigid substrate  $E = 10kPa$ .

solution of the problem even though these can alter the sensing ability of the cell [21]. Sabass *et al.* [93] illustrate the advantage of a combination of complementary fluorescent microscopy in order to capture the location and evolution of focal adhesions, in relation with traction forces, a method also proposed earlier in [15]. This enables to show an increased accuracy of all techniques, in all cases (Boundary Element Method [32], Fourier Transform Traction Cytometry [20], Traction Recovery with Point Forces [97]). In our case, we limit ourselves to the usual traction stress determination but it is possible to combine fluorescence and observe focal adhesions as well as the actin cytoskeleton development. As an example, figure 5.2 shows the actin cytoskeleton organized in stress fibers, in the case of T24 cells adhering on substrates with different rigidities (respectively the ones used before,  $E = 10 - 6.5 - 2kPa$ ). It is known that stress fibers are colocalized with focal adhesions [9] although recent authors have proposed new explanations [13, 99]. In figure 5.2, most of the stress fibers come close to the cell edges

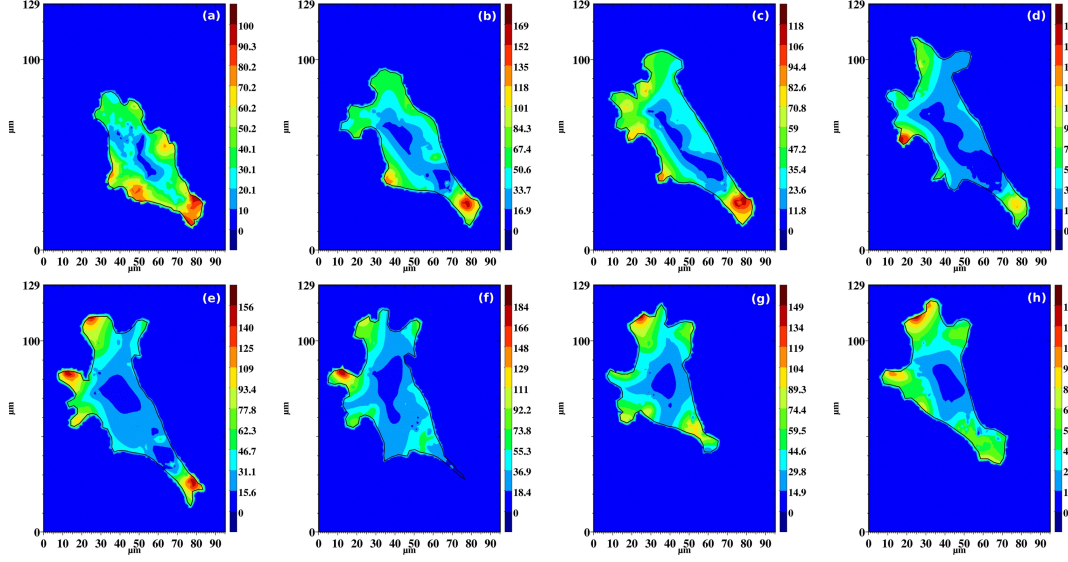


Figure 5.8: Migration of a T24 cell on a stiff gel ( $E = 10kPa$ ),  $t = 2, 14, 22, 26, 34, 38, 44, 50 \text{ min}$ . The cell first adheres strongly (red region) at its lower right part (a), then starts to exhibit protrusions (b-c-d-e) until it eventually forms new adhesion sites (e-f). At this precise time, it is able to pull on these adhesion sites, contract its rear (f-g); then it starts to move back towards the right direction (h). Note that the colour scale is reset to a range between minimum and maximum in each frame [86].

where focal adhesion complexes are usually localized. These photographs clearly indicate that T24 cells form many stress fibers on rigid substrates ( $E = 10kPa$ ) but less on soft ones ( $E = 2kPa$ ). The intermediate case also shows stress fibers but they are less numerous as compared to the case of the rigid substrate.

To continue on the effect of substrate rigidity further, let us concentrate on the stresses exerted by cells on such substrates, a subject already discussed by other authors [11, 36, 53, 74]. This current work emphasizes the ability of cells to adapt to a different environment. T24 cancer cells also seem to obey this principle; they develop similar strains when adhering to various rigid substrates. Indeed, the level of deformation does not seem to be affected by substrate rigidity in the relevant range: this comes out from figures 5.4-5.5-5.6 where it was mentioned that the displacements are very similar (of the order  $0.5\mu m$ ). Additionally the ratio between maximum stress and Young modulus

is almost a constant (strain) of the order 0.02 [11]. This is in agreement with previous works [36, 94]. It is likely that, as the substrate rigidity increases, such a (stress–rigidity) linear behaviour will fail and that there should be a saturation [53], figure 5.9, since one expects that cells cannot reinforce their integrin–cytoskeleton links indefinitely [25]. Such behaviours can be related to the cell micro–rheological properties [103], in particular their ability to modulate the growth of stress fibers.

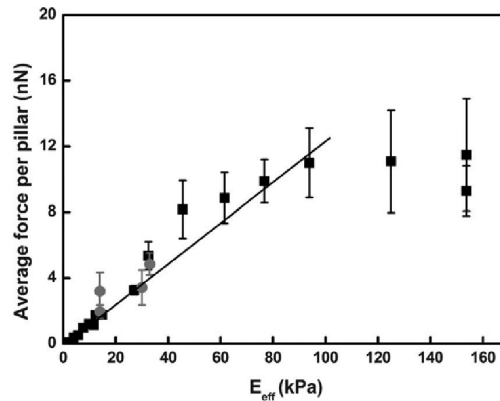


Figure 5.9: The forces increase with the Young modulus until a plateau is reached. Picture taken from Ghibauda *et al.* [53].

It has been also shown that migration of cancer cells on 2D–rigid substrates follows a rather classical picture divided into 4–5 steps. Indeed, figure 5.7 and figure 5.8 provide direct evidence of the motion which can be decomposed into these different steps. First, the cancer cell adheres and is not very active in figure 5.8(a), thus stresses are low. Then it searches for new adhesion sites until it reaches some places that will allow it to establish larger traction stresses. This is precisely where the tractions maxima are obtained in figure 5.7, at locations (e)–(f). Thanks to these forces, the rear (uropod) can be detached. The cell relaxes again its stresses in figure 5.8(g) until it will start again to try and move in another direction (figure 5.8(h)). Therefore, a clear connection has been made between the stress diagram in figure 5.7 and the migration patterns containing stresses maps in Figs 5.8.

Finally, our study also shows that cell contact area with the substrate

increases with substrate rigidity in close correspondence with the development of stress fibers (see figure 5.2). This fact was only observed previously regarding cell area [74].

The velocity of migration also varies in the usual way: cells probably with more stable focal adhesions on rigid substrates definitely move less rapidly as compared to soft substrates, where they move faster because of the difficulties to develop stable adhesions [36].

T24 cells seem to develop smaller stresses (typically  $0.05 - 0.2 \text{ kPa}$  here) in the range of the ones found for HSAM cells [20] although these cells were seeded on gels with a Young modulus of  $1.2 \text{ kPa}$ . Such stresses are still much lower than the ones found usually with fibroblasts [32] or endothelial cells [92]. This may be a possible explanation of the reason why cancer cells move rapidly to form metastases and therefore use small traction stresses in order to migrate faster.

This preliminary analysis of the features of T24 cancer cells on different substrate allowed us to choose the substrate rigidity for the subsequent experiments. The cells were well elongated and showed a wide lamellipodia on substrate with a rigidity of  $10 \text{ kPa}$ . Furthermore, following to the results of Ghibaudo [53], we chose to use the gel with a Young modulus of  $10 \text{ kPa}$  in order to be far enough from the plateau of the forces and to have measurable displacements.

Finally these first tests allowed us to check the validity of the adjoint method to produce relevant biophysical data.

# Chapter 6

## Comparison between three different cancer cell lines

In this chapter we will investigate the differences among the three cancer cell lines both in terms of forces exerted on the substrate and in terms of internal organization of the cell cytoskeleton and focal adhesions. We will first analyse the difference in time and then we will summarize the features for each cell line in order to correlate them with the biological characteristics.

This work is the object of a forthcoming paper to be submitted for publication (in preparation).

*Dans ce chapitre, nous étudierons la différence entre les trois lignées cellulaires cancéreuses à la fois en termes de forces exercées sur le substrat et en termes d'organisation interne du cytosquelette. Nous allons d'abord analyser la différence dans le temps et ensuite nous allons résumer les caractéristiques de chaque lignée cellulaire, afin de les corrélérer avec les caractéristiques biologiques.*

*Ce travail fait l'objet d'un article en cours de rédaction).*

## 6.1 Time-dependent traction stresses for each cell line

Cell migration is a highly dynamic process that involves different time scales and it cannot be understood only looking at one particular time step. We have already pointed out [11] that this process is characterized by specific time dependent features.

The cells of the three different lines have been observed for two hours and the images of cells and beads were recorded every two minutes. Afterwards, between twenty and thirty time steps have been analysed. The analysis has been carried out as explained in the sections 4.4 and 4.5.

Figure 6.1(a) shows the phase-contrast image of a T24 cancer cell adhering on polyacrylamide gel (with a Young modulus of 10 kPa). The cell is well flattened and polarized on the substrate and shows an extended lamellipodium. The cell was moving towards the upper right corner of the picture. The image is related to the configuration of the cell after 10 minutes of observation. Figure 6.1(b) represents the experimental beads displacements at that time as obtained with the ImageJ software. We detected around 2000 beads in all the pictures and 150 beads under the cell. These beads were followed in time for one hour. The displacement of the beads is at most  $1\mu m$  and these high values are detected at the front of the cell, near the cell boundary. The displacements, like the traction forces (figure 6.1(c)) are directed towards the interior of the cell.

When following the cell in time, we observe a significant variation of the traction stresses as shown in figure 6.2.

At the beginning the cell is well elongated on the gel and is extending a lamellipodium as we can see in figure 6.3(a). At this stage, the cell pulls at the front, where the stresses reach a maximum value around 120 Pa. After twelve minutes from the beginning of the observation (figure 6.3(b)) the cell contracts its tail, pulling on the front, where the highest values of the tractions are found, around 240 Pa. Then, it keeps on moving, spreading again the lamellipodium. During this period, the cell pulls on the substrate; the higher stresses are localized at the leading edge (maximum value around

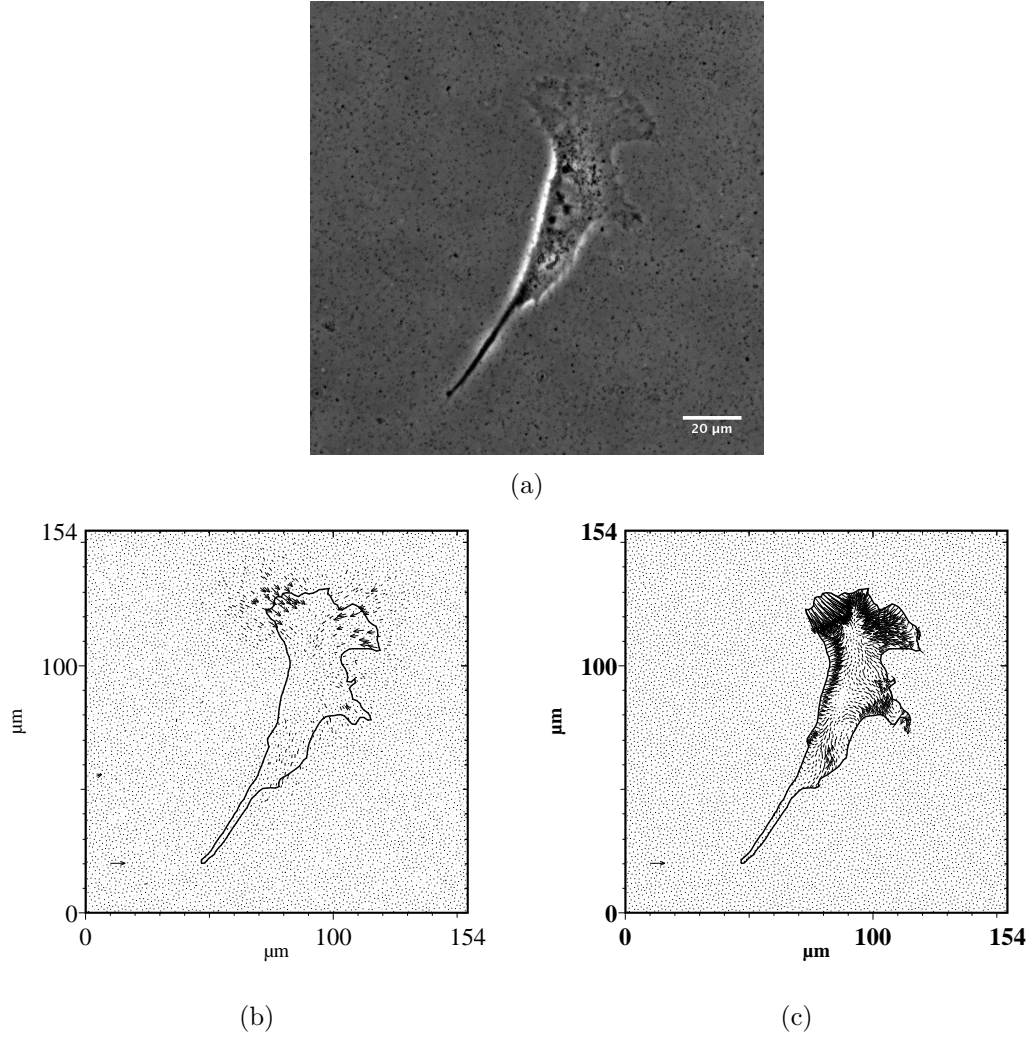


Figure 6.1: T24 cell adhering on polyacrylamide gel ( $E = 10 \text{ kPa}$ ). (a) Phase-contrast images of the cell. The cell looks well elongated with a well defined front and rear. (b) The experimental displacement field under and around the cell. The reference vector at the bottom left corner for displacements is 1  $\mu\text{m}$  long. (c) Traction stress field shown in terms of vectors. Reference vector 100 Pa.

140 Pa), figure 6.3(c-d). This cell exhibits a typical mesenchymal mode of migration with an extended lamellipodium in the direction of migration (supplementary data can be found in Appendix 2).

We now compare the T24 cell line with the J82, a cell line with a rather similar invasive type.

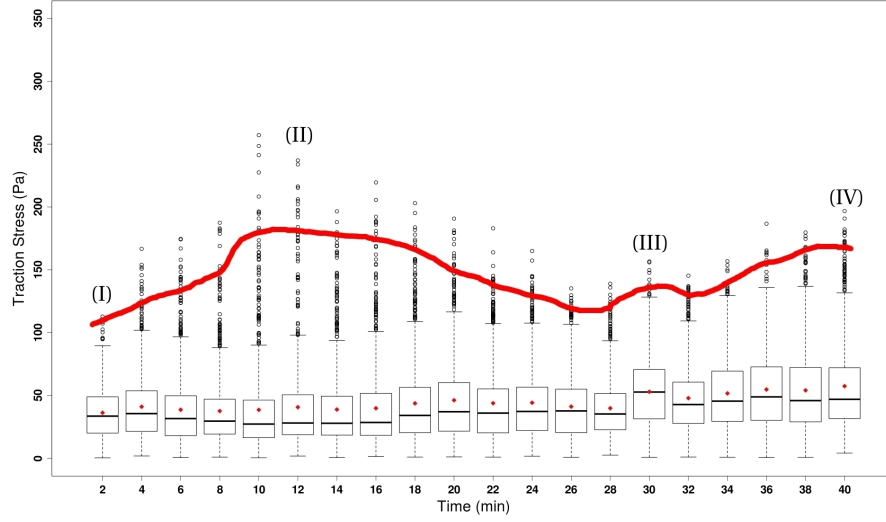


Figure 6.2: Evolution of the traction stresses in time for a T24 cancer cell. The boxplot representation has been chosen to display the stresses. The outliers, i.e. the points above the end of the whiskers, represent the higher values of the stresses.

Figure 6.4(a), shows the phase-contrast image of the J82 cell at the beginning of the experiment. This cell has a projected area bigger than the T24 cells. The related displacements are reported in the image 6.4(b). Also in this case, the number of beads detected was sufficiently high: 3000 beads in all the domain and around 200 under the cell. The maximum value of the displacements, was like in the previous case, around  $1\mu m$ . The cell is well flattened on the gel surface and it is directed towards the upper right corner of the picture.

The force with which the cell pulls on the substrate changes with time (figure 6.5). At the beginning (figure 6.5(b)) the cell is spreading on the polyacrylamide gel and is anchored at the front and at the rear (maximum value of the stresses around 150 Pa). After 30 minutes, the rear extension becomes thinner, figure 6.5(c-d); the higher stresses are found in this part as well as at the leading edge in two opposite areas. Finally, the cell contracts the tail ( $t = 90$  min), and the minimum stresses values are obtained. Then, it continues to advance, spreading again the lamellipodium, figure 6.5(e)



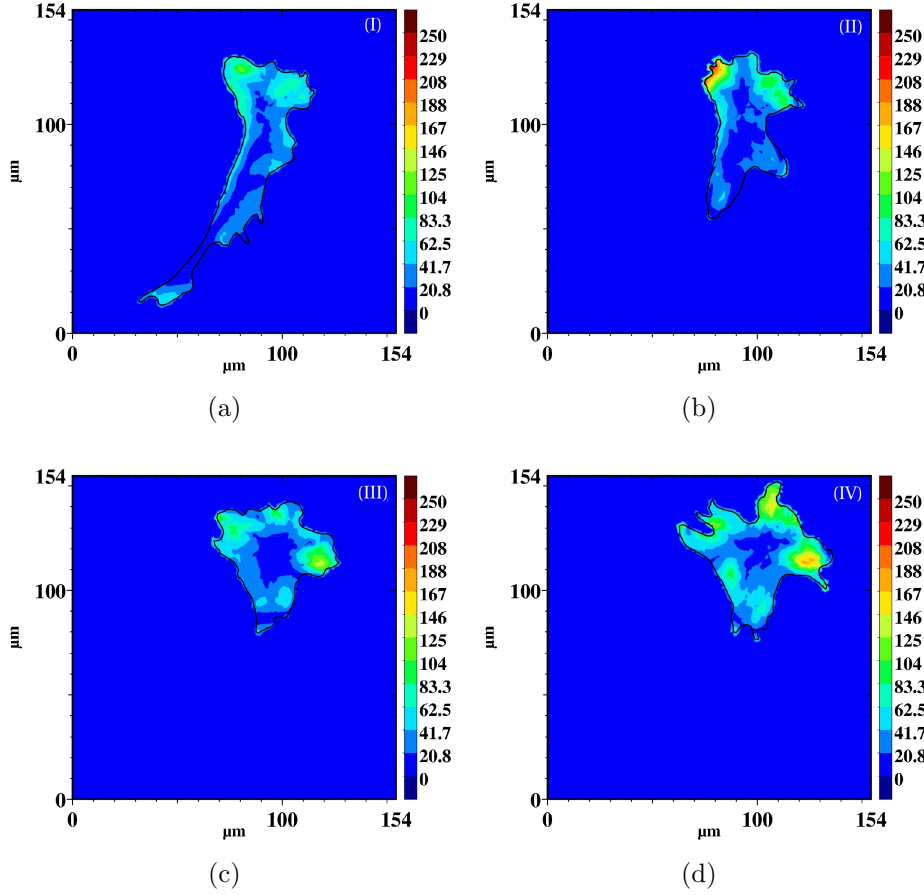


Figure 6.3: (a-d) Isocontours of traction stresses exerted by the cell at time  $t = 2$  min,  $t = 12$  min,  $t = 30$  min and  $t = 40$  min. The colour bar are in Pa.

(supplementary figures can be found in Appendix 2).

Like T24 cancer cell, the J82 cells usually contract the rear part and spreads the lamellipodium straight away again. Also in this case the migration of the cell can be depicted as that of a mesenchymal type, 6.5(b-e).

Changing the cell line and analysing the less invasive cells, i.e. RT112 cancer cells, the first evidence was the different morphologies of these cells. As shown in figure 6.6(a), the cell, well adherent on the gel, is less elongated and less polarized and does not present a wide lamellipodium. The number of beads used for the computation was around 2000 with 100 under the cell. The cell is pushing at the border and the beads move at least by  $0.5 \mu m$

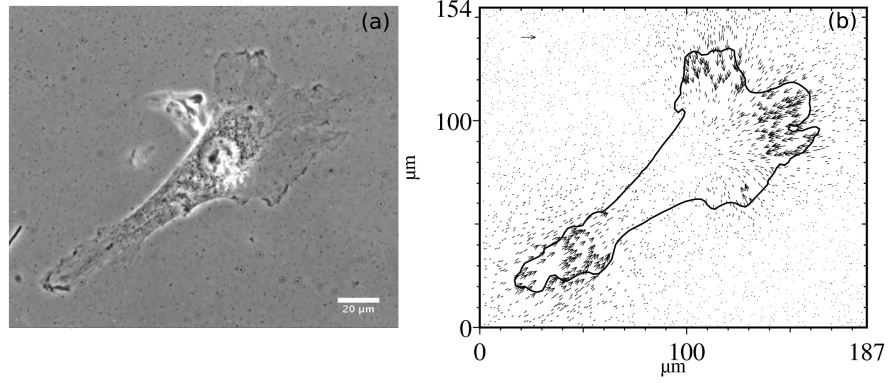


Figure 6.4: J82 cancer cells on polyacrylamide gel (10 kPa). (a) Phase-contrast image of the cell: the cell is well polarized and flattened on the substrate. (b) Displacement field of the fluorescent beads. Around 2000 beads were detected in all the domain. The reference arrow in the upper left corner is  $1 \mu m$  long.

under the action of the cell (figure 6.6(b)).

During the locomotion, no retraction of the tail was observed: the cell is moving slowly towards the upper left corner of the picture. It is not possible to define a distinct front and rear of the cell; the traction stresses are distributed along the cell contour and we found few areas with high stresses, as evident from the figure 6.7(b-d). Although the cell does not show a highly dynamic lamellipodium, few perturbations in the lamellipodium at the boundary of the cell are enough to generate high tractions on the gel, probably due to an efficient actin polymerization (supplementary figures can be found in Appendix 2)

For the statistical analysis of traction stresses, we focused our attention on the highest values of the stresses and in particular we only use the outlier values. These values are usually located at the cell boundary, as we can see in figure 4.13(b). As the analysis of the fluorescent images has shown, these are the locations where focal adhesions are found and where the forces may be transmitted to the substrate. We considered all the outliers for each cell of a specific line. After that, we considered the mean value in time and over all cells for each cell line. Figure 6.8 displays the mean values obtained for the T24, J82 and RT112 cancer cells.

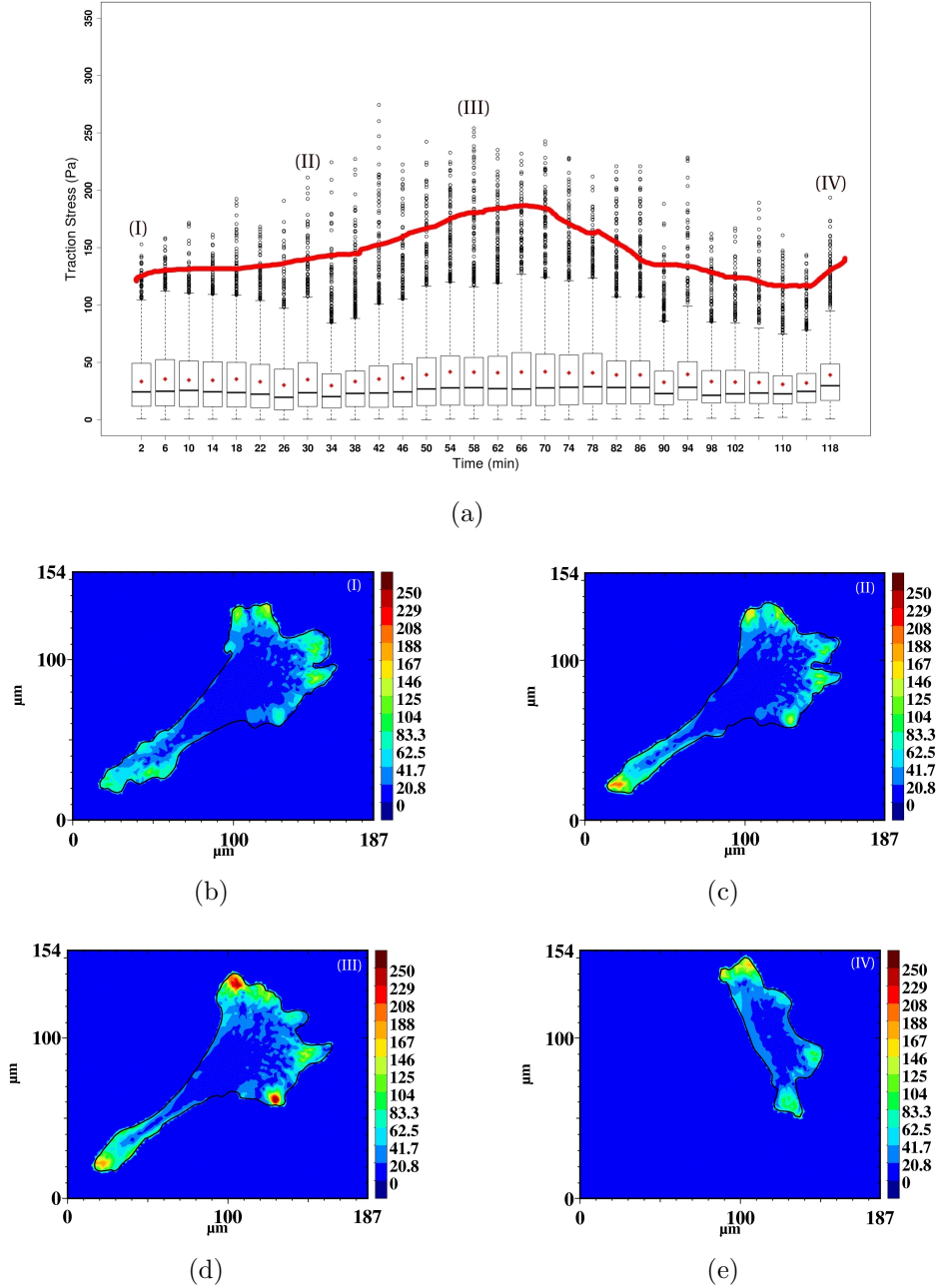


Figure 6.5: (a) Evolution of the traction stresses in time for a J82 cancer cell. Colour map of the traction stress field (b) at the beginning  $t = 2$  min , (c) at time  $t = 30$  min, (d) at  $t = 58$  min and (e) at  $t = 118$  min.

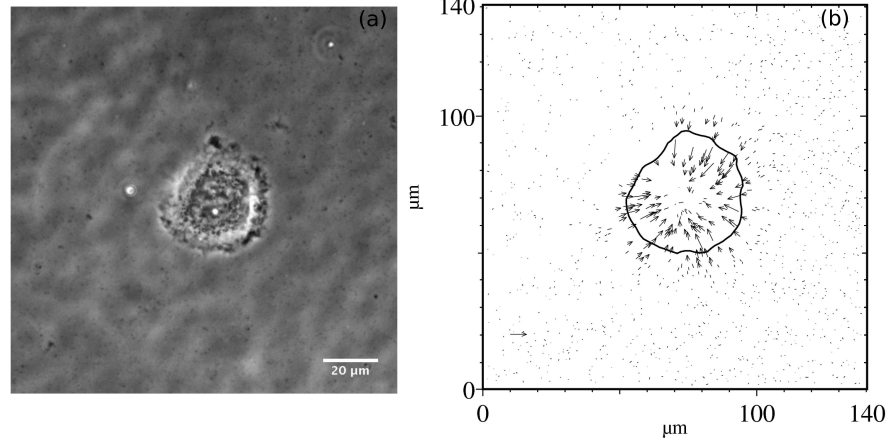


Figure 6.6: Typical RT112 cell adhering on polyacrylamide gel (10 kPa). (a) The phase-contrast image of the cell shows its rounded morphology with a thin lamellipodium. (b) Beads displacements in the whole domain. The displacements occur mainly at the cell edge and are uniformly distributed. The reference vector at the left bottom corner of the picture is  $1\mu m$  long.

We found that on average, the RT112 pulled stronger than the other two cell types on the substrate, with an average value of 173 Pa for the traction stresses. The T24 and J82 exhibit similar mean values for the traction stresses, respectively around 120 Pa and 130 Pa. Due to the time-dependence of the data for each cell, these values were fitted with a Generalized Estimating Equation function in the R-software and the results are given in terms of  $p$  values:  $p$  values smaller than 0.1 indicate that the difference is significant. The test allows us to conclude that the difference among the three cell lines is significant ( $p = 0.019$ ). Furthermore, the difference among the invasive cancer cells and the less invasive ones is significant: for the difference between T24 and RT112,  $p$  equals to 0.0069, and for the comparison J82–RT112 a value of 0.051 was obtained.

## 6.2 Global forces exerted on the lamellipodium

When observing the migration mode of the T24 cancer cells or the J82 cells, with extensions of the lamellipodium that drive the cell locomotion,

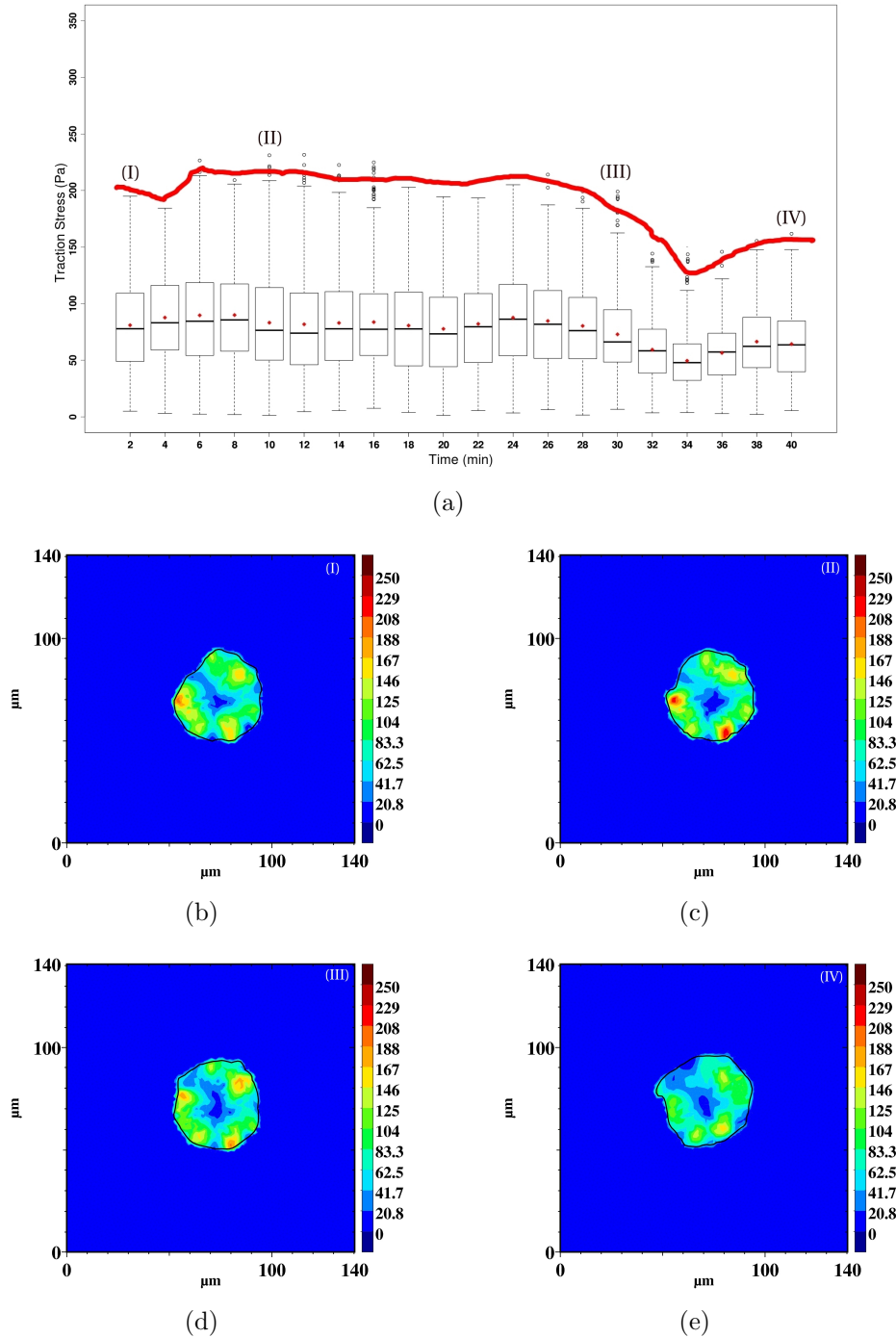


Figure 6.7: (a) Time evolution of the traction stresses of RT112 cancer cell on polyacrylamide gel (10 kPa). (b-e) Colour maps of the force field (a) at the beginning of the experiment, (b) at time  $t = 10$  min, (c) at  $t = 30$  min (d) at the end .

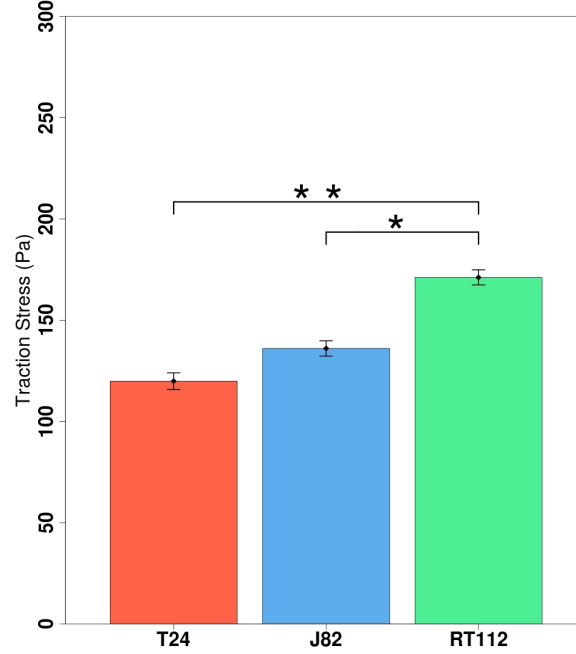


Figure 6.8: Time mean value of the outliers of the traction stresses for the three cell types. The difference among the three cell lines is significant,  $p = 0.019$ . The RT112 cells display values significantly different from the one displayed by T24 and J82 cells.  $p$  values equal to 0.051 and 0.069 respectively. The data are shown as mean  $\pm$  s.e.m ( $N_{cells} = 9$ ).

we wondered about the global forces exerted by the lamellipodium on the substrate.

The computation of the global force exerted on the lamellipodium was been explained in section 4.6 of the chapter “Experimental Methods”.

The computation of these forces has been done starting from components of the traction vectors obtained solving the system (3.2.16). The results showed below are referring to the same cells shown for the analysis of the traction forces.

Figure 6.9 shows the variations of the global force on the T24 cancer cell. While the cell is spreading on the gel, the force exerted on the lamellipodium slowly increases. When retracting the tail, all the forces are concentrated on the lamellipodium. After that, the cell re-organizes its extension, where

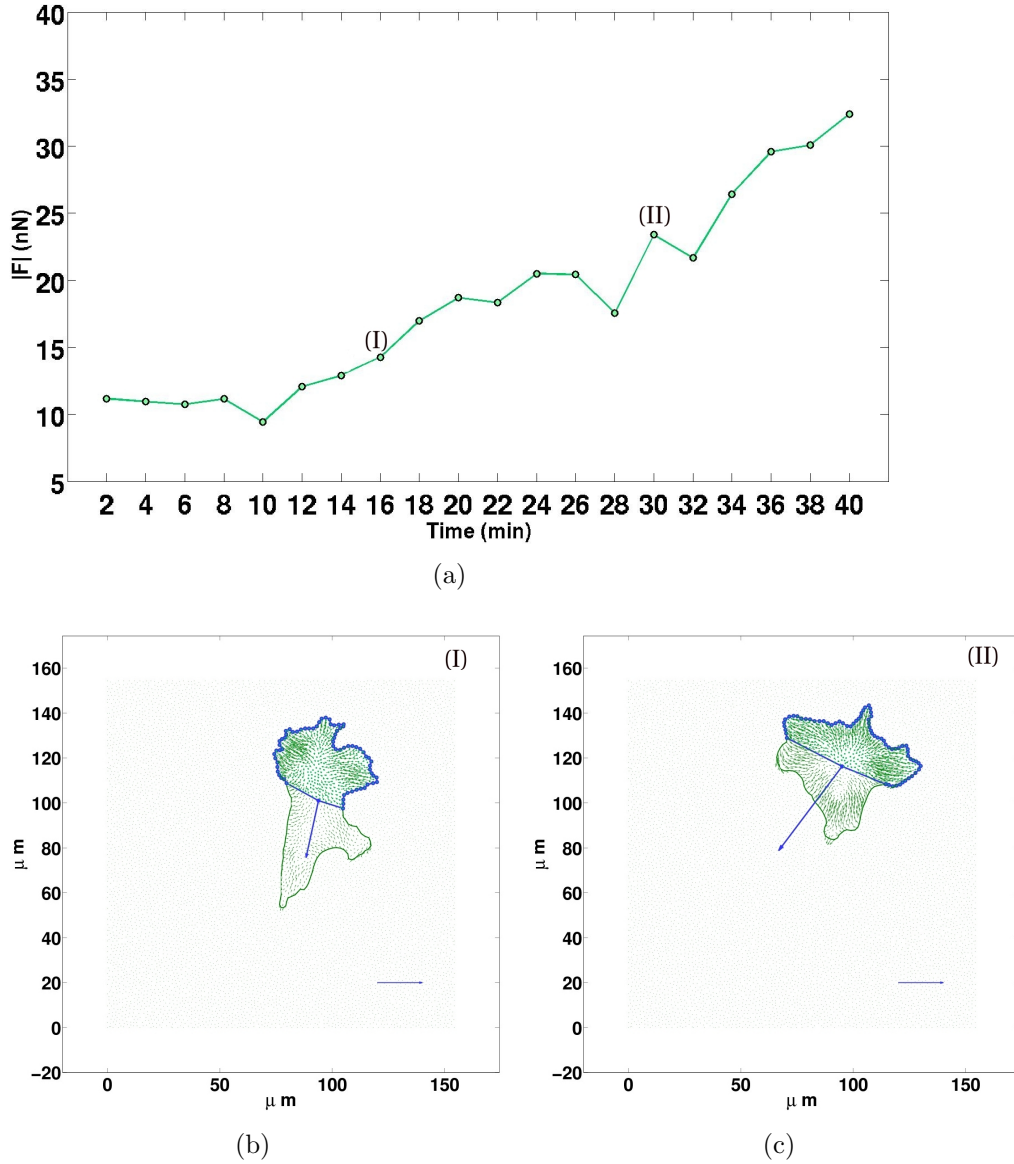
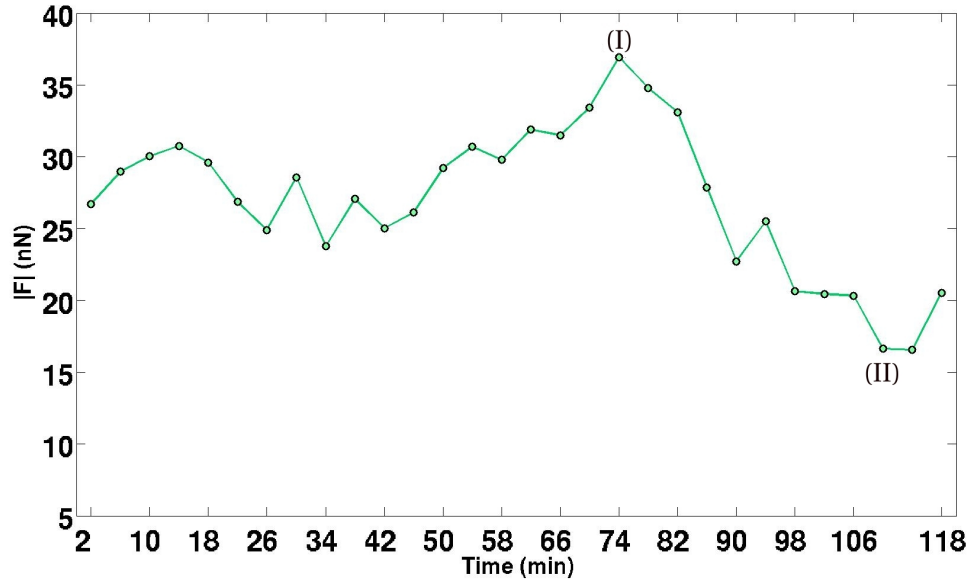


Figure 6.9: Resultant force on a half cell (including lamellipodium) of T24 cancer cell during time.

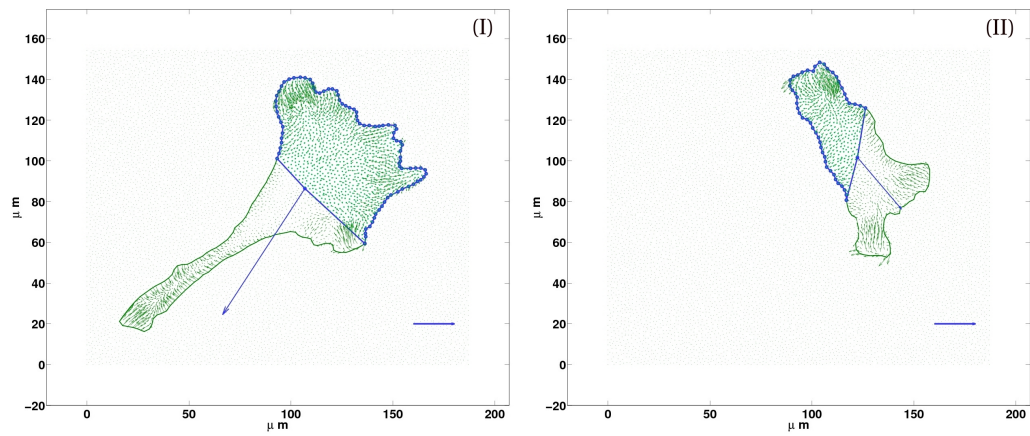
a variation of the force on the lamellipodium is observed. As soon as the cell engages a new direction of migration and there is a new extension of the lamellipodium, the force increases again ( $t = 32$  min).

A similar analysis can be done for the J82 cancer cells. Figure 6.10 shows





(a)



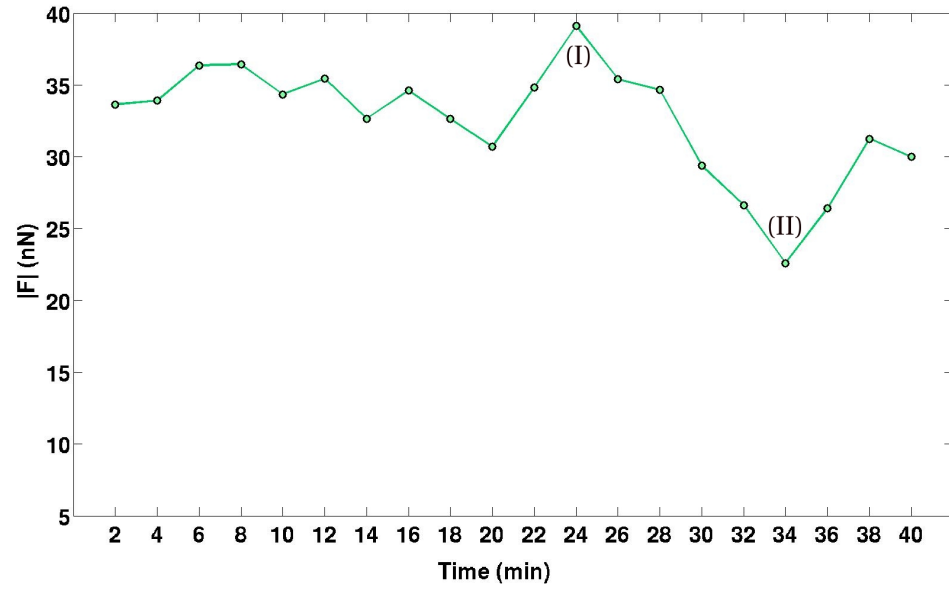
(b)

(c)

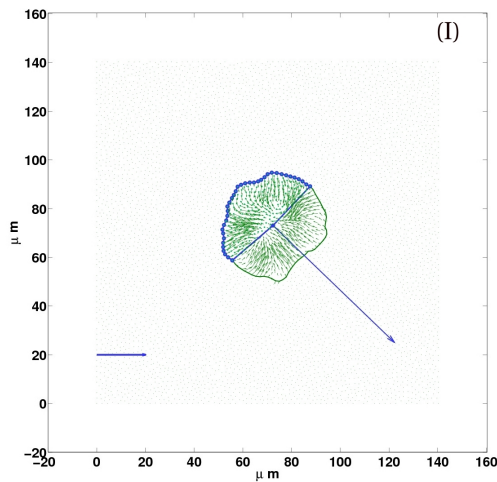
Figure 6.10: Resultant force on a half cell (including lamellipodium) of J82 cancer cell during time.

the time evolution of the global force for the J82 cancer cells. While the cell is spreading on the gel and the cell area is increasing, the force exerted on the lamellipodium is almost unchanged. It decreases as soon as the cell contracts the tail and increases again when the J82 starts to spread again on

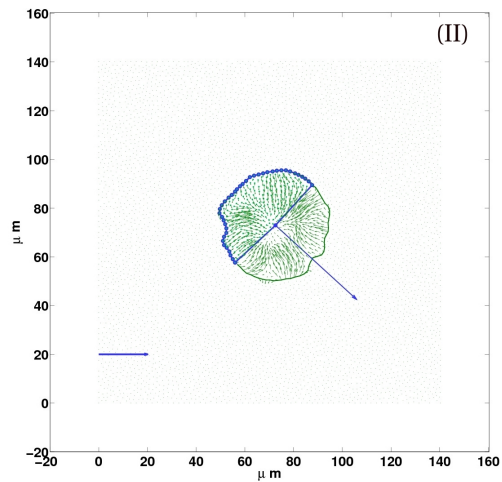




(a)



(b)



(c)

Figure 6.11: Resultant force on a half cell (including lamellipodium) of J82 cancer cell during time.

the substrate.

Figure 6.11 shows the time evolution of the global force for the RT112 cancer cells, the same one as shown for the analysis of the traction forces. While the cell is moving on the gel, it continuously arranges and re-arranges

the lamellipodium, the forces exerted on the lamellipodium are almost constant. The decreasing values of the force exerted on the lamellipodium are linked with a possible loss of adhesion at a specific location on the substrate.

We found that the three cell lines apply almost the same force on the lamellipodium, although different dynamics of extensions and protrusions of the lamellipodium of these cells are found. Mean values of  $17.4 \pm 0.8$  nN,  $22.6 \pm 1.1$  nN and  $22.8 \pm 0.6$  nN were respectively found for the T24, J82 and RT112 cells (figure 6.12). The GEE-test shows that the difference among the three cell types is not significant,  $p = 0.46$ .

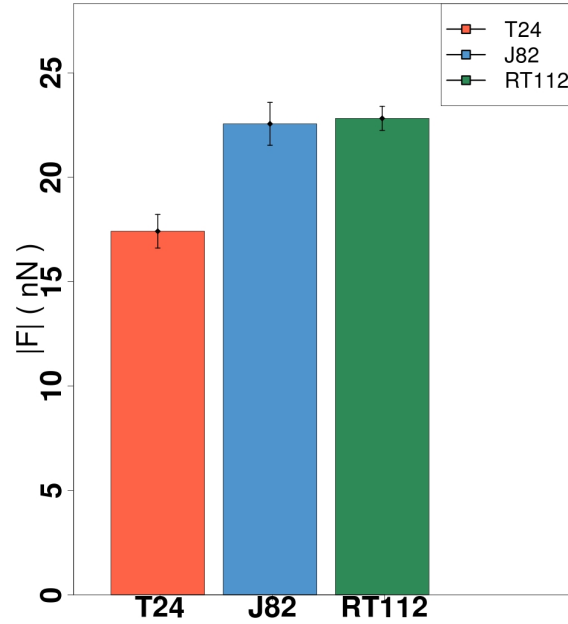


Figure 6.12: Mean value of the force exerted on the lamellipodium by the T24, J82 and RT112 cancer cells. The protrusive force used by the cells to move forward on the substrate are almost equivalent for the three cell lines, even though the dynamics of the lamellipodium extensions are different for these cells. The T24 and J82 have a fibroblast-like structure with a well defined front and rear, while the RT112 are less elongated on the gel. Data are shown as mean  $\pm$  s.e.m. ( $n_{cells} = 9$ ).

## 6.3 Characterization of the cell motion

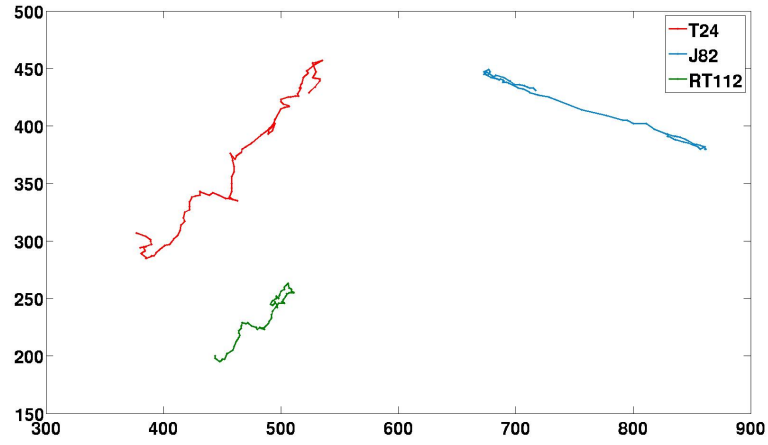
In order to characterize the motion of the three cell lines, the mean squared displacement (MSD) was calculated for each cell line, as explained in Chapter 3. Migration parameters were then estimated assuming that the cells migrate as persistent random walkers,  $MSD(t) \propto t^\alpha$ .

These experiments were performed on polyacrylamide gels with a Young modulus of 10 kPa. A set of seventeen cells was analysed for each cell line. The cells were followed for at least 5 hours and the phase-contrast images of the cell recorded every 5 minutes.

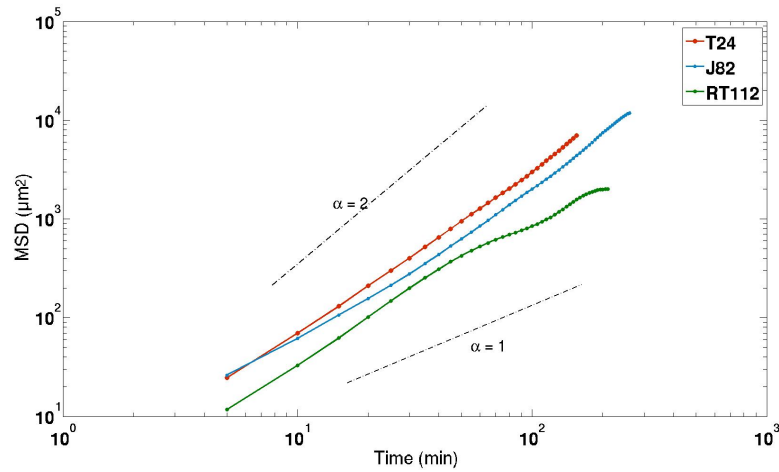
As explained in section 4.1.2, the mean square displacement has been analysed in terms of the slope in order to evaluate the diffusive parameter,  $\alpha$ . Figure 6.14(a) shows the evolution of the mean square displacement as a function of time for the three cell lines. The MSD increases with time. During the migration process, the cell extends the lamellipodium, starts to move in one arbitrary direction, then it stops in order to re-arrange the lamellipodium and continues the migration process in an other direction.

Even though the RT112 cancer cells do not show the four or five step motion of migration [70], their ability to migrate is comparable with the one of the other two cell lines. The T24 and RT112 have a similar super-diffusive behaviour as we can conclude from the analysis of the diffusive parameter  $\alpha$  in figure 6.14(a) while the J82 cells have almost a diffusive behaviour. This figure shows the mean value of  $\alpha$  for the three cell lines. All of them show a super-diffusive behaviour of migration. A GEE-test allows us to conclude that the difference among the three mean values of  $\alpha$  is significant,  $p < 0.000001$  ( $n_{cell} = 17$ ). Furthermore the difference between the T24 and J82 as well as between the T24 and RT112 is significant  $p < 0.000001$  ( $n_{cells} = 17$ ).

The velocity of migration has been calculated as the total distance travelled by the cells in time,  $v = \frac{\mathbf{r}_F - \mathbf{r}_i}{t_{tot}}$ . We indeed have considered the difference between the final and the initial position of the mass center. The T24 cancer cells migrate faster than the other two cell types, as shown in figure 6.14(b), while the J82 and RT112 cells move almost with the same rate. A GEE-test



(a)



(b)

Figure 6.13: (a) Typical trajectories of the position of mass center and (b) typical mean square displacement of three different cancer cells. The red curve is related to T24 cell, the blue one to J82 cell and the green one to the RT112 cell.

allows us to confirm that the difference among the rate of migration of the three cell lines is significant,  $p = 0.002$  ( $n_{cells} = 17$ ).

The T24 and RT112 cell lines have a super-diffusive motion while J82 cells have almost a diffusive-motion, as suggested by the mean values of the persistence parameter  $\alpha$  that we have obtained (figure 6.14(a)):  $1.57 \pm 0.04$

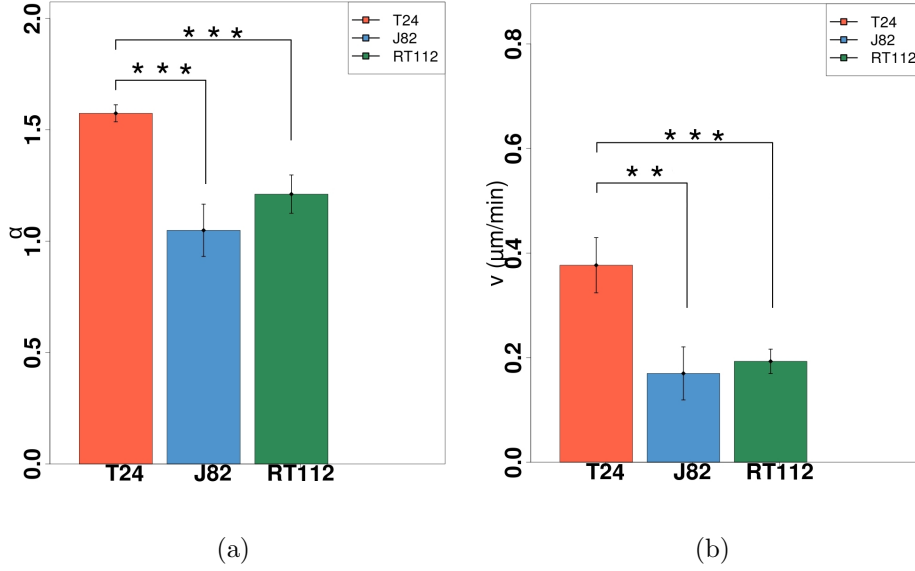


Figure 6.14: (a) The persistence parameter  $\alpha$  computed from the mean square displacement indicates that the cells have a super-diffusive motion ( $\alpha > 1$ ). \*\*\* indicates significant difference ( $p < 0.00001$ ) among the T24 and RT112 motion of cells, and between T24 and J82 cells. (b) Mean velocity of migration of the three cell types. The difference between the velocity of T24 and J82 cells as well as T24 and RT112 cells is significant ( $p = 0.004$  and  $p = 0.0009$  respectively). The data are displayed as mean  $\pm$  s.e.m.,  $n_{\text{cells}} = 17$ .

for the T24,  $1.05 \pm 0.12$  for the J82 and  $1.21 \pm 0.09$  for the RT112. The persistence of migration of the T24 differs significantly from the one of the RT112 (GEE-test,  $p < 0.00001$ ) as well as from the J82 cells (GEE-test,  $p < 0.00001$ ). The J82 and RT112 cells have a similar persistence (GEE-test,  $p = 0.2$ ), although these cells exhibit a different morphology: the first one has a wide lamellipodium with several lateral branches, while the later one has a thin extension that fluctuates during the locomotion of RT112 cells.

The cells coming from the three cell lines analysed in these experiments exhibit different morphologies and move with different rates. In particular, for T24 cells the velocity of migration is  $0.38 \pm 0.05 \mu\text{m}/\text{min}$ , in comparison of the migration rate of J82 cells ( $0.17 \pm 0.05 \mu\text{m}/\text{min}$ ) and RT112 ones ( $0.19 \pm 0.02 \mu\text{m}/\text{min}$ ) in figure 6.14(b). The difference between the T24 and J82 is quite significant ( $p = 0.004$ ) and a higher meaningful difference occurs

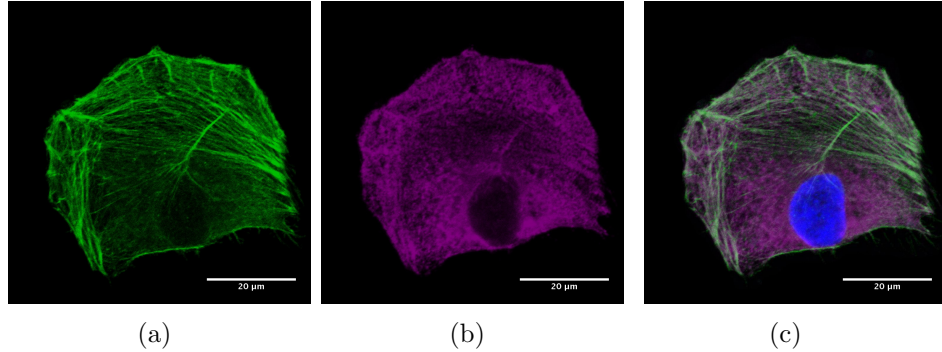


Figure 6.15: Fluorescent images of T24 cancer cells on cover-glass coated with collagen. The cells were stained for (a) actin with Phalloidin Alexa 488 (green). (b) The myosin IIA (deep purple) was visualized with the anti-myosin antibodies. (c) Superimposition of the images of the actin, the myosin and the nucleus in blue stained with Hoechst.

between the T24 and the less invasive RT112 cancer cells ( $p = 0.0009$ ).

## 6.4 Actin and myosin networks

Once the traction forces have been analysed, we wondered how the cells reorganise their cytoskeleton and how the cytoskeleton changes while the cells are adhering on the gels. To answer these questions, we proceeded with the immunofluorescence experiments, as explained in the section “Immunofluorescence” of the chapter “Experimental Methods”.

We looked at the fixed cells adhering on cover-glasses and polyacrylamide gels ( $E = 10$  kPa). For these experiments, nine cells were observed for each cell line ( $n_{cells} = 9$ ).

The same features are present in the structures of the actin filaments for cells adhering on glass or on polyacrylamide gels. In the first case (glass), the cells exhibited an extensive and complex array of actin structures as we can see in the figures 6.15- 6.16-6.17. For T24 and J82 cancer cells fixed on cover-glass, thick and long actin stress cables are present in all the cells and are directed towards the cell borders. These filaments are surrounded by the myosin II motors, as visible from the superimposition of the images related to actin and the myosin IIA. The J82 cell, (figure 6.16), in particular, shows

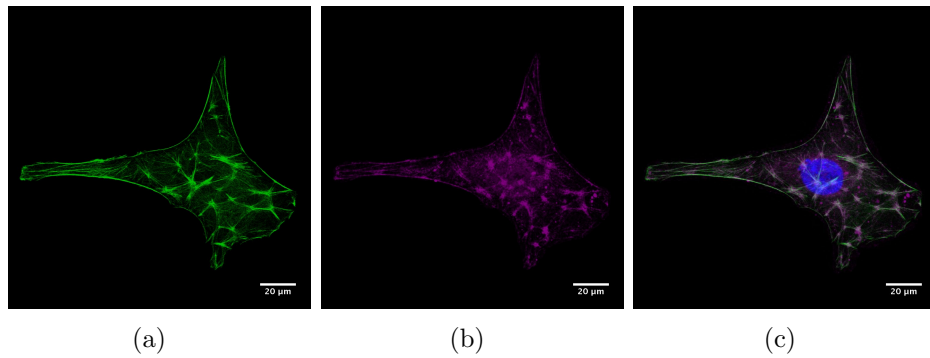


Figure 6.16: Fluorescent images of J82 cancer cells on cover-glass coated with collagen. The cells were stained for (a) actin with Phalloidin Alexa 488 (green). (b) The myosin IIA (deep purple) was visualized with the anti-myosin antibodies. (c) Superimposition of the images of the actin, the myosin IIA and the nucleus in blue stained with Hoechst.

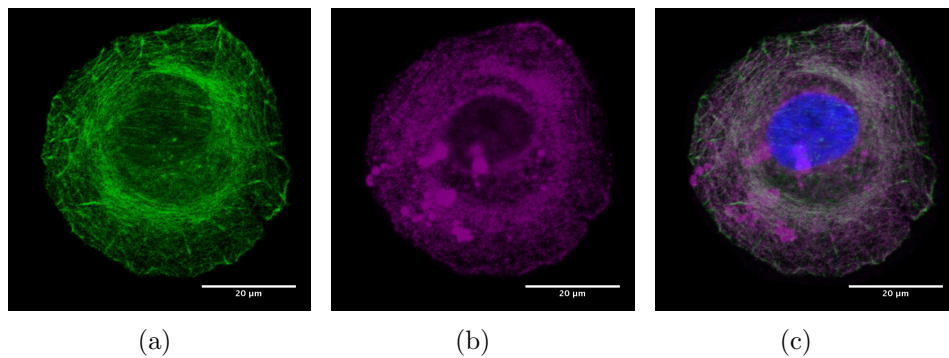


Figure 6.17: Fluorescent images of RT112 cancer cells on cover-glass coated with collagen. The cells were stained for actin with Phalloidin Alexa 488 (green). (b) The myosin IIA (deep purple) was visualized with the anti-myosin antibodies. (c) Superimposition of the images of the actin, the myosin and the nucleus in blue stained with Hoechst.

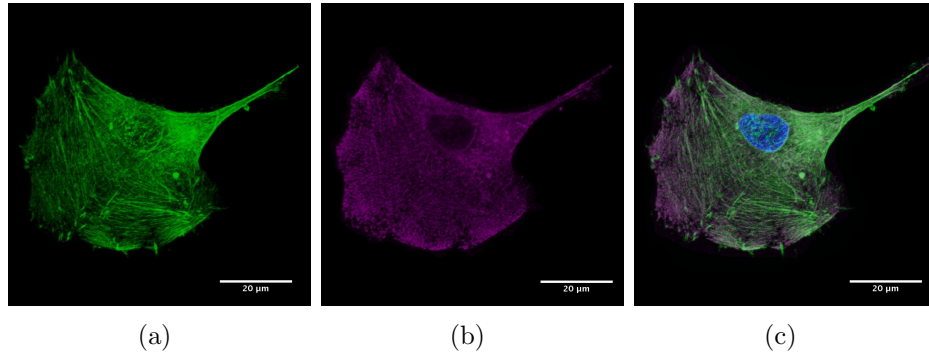


Figure 6.18: Fluorescent images of T24 cancer cells on polyacrylamide gel (10kPa). (a) Actin (green) and (b) myosin (deep purple) are stained with the anti-paxillin and anti-myosin antibodies respectively. (c) Superimposition image of the actin and myosin, with the nucleus stained in blue.

a very well developed actin network, in which actin filaments seem to diffuse from clustered point-rich in actin and circled by myosin. T24 cell (figure 6.15), has a polarized shape and a dense actin structure on the presumable leading edge of the cell, where the actin polymerization is required for cell locomotion. The RT112 cell (figure 6.17) shows actin filaments that match the round shape of the cell with short and thick actin filaments at the border of the cell. The myosin IIA is localized along the actin filaments.

The actin networks for the T24, J82 and RT112 cancer cells plated on polyacrylamide gels is shown in figure 6.18, figure 6.19 and figure 6.20 respectively. The T24 cancer cells present an actin network lightly “split up” in small filaments in comparison to the one showed on cover-glass. Nevertheless, this structure is still well defined, and the stress fibers come close the cell border, where the focal adhesions are localized as we will see in the next section. The J82 cells (figure 6.19) have thick stress fiber that define the cell contour and where myosin molecules are localized. In this case they do not present the same complex actin branched network displayed on the cover-glass. The actin organization for the RT112 cells seeded on polyacrylamide substrate is less defined (figure 6.20) in comparison with T24 and J82 actin structure. Few long and oriented fibers are present where myosin motors are located. Supplementary data can be found in Appendix 3.



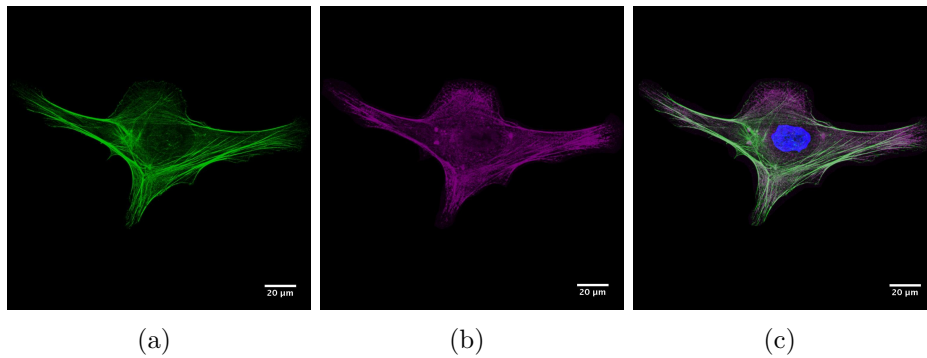


Figure 6.19: Fluorescent images of J82 cancer cells on polyacrylamide gel (10kPa). (a) Actin (green) and (b) myosin (deep purple) are stained with the anti-paxillin and anti-myosin antibodies respectively. (c) Superimposition image of the actin and myosin, with the nucleus stained in blue.

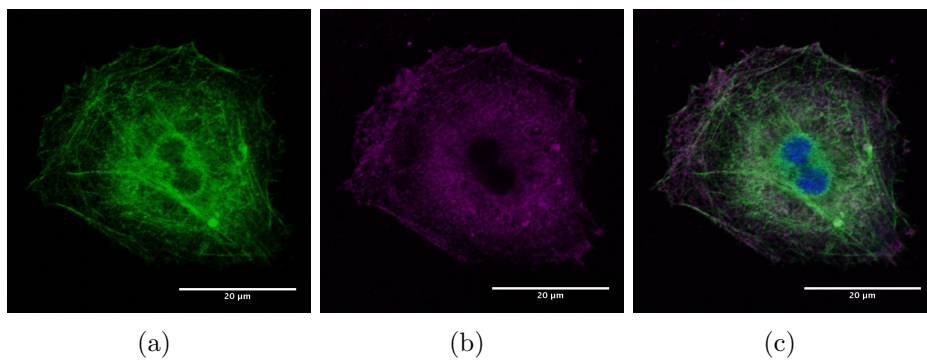


Figure 6.20: Fluorescent images of RT112 cancer cells on polyacrylamide gel (10kPa). (a) Actin (green) and (b) myosin (deep purple) are stained with the anti-paxillin and anti-myosin antibodies respectively. (c) Superimposition image of the actin and myosin, with the nucleus stained in blue.

## 6.5 Focal adhesion zones

Of particular interest are the focal adhesion complexes. They are the sites at the cell periphery where the forces can be transmitted to the substrate from the cytoskeleton, and their dynamics is involved in the cell migration process. Using these anchorages, the cell tests the environment and controls its behaviour. We have analysed the focal adhesion sites of the three cell lines plated on the cover-glass and on the polyacrylamide gel (Young modulus of 10 kPa). For the analysis, we considered only the focal adhesions located at the cell periphery and bigger than  $0.5 \mu m^2$ . This choice has been suggested by the fact that for the cells seeded on the gels, the background noise present around the cell nucleus makes it impossible to discriminate the structure of FAs from the noise itself.

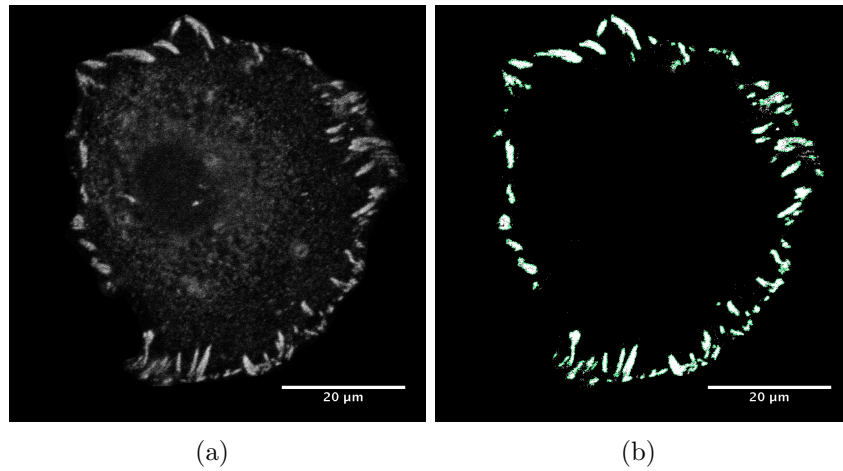


Figure 6.21: (a). Example of a fluorescent image of the paxillin visualized with the anti-paxillin antibody for the T24 cancer cells on cover-glass. (b) Detection of FAs with the “analyze particles” tool of ImageJ on the threshold image.

Starting with the images stained for the paxillin (see example in figure 6.21(a)), we apply a threshold to the image in order to determine the brightest areas; these areas correspond to the focal adhesion sites. Successively, we use the “analyze particles” plug-in from ImageJ to quantify the size of these zones. In the “analyze particle” dialog box, a range of  $0.5$  to  $20 \mu m^2$  for

the size of the particles and a range of 0 to 1 for the circularity have been defined. We obtained the outlines of the measured particles as shown in the figure 6.21(B) .

We first decided to investigate the focal adhesion sites for the cell seeded on glass, when it was coated with fibronectin and collagen, since these two components have different receptors on cancer cells.

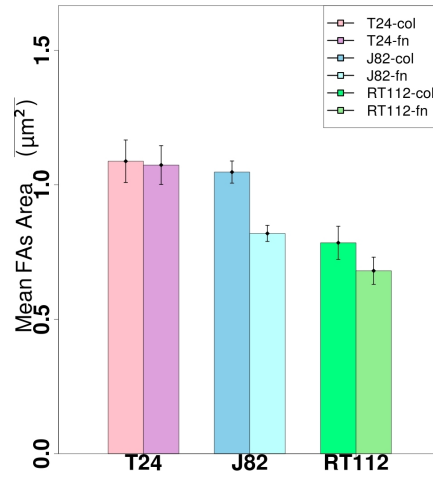


Figure 6.22: Comparison of the focal adhesions (FAs) area for the cells seeded on cover-glass coated with collagen and fibronectin. The difference among the three cell lines is non significant, (GEE-test,  $p = 0.5$ ). The data are shown as mean  $\pm$  s.e.m.,  $n_{cells} = 4$ .

We analysed a sample of four cells for each cell line and for the cells plated on the glass coated with fibronectin and collagen. We found that the area of the focal adhesion sites are almost equivalent sizes around  $1\mu m^2$  for the T24 and J82 and slightly smaller (around  $0.8\mu m^2$ ) for the adhesions of RT112, (figure 6.22). With the GEE-test for each cell line, we evaluate the difference among the fibronectin coated glass and collagen coated glass. This test allows us to conclude that the difference among the sizes of the focal adhesion sites for each cell line is not significant ( $p$  value equal to 0.5). These results allow us to use without distinction either the cells seeded on fibronectin-coated or collagen-coated cover-glasses.

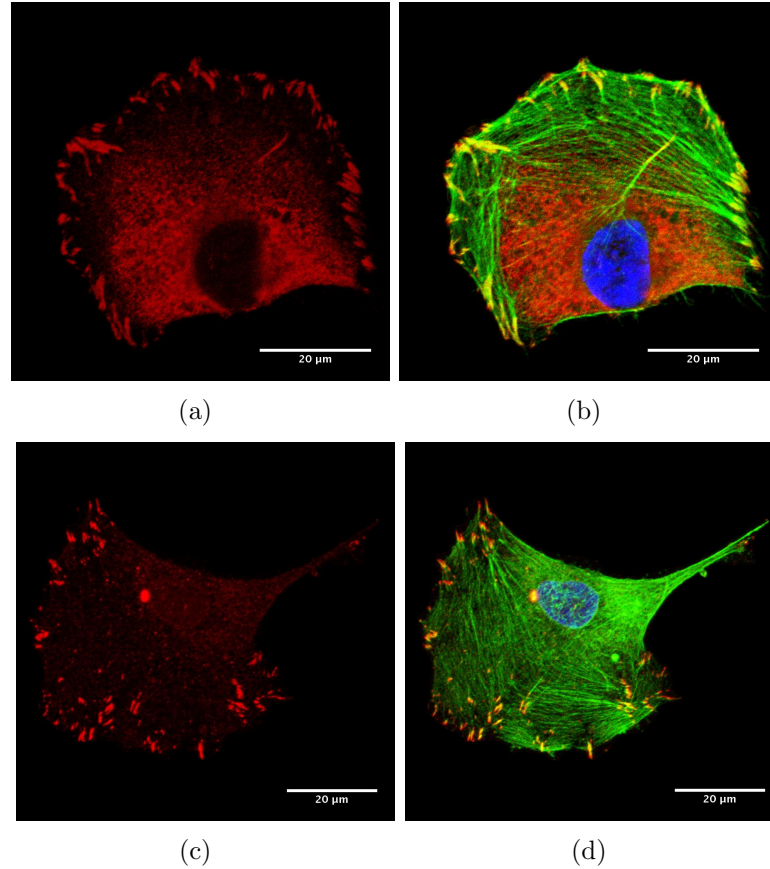


Figure 6.23: Focal adhesions of the T24 cancer cells stained for the paxillin on cover-glass (a) and on gel (c). (b,d) Composite image of the actin and paxillin, with the nucleus stained in blue. The focal adhesion sites, stained in red, are localized around the cell contour and correspond to the nascent the stress fibers.

For the following analysis, the focal adhesions with an area larger than  $0.5\mu m^2$  are used. This corresponds to analyse the mature focal adhesions, that are anchorages for the actin fibers of the cytoskeleton. In figure 6.23 the focal adhesion sites for a T24 cancer cell adhering on the cover-glass and gel, both coated with collagen, are shown. The cells have approximately the same projected area (around  $1400\mu m^2$  for the cell plated on glass and around  $1300\mu m^2$  for the one on gel). We detected more mature focal adhesion sites for the cell seeded on glass and a larger mean value for the area of focal adhesions. The differences among the J82 seeded on glass and on gel are less

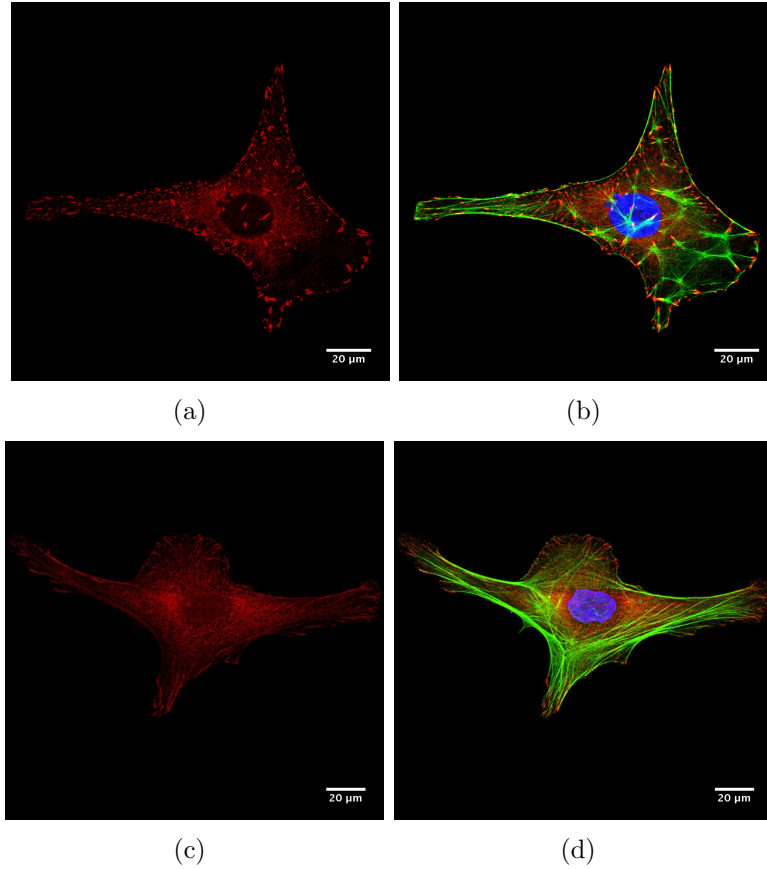


Figure 6.24: Focal adhesions of the J82 cancer cells stained for the paxillin on cover-glass (a) and on gel (c). (b,d) Composite image of the actin and paxillin, with the nucleus stained in blue. The focal adhesion sites, stained in red, are localized around the cell contour and correspond to the nascent the stress fibers.

marked (figure 6.24). Even if the number of the detected mature focal adhesions is bigger for the cells seeded on glass, the mean area is approximately the same, around  $1.5 \mu m^2$ . The J82 cell has a larger projected area on glass than on gel.

The RT112 cells in figure 6.25, instead presents some features similar the T24 cells: few mature focal adhesion sites are detected on gels, but mean value of the area is smaller  $0.8 \mu m^2$ , while on glass the area of mature focal adhesions reaches a mean value of  $1.5 \mu m^2$ .

For all the cells analysed, we found that the focal adhesions are co-

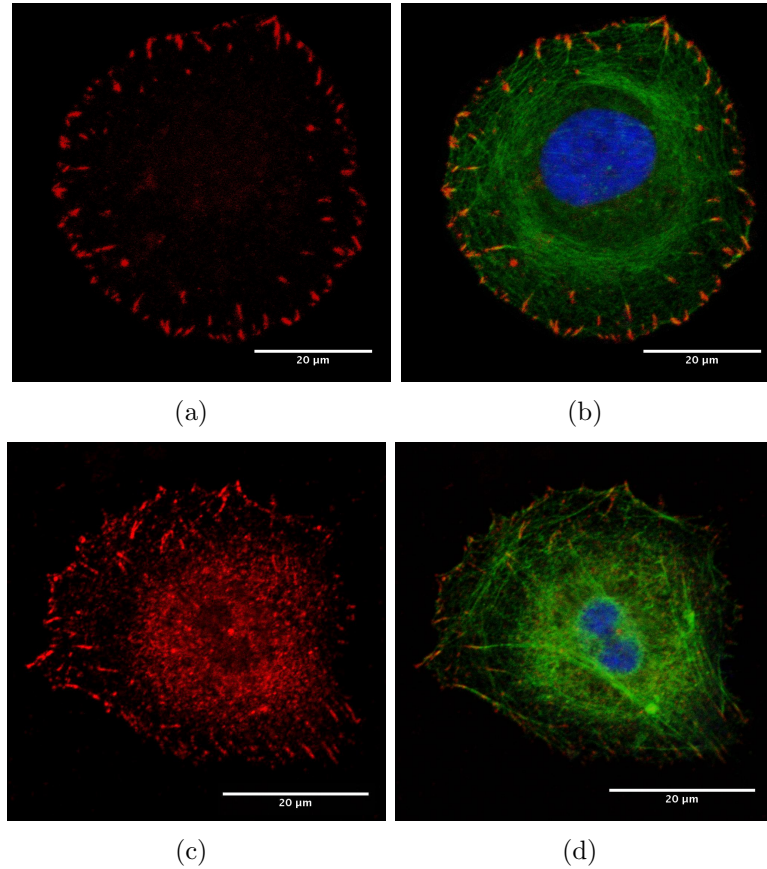


Figure 6.25: Focal adhesions of the RT112 cancer cells stained for the paxillin on cover-glass (a) and on gel (c). (b,d) Composite image of the actin and paxillin, with the nucleus stained in blue. The focal adhesion sites, stained in red, are localized around the cell contour and correspond to the nascent stress fibers.

localized with the end of the actin filaments (supplementary examples can be found in Appendix 3). Figures 6.23(b), 6.24(b), 6.25(b) show the superimposition of the cells stained in red with paxillin for the detection of the focal adhesions and stained in green for actin. The orange area corresponds to the co-localization area. As evident from the figures, focal adhesions are placed at the end of the actin fibers.

We observed that when the cells are plated on polyacrylamide gels, the actin structures are less organized in thick fibers in comparison to the ones that the cells form on glass. For the cells plated on the gel, we found thin

actin cables that finish at location of mature focal adhesions. The mean area of the focal adhesion sites vary from line to line: these sites are generally bigger for the J82 cells ( $1.47 \pm 0.07 \mu m^2$ ) than for the T24 ( $1.13 \pm 0.05 \mu m^2$ ). The less invasive cells (RT112) have the smaller focal adhesions,  $0.86 \pm 0.03 \mu m^2$ . The difference between the mean values of the focal adhesion areas for the two invasive cell lines is not very significant according the GEE-test,  $p = 0.05$ , while that difference becomes significant when comparing the most invasive cell line with the less invasive one, i.e. T24–RT112 and J82–RT112, where we found a  $p$  value smaller than 0.000001, in figure 6.26(a). For the cells fixed on the cover-glass, we found that generally the cells have focal adhesion sites bigger than the ones seeded on the gels and that this difference is significant (GEE-test,  $p < 0.000001$ ). The T24, the J82 and RT112 cancer cells on the cover-glass do not present relevant differences between the size of the focal adhesions, that is generally larger than  $1.5 \mu m^2$ , see figure 6.26(b).

When observing the cells under the microscope, the first outlook was that J82 cells, both on gels and on glass, have a bigger projected area than the two other cells type, figure 6.26(d). The ability of J82 cells to be well flattened on the substrate is enhanced on glass, while T24 and the less invasive cells do not show significant variations in the cell area on the two kinds of substrates.

The J82 cancer cells have a high number of focal adhesions on gels (figure 6.26(c)) that cover around the 1.5% of the cell surface, as we can see in figure 6.26(e). The T24 and RT112 have less mature focal adhesions that occupy around 1% of the cell area. On the contrary, for the cell observed on the glass cover slip, the area occupied by the focal adhesions is wider: on that substrate, the cells have more (figure 6.26(c)) and larger focal adhesion sites. The meaningful difference occurs between the T24 and the RT112 plated on glass,  $p < 0.00001$ .

We conclude that these cells behave differently on glass and on gel. Therefore it is pertinent idea to compare cells on gels, where major differences are notable. Finally gels simulate best the surrounding tissue.

## 6.6 Discussion

We have studied the process of the cancer cell migration looking at the mechanics of movement, the forces transmitted to the substrate, and the internal reorganization of the cell cytoskeleton as well as focal adhesions. This study reveals that the motion of the two invasive cancer cell lines, the T24 and J82, can be described as a mesenchymal one. Like fibroblasts, cells propel their membrane in one direction by orienting and reorganizing the actin network at the leading edge. Secondly, they adhere to the substrate at the front and release their uropod at the rear when contraction is achieved. Finally, contractile forces, largely generated by the acto-myosin network, pull the cells forward. During this process, traction stresses change in time (figure 6.2(a) and figure 6.5(a)) and the maximum values range from 120 Pa to 280 Pa for both cell types. The higher traction stresses are applied at the front and/or at the rear part of the cell, like has been found for other cells, like fibroblasts [32, 74, 79]. These high stresses are localized in several boundary areas for the T24 and J82 cells (figure 6.2(b) and figure 6.5(b)) while the RT112 cancer cells present few areas with high stresses, as seen in figure 6.7(b). They exhibit also a different morphology: they are quite round, less elongated on the substrates and do not present a wide lamellipodium. Consequently, the four-step motion observed for the most invasive cells is not found: the cells move forward thanks to small fluctuations of the lamellipodium. In fact, for this cell line we found that the actin structure is less organized in fibers and does not span the entire cell, figure 6.25(b). The stress fibers are well recognizable in the cytoskeleton structure of T24 and J82 cells. These results go in the same direction of the ones found by Mierke *et al.* [77]: for several lines of human cancer cells (colon, breast, skin, lung, prostate, pancreas, bladder, kidney, cervix, hypo pharynx) they observed a well-defined actin structure and a fibroblast-like morphology for the invasive cells and a less organized actin structure for the less invasive cells.

A different behaviour of the murine breast cancer cells instead has been found by Indra *et al.* [65]: the cytoskeleton organization and the number of



focal adhesions remain intact with metastatic progression of the cells. When we look at the mean values of the traction stresses in time, we found that the RT112 cells, the less invasive phenotype, develop higher stresses than the J82 and T24 cells. The same trend has been found by Indra *et al.* [65] and Munevar *et al.* [79]. In the first case, the tractions decrease with the metastatic capacity of the cells; in the second one, the overall magnitude of the NIH transformed 3T3 cells is markedly reduced in comparison with the NIH 3T3 cells. Furthermore, the traction forces are disorganized in transformed cells. Such disorganized pattern were not found for any of the three cell types.

From the analysis of the focal adhesion sites, it appears that the difference in the mean area as well as in the number of focal adhesion sites is significant either on glass and on gels. The number of the focal adhesions increase with the metastatic capacity of the cells as reported also by Mierke *et al.* [77] for cells seeded on cover-glass. Opposite results are presented by Indra *et al.* [65] for the cells seeded on the cover slip. Care must be taken that force  $F$  are transmitted properly due to the complexity of force transmission mechanism (figure 6.27): force is not always transmitted properly to the substrate and can lead to focal adhesions sliding on the substrate [12, 13, 99].

The cytoskeleton organization and the distribution of the focal adhesions affect the motion of the cell: the three cell types exhibit an anomalous types of migration, as was found also for wild-type and mutated transformed Madin-Darby canine kidney epithelial cells [33]. The mean square displacement increased with time with a power-law relationship:  $MSD(t) \propto t^\alpha$ , where  $\alpha$  is a measure of the persistence. In particular, T24 and RT112 cell lines show a super-diffusive migratory movement with the coefficient of persistence  $\alpha$  bigger than 1 while J82 cell lines show a diffusive behaviour with  $\alpha$  close to 1. The T24 cancer cells migrate more persistently than RT112 cells, as shown by the higher value of  $\alpha$ . Results are in agreement with the findings of Mierke *et al.* [77], even if they measured this parameter for three dimensional migration. The reduced persistence of J82 ( $\alpha \sim 1$ ) can be explained as a consequence of the many lateral lamellipodia of the cell: the absence of one dominant leading lamellipodia implies the presence of multiple directions of

migration that reduce its capacity to migrate in a persistent way [87].

We found that there is difference in the mean values of the velocity of migration of the three cell lines. Often the velocity of migration is explained with a biphasic migration-velocity model [34, 81] where the response of the cells is linked to the increased adhesion strength: at low adhesion, cells cannot develop high tractions at the front; at high adhesion, contraction cannot overcome adhesion at the cell rear; while at intermediate adhesion, an optimum is reached, with traction generated at the front coupled to adhesion detachment at the rear. We can propose, on the basis of this idea, to explain the observed features here, since the adhesion parameter is different for the three cell types, figure 6.28. J82 cells have very high adhesion and a low velocity; the T24 cells have an optimum adhesion, a large velocity while the RT112 have low adhesion and no lamellipodium, small velocity. This may be due to the recruitment of different adhesion molecules in particular integrins dependent on the cell type [38]. On the contrary, Gupton and Waterman-Storer [57], pointed out the high spatial and temporal variability of the organization and activity of actin, myosin II, and focal adhesions that do not exhibit a simple correlation with optimal motility rates. Further works are needed to understand these complex correlation better.

All the properties analysed for the three cell lines are summarized in figure 6.29.

It can be concluded, that studying cell migration on a 10 kPa gel allowed us to detect different migration behaviours. In particular, the most relevant parameter to differentiate such cells are: traction stresses (TS), mean area of the focal adhesions ( $\langle A_{FAs} \rangle$ ), velocity ( $v$ ), diffusive parameter  $\alpha$  and the migration type. Such studies may become relevant for testing different cancer cell lines.

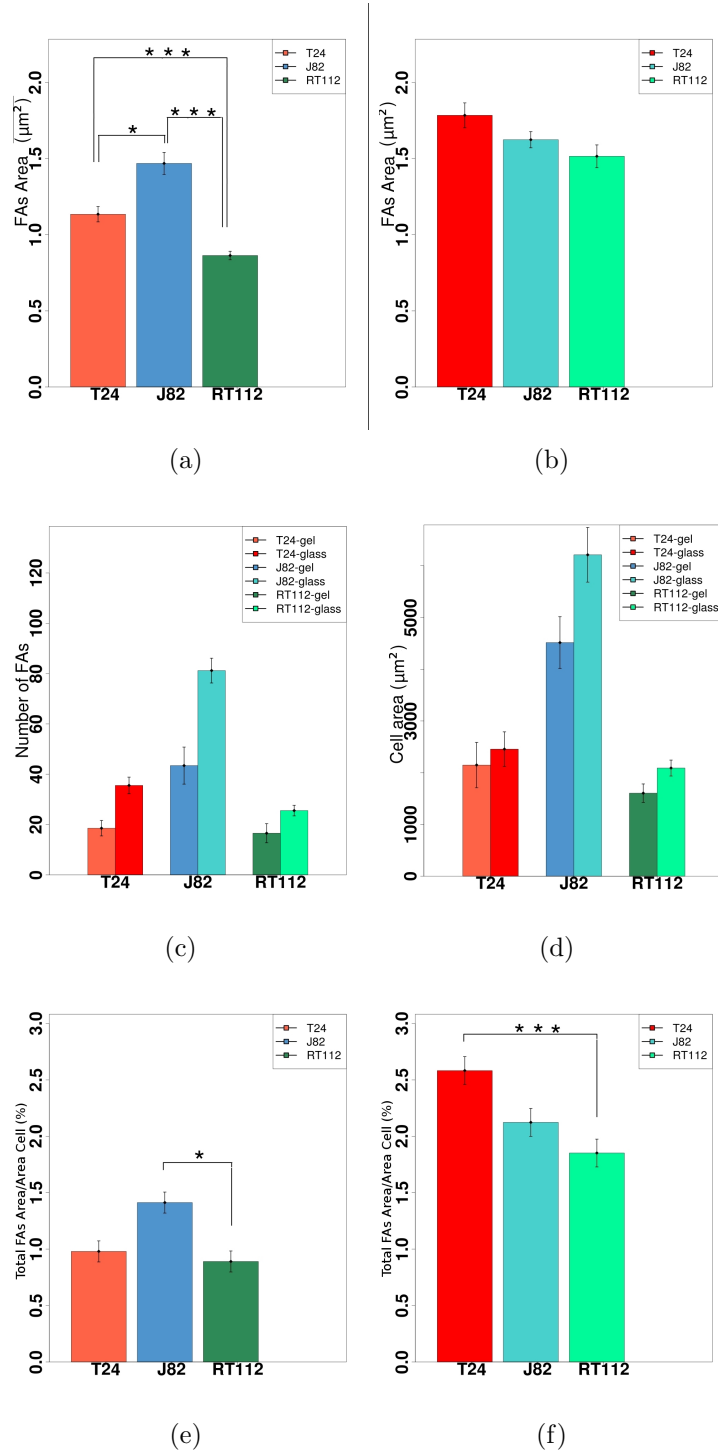


Figure 6.26: Mean value of the focal adhesion areas for the three cell lines analysed on polyacrylamide gel (a) and cover-glass (b). (c) Number of focal adhesion sites detected for the three cell lines seeded on the cover-glass and on gels. (d) Area of the cells (on polyacrylamide gels and cover-glass). Ratio of the total area occupied by focal adhesions and cell area for the three cell lines on gel (e) and on glass (f). Data shown as mean  $\pm$  s.e.m. ( $n_{cells} = 9$ ).

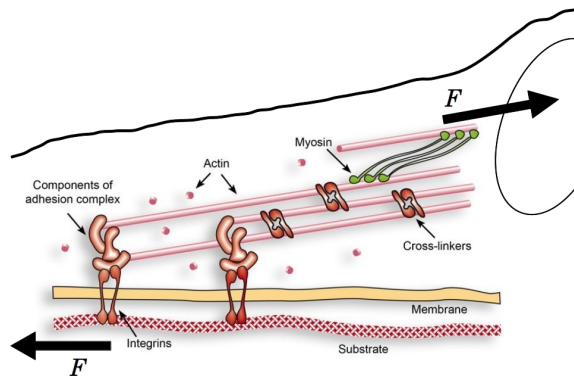


Figure 6.27: Complexity of the force transmission mechanism to the substrate. Picture adapted from <http://cellix.imba.oeaw.ac.at/traction/> [2].

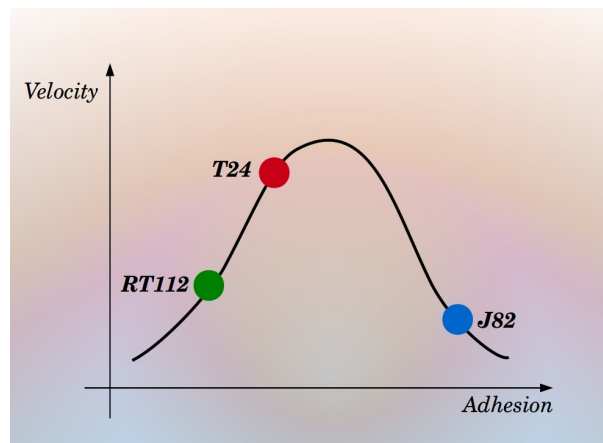


Figure 6.28: Possible relationship between the adhesion strength and the velocity for the three cancer cell lines.

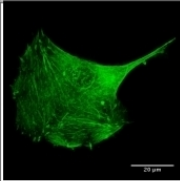
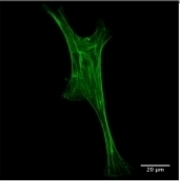
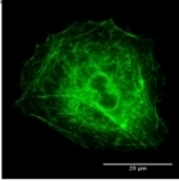





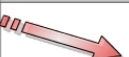

	<b>T24</b>	<b>J82</b>	<b>RT112</b>	
<i>Cytoskeleton</i>				
<i>Invasive Tumor</i>	++	++	-	
$E_{\text{cell}}$ (AFM)	+	++	-	
$\langle TS \rangle$ (Pa)	$117 \pm 4$	$130 \pm 4$	$170 \pm 4$	
$\langle  F  \rangle$ (nN)	$17 \pm 0.8$	$23 \pm 1.1$	$23 \pm 0.6$	
$\langle A_{FAs} \rangle$ ( $\mu\text{m}^2$ )	$1.1 \pm 0.05$	$1.5 \pm 0.07$	$0.8 \pm 0.03$	
$\langle \text{Number of FAs} \rangle$	$18 \pm 3$	$43 \pm 7$	$16 \pm 4$	
$\langle \% \text{ Tot Area FAs} / A_{\text{cell}} \rangle$	1%	1.4%	0.9%	
$\langle \text{Velocity} \rangle$ ( $\mu\text{m}/\text{min}$ )	$0.38 \pm 0.05$	$0.17 \pm 0.05$	$0.19 \pm 0.02$	
$\alpha$ ( $MSD \propto t^\alpha$ ) (superdiffusive)	$1.57 \pm 0.04$ (superdiffusive)	$1.05 \pm 0.12$ (diffusive)	$1.21 \pm 0.12$ (superdiffusive)	
<i>Migration Type</i>	4-step motion	4-step motion	Continuous motion	

Figure 6.29: Properties of the three cancer cell lines on polyacrylamide gels ( $E = 10$  kPa).



# Chapter 7

## Conclusions

The migration process, as defined by Lauffenburger and Horwitz, [70], is a physically integrated molecular process. It is known to contribute to many physiological motility processes *in vivo*, such as development, immune surveillance and cancer metastasis. During morphogenesis and cancer, single cells are able to position themselves in tissues or secondary growths thanks to the migration process [44]. To understand the migration phenomena we can not do without taking into account the cell's environment, the cell type and morphology as well as the internal organization of the cells. Protrusions and adhesions at the front and therefore traction as well as detachment at the rear part of the cell are often the four-steps used to described the migration process [45, 70]. Most eukaryotic cells sense and respond to the mechanical properties of their surroundings, adapting their area [36, 53, 74] their velocity of migration, [57, 74] and the organization of the cytoskeleton [54, 83].

This study underlines the ability of bladder cancer cells to adapt to their environment and probe it. In particular, T24 cells modify their mechanical response in order to adapt to different substrate stiffness. The adhesion growth and the cytoskeleton organization increase with the substrate stiffness. More precisely, the cells on stiffer polyacrylamide gels are well flattened and reveal a well defined actin structure. On the contrary, on soft substrate the cells are less elongated with a less developed actin structure. These results are similar to previous works of several authors [74, 36, 41, 54], who studied the

adaptation of normal cells to the underlying substrate. The traction forces increase with the Young modulus of the substrate, while the velocity of the cell migration decreases as was observed by other group [36, 94, 53]. In particular, Ghibaudo *et al.* [53] detect two distinct regimes for the force–rigidity link: first a linear increase of the force with the substrate stiffness and then a saturation for the largest rigidities. This is probably due to the fact that the cell cannot reinforce the actin–cytoskeleton indefinitely [25]. This preliminary study on the characterization of T24 cancer cells on different substrates allowed us to choose the substrate rigidity for the subsequent experiments: we chose to use the gel with a Young modulus of 10 kPa in order to be far enough from the plateau of the forces [53] and to get measurable displacements.

Several methods have been developed for the study of the traction forces on 2D deformable substrate starting from the displacement of fluorescent markers: the boundary element method, [32], the Fourier transform traction cytometry, [20], the traction reconstruction with point forces [97]. These methods are based on the exploitation of the Green tensor of the linear elasticity problem in a half space (Boussinesq problem), coupled with a minimization algorithm under force penalization. Another method has been proposed by Ambrosi [10]. The mathematical model is based on the classical functional analysis framework of Lions [73]; the general theory is applied to the specific problem of small deformation of a homogeneous elastic material subjected to body forces only. The major interest is that, instead of solving the CPU–consuming integral equation [32], it directly forces the 2D–averaged problem of partial differential equations to be solved by finite element method. The resolution becomes easier, and can be done in few seconds. The position of the fluorescent markers as detected from the images are used to build the computational mesh. In this way, we avoid an ulterior error of approximation, required for example in the FTTC method, where the building of a rectangular grid is necessary for the resolution of the problem. Moreover, a specific character of the adjoint method is that it automatically satisfies the force equilibrium condition.

For the series of experiments with the three cancer cell lines, some im-



provements have been done for the experimental setup. The quality of the images for the fluorescent beads as well as the quantity of the beads have a strong influence on the computation of the traction stresses, [97, 93] First, we increased the amount of beads in the gel solution in order to have a good compromise between good displacement field and the possibility to follow the beads in time with the particle tracker plugin of ImageJ. When recording the images for the beads, we used a piezo-motor that allows us to detect the best focus for all beads. Finally, in the computational domain around 2000 and 3000 beads were detected and followed in time. Thus the results of the numerical resolution of the FEM is more accurate.

The analysis of the three bladder cell lines point out some characteristics of these cells. Classified on the basis of their metastatic ability [17, 23], we can conclude that the traction stresses decrease with the metastatic capacity of the cell as recently observed by Indra *et al.* for murine breast cancer cells [65] and previously by Munevar *et al.* [79] for NIH 3T3 and the metastatic line of H-ras transformed NIH 3T3 cells.

Although the study of the traction forces exerted by migrating cells has been discussed by several authors, often the temporal component of this processes is missing: the cells are analysed only at one time point catching one particular aspect of the cell migration but not generally. In our study, we follow the cells in time and this reveals interesting time-dependent features for the three cell types. More precisely, the T24 and J82 cancer cells, the most invasive ones, show a mesenchymal-type of migration that can be decomposed into 4 steps: first, the cancer cell adheres and is not very active, thus stresses are low. Then while it is spreading on the gel surface, it searches for new adhesion sites that allow it to establish larger traction stresses. Thanks to these forces, the rear can be detached. The cell relaxes again its stresses until it starts again to try and move in another direction. A different way of migration has been found for the less invasive cells: the RT112 cancer cells lack in extended lamellipodium and do not show the 4-step locomotion: they move forward thanks to small perturbation of the lamellipodium and they strongly pull on the substrate. Therefore, we are able to describe the migration processes in terms of traction stresses.

Even though only based on a qualitative analysis, the cytoskeleton seems to be less organized in actin fibers for the less invasive cells seeded on polyacrylamide gels as was also recently observed by Mierke and co-workers [77]. The most invasive cells plated on cover-glass have a well structured actin and this could also explain the increased stiffness found for these cells.

The analysis and the comparison of the traction forces, the cytoskeleton and the focal adhesion areas have been made for cancer cells adhering on polyacrylamide gels (10 kPa) and this can explain some differences and discrepancies when our results are compared with the literature and in particular with two recent works of Indra *et al.* and Mierke *et al.* [65, 77]. In fact, they compare the traction forces for the cells adhering on polyacrylamide gels and the cytoskeleton organization or the focal adhesion sites for the cells seeded on cover-glass. In this way our study prevails because all the characteristics were measured on 10 kPa polyacrylamide gels.

Nevertheless a lot of improvements can still be made. The use of a higher number of cells for the analysis of the traction forces as well for the cytoskeleton could point out more differences, for example recent work of Tseng and co-workers [102]. A quantitative analysis of the cytoskeleton as well as the observation in real time of the actin polymerization could help to quantify and explain the different morphologies and to correlate the organization of the actin structure with the traction stresses. This can be achieved using transfected cells (T24 expressing GFP-actin, GFP-myosin and GFP-paxillin).

Finally, the use of a three-dimensional model will enable the description of the migration of cells and forces exerted during this process [30, 71, 75].

## 7.1 Conclusions en français

Le processus de migration, tels que défini par Lauffenburger et Horwitz [70] est un processus moléculaire intégré physiquement. Il est connu pour contribuer à de nombreux processus physiologiques de motilité *in vivo*, comme le développement, la surveillance immunitaire et les métastases du cancer. Durant la morphogenèse et le cancer, des cellules individuelles sont en mesure de se positionner dans des tissus ou excroissances secondaires grâce au pro-

cessus de migration [44]. Pour comprendre les phénomènes migratoires, nous ne pouvons pas ne tenir compte de l'environnement de la cellule, du type de cellules et de la morphologie ainsi que l'organisation interne. L'extension et les adhérences à l'avant et la traction ainsi que le détachement à de la partie arrière de la cellule sont souvent les quatre étapes utilisées pour décrire le processus de la migration [45, 70]. La plupart des cellules eucaryotes sent et répond aux propriétés mécaniques de leur environnement, en adaptant leur surface [36, 53, 74], leur vitesse de migration [57, 74], et l'organisation du cytosquelette [54, 83].

Cette étude souligne la capacité des cellules du cancer de la vessie à s'adapter à leur environnement. En particulier, les cellules T24 modifient leur réponse mécanique afin de s'adapter à la rigidité de différents substrats.

Les adhérences et l'organisation du cytosquelette augmentent avec la rigidité du substrat. Plus précisément, les cellules sur des gels de polyacrylamide plus rigides sont bien aplaties et révèlent une structure bien définie d'actine. Au contraire, sur substrat mou les cellules sont moins allongées avec une structure d'actine moins développée. Ces résultats sont similaires à des travaux antérieurs de plusieurs auteurs [74, 36, 41, 54], qui ont étudié l'adaptation de cellules normales sur un substrat. Les forces de traction augmentent avec le module de Young du substrat, tandis que la vitesse de migration des cellules diminue comme cela a été observé par d'autres groupes [36, 94, 53]. En particulier, Ghibaud *et al.* [53] ont détecté deux régimes distincts pour le lien entre la force et la rigidité: d'abord une augmentation linéaire de la force avec la rigidité du substrat, puis une saturation pour la plus grand valeur des rigidités. Cela est probablement dû au fait que la cellule ne peut pas renforcer le cytosquelette d'actine indéfiniment [25]. Cette étude préliminaire sur la caractérisation des cellules cancéreuses T24 sur différents substrats nous a permis de choisir la rigidité du substrat pour les expériences suivantes: nous avons choisi d'utiliser le gel avec un module de Young de 10 kPa pour être assez loin du plateau des forces [53] et pour obtenir des déplacements mesurables.

Plusieurs méthodes ont été développées pour l'étude des forces de traction sur un substrat déformable 2D à partir du déplacement des marqueurs

fluorescents: la méthode des éléments de frontière [32], la “Fourier Transform Traction Cytometry” [20], la reconstruction des tractions avec les forces ponctuelles [97]. Ces méthodes sont basées sur l’exploitation du tenseur de Green du problème d’élasticité linéaire dans un demi-espace (problème de Boussinesq), couplé avec un algorithme de minimisation. Une autre méthode a été proposée par Ambrosi [10]. Le modèle mathématique est basé sur l’analyse fonctionnelle de Lions [73], la théorie générale est appliquée au problème spécifique en petites déformations d’un matériau homogène élastique soumis à des forces seulement. L’intérêt majeur est que, au lieu de résoudre une équation intégrale [32], elle résout directement des équations aux dérivées partielles par la méthode des éléments finis. La résolution devient plus facile, et peut être fait en quelques secondes. Les positions des marqueurs fluorescents tels que détectés à partir des images sont utilisées pour construire le maillage de calcul. De cette façon, nous évitons une erreur d’approximation ultérieure, présente par exemple dans la méthode FTTC, où la construction d’une grille rectangulaire est nécessaire pour la résolution du problème. Par ailleurs, un caractère spécifique de la méthode adjointe est qu’elle satisfait automatiquement la condition d’équilibre des forces.

Pour la série d’expériences avec les trois lignées cellulaires cancéreuses, certaines améliorations ont été faites pour le dispositif expérimental. La qualité des images pour les billes fluorescentes ainsi que la quantité des billes ont une forte influence sur le calcul des contraintes [97, 93]. Premièrement, nous avons augmenté la quantité de billes dans le gel afin d’avoir un bon compromis entre champ de déplacement mesurable et possibilité de suivre les billes dans le temps avec le plugin “Particle Tracker” d’ImageJ. Lors de l’enregistrement des images des billes, nous avons utilisé un moteur piezo qui nous permet de détecter le meilleur plan pour toutes les billes. Enfin, dans le domaine de calcul, environ 2000 à 3000 billes ont été détectées et suivies dans le temps. Ainsi, les résultats de la résolution numérique de la FEM sont plus précis.

L’analyse des trois lignées cellulaires cancéreuses a souligné des caractéristiques variées de ces cellules. Classées sur la base de leur capacité métastatique [17, 23], nous pouvons conclure que les tractions diminuent avec la capacité

métastatique de la cellule. Cela a été récemment observé par Indra *et al.* pour des cellules cancéreuses du sein [65] et auparavant par Munevar *et al.* [79] pour une lignée métastatique transformée (H-ras) de cellules NIH 3T3.

Bien que l'étude des forces de traction exercée par les cellules qui migrent a été discutée par plusieurs auteurs, souvent la composante temporelle de ce processus est absente: les cellules sont analysées uniquement à un instant donné et l'analyse capture un aspect particulier de la migration cellulaire, mais non global. Dans notre étude, nous suivons les cellules dans le temps et cela révèle des caractéristiques intéressantes pour les trois types cellulaires. Plus précisément, les T24 et les cellules cancéreuses J82, les plus invasives, montrent un type de migration mésenchymateux qui peut être décomposé en quatre étapes: d'abord, la cellule cancéreuse adhère et n'est pas très active, donc les contraintes sont faibles. Ensuite elle s'étale sur la surface du gel et recherche à nouveau des sites d'adhésion qui lui permettent de développer des tractions plus forte. Grâce à ces forces, l'uropode peut être détaché. La cellule relâche à nouveau les forces jusqu'à ce qu'elle commence à migrer dans une autre direction. Une autre façon de migrer a été découvert pour les cellules moins invasives: les cellules cancéreuses RT112 ne montrent pas les 4 étapes de la locomotion: elles se déplacent en avant grâce à des petites perturbations du lamellipode et elles tirent fortement sur le substrat. Nous sommes en mesure de décrire le processus de migration de ces cellules en termes de contraintes.

Même si seulement basé sur une analyse qualitative, le cytosquelette semble être moins organisé en fibres d'actine pour les cellules moins invasives et ensemencées sur des gels de polyacrylamide; cela a été récemment observé par Mierke *et al.* [77]. Les cellules les plus envasives ont un réseau d'actine bien structurée sur le verre et cela pourrait aussi expliquer l'augmentation de rigidité trouvée pour ces cellules.

L'analyse et la comparaison des forces de traction, le cytosquelette et les zones d'adhésion focale ont été faites pour les cellules cancéreuses adhérant sur des gels de polyacrylamide (10 kPa) et cela peut expliquer certaines des différences et des divergences de nos résultats par rapport à la littérature et en particulier avec deux articles récents d'Indra *et al.* et Mierke *et al.* [65, 77].

En fait, ils comparent les forces de traction pour les cellules adhérant sur des gels de polyacrylamide et l'organisation du cytosquelette ou des sites d'adhésion focale pour les cellules ensemencées sur du verre. De cette façon, notre étude prévaut parce que toutes les caractéristiques ont été mesurées sur des gels de polyacrylamide de 10 kPa.

Cependant de nombreuses améliorations peuvent encore être apportées. L'utilisation d'un nombre plus élevé de cellules pour l'analyse des tractions ainsi que pour le cytosquelette pourrait mettre en évidence plus de différences, comme pour le travail récent de Tseng *et al.* [102]. Une analyse quantitative du cytosquelette ainsi que l'observation en temps réel de la polymérisation de l'actine pourrait aider à quantifier et expliquer les différentes morphologies et pourrait expliquer l'organisation de la structure de l'actine en relation avec les contraintes de traction. Ceci peut être réalisé maintenant en utilisant des cellules transfectées (exprimant la GFP T24 - actine, la GFP - myosine et la GFP - paxilline).

Enfin, l'utilisation d'un modèle tridimensionnel permettrait de décrire la migration des cellules et des forces exercées plus en détail lors de ce processus [30, 71, 75].

# Bibliography

- [1] Cell migration lab, <http://www.reading.ac.uk/cellmigration/adhesion.htm>.
- [2] <http://cellix.imba.oeaw.ac.at/traction/>.
- [3] <http://en.wikibooks.org/wiki/medical-physiology/cellular-physiology/cell-structure-and-function>.
- [4] <http://www.accessexcellence.org/lc/beon/data/phasethree/0030-beon/submission.php>.
- [5] Metamorph microscopy automation & image analysis software, <http://www.moleculardevices.com/>.
- [6] On-line biology book, <http://www.emc.maricopa.edu/faculty/farabee/biobk/biobooktoc.html>.
- [7] The r project for statistical computing <http://www.r-project.org/>.
- [8] Triangle, <http://www.cs.cmu.edu/quake/triangle.html>.
- [9] B. Alberts, D. Bray, J. Lewis, M. Raff, K. Roberts, and J. D. Watson. *Molecular Biology of the Cell*. Garland Publishing, 3rd edition, 2002.
- [10] D. Ambrosi. Cellular traction as an inverse problem. *Siam Journal On Applied Mathematics*, 66:2049–2060, 2006.
- [11] D. Ambrosi, A. Duperray, V. Peschetola, and C. Verdier. Traction patterns of tumor cells. *Journal of mathematical biology*, 58:163–181, 2009.

- 
- [12] Y. Aratyn-Schaus and M. L. Gardel. Transient frictional slip between integrin and the ecm in focal adhesions under myosin ii tension. *Current Biology*, 20:1145–1153, 2010.
- [13] Y. Aratyn-Schaus, P. W. Oakes, and M. L. Gardel. Dynamic and structural signatures of lamellar actomyosin force generation. *Molecular Biology of the Cell*, 22:1330–1339, 2011.
- [14] M. Bacac and S. I. Metastatic cancer cell. *Annual Review of Pathology: Mechanisms of Disease*, 3:221–47, 2008.
- [15] N. Balaban, U. Schwarz, D. Riveline, P. Goichberg, G. Tzur, I. Sabanay, D. Mahalu, S. Safran, A. Bershadsky, L. Addadi, and B. Geiger. Force and focal adhesion assembly: a close relationship studied using elastic micropatterned substrates. *Nature Cell Biology*, 3:466–472, 2001.
- [16] A. D. Bershadsky, N. Q. Balaban, and B. Geiger. Adhesion-dependent cell mechanosensitivity. *Annual Review of Cell and Developmental Biology*, 19:677–695, 2003.
- [17] E. Bindels, M. Vermey, N. De Both, and T. van der Kwast. Influence of the microenvironment on invasiveness of human bladder carcinoma cell lines. *Virchows Archiv*, 439:552–559, 2001.
- [18] T. Boudou, J. Ohayon, C. Picart, R. I. Pettigrew, and P. Tracqui. Nonlinear elastic properties of polyacrylamide gels: Implications for quantification of cellular forces. *Biorheology*, 46:191–205, 2009.
- [19] K. Burton, J. H. Park, and D. L. Taylor. Keratocytes generate traction forces in two phases. *Molecular Biology of the Cell*, 10:3745–3769, 1999.
- [20] J. Butler, I. Tolic-Norrelykke, B. Fabry, and J. Fredberg. Traction fields, moments, and strain energy that cells exert on their surroundings. *American Journal Of Physiology-cell Physiology*, 282:C595–C605, 2002.



- [21] A. Buxboim, I. L. Ivanovska, and D. E. Discher. Matrix elasticity, cytoskeletal forces and physics of the nucleus: how deeply do cells ‘feel’ outside and in? *Journal Of Cell Science*, 123:297–308, 2010.
- [22] C. L. Chaffer, J. P. Brennan, J. L. Slavin, T. Blick, T. x Thompson, and E. D. Williams. Mesenchymal-to-epithelial transition facilitates bladder cancer metastasis: Role of fibroblast growth factor receptor-2. *Cancer Research*, 66:11271–11278, 2006.
- [23] P. Champelovier, A. Simon, C. Garrel, G. Levacher, V. Praloran, and D. Seigneurin. Is interferon i3 one key of metastatic potential increase in human bladder carcinoma? *Clinical Cancer Research*, 9:4562–4569, 2003.
- [24] C. E. Chan and D. J. Odde. Traction dynamics of filopodia on compliant substrates. *science*, 322:1687–1691, 2008.
- [25] D. Choquet, D. P. Felsenfeld, and M. P. Sheetz. Extracellular matrix rigidity causes strengthening of integrin-cytoskeleton linkages. *Cell*, 88:39–48, 1997.
- [26] K. Clark, M. Langeslag, C. G. Figdor, and F. N. van Leeuwen. Myosin ii and mechanotransduction: a balancing act. *Trends in Cell Biology*, 17:178 – 186, 2007.
- [27] J. Condeelis. Life at the leading edge : the formation of cell protusions. *Annu. Rev. Cell Biol.*, 9:411–444, 1993.
- [28] G. M. Cooper and R. E. Hausman. *The Cell: A Molecular Approach*. Sinauer Associates, Inc., 2009.
- [29] S. E. Cross, Y.-S. Jin, Q.-Y. Lu, J. Rao, and J. K. Gimzewski. Green tea extract selectively targets nanomechanics of live metastatic cancer cells. *Nanotechnology*, 22:215101, 2011.
- [30] H. Delanoe-Ayari, J. P. Rieu, and M. Sano. 4d traction force microscopy reveals asymmetric cortical forces in migrating *Dictyostelium* cells. *Physical Review Letters*, 105:248103, 2010.

- 
- [31] M. Dembo, T. Oliver, A. Ishihara, and K. Jacobson. Imaging the traction stresses exerted by locomoting cells with the elastic substratum method. *Biophysical Journal*, 70:2008–2022, 1996.
- [32] M. Dembo and Y. Wang. Stresses at the cell-to-substrate interface during locomotion of fibroblasts. *Biophysical Journal*, 76:2307–2316, 1999.
- [33] P. Dieterich, R. Klages, R. Preuss, and A. Schwab. Anomalous dynamics of cell migration. *Proceedings Of The National Academy Of Sciences Of The United States Of America*, 105:459–463, 2008.
- [34] P. A. DiMilla, J. A. Stone, J. A. Quinn, S. M. Albelda, and D. A. Lauffenburger. Maximal migration of human smooth muscle cells on fibronectin and type iv collagen occurs at an intermediate attachment strength. *The Journal of Cell Biology*, 122:729–737, 1993.
- [35] E. K. Dimitriadis, F. Horkay, J. Maresca, B. Kachar, and R. S. Chadwick. Determination of elastic moduli of thin layers of soft material using the atomic force microscope. *Biophys Journal*, 82(5):2798–2810, 2002.
- [36] D. E. Discher, P. Janmey, and Y.-L. Wang. Tissue cells feel and respond to the stiffness of their substrate. *Science*, 310:1139–1143, 2005.
- [37] O. du Roure, A. Saez, A. Buguin, R. H. Austin, P. Chavrier, P. Siberzan, and B. Ladoux. Force mapping in epithelial cell migration. *Proceedings Of The National Academy Of Sciences Of The United States Of America*, 102:2390–2395, 2005.
- [38] A. Duperray, V. M. Laurent, and C. Verdier. Unpublished results.
- [39] H. W. Engl, M. Hanke, and A. Neubauer. *Regularization of Inverse Problems*. Kluwer Academic Publishers, 1996.
- [40] A. Engler, L. Bacakova, C. Newman, A. Hategan, M. Griffin, and D. Discher. Substrate compliance versus ligand density in cell on gel responses. *Biophysical Journal*, 86:617–628, 2004.

- 
- [41] A. J. Engler, S. Sen, H. L. Sweeney, and D. E. Discher. Matrix elasticity directs stem cell lineage specification. *Cell*, 126:677–689, 2006.
- [42] S. Even-Ram, A. D. Doyle, M. A. Conti, K. Matsumoto, R. S. Adelstein, and K. M. Yamada. Myosin iia regulates cell motility and actomyosin-microtubule crosstalk. *Nature Cell Biology*, 9:299–309, 2007.
- [43] D. A. Fletcher and R. D. Mullins. Cell mechanics and the cytoskeleton. *Nature*, 463:485–492, 2010.
- [44] P. Friedl and D. Gilmour. Collective cell migration in morphogenesis, regeneration and cancer. *Nature Reviews Molecular Cell Biology*, 10:445–457, 2009.
- [45] P. Friedl and K. Wolf. Tumour-cell invasion and migration: diversity and escape mechanisms. *Nature Reviews Cancer*, 3:362–374, 2003.
- [46] P. Friedl and K. Wolf. Plasticity of cell migration: a multiscale tuning model. *Journal Of Cell Biology*, 188:11–19, 2010.
- [47] A. Fuhrmann, J. R. Staunton, V. Nandakumar, N. Banyai, P. C. W. Davies, and R. Ros. Afm stiffness nanotomography of normal, metaplastic and dysplastic human esophageal cells. *Physical Biology*, 8:015007, 2011.
- [48] S. Féréol, R. Fodil, B. Labat, S. Galiacy, V. M. Laurent, B. Louis, D. Isabey, and E. Planus. Sensitivity of alveolar macrophages to substrate mechanical and adhesive properties. *Cell Motil Cytoskeleton*, 63:321–340, 2006.
- [49] M. L. Gardel, B. Sabass, L. Ji, G. Danuser, U. S. Schwarz, and C. M. Waterman. Traction stress in focal adhesions correlates biphasically with actin retrograde flow speed. *The Journal of Cell Biology*, 183:999–1005, 2008.

- [50] M. L. Gardel, I. C. Schneider, Y. Aratyn-Schaus, and C. M. Waterman. Mechanical integration of actin and adhesion dynamics in cell migration. *Annual Review of Cell and Developmental Biology*, 26:315–333, 2010.
- [51] B. Geiger, J. P. Spatz, and A. D. Bershadsky. Environmental sensing through focal adhesions. *Nature Reviews Molecular Cell Biology*, 10:21–33, 2009.
- [52] P. C. Georges and P. A. Janmey. Cell type-specific response to growth on soft materials. *Journal of Applied Physiology*, 98:1547–1553, 2005.
- [53] M. Ghibaudo, A. Saez, L. Trichet, A. Xayaphoummine, J. Browaeys, P. Silberzan, A. Buguin, and B. Ladoux. Traction forces and rigidity sensing regulate cell functions. *Soft Matter*, 4:1836–1843, 2008.
- [54] K. Ghosh, Z. Pan, E. Guan, S. Ge, Y. Liu, T. Nakamura, X.-D. Ren, M. Rafailovich, and R. A. F. Clark. Cell adaptation to a physiologically relevant ecm mimic with different viscoelastic properties. *Biomaterials*, 28:671–679, 2007.
- [55] K. Ghosh, C. K. Thodeti, A. C. Dudley, A. Mammoto, M. Klagsbrun, and D. E. Ingber. Tumor-derived endothelial cells exhibit aberrant rho-mediated mechanosensing and abnormal angiogenesis in vitro. *Proceedings Of The National Academy Of Sciences Of The United States Of America*, 105:11305–11310, 2008.
- [56] G. Giannone, B. J. Dubin-Thaler, O. Rossier, Y. Cai, O. Chaga, G. Jiang, W. Beaver, H.-G. Döbereiner, Y. Freund, G. Borisy, and M. P. Sheetz. Lamellipodial actin mechanically links myosin activity with adhesion-site formation. *Cell*, 128:561–575, 2007.
- [57] S. L. Gupton and C. M. Waterman-Storer. Spatiotemporal feedback between actomyosin and focal-adhesion systems optimizes rapid cell migration. *Cell*, 125:1361–1374, 2006.

- 
- [58] D. Hanahan and R. A. Weinberg. The hallmarks of cancer. *Cell*, 100:57–70, 2000.
- [59] D. Hanahan and R. A. Weinberg. Hallmarks of cancer: the next generation. *Cell*, 144:646–674, 2011.
- [60] A. K. Harris, P. Wild, and D. Stopak. Silicone rubber substrata: a new wrinkle in the study of cell locomotion. *Science*, 208:177–179, 1980.
- [61] H. Hertz. Ueber die berührung fester elastischer körper. *Journal für die reine und angewandte Mathematik (Crelles Journal)*, 92:0075–4102, 1882.
- [62] J. Howard. Molecular motors: structural adaptations to cellular functions. *Nature*, 389:561–567, 1997.
- [63] J. Huang, X. Peng, L. Qin, T. Zhu, C. Xiong, Y. Zhang, and J. Fang. Determination of cellular tractions on elastic substrate based on an integral boussinesq solution. *Journal Of Biomechanical Engineering-transactions Of The Asme*, 131:061009–1+, 2009.
- [64] A. Huttenlocher, R. R. Sandborg, and A. F. Horwitz. Adhesion in cell migration. *Current Opinion in Cell Biology*, 7:697–706, 1995.
- [65] I. Indra, V. Undyala, C. Kandow, U. Thirumurthi, M. Dembo, and K. A. Beningo. An in vitro correlation of mechanical forces and metastatic capacity. *Physical Biology*, 8:015015, 2011.
- [66] D.-H. Kim, K. Han, K. Gupta, K. W. Kwon, K.-Y. Suh, and A. Levchenko. Mechanosensitivity of fibroblast cell shape and movement to anisotropic substratum topography gradients. *Biomaterials*, 30:5433–5444, 2009.
- [67] D. Kong, Y. Li, Z. Wang, and F. H. Sarkar. Cancer stem cells and epithelial-to-mesenchymal transition (emt)-phenotypic cells: Are they cousins or twins? *Cancers*, 3:716–729, 2011.

- 
- [68] T. Laemmermann and M. Sixt. The microanatomy of t-cell responses. *Immunological Reviews*, 221:26–43, 2008.
- [69] L. Landau and E. Lifschitz. *Théorie de l'Elasticité*. 1967.
- [70] D. A. Lauffenburger and A. F. Horwitz. Cell migration: A physically integrated molecular process. *Cell*, 84:359 – 369, 1996.
- [71] W. R. Legant, J. S. Miller, B. L. Blakely, D. M. Cohen, G. M. Genin, and C. S. Chen. Measurement of mechanical tractions exerted by cells in three-dimensional matrices. *Nature Methods*, 7:969–71, 2010.
- [72] Z. Li, J. Song, G. Mantini, M.-Y. Lu, H. Fang, C. Falconi, L.-J. Chen, and Z. L. Wang. Quantifying the traction force of a single cell by aligned silicon nanowire array. *Nano Letters*, 9:3575–3580, 2009.
- [73] J. Lions. *Contrôle optimal de systèmes gouvernés par des équations aux dérivées partielles*. Dunod et Gauthier–Villard, 1968.
- [74] C. M. Lo, H. B. Wang, M. Dembo, and Y. L. Wang. Cell movement is guided by the rigidity of the substrate. *Biophysical Journal*, 79:144–152, 2000.
- [75] S. A. Maskarinec, C. Franck, D. A. Tirrell, and G. Ravichandran. Quantifying cellular traction forces in three dimensions. *Proceedings of the National Academy of Sciences*, 106:22108–22113, 2009.
- [76] R. Merkel, N. Kirchgessner, C. M. Cesa, and B. Hoffmann. Cell force microscopy on elastic layers of finite thickness. *Biophysical Journal*, 93:3314–3323, 2007.
- [77] C. T. Mierke, B. Frey, M. Fellner, M. Herrmann, and B. Fabry. Integrin  $\alpha 5 \beta 1$  facilitates cancer cell invasion through enhanced contractile forces. *Journal of Cell Science*, 124:369–383, 2011.
- [78] R. D. Mullins. Cytoskeletal mechanisms for breaking cellular symmetry. *Cold Spring Harbor Perspectives in Biology*, 2:a003392, 2010.

- 
- [79] S. Munevar, Y. Wang, and M. Dembo. Traction force microscopy of migrating normal and h-ras transformed 3t3 fibroblasts. *Biophysical Journal*, 80:1744–1757, 2001.
- [80] S. Palecek, C. Schmidt, D. Lauffenburger, and A. Horwitz. Integrin dynamics on the tail region of migrating fibroblasts. *Journal of Cell Science*, 109:941–952, 1996.
- [81] S. P. Palecek, J. C. Loftus, M. H. Ginsberg, D. A. Lauffenburger, and A. F. Horwitz. Integrin-ligand binding properties govern cell migration speed through cell-substratum adhesiveness. *Nature*, 385:537–540, 1997.
- [82] E. Papusheva and C.-P. Heisenberg. Spatial organization of adhesion: force-dependent regulation and function in tissue morphogenesis. *Embo Journal*, 29:2753–2768, 2010.
- [83] J. T. Parsons, A. R. Horwitz, and M. A. Schwartz. Cell adhesion: integrating cytoskeletal dynamics and cellular tension. *Nature Reviews Molecular Cell Biology*, 11:633–643, 2010.
- [84] M. J. Paszek, N. Zahir, K. R. Johnson, J. N. Lakins, G. I. Rozenberg, A. Gefen, C. A. Reinhart-King, S. S. Margulies, M. Dembo, D. Boettiger, D. A. Hammer, and V. M. Weaver. Tensional homeostasis and the malignant phenotype. *Cancer Cell*, 8:241–254, 2005.
- [85] R. Pelham and Y. Wang. Cell locomotion and focal adhesions are regulated by substrate flexibility. *Proceedings Of The National Academy Of Sciences Of The United States Of America*, 94:13661–13665, 1997.
- [86] V. Peschetola, C. Verdier, A. Duperray, and D. Ambrosi. *Cell Mechanics: from single scale-based models to multiscale modeling*. Chapman & Hall/CRC, 2009.
- [87] R. J. Petrie, A. D. Doyle, and K. M. Yamada. Random versus directionally persistent cell migration. *Nature Reviews Molecular Cell Biology*, 10:538–549, 2009.

- 
- [88] T. D. Pollard and G. G. Borisy. Cellular motility driven by assembly and disassembly of actin filaments. *Cell*, 112:453–465, 2003.
- [89] E. Puklin-Faucher and M. P. Sheetz. The mechanical integrin cycle. *J Cell Sci*, 122:179–186, 2009.
- [90] M. Raftopoulou and A. Hall. Cell migration: Rho gtpases lead the way. *Developmental Biology*, 265:23 – 32, 2004.
- [91] W. S. Rasband. *ImageJ*, U.S. National Institutes of Health, Bethesda, Maryland, USA, 1997-2007.
- [92] C. Reinhart-King, M. Dembo, and D. Hammer. The dynamics and mechanics of endothelial cell spreading. *Biophysical Journal*, 89:676–689, 2005.
- [93] B. Sabass, M. L. Gardel, C. M. Waterman, and U. S. Schwarz. High resolution traction force microscopy based on experimental and computational advances. *Biophysical Journal*, 94:207–220, 2008.
- [94] A. Saez, A. Buguin, P. Silberzan, and B. Ladoux. Is the mechanical activity of epithelial cells controlled by deformations or forces? *Biophysical Journal*, 89:L52–L54, 2005.
- [95] V. Sanz-Moreno, G. Gadea, J. Ahn, H. Paterson, P. Marra, S. Pinner, E. Sahai, and C. J. Marshall. Rac activation and inactivation control plasticity of tumor cell movement. *Cell*, 135:510–523, 2008.
- [96] I. F. Sbalzarini and P. Koumoutsakos. Feature point tracking and trajectory analysis for video imaging in cell biology. *Journal of Structural Biology*, 151:182–195, 2005.
- [97] U. Schwarz, N. Balaban, D. Riveline, A. Bershadsky, B. Geiger, and S. Safran. Calculation of forces at focal adhesions from elastic substrate data: The effect of localized force and the need for regularization. *Biophysical Journal*, 83:1380–1394, 2002.



- 
- [98] M. P. Sheetz, D. Felsenfeld, C. G. Galbraith, and D. Choquet. Cell migration as a five-step cycle. *Biochemical Society Symposia*, 65:233–243, 1999.
- [99] J. Stricker, Y. Aratyn-Schaus, P. W. Oakes, and M. L. Gardel. Spatiotemporal constraints on the force-dependent growth of focal adhesions. *Biophysical Journal*, 100:2883–2893, 2011.
- [100] J. L. Tan, J. Tien, D. M. Pirone, D. S. Gray, K. Bhadriraju, and C. S. Chen. Cells lying on a bed of microneedles: an approach to isolate mechanical force. *Proceedings Of The National Academy Of Sciences Of The United States Of America*, 100:1484–1489, 2003.
- [101] P. Tracqui, J. Ohayon, and T. Boudou. Theoretical analysis of the adaptive contractile behaviour of a single cardiomyocyte cultured on elastic substrates with varying stiffness. *Journal Theoretical Biology*, 255:92–105, 2008.
- [102] Q. Z. Tseng, I. Wang, E. Duchemin-Pelletier, A. Azioune, N. Carpi, J. Gao, O. Filhol, M. Piel, M. Thery, and M. Balland. A new micropatterning method of soft substrates reveals that different tumorigenic signals can promote or reduce cell contraction levels. *Lab On A Chip*, 11:2231–2240, 2011.
- [103] C. Verdier and J. M. Piau. Effect of nonlinear viscoelastic properties on tack. *Journal of Polymer Science: Part B: Polymer Physics*, 41:3139–3149, 2003.
- [104] K. Vleminckx, L. J. Vakaet, M. Mareel, W. Fiers, and F. van Roy. Genetic manipulation of e-cadherin expression by epithelial tumor cells reveals an invasion suppressor role. *Cell*, 66:107–119, 1991.
- [105] K. Wolf, I. Mazo, H. Leung, K. Engelke, U. von Andrian, E. Deryugina, A. Strongin, E. Brocker, and P. Friedl. Compensation mechanism in tumor cell migration: mesenchymal-amoeboid transition after blocking of pericellular proteolysis. *Journal Of Cell Biology*, 160:267–277, 2003.

- [106] T. Yeung, P. Georges, L. Flanagan, B. Marg, M. Ortiz, M. Funaki, N. Zahir, W. Ming, V. Weaver, and P. Janmey. Effects of substrate stiffness on cell morphology, cytoskeletal structure, and adhesion. *Cell Motility And The Cytoskeleton*, 60:24–34, 2005.

# Appendix 1

## FTTC method with Gaussian filter

Here, the matlab code used for computing the traction stresses via FTTC method. For the displacement field, a Gaussian filter is applied.

```
clear all
close all
clc
% %Define the screen size and the frame dimension
scrsz = [1 1 2000 1250]; % %1 pixel = 0.155883 micron
px = 0.155883;
% %Frame dimension in micron
bx1 = 1200*px; by1 = 990*px;
% %Read the input file
% %Read the file with the beads position and displacements and the cell
contour

[Beads, Xc1, xb, yb, dxb, dyb] = readfileinput(px,bx1,by1);

% %Parameters for  $K_{tilde}$  matrix
E = 10;
nu = 0.5;
A = E/(2*(1-nu
```

```

));
B = 2*(1+nu)/E;
sig = (0.05:0.005:0.1);

% %Mesh size
sizeMx = 2^n;
delta = bx1/sizeMx;
sizeMy = by1/delta;

% %Define deltax and deltay
xm = (0:sizeMx-1)*delta;
ym = (0:sizeMy-1)*delta;
Mx = length(xm);
My = length(ym);

[Xm,Ym] = meshgrid(xm,ym);

% %Build the uniform mesh

[Ux,Uy] = UniformMesh(Xm,Ym,xb,yb,dxb,dyb,Mx,My,Beads);
% %Mx1 = 2(nextpow2(Mx));
My1 = 2(nextpow2(My));

% % Build KTilde(-1)

kx1 = mod( 1/2 + (0:(Mx1-1))/Mx1 , 1 ) - 1/2;
KX = 2*pi*kx1/(delta);
ky1 = mod( 1/2 + (0:(My1-1))/My1 , 1 ) - 1/2;
KY = 2*pi*ky1/(delta);

[kx,ky] = meshgrid(KX,KY);

% %Compute the traction adding the Gaussian filter

```

```

[Tgx,Tgy] = ComputeTractionGuassinfilter(Ux,Uy,kx,ky,A,Mx1,My1,nu,shift,sigma);

% %Resize the matrix

Tgx = real(Tgx(1:My,1:Mx));
Tgy = real(Tgy(1:My,1:Mx));

% %Compute and compare the displacement obtained with the FFT

[Ugx,Ugy] = ComputeDisplacement(kx,ky,Tgx,Tgy,B,nu,Mx1,My1,shift);

[Tg, U] = PlotsResults( Xm, Ym, Ux, Uy, Tx, Ty, Mx, My, sizeMx);

```

## Functions

**% % This function reads the file with beads positions and displacements.**

```

function [B, Xc1, xb, yb, dxb, dyb] = readFileInput(px,bx1,by1)
beads = cell(1,6);
C = cell(1,2);
%%% Read the file with the beads position and displacements
Bi = Beads;
fid = fopen(Bi,r);
beads(1,:) = textscan(fid,'%f%f%f%f%f%f');
fclose(fid);
%beads position
xb = beads1,1;
yb = beads1,2;

%beads displacement
dxb = beads1,4;

```

```
dyb = beads1,5;
```

```
B = length(xb);
```

```
% % Read the cell contour from the file Cell*.txt
```

```
Ci='Cell02.txt';
```

```
fid = fopen(Ci,'r');
```

```
C(1,:)=textscan(fid,'%f%f');
```

```
fclose(fid);
```

```
Xc1=[ C{1,1}*px,by1-C{1,2}*px];
```

**This function builds the rectangular grid.**

```
function [Ux,Uy] = UniformMesh(Xm,Ym,xb,yb,dxb,dyb,Mx,My,B)
```

```
for i = 1:My
```

```
for j = 1:Mx
```

```
    Pm = [Xm(i,j), Ym(i,j)];
```

```
    for h = 1:B
```

```
        D(h) = sqrt( (xb(h)-Pm(1,1)).^2 + (yb(h)-Pm(1,2)).^2 );
```

```
    end
```

```
    dm = min(D);
```

```
    D1 = D;
```

```
    for s = 1:5
```

```
        d(s) = dm;
```

```
        idm(s) = find (D==dm);
```

```
        idm1(s) = find (D1==dm);
```

```
        D1(idm1(s)) = [];
```

```
        Bd(s,:) = [dxb(idm(s)),dyb(idm(s))];
```

```
    dm = min(D1);
```

```
end
```

```

n = 4;
a = sum(1./d.^n);

Ux(i,j) = (1./d.^n)*Bd(:,1)/a;
Uy(i,j) = (1./d.^n)*Bd(:,2)/a;
end
end

```

**This function computes the traction stresses field. We do it in the Fourier space via `fft2` and then we come back in the real space with the `ifft2`.**

```

function [Tx,Ty] = ComputeTractionGaussianFilter(Ux,Uy,kx,ky,A,Mx,My,nu,
shift,sigma)
    uxF = fft2(Ux-mean(Ux(:)),My,Mx)./Mx./My;
    uyF = fft2(Uy-mean(Uy(:)),My,Mx)./Mx./My;

    %% Define a Gaussian filter  $H(u,v) = \exp(-D^{(u,v)}/2/D0^2)$ , where D0 is
    the cut off frequency.
    D0 = sigma;
    D = sqrt(kx.^2+ky.^2);
    HGauss = exp(-(D.^2)./(2*(D0^2)));

    uxF = HGauss.*uxF;
    uyF = HGauss.*uyF;
    Txf = zeros(My,Mx);
    Tyf = zeros(My,Mx);

    for i = 1:Mx
        for j = 1:My
            k = sqrt( kx(j,i).^2 + ky(j,i).^2);
            if ( k==0 )
                KInv = zeros(2,2);

```

```

elseif ( i == My/2+1 ——— j == Mx/2+1 )
KInv = (A/k) * [ (1-nu)*k2 + nu*kx(j,i)2 0 ; ... 0 (1-nu)*k2 + nu*ky(j,i)2 ];
else
KInv = (A/k) * [ (1-nu)*k2 + nu*kx(j,i)2 nu*kx(j,i)*ky(j,i) ; ... nu*kx(j,i)*ky(j,i)
(1-nu)*k2 + nu*ky(j,i)2 ];
end
Tx(f,j,i) = KInv(1,:)*[uxF(j,i); uyF(j,i)];
Ty(f,j,i) = KInv(2,:)*[uxF(j,i); uyF(j,i)];
end
end
Tx(f) = Tx(f) - mean(Tx(f,:));
Ty(f) = Ty(f) - mean(Ty(f,:));
Tx = ifft2(Tx(f,My,Mx))*Mx*My;
Ty = ifft2(Ty(f,My,Mx))*Mx*My;

```

**This function computes the displacement field starting from the obtained tractions.**

```

function [Ux1,Uy1] = DomputeDisplacement(kx,ky,Tx1,Ty1,B,nu,Mx,My,shift);
Tx1f1 = fft2(Tx1-mean(Tx1(:)),My,Mx)./Mx./My;
Ty1f1 = fft2(Ty1-mean(Ty1(:)),My,Mx)./Mx./My;
for i = 1:Mx
for j = 1:My
k = sqrt( kx(j,i).2 + ky(j,i).2);
if ( k==0 )
K = zeros(2);
elseif (i==Mx/2+1 ——— j==My/2+1 )
K = (B./k3) * [ (1-nu)*k2 + nu*ky(j,i)2 0 ; ... 0 (1-nu)*k2 + nu*kx(j,i)2 ];
else
K = (B./k3) * [ (1-nu)*k2 + nu*ky(j,i)2 -nu*kx(j,i)*ky(j,i) ; ... -nu*kx(j,i)*ky(j,i)
(1-nu)*k2 + nu*kx(j,i)2 ];
end
KKi,j = K;
Uxf1(j,i) = K(1,:)*[Tx1f1(j,i); Ty1f1(j,i)];

```



---

```
Uyf1(j,i) = K(2,:)*[Txf1(j,i); Tyf1(j,i)];  
end  
end  
Uxf1(1,1)=0;  
Uyf1(1,1)=0;  
Ux1 = ifft2(Uxf1,My,Mx)*Mx*My;  
Uy1 = ifft2(Uyf1,My,Mx)*Mx*My;
```



# Appendix 2

## T24 cancer cells

The migration of T24 cancer cells can be described by the 4-step motions: protrusion of lamellipodium, adhesion at the leading edge, contraction and disassembly at the rear. The following pictures show the phase-contrast images and the colour maps of two different T24 cancer cells.

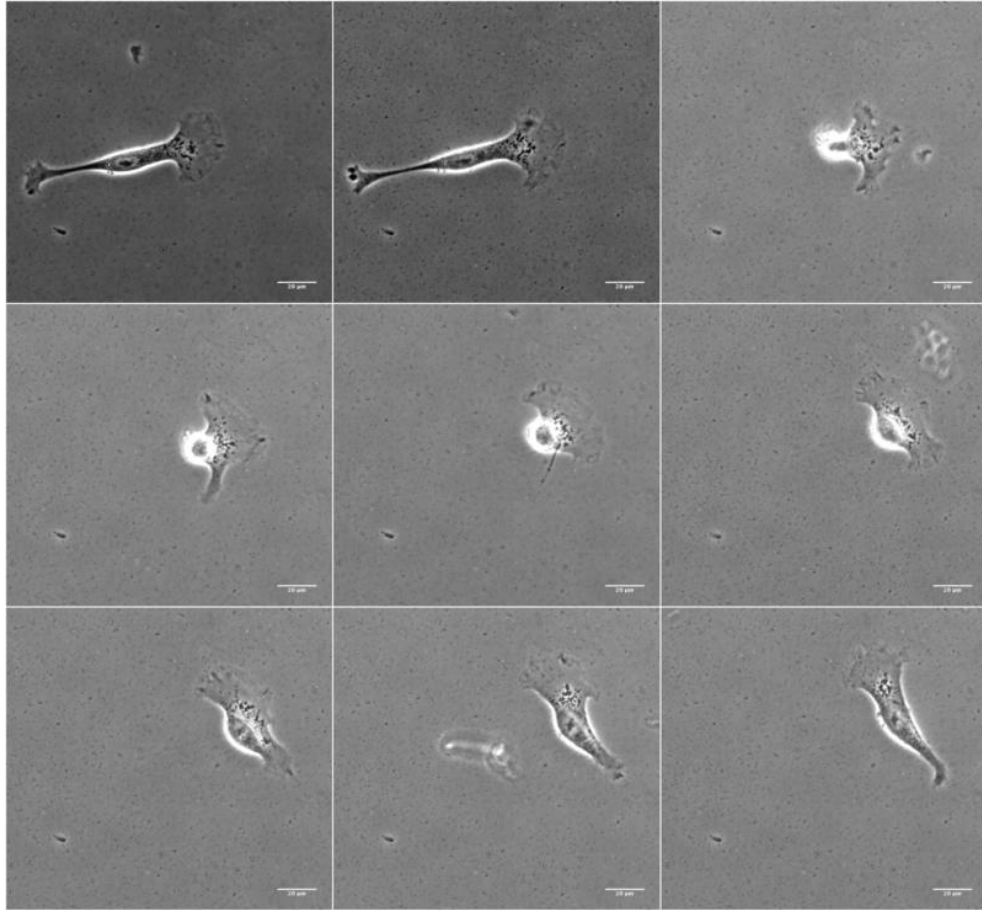


Figure 7.1: Phase-contrast images of a T24 cancer cell migrating on a rigid gel ( $E=10$  kPa). The time interval between frames is 4 minutes. The scale bar at the bottom right corner represents  $20\ \mu m$ .

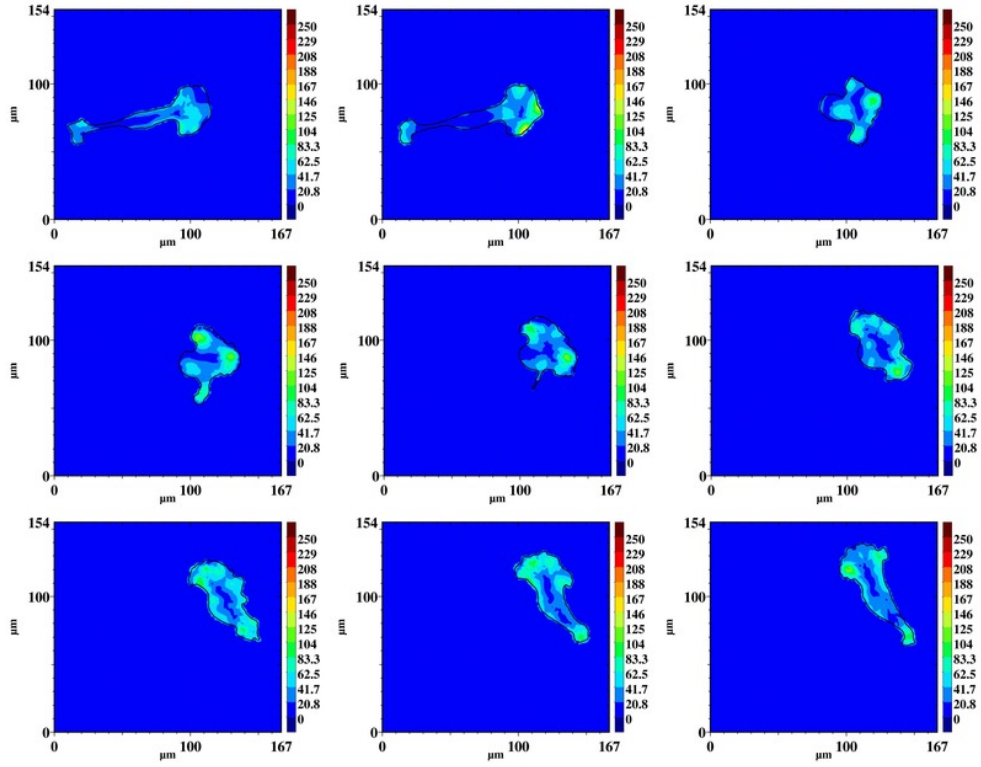


Figure 7.2: Colour maps of a T24 cancer cell migrating on a rigid gel ( $E=10$  kPa). The time interval between frames is 4 minutes. The colour bar is in Pa.

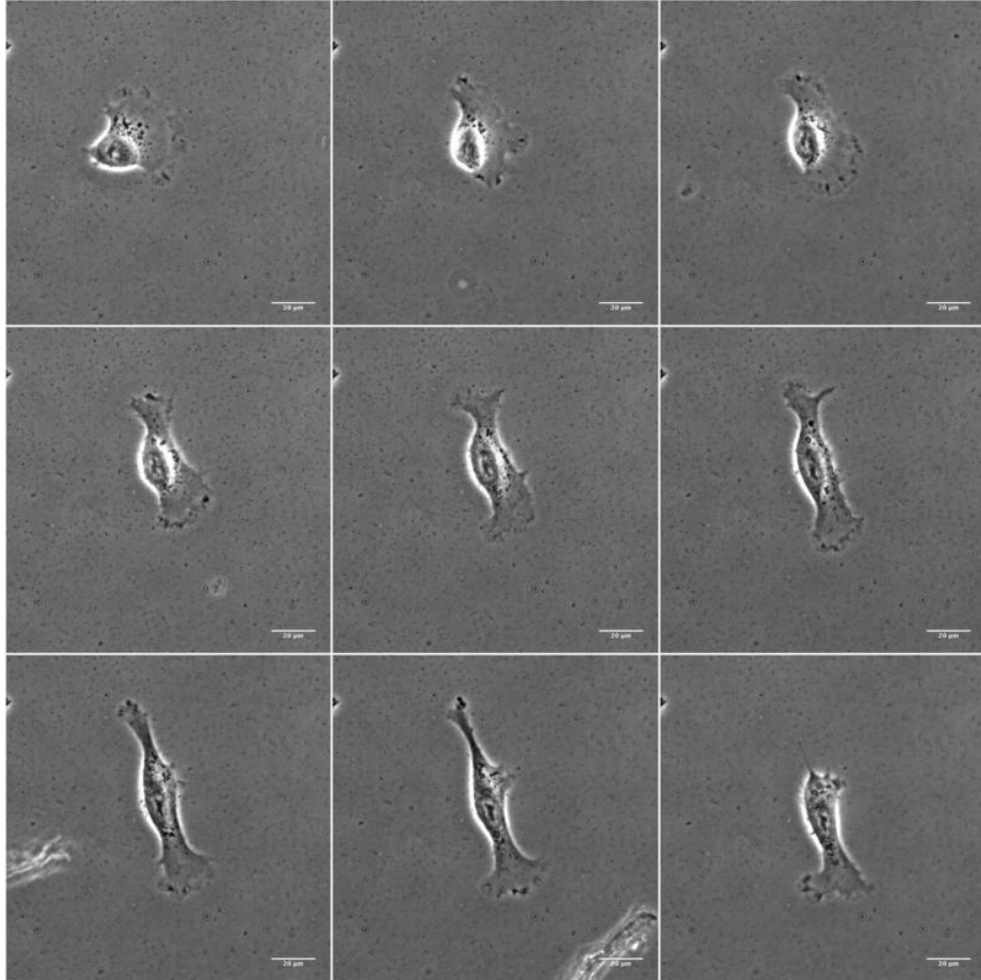


Figure 7.3: Phase-contrast images of a T24 cancer cell migrating on a rigid gel ( $E=10$  kPa). The time interval between frames is 4 minutes. The scale bar at the bottom right corner represents  $20\text{ }\mu\text{m}$ .

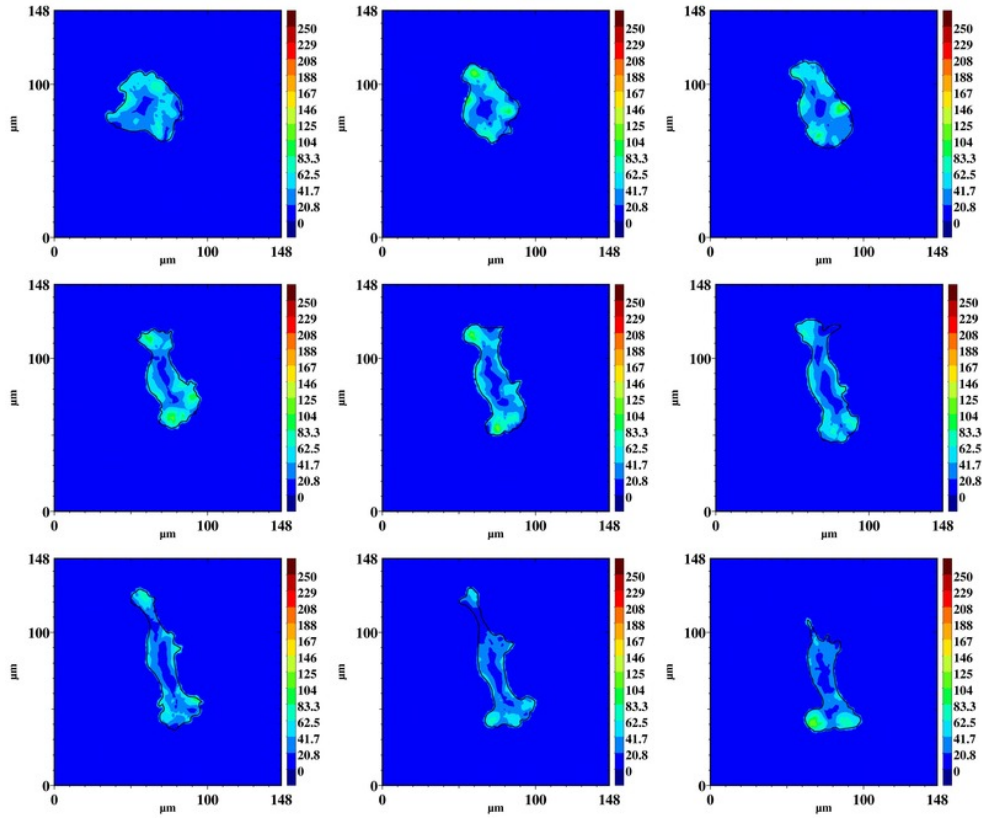


Figure 7.4: Colour maps of a T24 cancer cell migrating on a rigid gel ( $E=10$  kPa). The time interval between frames is 4 minutes. The colour bar is in Pa.

## J82 cancer cells

The migration of J82 cancer cells can be described by the 4-step motions: protrusion of lamellipodium, adhesion at the leading edge, contraction and disassembly at the rear. The following pictures shows the phase-contrast images and the colour map of two different J82 cancer cells.

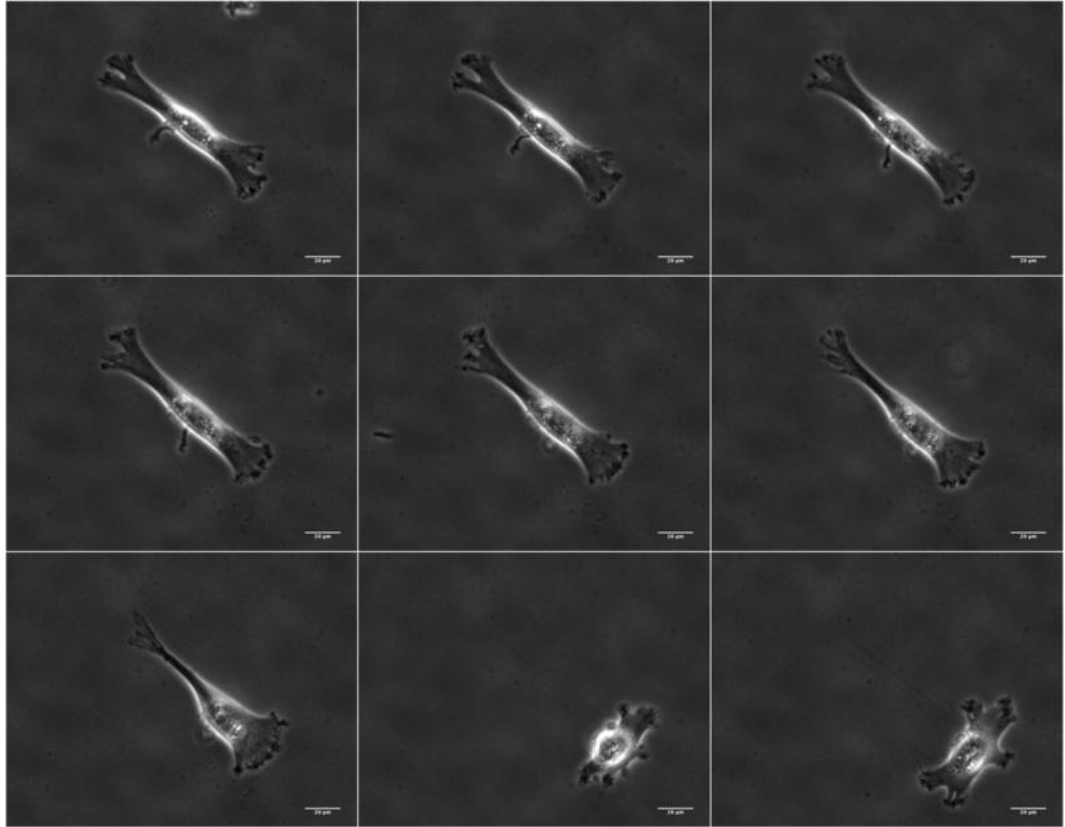


Figure 7.5: Phase-contrast images of a J82 cancer cell migrating on a rigid gel ( $E=10$  kPa). The time interval between frames is 4 minutes. The scale bar at the bottom right corner represents  $20 \mu m$ .



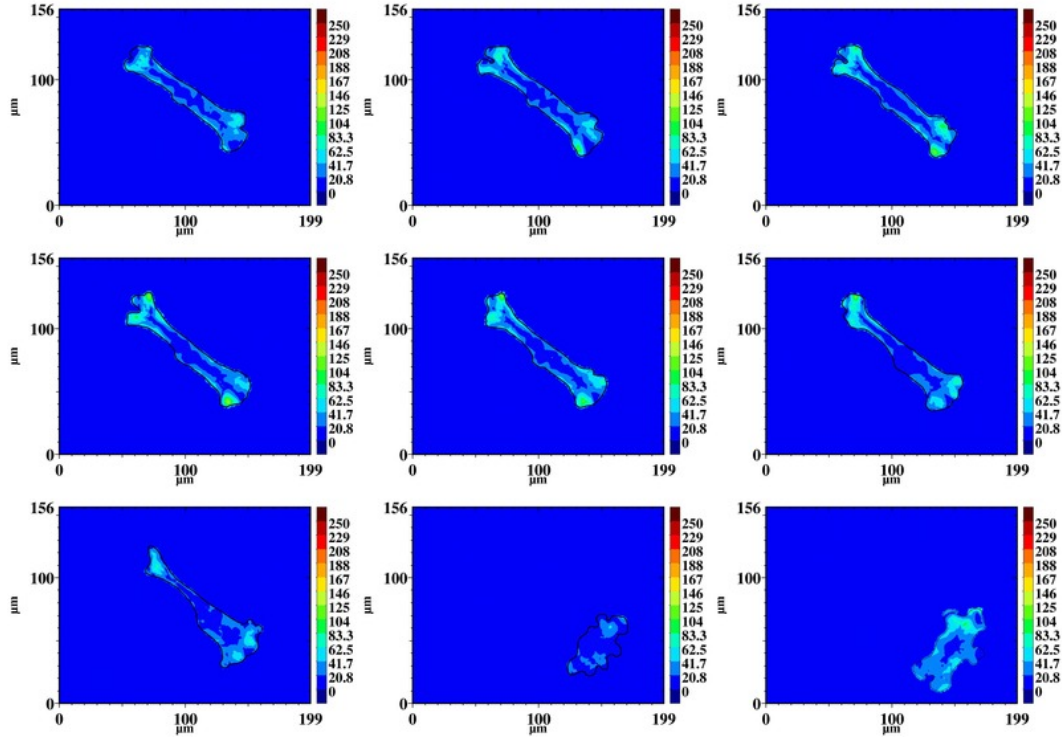


Figure 7.6: Colour maps of a J82 cancer cell migrating on a rigid gel ( $E=10$  kPa). The time interval between frames is 4 minutes. The colour bar is in Pa.

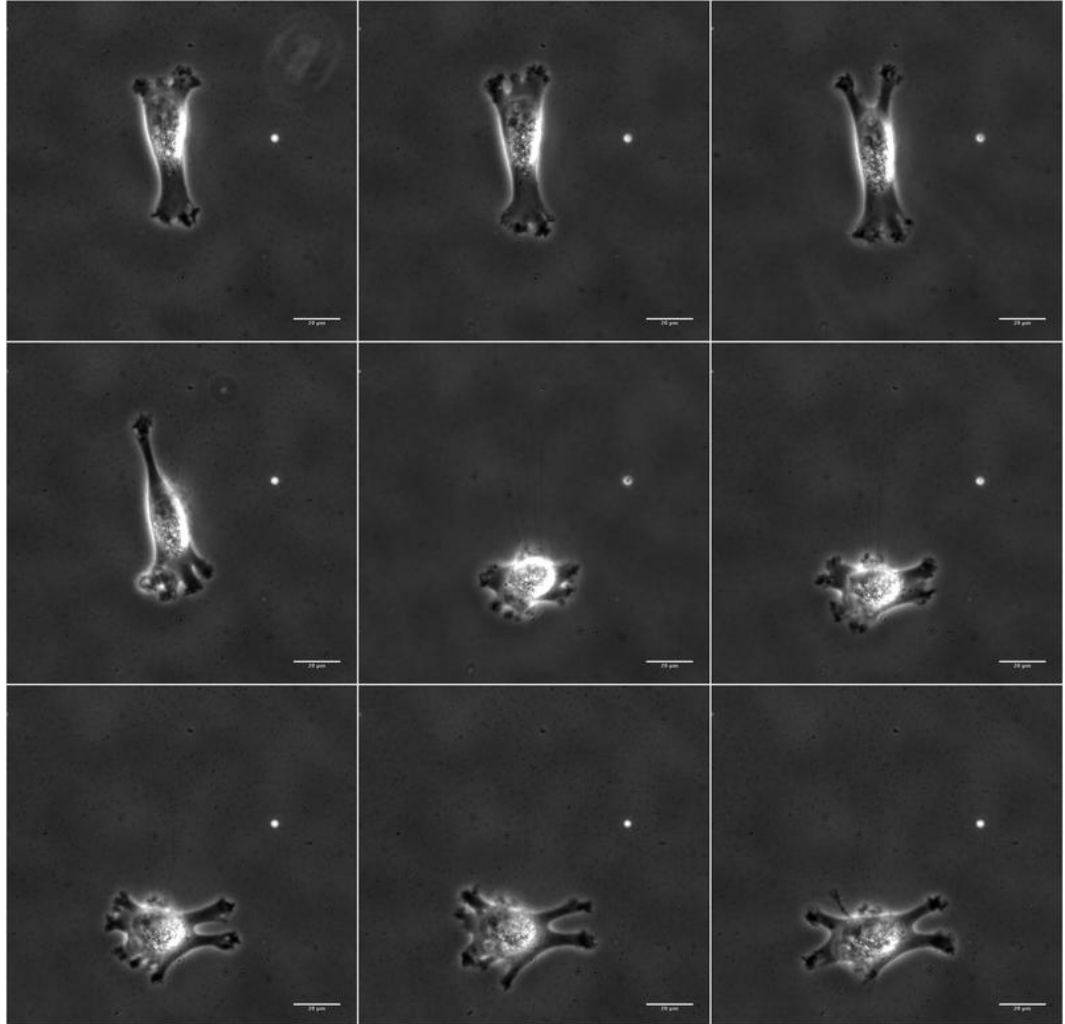


Figure 7.7: Phase-contrast images of a J82 cancer cell migrating on a rigid gel ( $E=10$  kPa). The time interval between frames is 4 minutes. The scale bar at the bottom right corner represents  $20\text{ }\mu\text{m}$ .

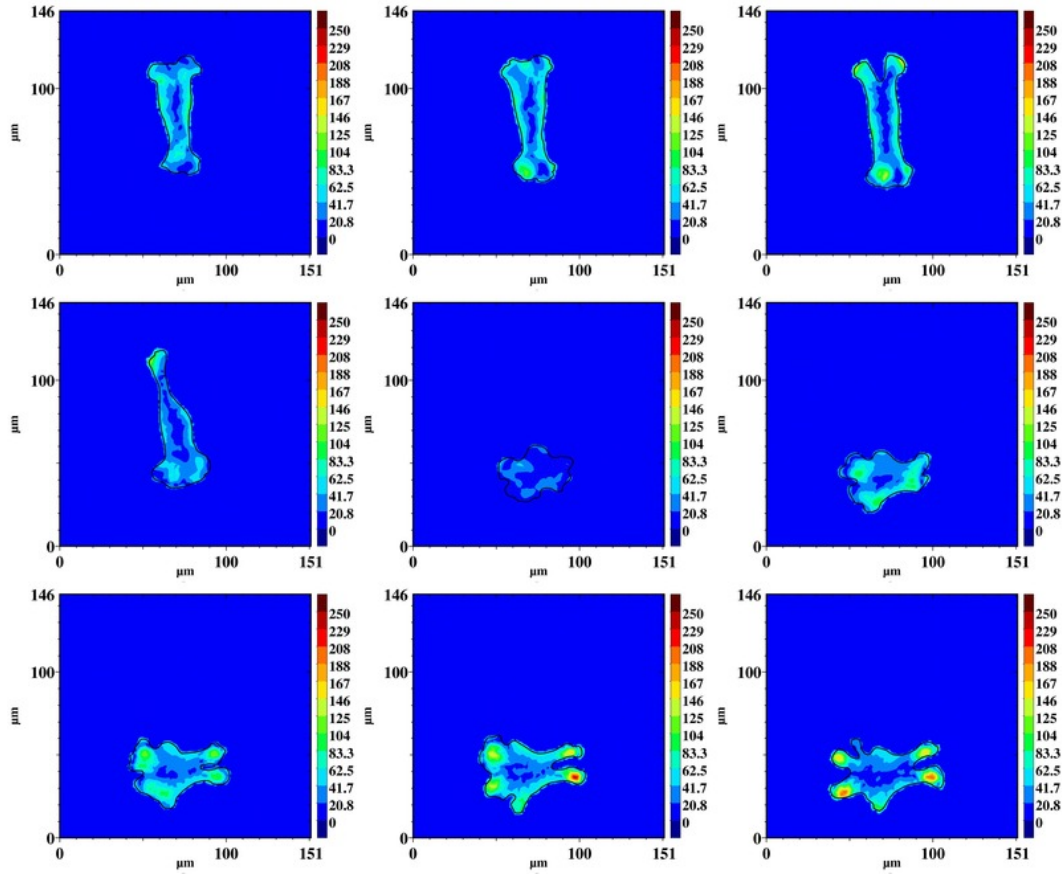


Figure 7.8: Colour maps of a J82 cancer cell migrating on a rigid gel ( $E=10$  kPa). The time interval between frames is 4 minutes. The colour bar is in Pa.



## RT112 cancer cells

RT112 cells do not show the four-step motion during the migration process: they are able to move thanks to small perturbations in the lamellipodium. The following pictures show the phase-contrast images and the colour map of two different RT112 cancer cells.

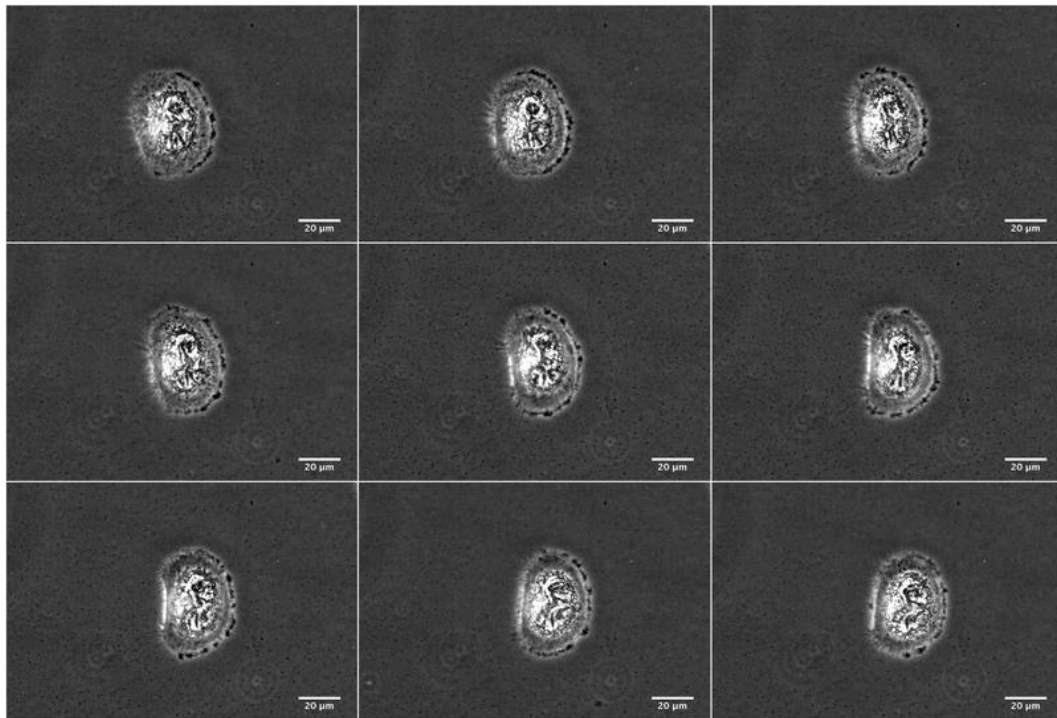


Figure 7.9: Phase-contrast images of a RT112 cancer cell migrating on a rigid gel ( $E=10$  kPa). The time interval between frames is 4 minutes. The scale bar at the bottom right corner represents  $20 \mu m$ .

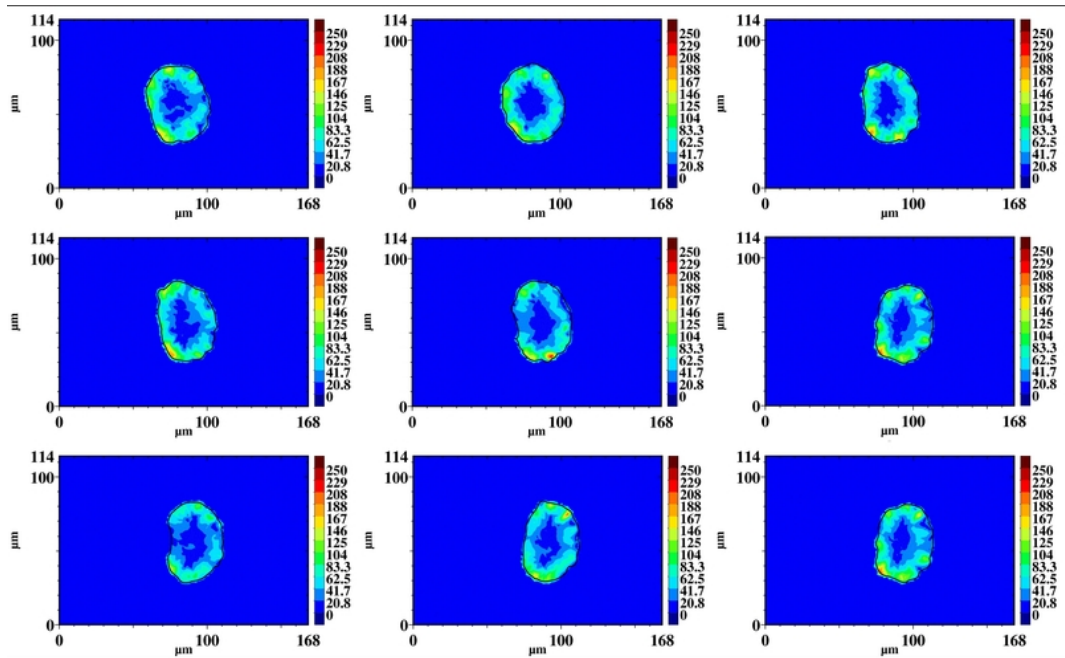


Figure 7.10: Colour maps of a RT112 cancer cell migrating on a rigid gel ( $E=10$  kPa). The time interval between frames is 4 minutes. The colour bar is in Pa.

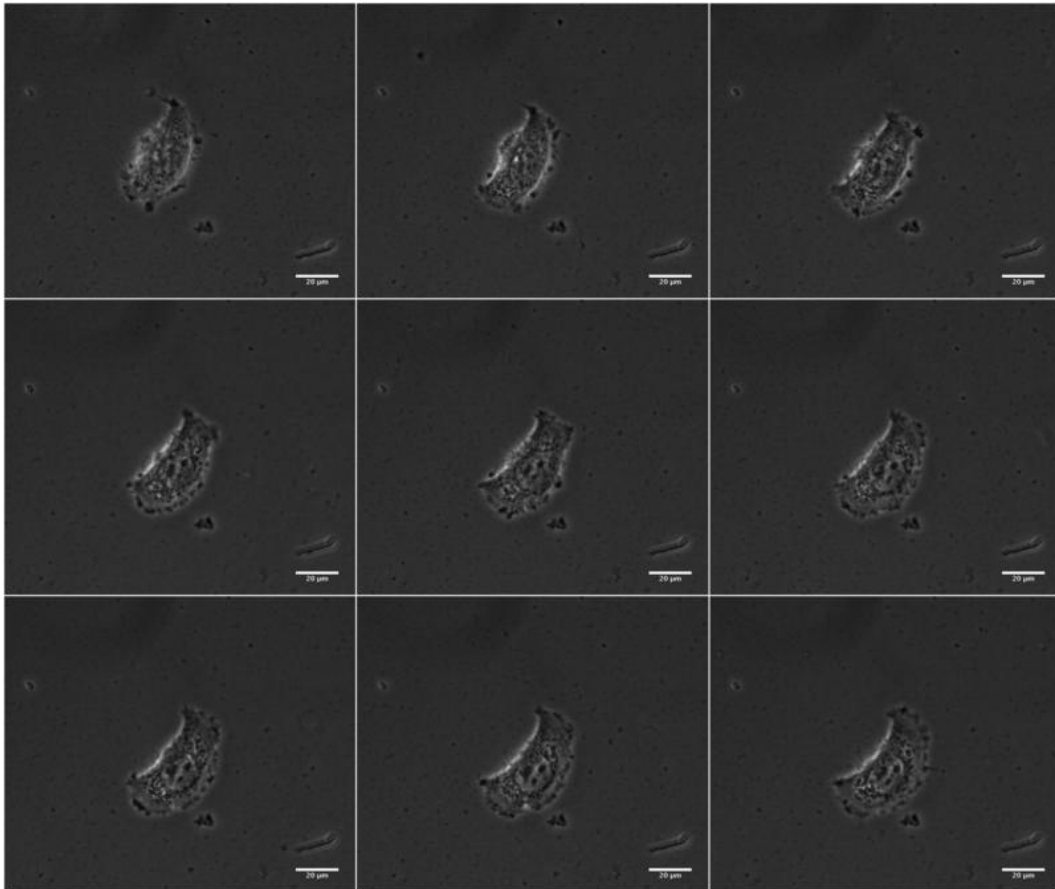


Figure 7.11: Phase-contrast images of a RT112 cancer cell migrating on a rigid gel ( $E=10$  kPa). The time interval between frames is 4 minutes. The scale bar at the bottom right corner represents  $20\ \mu m$ .

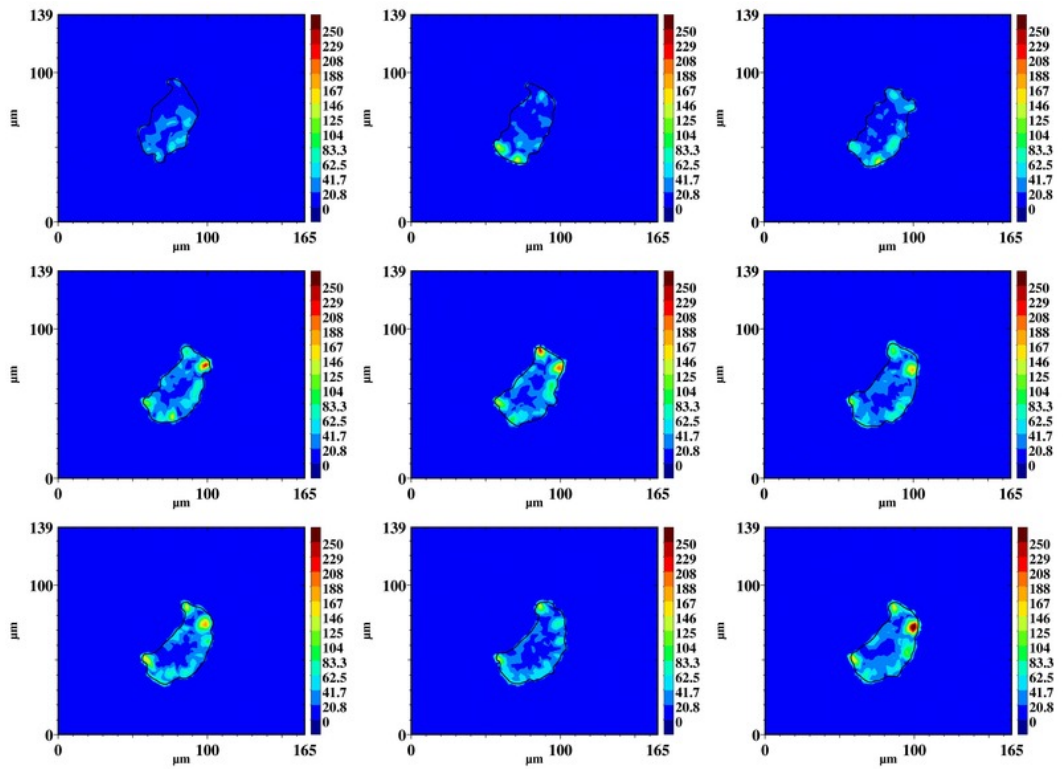


Figure 7.12: Colour maps of a RT112 cancer cell migrating on a rigid gel ( $E=10$  kPa). The time interval between frames is 4 minutes. The colour bar is in Pa.



## Appendix 3

Fluorescent images of three cells for each cell type (T24, J82, RT112).

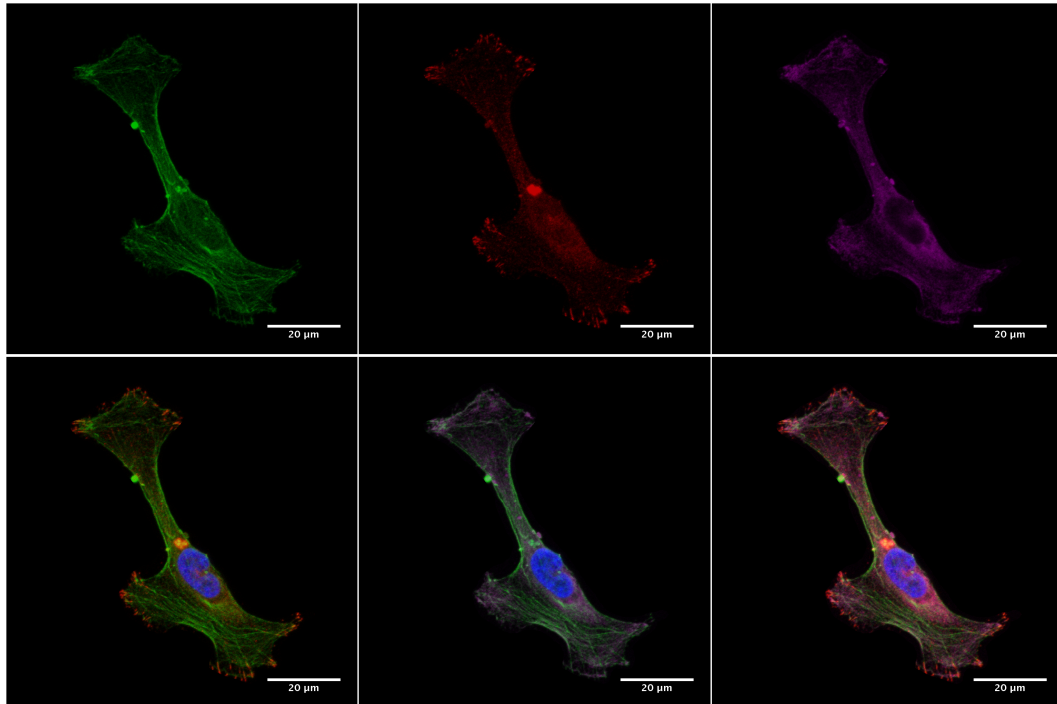


Figure 7.13: Fluorescent images of T24 cell adhering on polyacrylamide gel ( $E = 10$  kPa). Top panels show staining of actin in green (left), paxillin in red (middle) and myosin II in deep purple (right). Bottom panels show combined actin-paxillin-nucleus (left), actin-myosin-nucleus (middle) and actin-paxillin-myosin-nucleus (right). The nucleus is stained in blue.

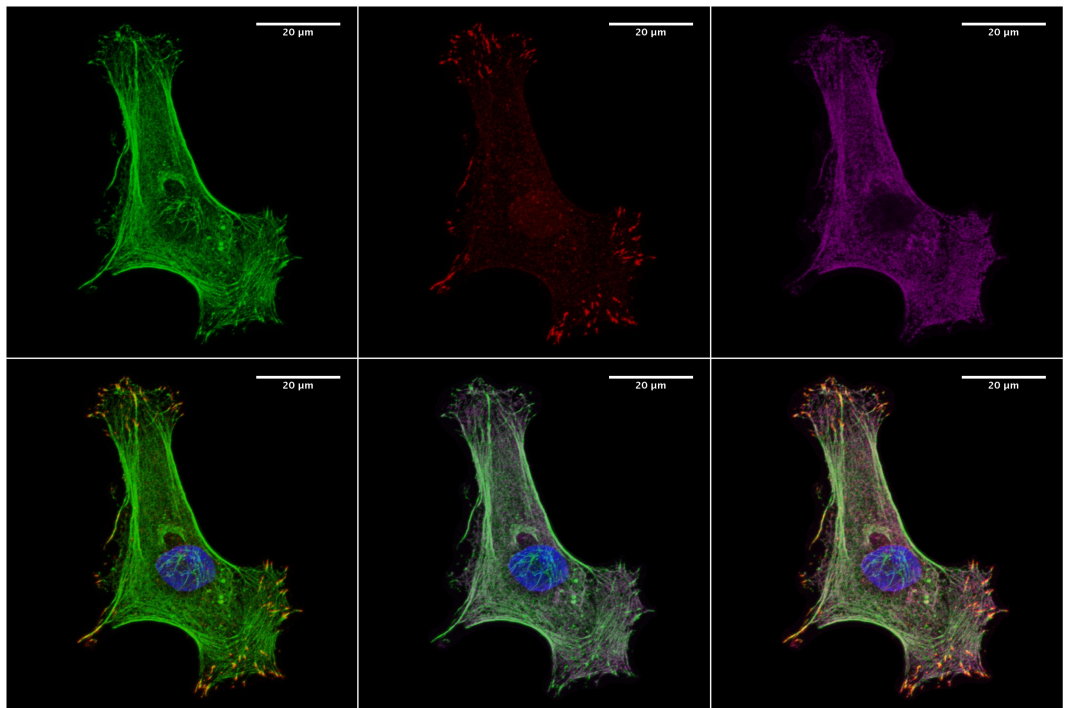


Figure 7.14: Fluorescent images of T24 cell adhering on polyacrylamide gel ( $E = 10$  kPa). Top panels show staining of actin in green (left), paxillin in red (middle) and myosin II in deep purple (right). Bottom panels show combined actin-paxillin-nucleus (left), actin-myosin-nucleus (middle) and actin-paxillin-myosin-nucleus (right). The nucleus is stained in blue.

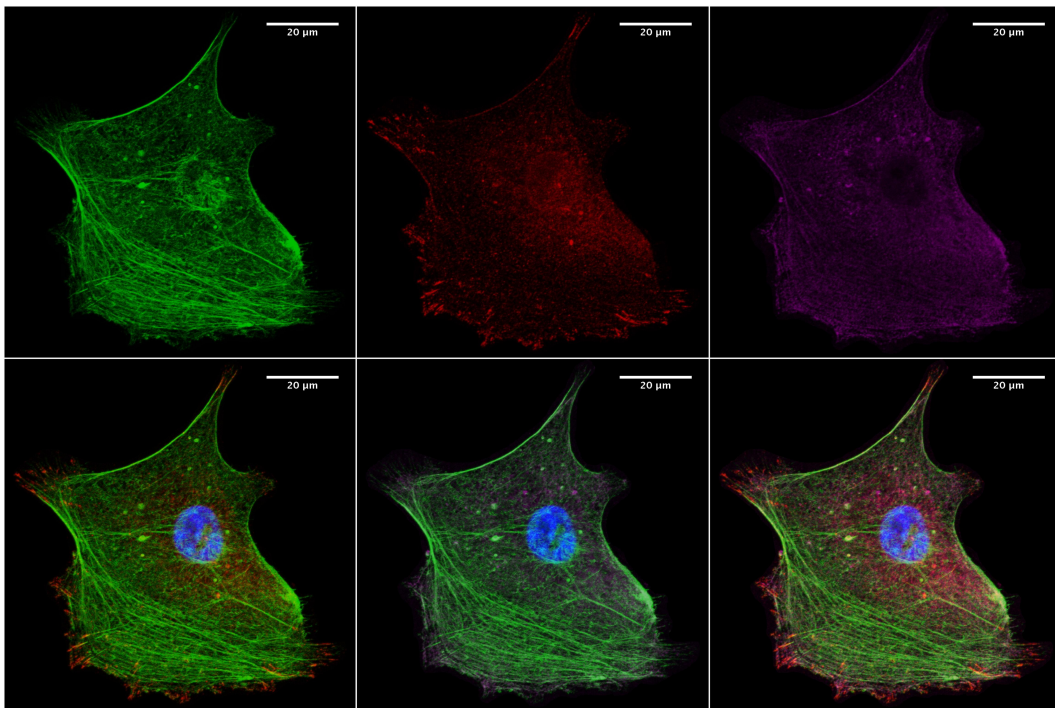


Figure 7.15: Fluorescent images of T24 cell adhering on polyacrylamide gel ( $E = 10$  kPa). Top panels show staining of actin in green (left), paxillin in red (middle) and myosin II in deep purple (right). Bottom panels show combined actin-paxillin-nucleus (left), actin-myosin-nucleus (middle) and actin-paxillin-myosin-nucleus (right). The nucleus is stained in blue.

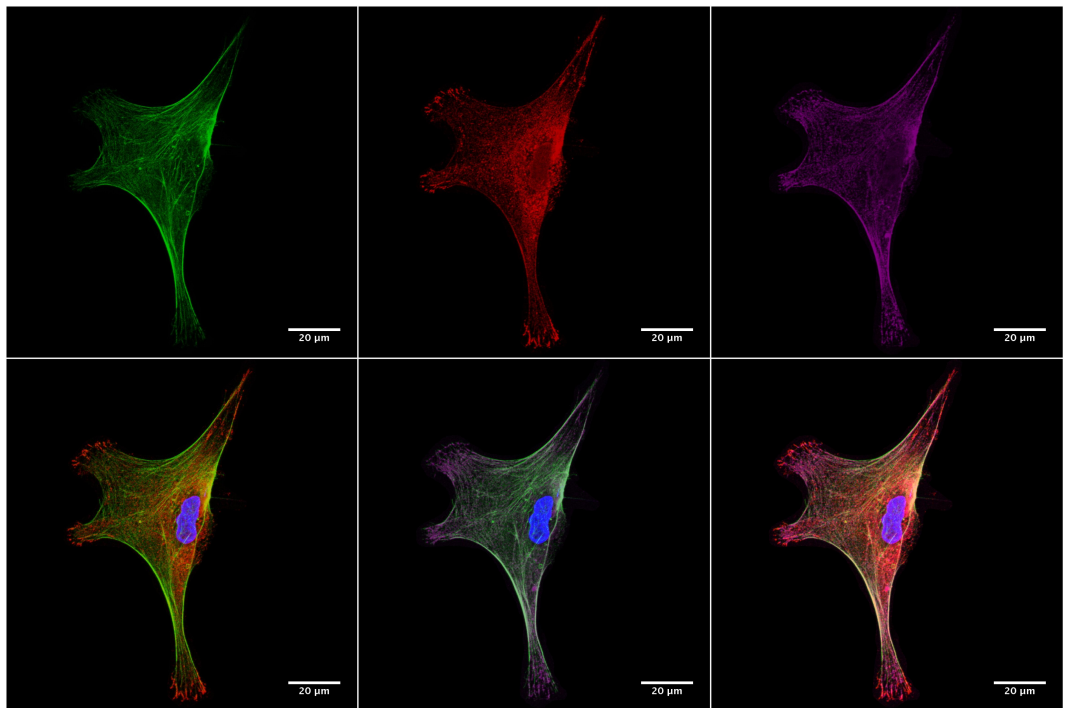


Figure 7.16: Fluorescent images of J82 cell adhering on polyacrylamide gel ( $E = 10$  kPa). Top panels show staining of actin in green (left), paxillin in red (middle) and myosin II in deep purple (right). Bottom panels show combined actin-paxillin-nucleus (left), actin-myosin-nucleus (middle) and actin-paxillin-myosin-nucleus (right). The nucleus is stained in blue.

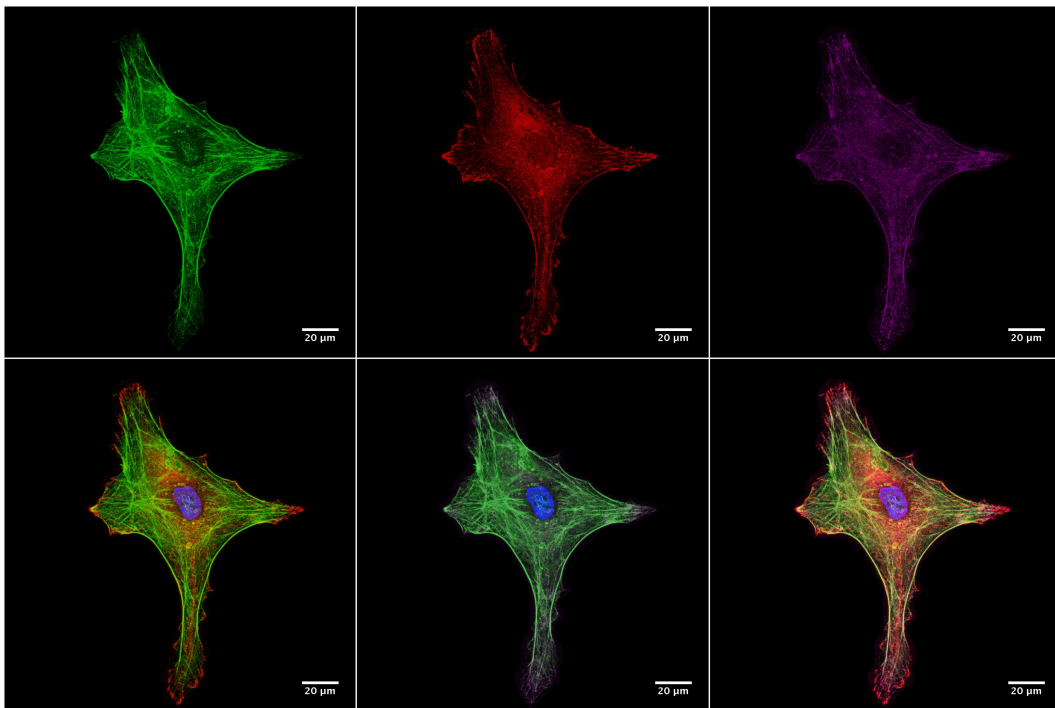


Figure 7.17: Fluorescent images of J82 cell adhering on polyacrylamide gel ( $E = 10$  kPa). Top panels show staining of actin in green (left), paxillin in red (middle) and myosin II in deep purple (right). Bottom panels show combined actin-paxillin-nucleus (left), actin-myosin-nucleus (middle) and actin-paxillin-myosin-nucleus (right). The nucleus is stained in blue.

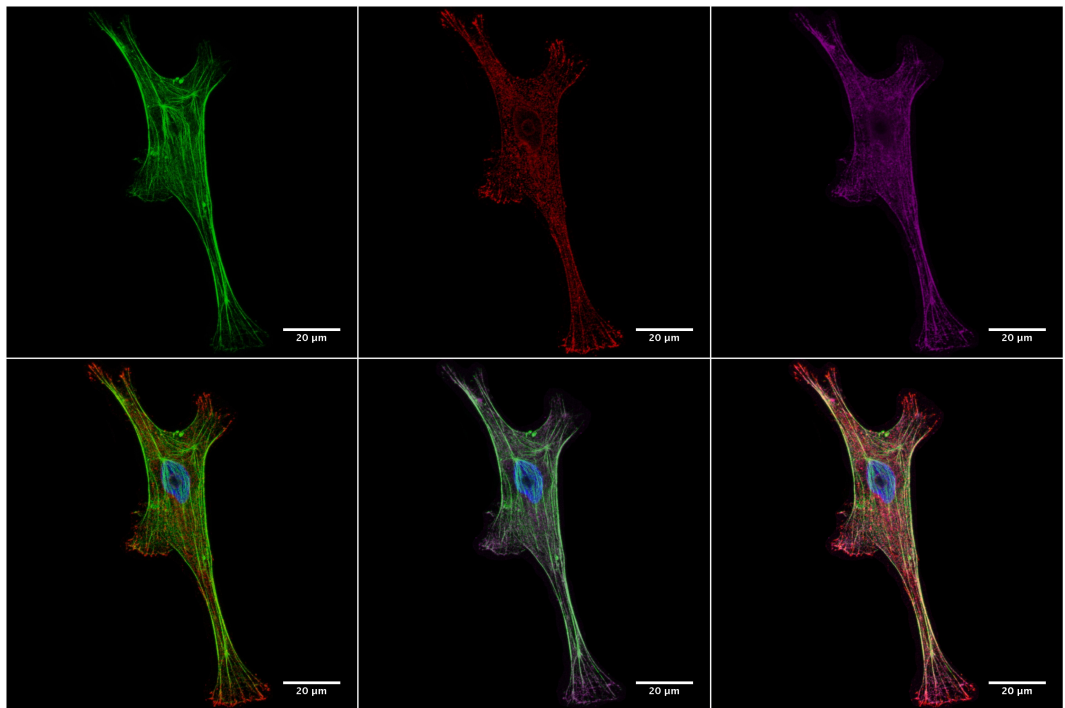


Figure 7.18: Fluorescent images of J82 cell adhering on polyacrylamide gel ( $E = 10$  kPa). Top panels show staining of actin in green (left), paxillin in red (middle) and myosin II in deep purple (right). Bottom panels show combined actin-paxillin-nucleus (left), actin-myosin-nucleus (middle) and actin-paxillin-myosin-nucleus (right). The nucleus is stained in blue.

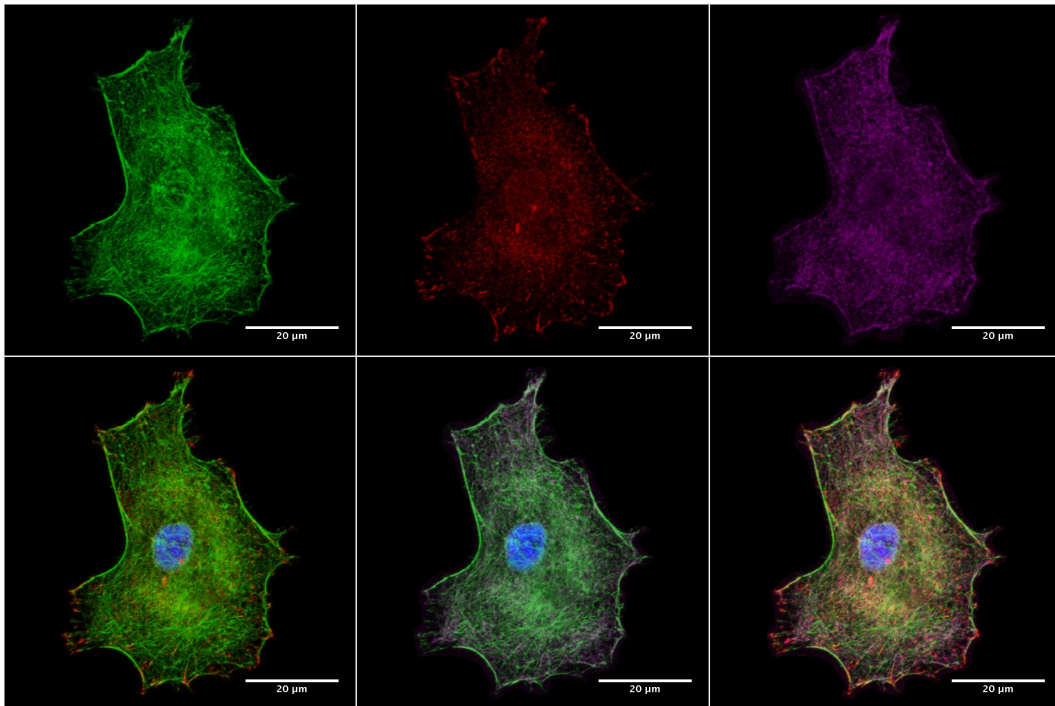


Figure 7.19: Fluorescent images of RT112 cell adhering on polyacrylamide gel ( $E = 10$  kPa). Top panels show staining of actin in green (left), paxillin in red (middle) and myosin II in deep purple (right). Bottom panels show combined actin-paxillin-nucleus (left), actin-myosin-nucleus (middle) and actin-paxillin-myosin-nucleus (right). The nucleus is stained in blue.

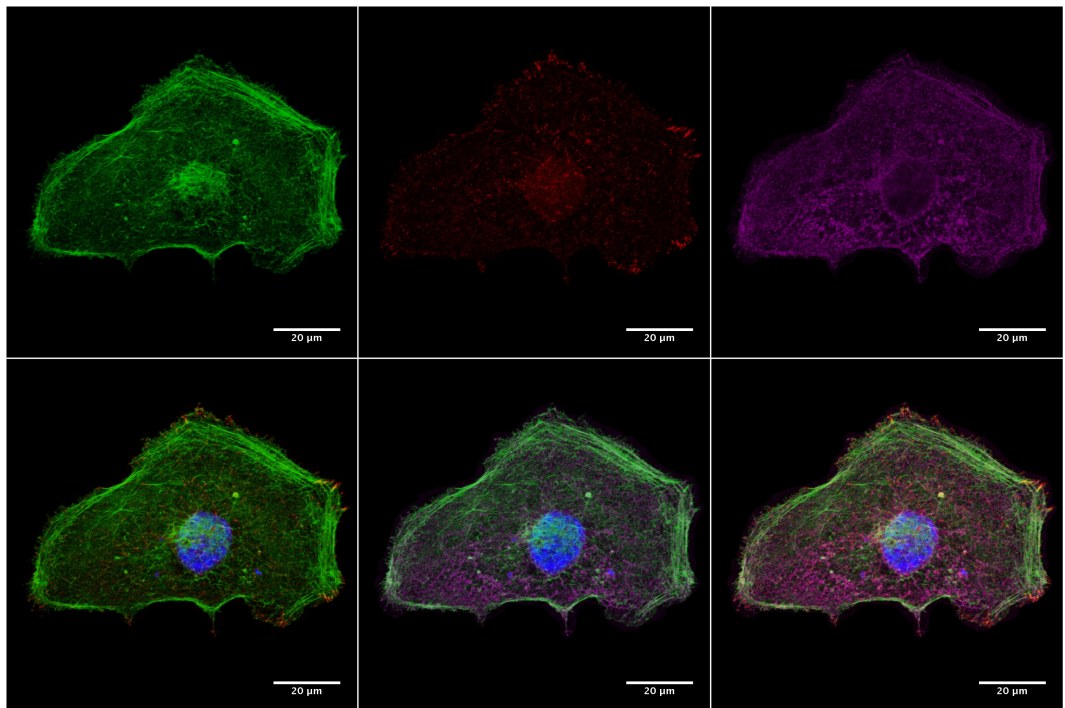


Figure 7.20: Fluorescent images of RT112 cell adhering on polyacrylamide gel ( $E = 10$  kPa). Top panels show staining of actin in green (left), paxillin in red (middle) and myosin II in deep purple (right). Bottom panels show combined actin-paxillin-nucleus (left), actin-myosin-nucleus (middle) and actin-paxillin-myosin-nucleus (right). The nucleus is stained in blue.



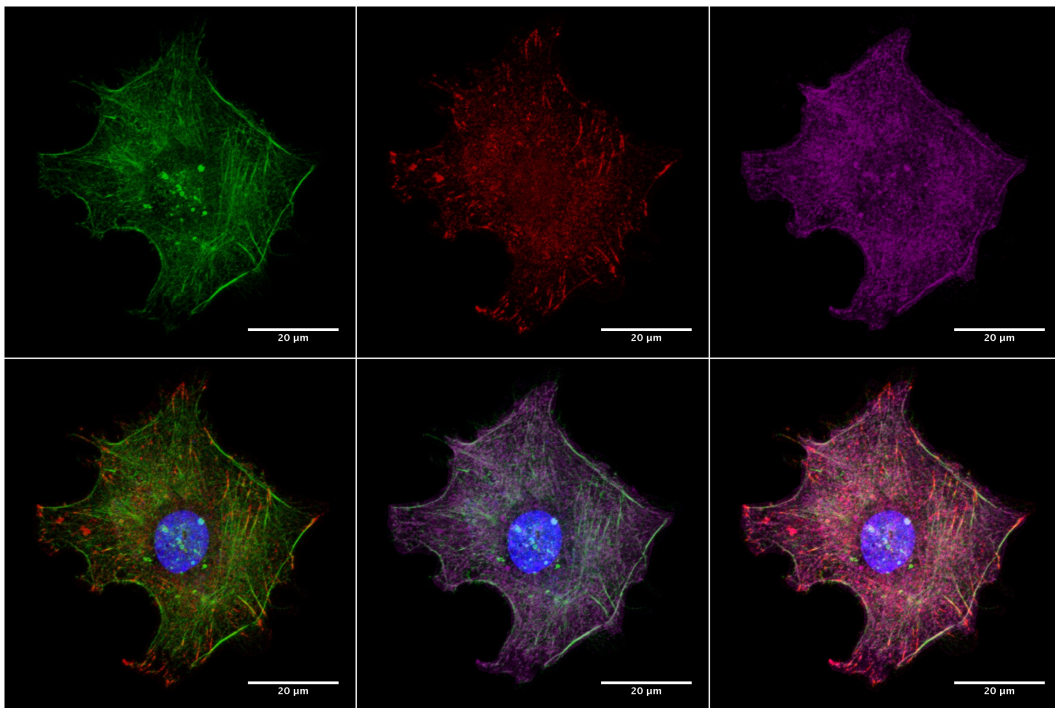


Figure 7.21: Fluorescent images of RT112 cell adhering on polyacrylamide gel ( $E = 10$  kPa). Top panels show staining of actin in green (left), paxillin in red (middle) and myosin II in deep purple (right). Bottom panels show combined actin-paxillin-nucleus (left), actin-myosin-nucleus (middle) and actin-paxillin-myosin-nucleus (right). The nucleus is stained in blue.



Article in *Journal of*  
*Mathematical Biology*

## Traction patterns of tumor cells

D. Ambrosi · A. Duperray ·  
V. Peschetola · C. Verdier

Received: 5 September 2007 / Revised: 15 February 2008  
© Springer-Verlag 2008

**Abstract** The traction exerted by a cell on a planar deformable substrate can be indirectly obtained on the basis of the displacement field of the underlying layer. The usual methodology used to address this inverse problem is based on the exploitation of the Green tensor of the linear elasticity problem in a half space (Boussinesq problem), coupled with a minimization algorithm under force penalization. A possible alternative strategy is to exploit an adjoint equation, obtained on the basis of a suitable minimization requirement. The resulting system of coupled elliptic partial differential equations is applied here to determine the force field per unit surface generated by T24 tumor cells on a polyacrylamide substrate. The shear stress obtained by numerical integration provides quantitative insight of the traction field and is a promising tool to investigate the spatial pattern of force per unit surface generated in cell motion, particularly in the case of such cancer cells.

**Mathematics Subject Classification (2000)** 92C17

---

D. Ambrosi (✉)  
Dipartimento di Matematica, Politecnico di Torino,  
corso Duca degli Abruzzi 24, 10129 Turin, Italy  
e-mail: davide.ambrosi@polito.it

A. Duperray  
INSERM, U823 Grenoble, France

A. Duperray  
Université Joseph Fourier-Grenoble I, Faculté de Médecine,  
Institut d'oncologie/développement Albert Bonniot et Institut Français du Sang,  
UMR-S823 Grenoble, France

V. Peschetola · C. Verdier  
Laboratoire de Spectrométrie Physique, CNRS and Université Grenoble I, UMR 5588,  
140 avenue de la physique, BP 87, 38402 Saint-Martin d'Hères cedex, France

## 0 Introduction

Cell locomotion occurs through complex interactions that involve, among others, actin polymerization, matrix degradation, chemical signaling, adhesion and pulling on substrate and fibers [27]. When focusing on mechanical aspects only, a major issue is the determination of the dynamic action of the cells on the environment during migration: the cells adhere, pull on the surrounding matrix and move forward. As a cell can have more than one hundred focal adhesion sites, it is quite difficult to obtain a pointwise description of the force per unit surface exerted by moving cells on a direct basis. Considerations of this kind suggest that the dynamics of cell locomotion can be fruitfully studied as an *inverse* problem, an idea that dates back to the seminal paper of Harris and coworkers [17]. A thin elastic film is deformed by cell traction into a wrinkled pattern and the size of the crimps is correlated to the shear load. Unfortunately, buckling of thin film is an essentially nonlinear phenomenon and a quantitative reconstruction of the exerted traction field would call for a non-trivial stability analysis in nonlinear elasticity.

A quantitative methodology that obviates such a problem has been proposed in 1996 by Dembo et al. [10], using pre-stressed silicone rubber, an approach further improved by Dembo and Wang in 1999 [9]. They deduce the traction exerted by a fibroblast on a polyacrylamide substrate from the measured displacement of several fluorescent beads merged in the upper layer of the gel. The gel is soft enough to remain in a linear elasticity regime and no wrinkles form.

In a recent paper [2], the same biomechanical issue studied by Dembo and Wang has been addressed using a different mathematical approach, based on the classical functional analysis framework due to Lions [21]. The minimization of the distance between the measured and the computed displacement under penalization of the force magnitude is stated *before* the elasticity equations are solved [28]. Standard derivation of the cost function leads to two sets of elastic-type problems: the direct and the adjoint one. The unknown of the adjoint equation is just the shear stress exerted by the cells we are looking for. The two systems of equations are then solved numerically by a coupled finite element discretization.

In the present work, the adjoint method is applied to determine the traction field exerted by tumoral T24 cells on a polyacrylamide substrate of known mechanical properties. Our aim is to obtain a spatial detail of the tension field on substrates of different stiffness, and to compare the behaviour of the cells in such a varying environment (forces, displacements, migration velocities).

The paper is organized as follows. Methods for measuring traction forces are first presented Sect. 1.1, with emphasis on the classical methodology by Dembo and Wang detailed in Sect. 1.2. Then the adjoint method is summarized in Sect. 2. Materials and methods are detailed in Sect. 3. Section 4 contains the results of the computed shear stress field as exerted by a T24 cell on a flat surface. The last section is devoted to a comparison between the different methods including a discussion about the present results.

## 1 Determination of traction forces

### 1.1 Methods for measuring traction forces

Several methods are available to determine traction forces exerted by cells as they move on rigid substrates. They can be classified as follows:

- *Wrinkles on elastomeric surfaces*

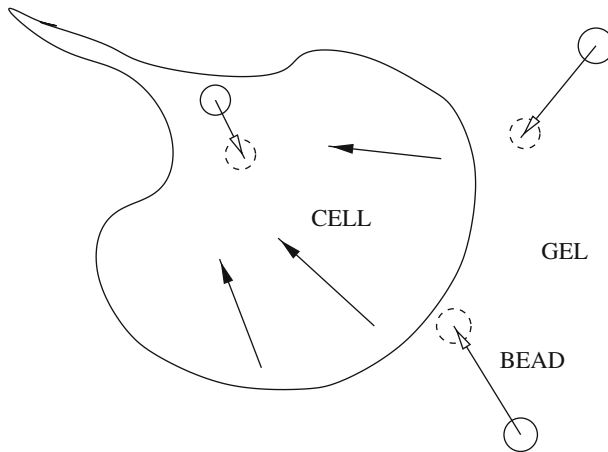
This is the original method proposed earlier by Harris [17] who showed that cells in contact with an elastic medium deform the latter, enabling the formation of wrinkles. The wrinkling patterns come from the large deformations of the substrate undergoing buckling. Previous observations first reported on the possibility to follow cell division using silicone–rubber substrates [5]. The method was further improved when coupled with DIC-microscopy to determine accurate forces as in the case of keratocyte migration [6]. This method is interesting but requires complex integration due to the nonlinearity of the buckling equations.

- *Beads in an elastic matrix*

This is certainly the most popular method as originally proposed by Lee et al. [20] who used silicone substrates to study cell migration after inserting 1- $\mu\text{m}$  beads at the substrate surface. Calibration was achieved by looking at the bead motion while applying known forces with needles (whose deflection was measured). Using this idea, the authors determined the traction forces exerted by keratocytes, which are larger on the sides (around 20 nN), due the special motion of such crawling cells. Using this concept, Dembo and Wang [9] used smaller fluorescent beads (200 nm in size) and determined their positions as compared to the initial one, to obtain displacements. Then they solved the elasticity problem using the method which is presented in more details in the next part. Usually, polyacrylamide gels are used because their mechanical properties can be tuned (generally between 5–30 kPa). Several issues have been addressed by these authors, in particular the “durotaxis” problem [22], i.e. cells move from less rigid surfaces to more rigid ones, this being correlated with larger traction forces (i.e. stronger focal adhesions) on the rigid substrate. Another approach [26] has focused on the levels of forces exerted by endothelial cells over time during spreading, showing levels reaching around 8 kPa after a few hours. This method can give a continuous description of the force field when carried out with the proper integration method.

- *Regular arrays of microneedles: the “fakir carpet”*

A direct way to determine local forces was proposed by Galbraith and Sheetz [16] who developed a microsystem allowing small pillars/needles deflections to give access to local forces exerted by cells at the adhesion sites. The method was further improved by Balaban et al. [3] who measured stresses at focal adhesion sites (around 5 nN/ $\mu\text{m}^2$ ) on different micropatterned surfaces. Finally, Tan et al. [33] engineered arrays of microneedles regularly spaced, which improved the accuracy of the method without further calculations. Using this tool, they showed that cell morphology controls the levels of forces exerted. Furthermore, it seems that cells adapt their forces [29] according to the substrate’s rigidity in a linear manner. Finally the use of similar microneedles arranged in an anisotropic fashion proved



**Fig. 1** The experiment by Dembo and Wang. The cell exerts a traction (*filled-head arrows*) on the gel. The beads, embedded in the substrate, move from the former position (*continuous-line circle*) to the new one (*dashed circles*). The difference in these positions gives the displacement of the gel (*empty-head arrows*)

that epithelial growth can be controlled by anisotropic rigidity [30]. Although this method is quite promising and has a good resolution, it can only give a discrete map of traction forces, as opposed to the classical method of Dembo and Wang [9] which, in principle, provides the value of traction forces at any point.

## 1.2 The method of Dembo and Wang (1999) and recent improvements

### 1.2.1 Description

We assume that the polyacrylamide substrate (on which cells are deposited) is elastic when observed at a time scale of the order of minutes to hours; this means that such a material may actually be viscoelastic, but relaxation times are much larger than the observation time. Under assumptions of isotropy (no preferential directions) and homogeneity (no explicit dependence on space), the deformations are supposed to be small: in a quantitative sense, this means that (Fig. 1)

$$\text{trace} \left( (\nabla \mathbf{u})^T \nabla \mathbf{u} \right) \ll 1, \quad (1.1)$$

where  $\mathbf{u}(x, y, z) = (u, v, w)$  is the displacement field. Neglecting body forces and inertia, the balance equations for the substrate read

$$-\nabla \cdot \mathbf{T} = 0, \quad (1.2)$$

where

$$\mathbf{T} = \mu(\nabla \mathbf{u} + (\nabla \mathbf{u})^T) + \lambda \nabla \cdot \nabla \mathbf{u}, \quad (1.3)$$

is the Cauchy stress tensor and  $\mu, \lambda$  are the Lamé coefficients [15]. The following boundary conditions apply:

$$\begin{aligned} \mathbf{T}\mathbf{n} &= \mathbf{f}(x, y), \quad z = 0, \\ \mathbf{u} &\rightarrow 0, \quad z \rightarrow -\infty. \end{aligned} \quad (1.4)$$

where  $\mathbf{n}$  is the vector pointing in the  $z$  direction (vertical) and  $\mathbf{f}$  is the traction exerted by the cell at the surface. If the displacement of the substrate is known at some points on the surface, say  $\mathbf{u}_0$  its value, it is quite obvious that we cannot plug this directly into (1.2) to obtain  $\mathbf{f}$ . The motivations are twofold: since  $\mathbf{u}$  is constrained to equal  $\mathbf{u}_0$  in some portions of the domain only, there are many  $\mathbf{f}$  that can produce this known displacement. Secondly, inverse problems are well known to excite high frequency components of the (always present) experimental error and a regularization procedure is therefore needed [32].

Simple dimensional arguments can show that the substrate displacement is non-negligible within heights of a few microns [32]. Since substrates are typically  $100 \mu\text{m}$  in height, the approximation of infinitely deep half space applies and a relatively simple Green function provides the solution of the elasticity problem. For thinner and finite substrates, there is a much more intricate Green formulation [23]. The solution of the problem (1.2–1.4) can then be rewritten in integral form using the Green tensor  $\mathbf{G}$  of the elasticity equation for the half space domain [19]:

$$\mathbf{u}(\mathbf{x}) = \int \mathbf{G}(\mathbf{x} - \mathbf{x}')\mathbf{f}(\mathbf{x}')d\mathbf{x}', \quad (1.5)$$

where the integration domain is the support of  $\mathbf{f}$ , that is the area covered by the cell. If any information about the focal adhesion points is available, they can be used at this stage. In practice, for every non-trivial  $\mathbf{f}$  the integral (1.5) has to be evaluated numerically. Three assumptions are now commonly adopted before solving the problem numerically:

1. The substrate material is incompressible.
2. The cell exerts shear stress only, so that  $\mathbf{f} = (f_x, f_y, 0)$ .
3. The measured displacement  $\mathbf{u}_0$  corresponds to beads located at the very surface of the matrigel. From a practical point of view, the focus length of the experimental pictures must be much smaller than the characteristic vertical length of decay of the tensional field. As the latter is of the order of few microns, both beads radius and focus length should be order of a micron at most.

If Assumptions 1 and 2 apply, the vertical component of the displacement at the surface is identically zero and the Green tensor takes the following simplified form [32]

$$G_{ij} = \frac{3}{4\pi E r} \left( \delta_{ij} + \frac{x_i x_j}{r^2} \right), \quad (1.6)$$



where  $x_1 = x$ ,  $x_2 = y$ ,  $r^2 = x^2 + y^2$ . In terms of the Lamé coefficients, the Young modulus  $E$  is defined by

$$E = \frac{\mu(3\lambda + 2\mu)}{\lambda + \mu}. \quad (1.7)$$

The Green tensor allows one to calculate the surface displacement by the following simplified version of the convolution (1.5)

$$u_i(x, y) = \int G_{ij}(x - x', y - y') f_j(x', y') dx' dy' \quad (1.8)$$

Formula (1.8) provides the horizontal displacement at  $z = 0$  given a pure shear stress  $f_i$ . If the beads are sufficiently small and shallow, Assumption 3 applies and the computed displacement field  $u_j$  can be compared with the measured one.

The target of this methodology is to find the force per unit surface  $f_i$  generating a displacement very near to the experimental one in a suitable sense. The usual approach is to minimize the quadratic mean error under force penalization [9, 32] to ensure regularization. The basic idea of the Tikhonov regularization method is also used in the next section in a different framework; therefore no details are provided herein and the reader is referred to the cited literature for details. In this context we just remark that the error minimization procedure is decoupled from the mechanical one and applies to the discrete problem obtained covering the cell area by polygons (triangles or quadrilaterals) where the numerical integration (1.8) is carried out.

### 1.2.2 Improvements

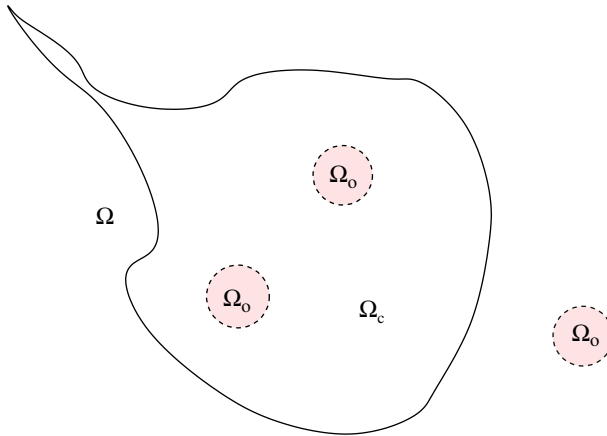
The Fourier Transform Traction Cytometry (FTTC) method used by Butler and co-workers [7] is based on the observation that Eq. (1.8) can be conveniently solved in the Fourier components space, taking advantage of the properties of the convolution product. A simple linear relationship between the displacements and the forces in the Fourier space is obtained. The method has been used successfully to compute the motion of smooth muscle cells on elastic substrates [7].

Recently, the use of thinner substrates [23] has been proposed and it seems to give rise to accurate results, due to improved spatial resolution. This has been made possible thanks to the use of the Green function for finite thickness elastic layer.

Finally, a recent paper [31] came to our attention recently where the authors compared the efficiency and accuracy of the methods above (Boundary Element Method, BEM [9]; Fourier Traction Force Cytometry, FTTC [7], and Traction Reconstruction with Point Forces [32]). It was shown that the first two methods can be improved to reach spatial resolutions of 1  $\mu\text{m}$ , and combined with the third one can lead to new advances in cell mechanics understanding.

## 2 Force balance and adjoint equation

In this section we briefly describe an alternative approach to obtain the pattern of the shear stress exerted by the cell: the adjoint method [2]. If  $\Omega$  is the half space, the



**Fig. 2** The domain  $\Omega$  of the elasticity equation contains the subdomain  $\Omega_c$ , the area covered by the cell, where the force applies: in the figure it is enclosed by the *continuous bold line*. The *dashed circles* are centered at the beads location and their collection represents the  $\Omega_0$  subdomain where the displacement is known

displacement vector field  $\mathbf{u}(\mathbf{x})$  is known in a subset of the domain of the elasticity equation  $\Omega_0 \subset \Omega$ , where beads are located. The target function  $\mathbf{u}_0(\mathbf{x})$  has support in  $\Omega_0$ . In this problem the shear stress is exerted just on the portion of the domain where the cell lies; let us call this subdomain  $\Omega_c \subset \Omega$  (see Fig. 2). The cell actually adheres to the substrate just in specific small regions called focal adhesion sites, which can be experimentally localized [1] using fluorescence for instance. No reason prevents restricting the force support to these areas and, as a matter of fact, this information is included in refinements of the algorithm of Dembo and Wang [31]. This assumption is not applied here just because the information is missing from the experiments.

Here the three-dimensional elasticity system of equations is approximated by a two-dimensional plane-stress one by vertical averaging along an *effective thickness*  $h$ :

$$-\hat{\mu} \Delta \mathbf{u} - (\hat{\mu} + \hat{\lambda}) \nabla (\nabla \cdot \mathbf{u}) = \mathbf{f}, \quad \mathbf{u}|_{\partial\Omega} = 0, \quad (2.1)$$

where

$$\hat{\mu} = h \frac{E}{2(1+\nu)}, \quad \hat{\lambda} = h \frac{E\nu}{1-\nu^2}.$$

and  $E$  and  $\nu$  are the Young modulus and the Poisson ratio, respectively.  $h$  is the averaging depth fixed by the depth of field of the microscope. In our case  $h$  is  $1.5 \mu\text{m}$ ; the beads lying below such vertical coordinate are not in focus and therefore their position is not measured. Consequently the displacement  $\mathbf{u}$  should be understood as the average displacement along  $h$ , which is nearly the displacement of the center of the beads.

The functional  $J(\mathbf{f})$  measures the difference between the displacement field produced by  $\mathbf{f}$  and the experimental one  $\mathbf{u}_0$  under penalization of the square norm of the

force field itself. It is defined as follows:

$$J(\mathbf{f}) = \int_{\Omega_0} |\mathbf{u} - \mathbf{u}_0|^2 dV + \varepsilon \int_{\Omega} |\mathbf{f}|^2 dV, \quad (2.2)$$

where  $\varepsilon$  is a real positive number. We look for  $\mathbf{g}$  minimizing  $J$ :

$$J(\mathbf{g}) \leq J(\mathbf{f}), \quad \forall \mathbf{f} \in V_c, \quad (2.3)$$

where  $V_c \subset L^2(\Omega)$  is the space of the finite energy functions with support in  $\Omega_c$ . The minimization of  $J$  accomplishes the minimization of the distance of the solution from the measured value  $\mathbf{u}_0$  under penalization of the magnitude of the associated force per unit surface  $\mathbf{f}$ . The penalty parameter  $\varepsilon$  balances the two requirements.

Variational derivation of  $J(\mathbf{f})$  and introduction of the adjoint differential equation yields the following direct and inverse systems of partial differential equations [2]

$$\begin{aligned} -\hat{\mu} \Delta \mathbf{u} - (\hat{\mu} + \hat{\lambda}) \nabla (\nabla \cdot \mathbf{u}) &= -\frac{\chi_c}{\varepsilon} \mathbf{p}, \quad \mathbf{u}|_{\partial\Omega} = 0, \\ -\hat{\mu} \Delta \mathbf{p} - (\hat{\mu} + \hat{\lambda}) \nabla (\nabla \cdot \mathbf{p}) &= \chi_0 \mathbf{u} - \mathbf{u}_0, \quad \mathbf{p}|_{\partial\Omega} = 0. \end{aligned} \quad (2.4)$$

The value of the penalty parameter  $\varepsilon$  and the averaging depth  $h$  can be fixed on the basis of arguments suggested by modal analysis. In the special case  $\Omega_0 = \Omega_c = \Omega$  under periodic boundary conditions, modal analysis applies and the system of equations (2.4) rewrites just like a Tikhonov filter. The amplitude of the Fourier components of the solution  $u_k$ ,  $p_k$  satisfies the algebraic relation

$$\begin{aligned} hEk^2 u_k &\simeq -\frac{1}{\varepsilon} p_k, \\ hEk^2 p_k &\simeq u_k - u_{0,k}, \end{aligned} \quad (2.5)$$

that is

$$u_k \simeq \frac{u_{0,k}}{1 + \varepsilon h^2 E^2 k^4}, \quad (2.6)$$

where  $u_{0,k}$  represents the amplitude of the  $k$ th Fourier component of  $u_0$ . According to Eq. (2.6), if the data are known all over the domain the system of equations (2.4) is nothing but a filter damping the modes corresponding to wavenumbers  $\gtrsim \varepsilon^{-1/4} h^{-1/2} E^{-1/2}$ . The choice of  $\varepsilon$  can be interpreted in terms of filtering modes falling below the experimental accuracy. A closer inspection of Eq. (2.6) reveals that the key parameter of the inversion procedure is actually  $h^2 \varepsilon$  and the solution does not change for combinations of the averaging layer  $h$  and penalty parameter  $\varepsilon$  that preserve this quantity.

The choice of the penalty parameter (also called *regularization parameter* in discrete inverse problems) is a delicate subject and it has been extensively discussed in the relevant literature. Basically it should be chosen to damp components whose wavenumber has no physical meaning because they are below the experimental resolution. It is evident that no inversion technique can account for variations of the

shear stress at a spatial scale smaller than the minimum distance between two beads and, even though the beads are quite dense, the determination of the position of their centers is subject to a noise. Several possible strategies can be addressed to find out the optimal value of  $\epsilon$  in a suitable way; the interested reader can refer to the very detailed paper by Schwarz et al. [32]. In this work we simply take the minimum value of  $\epsilon$  that does not yield erratic results in the displacement (the L-curve criterion).

### 3 Materials and methods

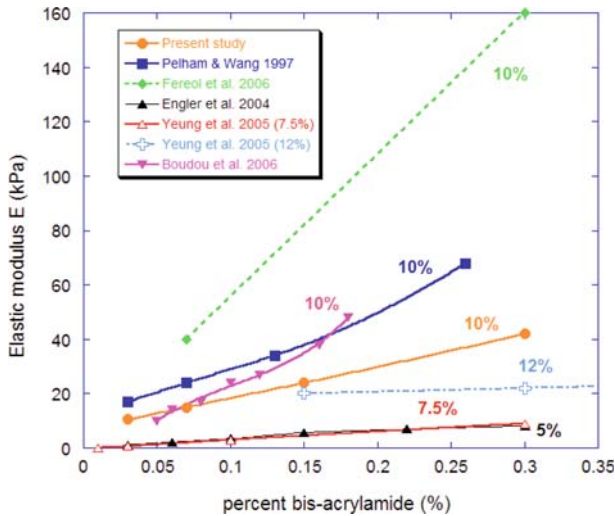
In this paper the mathematical methodology illustrated above is applied to determine the stress field exerted by T24 tumor cells on a flat deformable substrate. The experimental procedures that have been used are based on the work by Dembo and Wang [9] and are given below.

- Gels of different stiffness have been prepared by tuning the ratio between polyacrylamide and bis-acrylamide components. Three different gels have been used containing  $x\%$  of polyacrylamide ( $x$  taking the values 5–7.5–10 going from the softer to the harder gel) and the bis-acrylamide percentage is 0.03%. Their mechanical properties have been measured by conventional dynamic rheometry tests (Malvern rheometer, Gemini 150). Sinusoidal oscillations with a known deformation  $\gamma = \gamma_0 \sin(\omega t)$  are applied within the linear regime (small enough deformation  $\gamma_0 \sim 0.01$ ) at different angular frequencies  $\omega$ . The stress response  $\sigma = \sigma_0 \sin(\omega t + \phi)$  (where  $\sigma_0$  is a constant stress and  $\phi$  is the phase angle) is measured and the elastic ( $G'$ ) and viscous moduli ( $G''$ ) are deduced.

Experiments show a constant  $G'$  (elastic modulus) when the frequency  $\omega$  ranges from 0.1 to 10 Hz. The loss modulus  $G''$  is usually lower by two orders of magnitude (data not shown). We deduce the value of the elastic modulus  $E = 3G'$  and find 1.95, 6.3 and 9.9 kPa for the soft, medium and hard gels, respectively. Note that the hypothesis that  $E = 3G'$  is relevant here in view of a recent work [4] showing that  $\nu \sim 0.48$  in such polyacrylamide gels. This means that our hypothesis of incompressible material (i.e.  $\nu = 0.5$ ) is quite good, and is not responsible for the differences found as compared to other methods. Such comparisons are shown in Fig. 3 where our results are found to be close to the ones obtained by Pelham and Wang [25] or Boudou et al. [4]. Since our method relies on no further hypotheses and is based on the use of large samples, we have good confidence in our data. Other techniques which can be used are traction tests [13, 25], micropipette experiments [4], AFM [13, 14], or rheometry [35].

Gels were prepared on a silanated square coverglass 22 mm  $\times$  22 mm and covered with a circular coverglass (35 mm diameter) functionalized with NaOH (0.1 M), APTMS (10 min), and 0.5% glutaraldehyde (30 min).

- Fluorescent beads (Molecular Probes) of 0.2  $\mu\text{m}$  of radius were seeded as the gels were prepared. After addition of the cross-linker, beads were added, the gels were set onto the square coverglass, and the circular coverglass was brought carefully to capture the gel and the square coverglass. This avoided to flip the preparation. Indeed beads need to sediment fast so that there will come close to the gel upper surface.

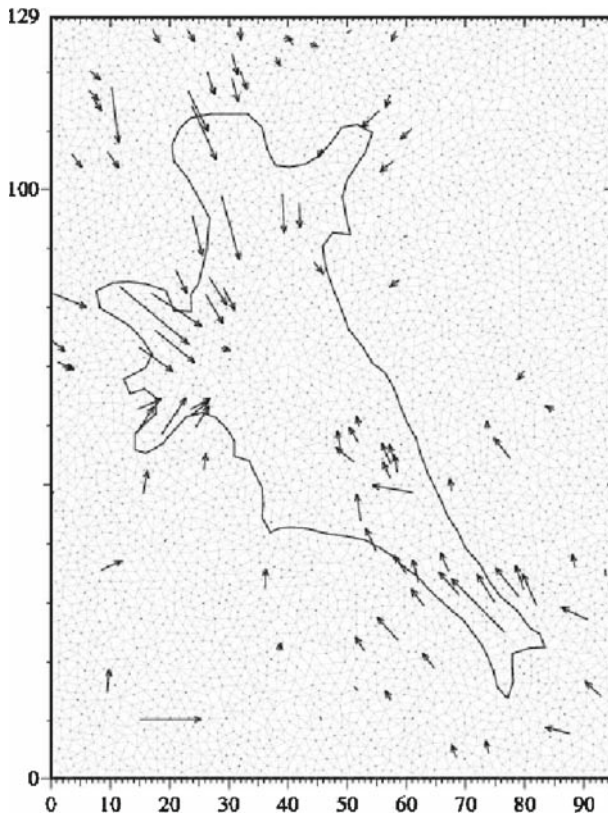


**Fig. 3** Elastic moduli  $E$  (kPa) as a function of the bis-acrylamide percent. Values from other authors are also reported [14,4,25,35,13] for the case of 10% polyacrylamide concentration and a few other concentrations

- After the gel was polymerized (nearly 30 min), the square coverglass was removed and sulfo-Sanpah 1 mM was added to functionalize the gel (15 min under UV). This was achieved twice, and the surface was rinsed with PBS. Finally a 20  $\mu\text{g}/\text{ml}$  fibronectin solution was used overnight to bind the above surface.
- Cancer cells of epithelial bladder type (T24) were then seeded. They adhered usually rapidly and spread. This cell line is known to be of an average invasive type.
- The coverglass was attached at the bottom of a 35 mm-culture dish (containing culture medium) in order to carry out microscopic observations. Two types of images were made: a phase contrast one to observe the cell and its contour, and a fluorescent one focused on the beads (at a slightly different  $z$ -position). The depth of field of the images was 1.5  $\mu\text{m}$ . Everything was carried out automatically in order to take one set of images at regular time steps (e.g. 10 min).
- Images were then collected and treated using the ImageJ software [18], to determine trajectories and/or displacements with respect to the initial position. The initial beads position was determined at the end of the experiment by adding distilled water to detach the cells.

#### 4 Numerical results

Equations (2.4) have been discretized by a finite element method using linear basis functions on an unstructured mesh. The two resulting linear systems were solved numerically using a global conjugate gradient method, thus avoiding any iterative coupling [28]. The computational domain was a square box with side of about 100  $\mu\text{m}$ . The Young moduli of the substrates are 9.9, 6.3, 1.95 kPa, as detailed in the previous section.



**Fig. 4** Graphical representation of the numerical setup: the computational mesh, made of *triangles*, is represented in *light grey*. The mesh satisfies two constraints: it has a node at every point where displacement is known (the *arrows* have been measured and a sequence of element sides coincides with the boundary of the cell. The reference vector at the *bottom left corner* is  $0.5 \mu\text{m}$  long

In Fig. 4 an example of the numerical setup is shown: in a part of the domain, the cell contour, the displacement of the beads and the computational mesh are plotted. The cell contour represents the boundary between internal and external elements. Note that some nodes of the mesh correspond to the original beads location while others do not: they have been created for the sake of regularity of the computational grid. The present approach ensures a full flexibility in this respect. According to the notations introduced in the previous sections, the cell contour defines  $\Omega_c$  while the collection of the elements that have at least one node with measured displacement defines  $\Omega_0$ .

The computed displacement  $\mathbf{u}$  is in general different from  $\mathbf{u}_0$ , the difference increasing for larger  $\varepsilon$ . The root mean difference between the calculated and the measured solution for the specific case of Fig. 4 is

$$\frac{1}{n} \sqrt{\sum_{i=1}^n (\mathbf{u}_i - \mathbf{u}_{0,i})^2} = 5.3 \times 10^{-3} \mu\text{m} \quad (4.7)$$

where the sum runs over all the nodes where  $\mathbf{u}_0$  is known. The mean quadratic error has this order of magnitude for all the computations to be shown below.

In Figs. 5, 6 and 7 cell pictures are shown together with the numerical results corresponding to gels showing decreasing stiffnesses. The first image is (a) the phase-contrast image of the cell; note that in this representation the beads are not visible: as they fluoresce they are recorded with the fluorescent microscopy technique. Beads displacements are shown in (b) after particle tracking is performed thanks to the ImageJ software. The shear stress is shown in terms of vectors (c) or color map showing the magnitude (d).

The experimental and numerical results show some features that are well known in the relevant literature and here read as a confirmation of the validity of the procedures. Cells are more convex and more active when adhering to a soft substrate, whereas they are more elongated and develop larger forces on a stiff substrate. Second, the force per unit surface generated by tumor cells ( $\sim 100 \text{ pN}/\mu\text{m}^2$ ) is weaker than the one typically exerted by fibroblasts, which is of the order of thousands of picoNewton per micron squares, and have been originally used in the literature to apply this kind of methodology [9, 22].

The migration of T24-cells on the most rigid substrate, as an example of random migration for such invasive cells, is shown in Fig. 8. The T24-cell is first adhering in the lower right part. Then it begins to move in a random manner until it elongates a bit then it starts to move its upper right part to each side to see whether it can bind efficiently. This is achieved after roughly 16 min, when new adhesions are formed in the upper left part. This can be seen by the larger forces in red in Fig. 8d, e. At the same time, the high forces produced break the lower right adhesion site (in red also) as seen in Fig. 8e, f. This large adhesion site is removed and the cell contracts its rear part to join the rest of the cell (upper right).

## 5 Discussion

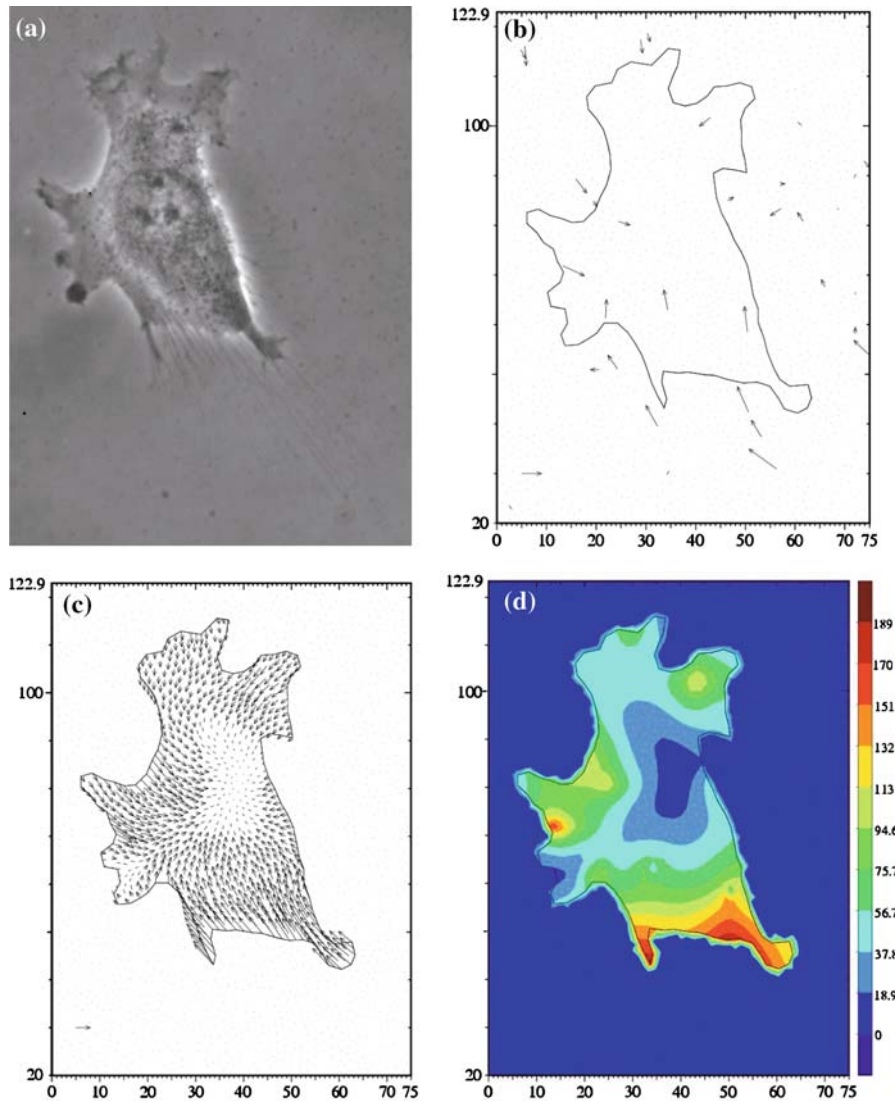
### 5.1 Modelling aspects

In this paper an adjoint-based method has been applied for solving the inverse problem to obtain the shear stress exerted by T24 tumor cells on an elastic substrate. The novelty of the paper is the application of a recent methodology (alternative to Dembo and Wang) to determine the stress exerted by a particular cell line (T24 tumor cells) not yet investigated.

A few comments can be drawn on a theoretical basis. The classical method of Dembo and Wang is based on the knowledge of the exact solution of the elasticity equation in a half plane under linearity assumptions, and for an isotropic and homogeneous medium. By numerical quadrature such an exact solution is part of a discrete minimization algorithm that provides the shear stress under regularization based on the Tikhonov method.

Conversely, the adjoint method does not exploit the knowledge of an exact solution and does not decouple the direct and inverse problems: variational arguments yield two coupled sets of partial differential equations to be solved by a suitable numerical method (Finite Elements, for instance).

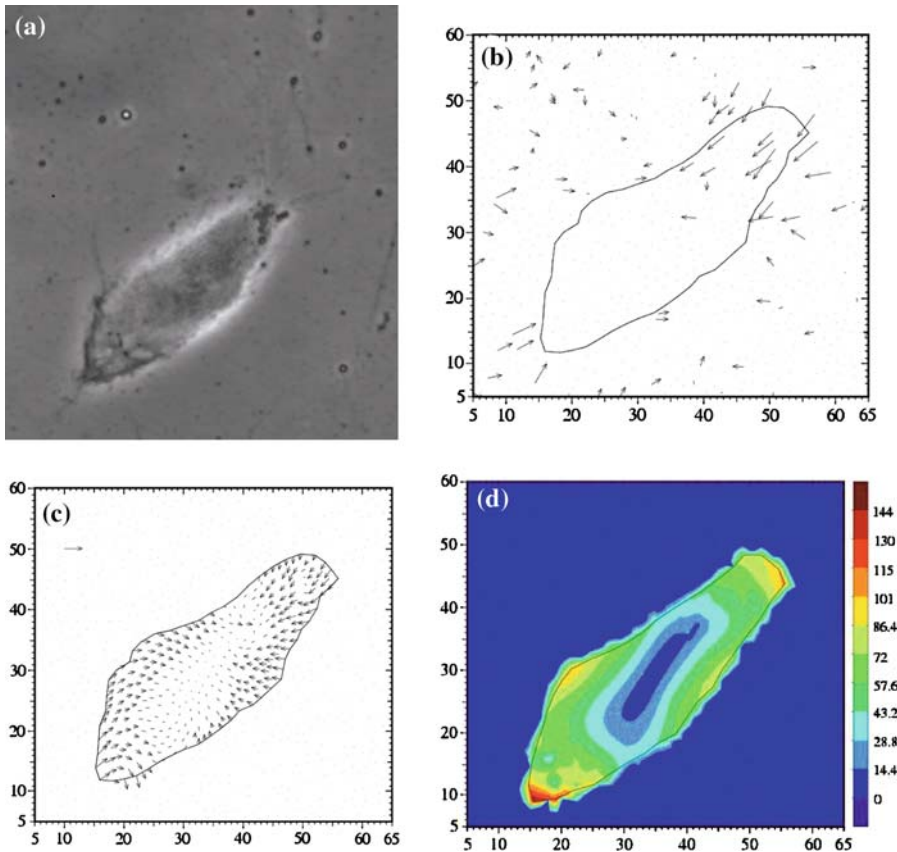




**Fig. 5** T24 cell adhering on a stiff polyacrylamide substrate ( $E = 9.9$  kPa). The cell is quite flattened on the surface and exhibits a spiky contour (a). Some displacement vectors below and around the cell are known (b). The axis scale is in microns. The shear stress is shown in terms of vectors (c) or color map of the magnitude (d). The traction force has maximum magnitude corresponding to about  $200 \text{ pN}/\mu\text{m}^2$ . Note that on this substrate the cell produces filopodia which appear on the edges and attach the gel out of the cell contour. Filopodia seem to have a minor dynamical effect being essentially aimed at addressing the direction of the motion and their role is not taken into account in the present model. Reference vectors for displacement and stress stand for  $0.5 \mu\text{m}$  and  $100 \text{ pN}/\mu\text{m}^2$ , respectively

The computational cost of the two methods can be estimated for a shear force  $\mathbf{f}$  to be calculated at  $N$  points. The method by Dembo and Wang requires  $N$  sums to compute the integral (1.8) for all the  $N$  nodes, while the solution of the linear system

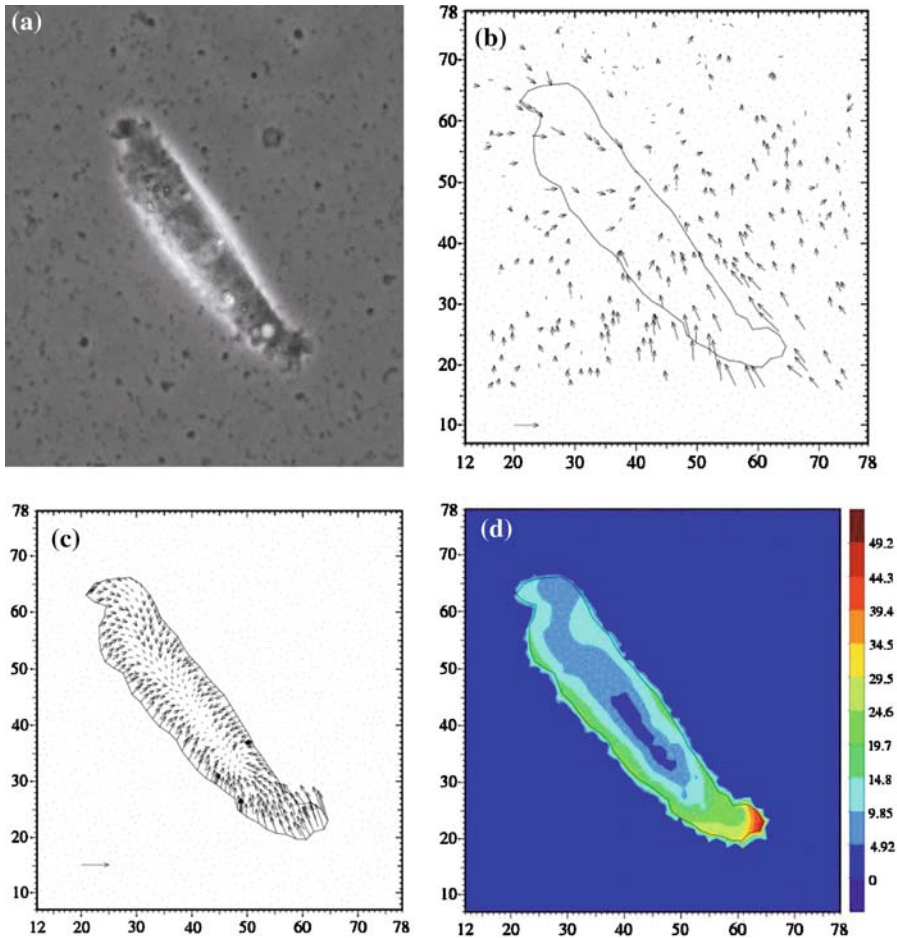




**Fig. 6** T24 cell adhering on a medium stiffness polyacrylamide substrate ( $E = 6.3$  kPa). The cell is more rounded than in the rigid case (a) while the displacement field appears to be of the same order of magnitude (b). The axis scale is in microns. The shear stress is shown in terms of vectors (c) or color map of the magnitude (d). The traction force has maximum magnitude corresponding to about  $140 \text{ pN}/\mu\text{m}^2$ . Note that in this case few beads are detected in focus under the cell and consequently the stress field is less reliable. Reference vectors for displacement and stress stand for  $0.5 \mu\text{m}$  and  $100 \text{ pN}/\mu\text{m}^2$ , respectively

arising from the finite element discretization is usually solved by an iterative linear solver that typically involves order  $N$  operations. Therefore the computational cost of the adjoint method scales like  $N$ , while the usual one scales like  $N^2$ . This difference is essentially due to the local nature of the finite element basis, leading to a sparse stiffness matrix. Conversely, the quadrature (1.8) is an (explicit) sum spanning the whole computational domain. This drawback has been addressed by Sabass et al. [31] who proposed a splitting of the elastic field into spatial ranges that require a different numerical accuracy.

The adjoint method is approximate because it does not use an exact solution of the elasticity equation, but a vertically averaged system of equations between 0 and  $-h$ . However, the non-dimensional number characterizing the differential equations involves this somehow arbitrary vertical height through a combination of  $h$  and  $\epsilon$ ,

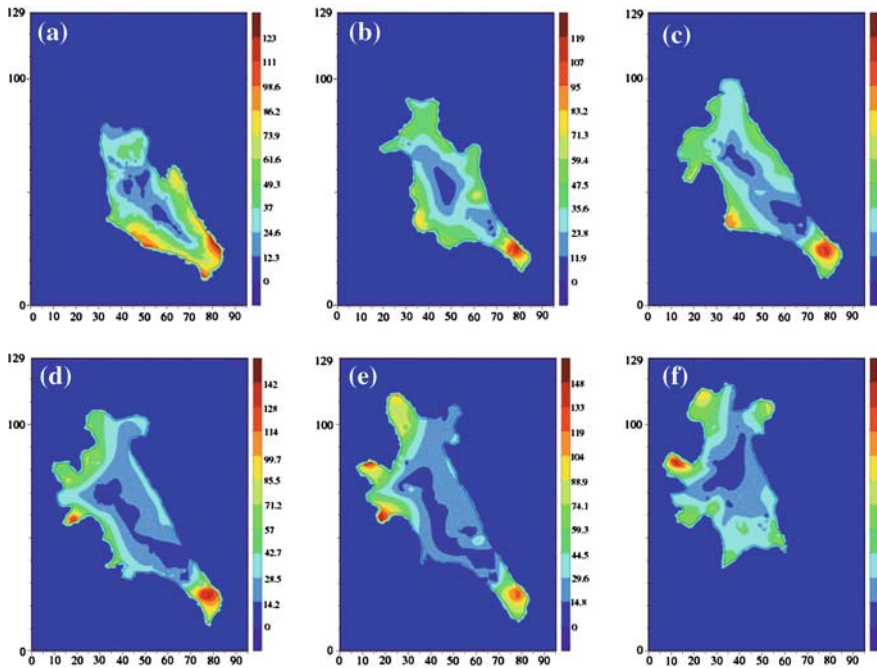


**Fig. 7** T24 cell adhering on a very soft polyacrylamide substrate ( $E = 1.95$  kPa). The cell is more convex than in the rigid case (a) while the displacement field appears to be of the same magnitude (b). The axis scale is in microns. The shear stress is shown in terms of vectors (c) or color map of the magnitude (d). The traction force has maximum magnitude corresponding to nearly  $50 \text{ pN}/\mu\text{m}^2$ . Reference vectors for displacement and stress stand for  $0.5 \mu\text{m}$  and  $100 \text{ pN}/\mu\text{m}^2$ , respectively

which is an actual parameter to be fixed by the regularization method. Both methods require numerical integration. A specific character of the adjoint method is that it automatically satisfies the force equilibrium condition: integrating equation (2.4) over a domain containing  $\Omega$ , making use of the divergence theorem, then one immediately finds that the average force  $\mathbf{f}$  is zero, as expected for a system in equilibrium.

## 5.2 Experimental results

In order to compare our results with previously published works, we first looked at the results by Dembo and Wang [9] and compared them with Lo et al. [22] where migrating



**Fig. 8** Motion of a T24 cell on a rigid gel ( $E = 9.9$  kPa),  $t = 0, 8, 16, 24, 32, 40$  min. The cell first adheres strongly (*red region*) at its *lower right part* (a), then starts to move upward left by random migration (b–d) until it eventually forms new adhesion sites at the *upper left sites* (d, e). At this precise time, it is able to contract and detach its rear by first decreasing forces while elongating (e), then achieving detachment to bring the rest of the body to the *upper left part* (f). Note that the colour scale is reset to range between minimum and maximum in each frame

3T3 fibroblasts on collagen-coated gels are studied. For the 6 kPa polyacrylamide gel, maximum traction forces on the edges are about 7 kPa [9]. In the second paper [22], respective values of 6 and 11 kPa are found for the forces exerted on gels of rigidity 14 and 30 kPa, respectively, and velocities are roughly 0.4 and 0.2  $\mu\text{m}/\text{min}$ . This means that lower values are found. Finally, in the recent work of Sabass et al. [31], mouse embryo fibroblasts are shown to develop maximum traction forces of 2 on a 10 kPa polyacrylamide substrate. These values are more or less in the same range and give an order of magnitude, although they do not seem to be reproducible. Another approach uses epithelial Madin-Darby canine kidney cells (MDCK) on an array of microneedles [12]. It is a bit difficult to compare the data because the matrix rigidity is not exactly determined (the crosslinked silicone substrate making the microneedles is known to have an elastic modulus of 1.5 MPa, but nothing is said about the whole equivalent substrate). On such a substrate, MDCK cells exert stresses of 1 kPa, a value similar to the ones developed by fibroblasts. Our results on T24 cell migration clearly show much smaller values of maximum forces, in the range 0.05–0.2 kPa. This is a new and promising result, suggesting possible applications of this study to cancer cell migration in general. Other comparisons can be made with endothelial cells [26] moving on RGD-coated polyacrylamide gels (2.5 kPa) with traction forces in the range

**Table 1** Features of T24 cells on different gels

Gel rigidity (kPa)	Max. stress (kPa)	Velocity of migration ( $\mu\text{m}/\text{min}$ )	Stress/rigidity (adimensional)
1.95	0.05	1.2	0.026
6.3	0.14	0.4	0.022
9.9	0.2	0.2	0.02

of 2–8 kPa. To our knowledge, the only case where such small forces are found is that of airway smooth muscle cells (HASM) advancing on collagen-coated polyacrylamide gels ( $E = 1.2$  kPa) [7] exhibiting traction forces in the range of 0.1–0.4 kPa. The precise mechanisms to explain such behaviors still need to be understood.

Durotaxis has been studied previously and reveals the ability of cells to develop large focal adhesions when in contact with a rigid substrate. This type of mechanism, discussed by Choquet et al. [8] is dependent on the growth of contact adhesions mainly of the integrin-cytoskeleton type. In particular, it was shown [22] that traction forces are stronger when the matrix rigidity increases. This work is another confirmation of this result because, as shown in Table 1, the maximum force exerted by T24 cells increases (from 0.05 to 0.2 kPa) with the elastic gel modulus (from 1.95 to 9.9 kPa). Although this result is not new, it shows that this cancer cell line behaves in a similar manner on an elastic gel. In another approach, Saez et al. [29] have shown that MDCK cells on a “fakir” substrate with different needles rigidity exert traction forces proportional to the elastic spring constant of the needles. This would mean that the ratio of force to elasticity is constant, in other words the deformations are the same whatever the rigidity. This is also what was postulated by Discher et al. who made the same observations [11] and found that typical strains on such deformable substrates come close to 3–4%. As shown in Table 1, it seems that such an assumption is not so crude, because our findings come close to a constant ratio of the parameter  $\frac{\text{Max. stress}}{\text{Rigidity}}$ , of the order 2% within experimental uncertainty.

In Fig. 8, we exhibited for the first time the motion pattern of a whole cell in terms of traction forces. This way of locomotion is similar for several types of cells. Only keratocytes [6, 20] have the ability to move with a “crescent” shape by pulling mainly on the sides. The way T24 cells move is more standard and comparable to the classical four-step picture [1] which requires the formation of a lamellipodium at the front, the development of new focal adhesions, the contraction of the cell, and the release of bonds at the rear. Figure 8 illustrates these mechanisms perfectly in terms of forces. Our T24 cell first explores new regions until it binds, then it pulls on these bonds to detach the rear part (uropod). We have determined the velocity of migration of such a motion; it is presented in Table 1. We can clearly see that the cell velocity is larger on less rigid gels. This is in agreement with other works [11, 22], and this idea is explained by the ability of a less-adhering cells to move faster, as they do not require to detach strong bonds. Finally, we may conclude that cell migration is a very complex mechanism which requires to take into account several aspects: cell adhesion/substrate affinity, cell microrheology [34], i.e. its ability to change its mechanical properties, and cell signaling as well as biochemical activity. A clear example of this complexity is given by the bell shape of the migration velocity curve as a function of substrate

ligand density [24]. We do not pretend to give an answer to this difficult mechanism, but the simple resolution proposed here already retains the major common aspects of cell migration.

The present method has been applied to study the traction ability of T24 cancer cells adhering to a polyacrylamide substrate of tuned stiffness, with Young moduli ranging roughly from 2 to 10 kPa. Further statistical analysis are still required to investigate more results. Although this technique may not be as accurate as recently proposed ones [23,31], it still allows to confirm features already observed with other cells (influence of substrate rigidity, forces, velocities), as shown here. It may become a very valuable tool to quickly study the dynamics of migrating cancer cells, in relation with their invasiveness. In addition, other aspects of cell properties (interactions, collective effects, time-dependent processes) might also be studied efficiently.

**Acknowledgments** The authors are indebted to Luigi Preziosi for fruitful discussions about the content of this paper. This research was partially supported by the EU Marie Curie Research Training Network MRTN-CT-2004-503661 “Modelling, Mathematical Methods and Computer Simulation of Tumour Growth and Therapy”. Image acquisition was performed using the microscopy facility of the Institut Albert Bonniot. This equipment was partly funded by “Association pour la Recherche sur le Cancer” (Villejuif, France), and the Nanobio program.

## References

1. Alberts, B., et al.: *Molecular Biology of the Cell*, 3rd edn. Garland, New York (1994)
2. Ambrosi, D.: Cellular traction as an inverse problem. *SIAM J. Appl. Math.* **66**, 2049–2060 (2006)
3. Balaban, N.Q., Schwarz, U.S., Riveline, D., Goichberg, P., Tzur, G., Sabanay, I., Mahalu, D., Safran, S., Bershadsky, A., Addadi, L., Geiger, B.: Force and focal adhesion assembly: a close relationship studied using elastic micropatterned substrates. *Nat. Cell Biol.* **3**, 466–472 (2001)
4. Boudou, T., Ohayon, J., Picart, C., Tracqui, P.: An extended relationship for the characterization of Young’s modulus and Poisson’s ratio of tunable polyacrylamide gels. *Biorheology* **43**, 721–728 (2006)
5. Burton, K., Taylor, D.L.: Traction forces of cytokinesis measured with optically modified elastic substrata. *Nature* **385**, 450–454 (1997)
6. Burton, K., Park, J.H., Taylor, D.L.: Keratocytes generate traction forces in two phases. *Mol. Biol. Cell* **10**, 3745–3769 (1999)
7. Butler, J.P., Toli-Nørrellykke, I.M., Fabry, B., Fredberg, J.J.: Traction fields, moments, and strain energy that cells exert on their surroundings. *Am. J. Physiol. Cell Physiol.* **282**, C595–C605 (2002)
8. Choquet, D., Felsenfeld, D.P., Sheetz, M.P.: Extracellular matrix rigidity causes strengthening of integrin-cytoskeleton linkages. *Cell* **88**, 39–48 (1997)
9. Dembo, M., Wang, Y.L.: Stresses at the cell-to-substrate interface during locomotion of fibroblasts. *Biophys. J.* **76**, 2307–2316 (1999)
10. Dembo, M., Oliver, T., Ishihara, A., Jacobson, K.: Imaging the traction stresses exerted by locomoting cells with elastic substratum method. *Biophys. J.* **70**, 2008–2022 (1996)
11. Discher, D.E., Janmey, P., Wang, Y.: Tissue cells feel and respond to the stiffness of their substrate. *Science* **310**, 1139–1143 (2005)
12. du Roure, O., Saez, A., Buguin, A., Austin, R.H., Chavrier, P., Silberzan, P., Ladoux, B.: Force mapping in epithelial cell migration. *Proc. Natl Acad. Sci. USA* **102**, 2390–2395 (2005)
13. Engler, A., Bacakova, L., Newman, C., Hategan, A., Griffin, M., Discher, D.: Substrate compliance versus ligand density in cell on gel responses. *Biophys. J.* **86**, 617–628 (2004)
14. Féréol, S., Fodil, R., Labat, B., Galiacy, S., Laurent, V.M., Louis, B., Isabey, D., Planus, E.: Sensitivity of alveolar macrophages to substrate mechanical and adhesive properties. *Cell Motil. Cytoskeleton* **63**, 321–340 (2006)
15. Fichera, G.: Existence theorems in elasticity. In: Truesdell, C. (ed.) *Handbuch der Physik*, Band VIa/2. Springer, Heidelberg (1972)

16. Galbraith, C.G., Sheetz, M.P.: A micromachined device provides a new bend on fibroblast traction forces. *Proc. Natl Acad. Sci. USA* **94**, 9114–9118 (1997)
17. Harris, A.K., Wild, P., Stopak, D.: Silicone rubber substrata: a new wrinkle in the study of cell locomotion. *Science* **208**, 177–179 (1980)
18. Rasband, W.S.: ImageJ, U.S. National Institutes of Health, Bethesda, Maryland, USA (1997–2007). <http://rsb.info.nih.gov/ij/>
19. Landau, L., Lifschitz, E.: *Théorie de l'Élasticité*. Mir, Moscou (1967)
20. Lee, J., Leonard, M., Oliver, T., Ishihara, A., Jacobson, K.: Traction forces generated by locomoting keratocytes. *J. Cell Biol* **127**, 1957–1964 (1994)
21. Lions, J.L.: *Contrôle optimal de systèmes gouvernés par des équations aux dérivées partielles*, Dunod et Gauthier-Villard, Paris (1968)
22. Lo, C.M., Wang, H.B., Dembo, M., Wang, Y.L.: Cell movement is guided by the rigidity of the substrate. *Biophys. J.* **79**, 144–152 (2000)
23. Merkel, R., Kirchgessner, N., Cesa, C.M., Hoffman, B.: Cell force microscopy on elastic layers of finite thickness. *Biophys. J.* **93**, 3314–3323 (2007)
24. Palecek, S.P., Loftus, J.C., Ginsberg, M.H., Lauffenburger, D.A., Horwitz, A.F.: Integrin-ligand binding properties govern cell migration speed through cell-substratum adhesiveness. *Nature* **385**, 537–540 (1997)
25. Pelham, R.J., Wang, Y.: Cell locomotion and focal adhesions are regulated by substrate flexibility. *Proc. Natl Acad. Sci. USA* **94**, 13661–13665 (1997)
26. Reinhart-King, C.A., Dembo, M., Hammer, D.A.: The dynamics and mechanics of endothelial cell spreading. *Biophys. J.* **89**, 676–689 (2005)
27. Ridley, A.J., Schwartz, M.A., Burridge, K., Firtel, R.A., Ginsberg, M.H., Borisy, G., Parsons, J.T., Horwitz, A.R.: Cell Migration: integrating signals from front to back. *Science* **302**, 1704–1709 (2003)
28. Rincon, A., Liu, I.S.: On numerical approximation of an optimal control problem in linear elasticity. *Divulgaciones Matemáticas* **11**, 91–107 (2003)
29. Saez, A., Buguin, A., Silberzan, P., Ladoux, B.: Is the mechanical activity of epithelial cells controlled by deformations or forces? *Biophys. J.* **89**, L52–L54 (2005)
30. Saez, A., Ghibaudo, M., Buguin, A., Silberzan, P., Ladoux, B.: Rigidity-driven growth and migration of epithelial cells on microstructured anisotropic substrates. *Proc. Natl Acad. Sci. USA* **104**, 8281–8286 (2007)
31. Sabass, B., Gardel, M.L., Waterman, C.M., Schwarz, U.S.: High resolution traction force microscopy based on experimental and computational advances. *Biophys. J.* **94**, 207–220 (2008)
32. Schwarz, U.S., Balaban, N.Q., Rivelino, D., Bershadsky, A., Geiger, B., Safran, S.A.: Calculation of forces at focal adhesions from elastic substrate data: the effect of localized force and the need for regularization. *Biophys. J.* **83**, 1380–1394 (2002)
33. Tan, J.L., Tien, J., Pirone, D.M., Gray, D.S., Bhadriraju, K., Chen, C.S.: Cells lying on a bed of micro-needles: an approach to isolate mechanical force. *Proc. Natl Acad. Sci. USA* **100**, 1484–1489 (2003)
34. Verdier, C.: Review. Rheological properties of living materials: from cells to tissues. *J. Theor. Med.* **5**, 67–91 (2003)
35. Yeung, T., Georges, P.C., Flanagan, L.A., Marg, B., Ortiz, M., Funaki, M., Zahir, N., Ming, W., Weaver, V., Janmey, P.A.: Effects of substrate stiffness on cell morphology, cytoskeletal structure, and adhesion. *Cell Motil Cytoskelet.* **60**, 24–34 (2005)